DISSERTATION

CHARACTERIZATION OF THE UNIQUE BIOMECHANICAL BEHAVIOR OF RIGHT VENTRICLE USING EXPERIMENTAL AND CONSTITUTIVE MODELING APPROACHES

Submitted by

Wenqiang Liu

School of Biomedical Engineering

In partial fulfillment of the requirements

For the Degree of Doctor of Philosophy

Colorado State University

Fort Collins, Colorado

Summer 2022

Doctoral Committee:

Advisor: Zhijie Wang

Christian Puttlitz
David Bark
Adam Chicco

ABSTRACT

CHARACTERIZATION OF THE UNIQUE BIOMECHANICAL BEHAVIOR OF RIGHT VENTRICLE USING EXPERIMENTAL AND CONSTITUTIVE MODELING APPROACHES

Ventricle dysfunction leads to high morbidity and mortality in heart failure patients. It is known that right and left ventricles (RV&LV) are distinct in their embryologic origins, anatomies and functions, as well as the pathophysiology of ventricular failure. However, how exactly the RV is distinct from the LV in their biomechanical properties remains incompletely understood. Furthermore, the prevalence of RV failure is significantly increased in the later stages of diseases such as pulmonary hypertension (PH) and heart failure with preserved ejection fraction, and the clinical management and treatment of RV failure are persistently challenging. This calls for a further understanding of the mechanisms of RV failure including the biomechanical mechanism. In addition, ventricular tissues are viscoelastic, which means both energy storage (originated from elasticity) and energy loss (originated from viscosity) are present during the deformation. However, the investigation of ventricular tissue viscoelasticity is much less than that of the elasticity, and it is largely unknown how the RV viscoelastic behavior changes during RV failure progression and impacts on the physiological function of the chamber.

To fill these knowledge gaps, the overall goal of my study was to investigate the unique biomechanical properties of the RV in its physiological and pathological functions using experimental and constitutive modeling approaches. The Specific Aims are: 1) Develop the experimental protocols and characterize ventricular tissue passive static and dynamic mechanical properties in both large and small animals; 2) Adapted and performed constitutive modeling of ventricular tissue static and dynamic mechanical behaviors; 3) Quantify the changes in RV biomechanics during the maladaptive remodeling induced by pulmonary hypertension. At the completion of my study, I established the ex vivo testing protocols and provided fundamental data regarding static and dynamic mechanical differences between the healthy left and right chambers to delineate the unique biomechanical properties of the RV. I also adapted

the constitutive models to capture static and dynamic mechanical behaviors of the RV. Finally, I quantified the biomechanical changes of the RV during the RV failure development and offered new insights in the contributions of the RV tissue biomechanics to the organ function.

The findings were obtained from both large and small animals' species, which are translational to human diseases and a strong addition to the current literature of RV failure. More importantly, the investigation on the viscoelastic (dynamic) mechanical properties of the RV and the changes of viscoelasticity in RV failure progression is highly novel. The constitutive modeling of the RV biaxial viscoelastic behavior is pioneering and unique in the computational study of the RV. In summary, this study will deepen the understanding of the biomechanical mechanisms of RV failure and assist with the development of new computational tools for diagnosis and treatment strategies.

ACKNOWLEDGEMENTS

This work could not be done without the support of many individuals. Foremost, I would like to express my sincerest gratitude to my advisor, Dr. Zhijie Wang for her guidance and continuous support. I would also like to thank her for giving me the opportunity to join the lab, attending numbers of national wide conferences, training me different skills and giving me the opportunity to pursue a Ph.D. and work on many interesting and challenging projects. These allow me to expand my skill set in multiple areas.

I would also like to express my sincere gratitude to my committee members Drs. Christian Puttlitz, David Bark and Adam Chicco. I am grateful for their continuous support and guidance includes both academic and daily life, and all the helps for my future career development. Furthermore, I would also like to further send my sincerest gratitude to my committee members, individually. Thanks Dr. Puttlitz for bringing me to the modeling world, without taking your finite element class and discussing with you, I could not reach so far. Thanks Dr. Bark for training me the presentation skills and teaching me to enjoy the conference and academicals life. Thanks Dr. Chicco for helping me run the animal study and continuous guidance for my self-improvement.

I would also like to express my sincere gratitude to Dr. Kevin Labus and Dr. Reza Avazmohammadi for their continuous support and guidance for the mechanical testing and modeling development. And thanks Drs. John Petro, Wade Troxell, Bonnie Roberts and Brebbab-Pierce Ellen for their support during my TA life. Thanks for the CVB team: Michael Nguyen-Truong, Kristen LeBar, Kellan Roth, Brian Funfgeld, Matt Ahern, Katie Evans, Elisabeth Gray, Ethan Barron, Courtney Doherty, Megan Frederes and Eddie Kitahara. Thanks for the OBRL team: Dr. Kirk McGilvray, Lucas Nakamura and Cecily Broomfield and Preclinical Surgical Research team: Drs. Eric Monnet, Jeremiah Easley, Brad Nelson and Jun Boon.

Last but not least, I would like to thank my family and friends for their unwavering company and support.

TABLE OF CONTENTS

CHAPTER 1: SIGNIFICANCE AND MOTIVATION [1]

1.1 Background

Cardiovascular diseases (CVDs) are the leading diseases that cause the human death in the U.S even in the world-wide. Arterial stiffening (correspond with hypertension) and ventricles' dysfunction are the key risk factors for cardiovascular morbidity and mortality [1]. Previous studies have shown that the cardiovascular tissue has the viscoelastic property, which means it has both elasticity (stiffness) and viscosity [2], and also showed that the right ventricle (RV) is distinct from the left ventricle (LV) in embryologic origin, anatomy and function [3]. Furthermore, studies have shown that arterial viscoelasticity changes with CVD [4–7], and arterial viscosity is linked with the endothelial function [8]. The RV mechanical property changes with the CVD and the mechanical property is correlated with the chamber function [9,10]. However, the protocols for cardiovascular tissue viscoelasticity measurements have not yet been standardized, furthermore, most previous studies only focused on the elasticity (stiffness) and have ignored the cardiovascular tissue viscoelastic (viscous) behavior and the comparison of the mechanical property between the LV and RV. As a result, there are knowledge gaps of the differences in viscoelastic behavior between the ventricles and the clinical implications of cardiovascular tissue viscoelasticity in disease (hypertension, RV failure) progression. In order to completely understand the mechanism of the CVD progression, it is critical to investigate the **cardiovascular tissue viscoelasticity** under the physiological and pathological conditions.

[1] *This chapter is published as a peer reviewed review article in the Bioengineering (doi.org/10.3390/bioengineering7010002).*

1.2 Significance of Characterize the Ventricle Mechanical Property

Despite the advances in modern management, heart failure (HF) leads to high mortality and morbidity in the U.S.. More than 5 million Americans have HF, and around 550,000 new cases occur every year [11,12]. It is shown that the lifetime risk for developing HF at the age of 40 years old is around 20%, and the risk of HF increases with aging. As the number of elderly (≥65 years old) is expected to grow to 70.3 million in 2030, the prevalence of HF will continue to increase [11,13–15]. Economically, HF is the leading cause of hospitalization [12] with more than $33 billion of expense annually in the U.S. [11]; and in developed countries the burden of HF is likely keep increasing [14,16].

Ventricle dysfunction is the most common cause of heart failure including left-sided HF with preserved ejection fraction (HFpEF) and reduced ejection fraction (HFrEF), as well as right-sided HF secondary to pulmonary hypertension (PH) and congenital heart disease (CHD) [17–24]. The malfunction of the myocardium in these diseases can occur in the left ventricle (LV), right ventricle (RV), or both ventricles (biventricular HF). It is known that the LV and RV have distinct embryological, geometrical and structural properties [25–27], and the mechanism of RV failure is likely to be different than that of the LV failure [28]. However, compared to the LV failure, RV failure has been less understood, and it remains unclear if the two ventricles present similar mechanical behaviors or adaptations in the pathogenesis of ventricular dysfunction.

It is generally accepted that the mechanical property of the myocardium is an important determinant of the ventricular function [9,29]. Indeed, changes in the ventricular mechanical properties during the HF progression have been reported in numerous studies for both LVs and RVs. The alteration of the extracellular environment can result in the dysfunctions of cardiac cells and thus the overall organ function is impaired, which forms a vicious cycle in the maladaptive remodeling of the ventricle. Therefore, it is critical to unravel the roles of the tissue biomechanics in the ventricular dysfunction to inspire new therapies for HF patients.

RVF contributes significantly to the mortality and morbidity in a variety of cardiovascular diseases including pulmonary hypertension, congenital heart disease and left heart failure with preserved ejection

fraction [20–24]. RVF is associated with serious pulmonary diseases that contribute significantly to the morbidity and mortality of patients. The prevalence of RVF is significantly increased in the later stages of pulmonary hypertension. The biomechanical properties of the RV free wall are considered to play a role in its organ function [30,31], and a recent rodent study has reported a correlation between the passive elastic modulus and the end-diastolic volume of the RV [9], with the latter often being used as an index of RV function [32]. However, the comprehensive understanding of the roles of RV biomechanical properties in the *in vivo* function remains a key knowledge gap.

1.3 Characterization of Ventricle Mechanical Behavior

The ventricular free wall is known as an anisotropic and viscoelastic material, which means it has different mechanical behaviors in different directions and presents both elastic and viscous features in dynamic deformations (**Fig. 1.1**). Depending on the mechanical behavior to measure, the mechanical tests can be uniaxial or biaxial (for anisotropic behavior), static or dynamic (for elastic or viscoelastic behavior), and in different testing conditions (e.g., bath medium, temperature, preconditioning protocol, removal of residue stress). To obtain the viscoelastic properties, either stress relaxation/creep tests or cyclic tensile mechanical tests can be used (**Fig. 1.2, detailed discussions in 1.2.2 & 1.2.3**). Then, the viscous behavior is quantified to capture the time-, strain rate-, or frequency-dependent character [28]. In this review, we will focus on the macroscopic mechanical measurements and thus the experimental methods using atomic force microscopy (AFM) or length-tension tests on the isolated cardiac muscle (e.g., papillary muscle) or cardiomyocytes are not included.

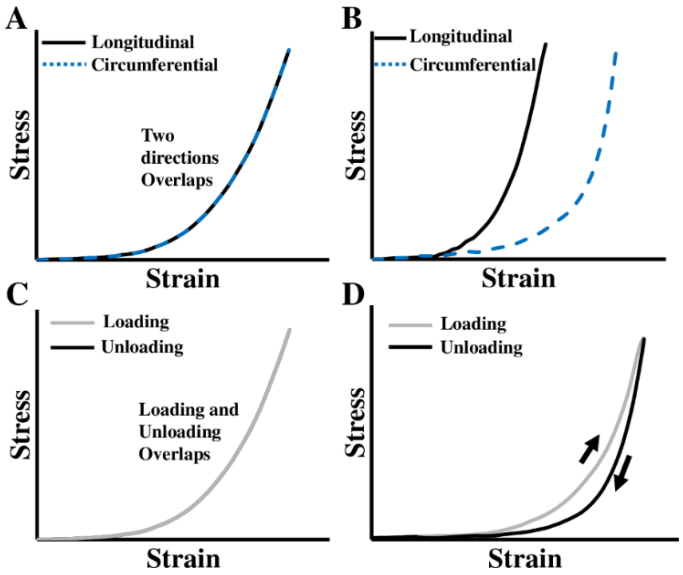

Fig. 1.1 (A)-(B) Stress-strain curves obtained from different directions in isotropic and anisotropic materials, respectively; (C)-(D) Stress-strain curves obtained from loading and unloading periods of cyclic deformation in nonlinear elastic and viscoelastic materials, respectively.

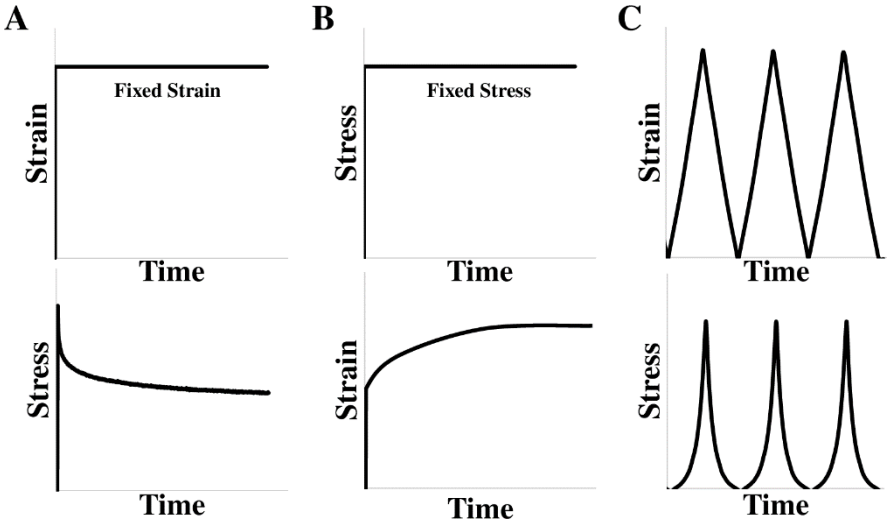

Fig. 1.2 Different mechanical tests for the viscoelastic properties measurement. (A) Stress relaxation test, (B) creep test and (C) displacement-controlled cyclic tensile mechanical test. The upper panels illustrate the mechanical inputs and the lower panels illustrate the mechanical responses of the material in these tests.

1.3.1 Preconditioning and Residual Stress Measurement

As is needed in other biological tissues' mechanical tests, preconditioning is often performed prior to the data acquisition to ensure a constant and accurate mechanical behavior of the tissue [33]. This procedure has been described in the mechanical tests of the cardiac tissues [27,34–41]. The number of preconditioning cycles in the biaxial/uniaxial tests varied among 5-10 cycles for the animal (canine, bovine and murine) myocardium [27,34,36–41], whereas Sommer et al. and Fatemifar et al. showed that after 3-5 cycles the human

heart tissue reached stable biaxial behavior [35,42]. Due to the viscoelastic nature of the tissue, sufficient resting period should be given between the tests. It is suggested that ten times of the previous mechanical testing period is appropriate for the tissue to be free from the 'memory' of former deformations [43,44].

The residual stress is the stress that remains in the tissue after all external loads are removed [45]. The presence of residual stress in myocardium has been observed in both large animal (porcine) and small animal (rat) ventricles [46–49]. The exact cause of residual stress in biological tissues is not fully clear, but the different growth rates at different layers or directions of the tissue are likely the reason [48]. The residual stress is generally considered 'beneficial' to the tissue. From the study of opening angle in an arterial ring, it is found that the presence of residual stress leads to a homogenous distribution of the circumferential wall stress through the vessel thickness [50]. For myocardium, Shi et al. measured the residual stress by a curling angle characterization and found that the residual stress protected the ventricle wall by reducing myocardial stress during LV diastolic expansion [46]. The measurement of residual stress in myocardium is seldom seen in *ex vivo* mechanical tests and future experimental studies may consider to include such measurement.

1.3.2 Uniaxial and Biaxial Tensile Mechanical Tests

Uniaxial and biaxial mechanical tests are the most common methods to investigate the ventricular mechanical property after tissue harvest (**Fig. 1.3**). While the uniaxial mechanical test offers a quicker and easier examination of the material mechanical property, the biaxial mechanical test better mimics the in vivo loading conditions and provides more comprehensive measurements of the anisotropic mechanical behavior [9,27,29,34,51–53]. Both methods have been used in prior studies of LV and RV mechanical properties [9,27,42,51–58,34–41] (please see **Table 1.1** for a summary of these studies).

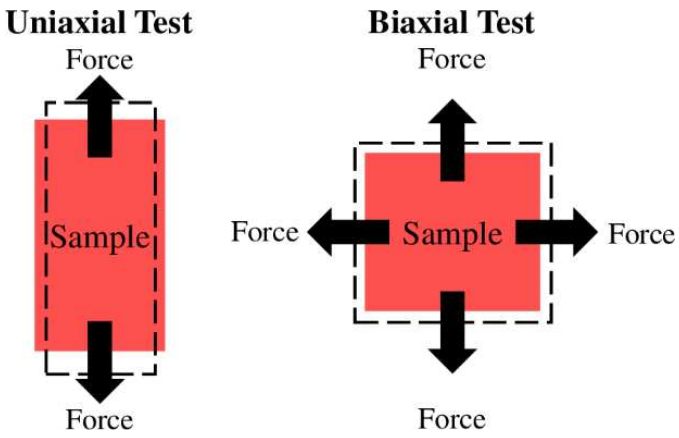

Fig. 1.3 Diagrams of the uniaxial (left) and biaxial (right) tissue mechanical tests. Dashed rectangles illustrate the deformed configurations of the sample after the mechanical stretch.

Furthermore, when the entire cycle of stress-strain data is used (i.e., including loading and unloading curves), the ventricular viscoelastic behavior can be derived from the hysteresis stress-strain loop (**Fig. 1.4**). However, the biaxial measurement of viscoelasticity is less common than the elasticity measurement and only sporadic studies have examined canine [51], porcine [58] and human ventricles [35]. Recently, the viscoelasticity of neonatal porcine LVs and RVs was obtained using the cyclic uniaxial mechanical tests. The myocardial hysteresis was quantified by the ratio of the area enclosed in the hysteresis loop over the area beneath the loading curve, but the elasticity of these ventricles was not quantified [58]. To our knowledge, the first human myocardium viscoelastic behavior quantified by biaxial testing was reported by Sommer et. al. [35]. Increased stress and hysteresis area were evident with increased stretch rate (from 3 mm/min to 30 mm/min), but no viscoelastic property (e.g., elasticity or viscosity) was quantified from these biaxial tests.

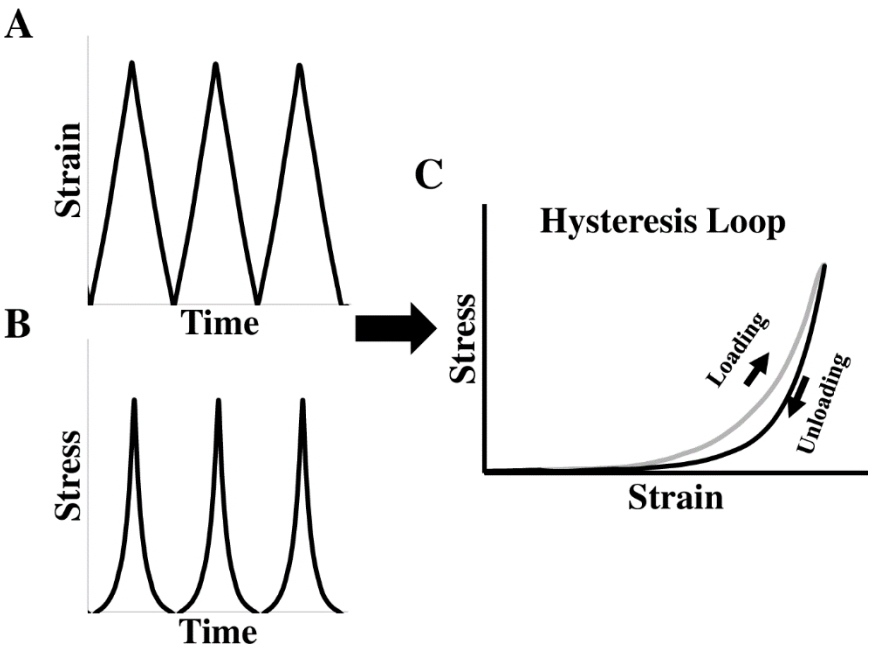

Fig. 1.4 Hysteresis stress-strain loop obtained from the cyclic tensile mechanical tests. Triangle or sinusoidal mechanical loadings are typically applied during the cyclic stretches. (A) – (B) Representative strain and stress curves as a function of time in the tensile mechanical test; (C) Representative hysteresis loop derived from the synchronized stresses and strains in (A) and (B).

Table 1.1 Summary of the prior biaxial/uniaxial tensile mechanical tests performed in ventricular tissues. The experimental details on testing methods and conditions are listed as well. Viscoelastic mechanical studies are marked with * in the Method.

Sample	Method	Axial Definition	Preconditioning Cycles	Strain Range/Rate	Bath Medium	Temperature	Immerse Condition
Canine RV [27]	Biaxial	Main fiber direction	10	30% /	Water with recycle required oxygenated carioplegic solution	Room temperature	Immersed
Rat RV [9]	Biaxial	Outflow tract	/	/ /	Modified Kreb's solution with 2,3-butanedione 2-monoxime and oxygen	/	Immersed
Bovine LV/RV [34]	Biaxial and uniaxial	Main fiber direction	5	20% 0.1-0.75 cm/s	Saline with O_2 and CO_2 (pH=7.4)	Physiological range	Immersed
Human LV/RV [35]	Biaxial* and Triaxial	Main fiber direction	4	20% Quasi-static	CPS with 20 mM BDM	37°C	Immersed
Canine LV [36]	Biaxial	Main fiber direction	≥7	/ 50s/cycle	Modified Kreb's Ringers solution with a ~ 10 mM potassium, O_2 and CO_2 (pH=7.4)	30°C	Float
Canine LV [37]	Biaxial	Main fiber direction	5-7	20% 0.05 or 0.1Hz	bath containing the oxygenated solution	Room temperature	Immersed
Canine LV [38]	Biaxial	Main fiber direction	7-10	5-27% 0.1 Hz	oxygenated cardioplegic solution	Room temperature	Immersed
Rabbit LV [39]	Biaxial	Main fiber direction	Several	/	BDM-Krebs solution	/	Immersed
Ovine LV [40]	Biaxial	/	10	20-25% 0.5Hz	isotonic cardioplegic solution (pH:7.4)	20°C	Immersed
Murine RV [41]	Biaxial	Outflow tract	10	5-25 kPa /	Modified Kreb's solution with BDM	Room temperature	Immersed
Human LV/RV [42]	Biaxial and uniaxial	Main fiber direction	5	40% ~6 mm/min	Phosphate-buffered saline	37°C	Immersed
Canine LV [51]	Biaxial and uniaxial*	Main fiber direction	9	/ 0.0025-0.25 mm/s	Tyrode solution with O2 and CO2 (pH:7.4)	29.5-30.5°C	Float

Rat RV [52]	Biaxial	Outflow tract	/	/ /	Modified Kreb's solution with BDM and oxygen	Room temperature	Immersed
Canine LV/RV [55]	Biaxial	Apex to base	/	/ /	Oxygenated solution	Room temperature	Immersed
Ovine LV/RV [56]	Biaxial	Main fiber direction	10	40% 8s per cycle	Saline bath	37°C	Immersed
Rat LV [57]	Biaxial and uniaxial	/	10	/ 0.5mm/s	PBS	37°C	Submerged
Porcine LV/RV [58]	Biaxial and uniaxial*	Main fiber direction	/	/ 0.5mm/s	PBS	37°C	Submerged

1.3.3 Stress Relaxation and Creep Tests

Stress relaxation and creep tests are traditional methods to measure the viscoelasticity of soft tissues such as tendon, cartilage and heart valves [59–65]. The stress relaxation test is the recording of a time-dependent stress reduction under a fixed strain/stretch, whereas the creep test is the recording of a time-dependent strain increase under a constant stress/load (**Fig. 1.2**) [28]. These methods have been applied to the myocardium or papillary muscle [35,66–70], although slightly different testing protocols and conditions were adopted (please see **Table 1.2**).

Table 1.2 Summary of the prior studies with stress relaxation or creep tests on ventricular tissues.

Sample	Method	Ramp Speed	Stretch Level	Duration	Bath Condition
Human LV/RV [35]	Stress relaxation	100 mm/min	10%	5 min	CPS with 20 mM BDM at 37°C
Rabbit LV papillary muscle [66]	Stress relaxation and creep	/	/	5 min	Ringer-Lacke solution with O_2, CO_2, pH=7.38
Cats, Rabbits papillary muscle; Frog and Turtle LV [67]	Stress relaxation and creep	/	20%, 30%	/	Tyrode solution with O_2, CO_2, pH=7.3, at 24°C (for papillary muscles); Modified PBS solution at pH=7.3 (for LVs)
Chicken embryonic heart [68]	Stress relaxation	Fast linear	10%, 20%, 40%	10 min	Oxygenated KHB-cardioplegia solution at 35°C
Chicken LV/RV [69]	Stress relaxation	1000% axial strain/s	5%, 10%, 20%, 30%	5 min	Oxygenated KHB-cardioplegia solution at 35°C
Cat LV papillary muscle [70]	Stress relaxation	/	/	/	Oxygenated Krebs-Ringer's solution at 20°C

The *ex vivo* measurement discussed above can provide better controls of the experimental conditions (e.g., the strain rage, cardiac muscle tone, etc.) and eliminate the interference of physiological factors (e.g., blood pressure, heart rate, hormone levels) in the mechanical properties of the ventricle tissues. However, the *ex vivo* tests require tissue removal and are often limited by the contractile state of cardiomyocytes (passive only) and the configuration of the tissue (non-physiological stretches in the biaxial directions). Therefore, the *in vivo* measurements could provide useful information of the tissue mechanical behavior that is absent in the *ex vivo* conditions.

1.3.4 The Elasticity Measurement for Ventricles: In Vivo

At the whole-organ level, pressure-volume (PV) loop measurement (**Fig. 1.5**) is the golden standard to assess the ventricle performance invasively by inserting a PV catheter into the ventricle lumen [29]. The end-diastolic pressure-volume relation (EDPVR) derived from the steady-state PV loops is often used to represent the ventricular passive stiffness. Similarly, diastolic stiffness can also be estimated by the ratio of end-diastolic pressure (EDP) to end-diastolic volume (EDV) [71,72]. In addition, chamber compliance, which is the ratio of ventricular volume change over pressure change during a cardiac cycle ($\Delta V/\Delta P$), has also been used to describe the ventricle stiffness [73–75]. Another type of ventricular elastance, end-systolic pressure-volume relation (ESPVR or Ees), can be derived from a serious PV loops during a temporal vena cava occlusion or estimated by other formulas with a single beat technique. Ees is considered a measure of load-independent contractility of the ventricle [76]. Interestingly, this parameter has been viewed as an index of *systolic* stiffness of the ventricle [71,72].

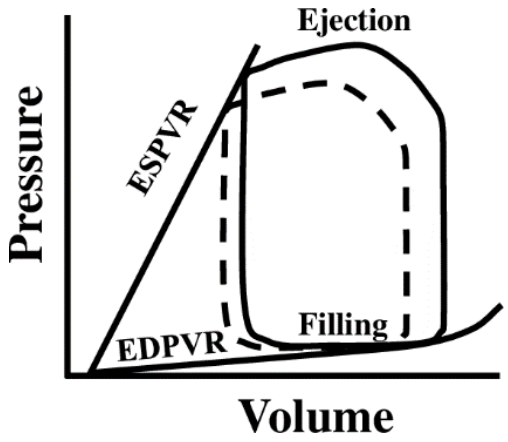

Fig. 1.5 Diagram of the pressure-volume (PV) loop obtained from cardiac catheterization. The loop in solid line denotes a steady-state PV loop, whereas the loop in dotted line denotes a transient loop obtained by brief vena cava occlusion to reduce the ventricle filling. ESPVR: end-systolic pressure-volume relationship; EDPVR: end-diastolic pressure-volume relationship.

Non-invasively, cardiovascular magnetic resonance (CMR) and speckle-tracking echocardiography (STE) are alternative methods to measure the myocardial performance [77–79]. Depend on the imaging technique, 3D geometry is reconstructed and the strain and strain rate are then calculated as the indicators of ventricle stiffness. The *in vivo* 3D strain analyses can be achieved by applying a so-called hyperelastic warping method to various types of medical images such as cine CMR or echocardiography, from which global or regional myocardial strain can be calculated [80–82]. The hyperelastic warping method is a deformable image registration technique, which uses a deformable finite element mesh to register the target image to the reference image. The reference image is typically selected as the image at the end-diastole [83,84]. Then, the 3D deformation of the ventricular geometry can be derived over a cardiac cycle, and the strains in different directions (longitudinal, circumferential and radial) are calculated [82–85]. This technique is powerful because it enables the measurement of the myocardial strain temporally and spatially, and both ventricles can be examined at the same time to further investigate the ventricular interactions in HF patients. These strain measurements could potentially offer new diagnostic or prognostic indices for LV or RV dysfunction [82,86]. However, it should be noted that the strain is essentially a measure of relevant deformation of the ventricular chamber, and such deformation is affected by both the passive stiffness and active contraction of the ventricular wall. Therefore, it is not a direct measurement of ventricular stiffness.

The direct non-invasive measurement of ventricular stiffness (e.g., elastic modulus) can be obtained by magnetic resonance elastography (MRE) [87,88]. MRE is a phase contrast magnetic resonance imaging (MRI) technique. The underlying principle of this imaging method is based on the fact that the different stiffness of a material generates different shear wave length. With an induction of shear waves in the tissue region of interest, the waves are encoded in the phase of MR image and the wave images can be converted to the stiffness maps with temporal and spatial information included. MRE has been investigated in animals and a couple of clinical studies to study the effect of myocardial infarction, aging, hypertension or hypertrophic cardiomyopathy on cardiac stiffness. A good review of MRE in cardiovascular tissues is given by Khan et. Al [87]. However, although the methodology has been validated in animals with the gold standard PV loop, the elastic moduli reported in human subjects (<12 kPa) are much lower than the values reported in animals or in *ex vivo* measurements (in hundreds of kPa) [87]. Thus more work is warranted in this area.

Finally, with the combination of medical imaging and computational modeling such as finite element methods, it is also possible to estimate the ventricular material properties using 'inverse modeling' [89–94]. These computational methods are briefly reviewed in [95–97].

1.3.5 The Viscoelasticity Measurement for Ventricles: In Vivo

The viscoelasticity of ventricles has been occasionally reported with the measurement of cyclic stress-strain relations. Some early studies measured the viscoelasticity of the LV from healthy canine and human hearts by individual measurements of pressure and volume *in vivo* [98–100]. Briefly, cardiac catheterization was performed and a micromanometer was introduced into the LV to measure the pressure. In the meanwhile, echocardiogram was performed and the endocardial diameter and the posterior wall thickness were recorded. These data were synchronized and further used to calculate the meridional wall stress and midwall strain during the diastolic phase. Viscoelastic properties in the 'passive' state of the LV were then derived from the nonlinear stress-strain curve using an empirical model of viscoelasticity. Interestingly, these studies were all published in late 1970s and early 1980s, and there is no further investigation of the *in vivo* measurement of ventricular viscoelasticity.

1.4 Current Understanding of Ventricles – Tissue with Anisotropy and Viscoelasticity

1.4.1 Anisotropic Behavior of Ventricles

The characterization of the anisotropic behavior of ventricles is highly dependent on the definition of biaxial coordinate system. To date, there are two main types of coordinate system: the main fiber and cross-fiber coordinate system [27,42,56], and the outflow tract and cross-outflow tract coordinate system [9,41,52]. By using the former coordinate system, it is consistently observed that the tissue behaves stiffer in the fiber direction compared to the cross-fiber direction [34]. However, the degrees of anisotropy in the ventricles are not consistent among observations. Sacks et al. reported that the canine RV had greater anisotropy than the LV [27]. Similarly, Ahmad et al. found that the neonatal porcine RV had significantly greater anisotropy than the LV in different anatomic regions [101]. However, Javani et al. reported that the ovine LV was more anisotropic than the RV [56]. Ghaemi et al. reported that both LV and RV were anisotropic but there was no comparison between these chambers [34]. Therefore, there is no consensus about the difference in anisotropic behavior between a healthy LV and RV. The discrepancies may depend on the age and species of samples, methods of tissue selection and preparation and testing protocols. Besides, it has been noted that the determination of the main fiber direction is challenging and could induce variations in the anisotropic behavior as well [27].

By using the second coordinate system, Valdez-Jasso et al. found that the rat RV had greater stiffness in the outflow tract direction compared to the cross-outflow tract direction [41], and Hill et al. found that the degree of rat RV anisotropy increased in the pressure overload state [52]. However, the mechanical difference between the RV and LV *in healthy adults* remains inconclusive. The comparison between the LV and RV will lay down fundamental information for RV mechanics and will aid in the understanding of the unique biomechanical mechanisms of RV dysfunction.

1.4.2 Viscoelastic Behavior of Ventricles

The viscoelastic property of a material is manifested by the non-overlapping of loading and unloading stress-strain curves over an entire cycle [28]. Such behavior has been observed for both LV and RV tissues [28,51,102], which implies that the ventricular elasticity (or stiffness) is dependent on the strain rate, and there is energy loss during the cyclic deformation due to the viscous property of the ventricle. The viscoelasticity of ventricular tissues was initially thought to be negligible but recent evidence suggesting that this is not true. Furthermore, there are lack of studies reported the ventricle viscoelasticity experimentally. Particularly, Ahmad et al. found that the neonatal porcine ventricles exhibited greater viscoelasticity at the mean-fiber direction compared to the cross-fiber direction, and the LV had greater viscoelasticity than the RV [58]. Sommer et al. firstly measured the viscoelastic property of human LVs and RVs, and their findings also showed a larger hysteresis in the mean-fiber direction than the cross-fiber direction [35]. Our own recent study in ovine RVs showed that the chronic pressure overload increased hysteresis (viscosity) in both directions (unpublished data (**Fig. 1.6**)).

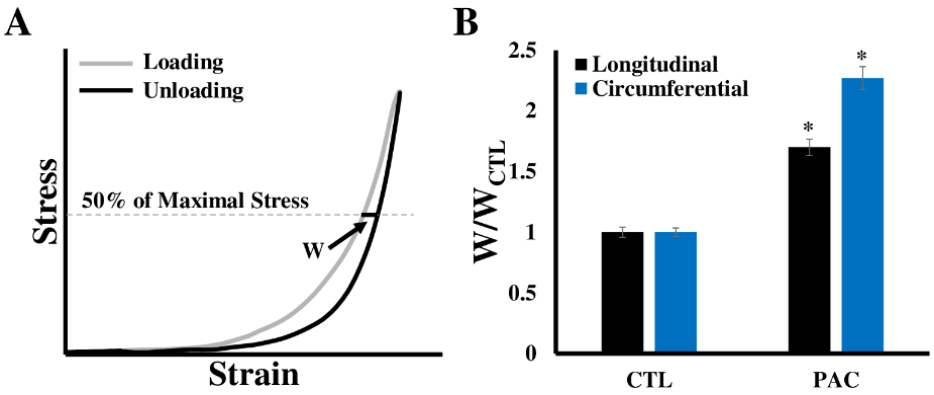

Fig. 1.6. Change in the right ventricle (RV) viscosity after three-month pressure elevation in adult sheep. Pressure elevation was induced by pulmonary artery constriction (PAC). (A) Viscosity is defined as the loop width (w) at the 50% of the maximal stress of the loop; (B) Loop width normalized by the average loop width of the control RVs in the individual direction. CTL: control; PAC: pulmonary artery constriction. *$p < 0.05$ vs. CTL in the same direction.

1.5 Computational Modeling of Ventricular Biomechanics

Both empirical models and constitutive models have been applied to characterize the nonlinear, biaxial mechanical behavior of ventricles. Because of the nonlinear, 'J'-shaped stress-strain curve, the use of an

exponential component is common in empirical models. But these models provide little information on the relations of physical quantities or physiological conditions of the tissue, and thus constitutive models are developed to better describe the myocardium tissue mechanics [54]. With certain assumptions (hyperelasticity, incompressibility, homogeneity, etc.), a strain energy function (W) is defined to relate the mechanical loadings (stress) to the geometry changes (strain). The determination of the strain energy function is the key in constitutive models. Based on the model parameters included in the strain energy function, different material's properties can then be derived. A thorough review of the modeling for tissues biaxial mechanical properties can be found in Ref [53,54].

Classic empirical models to describe the tissue viscoelasticity are composed of springs and dashpots that represent the elastic and viscous behaviors, respectively. The two basic models of these are also known as the Maxwell model (consisting of a spring and a dashpot in series) and Kelvin-Voight model (consisting of a spring and a dashpot arranged in parallel). Different combinations of the spring and dashpot elements have been used to describe the ventricle and papillary muscle viscoelasticity. For example, a spring connected to two Maxwell elements in parallel was used to form a 1D viscoelastic model for the papillary muscle of the LV [70]. An elastic term and a viscous term in parallel were used to describe the viscoelasticity of the LV in different conditions [51,99,100,103,104]. In the constitutive models of ventricular viscoelasticity, a finite element analysis with orthotropic viscoelastic model has been used to describe the passive myocardium viscoelastic behavior [30]. Another option to represent the viscoelastic behavior is by the hereditary (or convolution) integral with a strain-dependent Prony series, which has been found to successfully capture the strain- and time-dependent behavior in *non-cardiovascular* tissues [63,105–107]. A nice review of constitutive models of cardiac tissue viscoelasticity can be found in Ref [30,108,109].

1.6 Biomechanical Changes of Ventricles in Heart Failure Development

Heart failure is associated with extensive remodeling of the tissue involving changes in extracellular matrix (ECM) (e.g., fibrosis or accumulation of collagen), recruitment of inflammatory cells (e.g., macrophage infiltration), upregulated oxidative stress (e.g., increased ROS), and altered metabolic activity

(e.g., increased glycolysis) [110–113]. These changes not only lead to the malfunction of various cells in the myocardium but also result in the impairment in the mechanical and hemodynamic functions of the organ. Because of our focus on the biomechanical behavior of the ventricle in this review, we will restrict our discussions to the extracellular matrix (ECM) proteins (particularly collagen) as they are the main determinant of mechanical properties including viscoelasticity [28,104,114].

The myocardium ECM consists of proteins such as collagen, elastin, fibronectin, proteoglycan and laminin. Among these molecules, collagen is the most abundant ECM protein in the adult heart, with at least 5 different types of collagen (I, III, IV, V and VI) that have been identified [115]. Types IV and V collagen are mostly found in the basement membrane of the cardiomyocytes, and types I and III collagen are the main constituents in the ECM: type I collagen represents 75~80% of total collagen content and type III collagen represents approximately 15~20% of the total collagen [111]. The collagen metabolism, i.e., the balance of collagen synthesis and degradation, is regulated by the mechanical loadings (i.e., pressure-overload, volume-overload) and leads to rapid changes in cardiac ECM and mechanical properties [116–118].

Ventricular fibrosis (i.e., collagen accumulation) is frequently observed in cardiac remodeling in both LV failure and RV failure [115,119,120], and the cessation of the accumulation or cross-linking of collagen has been shown to reverse the maladaptive remodeling and improve ventricular function [118,121,122]. However, the story about collagen accumulation is not as simple as firstly viewed if more aspects are considered. For example, in the late stage of HF with the LV dilation and wall thinning, conflicting results are given in collagen metabolism: some report that (type I) collagen is degraded and the extent of collagen cross-linking is reduced [117,123,124], whereas other report elevated collagen content or cross-linking [122,125]. In response to pressure overload, the findings on LV collagen deposition are not consistent either: increased collagen [126], decreased collagen [127,128], and no change in collagen [129] in the ventricles were all reported. During the progression of RV dysfunction in pulmonary hypertension, the total collagen was increased with respect to time but the percentage of collagen cross-linking was decreased [73]. This suggests that the role of collagen content and cross-linking in RV dysfunction may be different. Overall, the variations in collagen deposition depending on the etiology or the specific phase of the heart disease development suggest that collagen

metabolism is a key factor contributing to the heterogeneity of the heart failure. Therefore, further examination of the collagen metabolism in LV/RV failure progression is required.

While these previous studies investigated the role of fibrosis in the HF progression, the link of collagen deposition to the mechanical changes is another open area of research. Some biomechanical studies have quantified both biaxial mechanical properties and collagen/myo-fiber orientation in the ventricle (mouse RV, infarcted LV) [35,41,57]. However, how the collagen orientation or total amount is correlated with the ventricular anisotropy or elasticity remains unknown. We recently exposed the ovine RVs to pressure overload using a pulmonary artery constriction model. The chronic remodeling of the RV led to increased collagen deposition. More interestingly, we observed a larger increase in type III collagen than in type I collagen (unpublished data) (**Fig. 1.7**). Further investigations on the structure-function relations of the ventricles in different physiological conditions will provide more insights into the role of fibrosis in heart failure development.

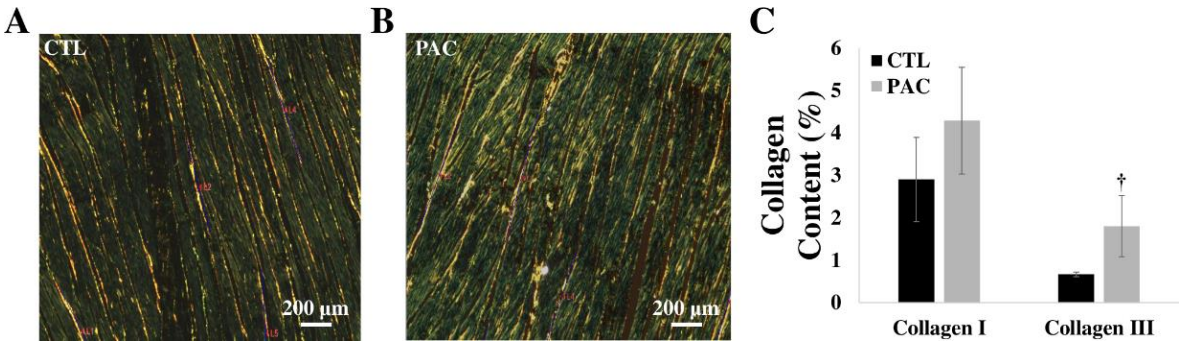

Fig. 1.7. Collagen accumulation in hypertensive ovine RVs. (A)–(B) Representative histology images of the Picro Sirius Red staining of RVs in control and hypertensive groups, respectively; (C) Increase in type III collagen in the hypertensive RVs. CTL: control; PAC: pulmonary artery constriction. †p = 0.05 vs. CTL.

1.7 Clinical Relevance of Ventricular Mechanical Alterations

1.7.1 Significance of Ventricular Stiffening in Heart Failure

In chronic heart diseases, the myocardial structure and morphology changes lead to the stiffening of the ventricles [17–19,130–132]. These mechanical changes are considered as the changes in the passive mechanical behavior of the tissue, which is often related to the diastolic dysfunction [99,133]. The stiffening of the ventricle impedes the filling of blood during diastole and thus leads to an increased filling pressure (EDP) at the same

chamber volume. This is a key mechanism for the progression of LV dysfunction, particularly in the heart failure with preserved ejection fraction (HFpEF) [133,134]. It is further demonstrated recently that the increase in passive stiffness proceeds the LV diastolic dysfunction [135]. Consequently, reducing LV stiffness has become one therapeutic target for HFpEF patients [136]. Ventricular stiffening also occurs in other conditions such as hypertension, aging and hypertrophic cardiomyopathy [71,87], and the former two conditions are well-known risk factors of heart failure.

In addition, the increased myocardium passive stiffness could result in an increase in stiffness during the systolic contraction, which is why the age-related increases in Ees (ESPVR, the elastance at systole) and EDPVR are correlated, regardless of the changes in arterial load [72]. While Ees is considered as a measure of ventricular contractility, it is possible that the systolic function of the ventricle is affected by the passive stiffness. Indeed, reduced LV strains in longitudinal and circumferential directions have been reported in HFpEF patients compared to the normal and hypertensive heart disease patients, which indicates the stiffening of the LV. Furthermore, these strains were correlated to the LV systolic function (ejection fraction) but not the diastolic function (E' or E/E'), suggesting a link of the LV strain (indicator of stiffness) with the systolic performance [137].

Finally, the stiffening of LV could impact on the pulmonary circulation as well. Pulmonary edema and elevation in pulmonary venous pressures are observed as a result of the backward transmission of elevated left-sided pressures into the pulmonary circulation. This leads to the development of post-capillary pulmonary hypertension (PH), which is commonly found in HFpEF patients [138]. Therefore, both ventricles become dysfunctional and this is probably why HFpEF is a more challenging type of heart failure to manage.

RV stiffening is consistently observed in a variety of PH etiologies as well as left-sided heart failure. Using non-invasive echocardiography, reduced RV longitudinal strains have been reported in pre-capillary PH (pulmonary arterial hypertension) patients and PH patients with other etiologies [139–141]. Increased RV stiffness was frequently reported in the preclinical studies of PH via the *ex vivo* tissue mechanical tests [9,41,52]. But the impact of RV stiffening in the ventricular performance is rarely investigated. Recently, a

correlation of RV longitudinal elastic modulus and the end-diastolic volume (EDV) was found in rodent RVs during PH development [9]. This is the first study to correlate the RV mechanics to the hemodynamic function of the organ. In another study of patient-specific biventricular constitutive modeling, a ratio of RVEDV/LVEDV was found to increase with increased RV free wall stiffness in PH patients, and this new index was strongly and inversely correlated with the RV peak contractility [142]. A following study from the same group suggested that this index can be used to estimate RV contractility [86]. Therefore, in both left and right sides of the heart, the passive mechanical behavior is linked to the diastolic function as well as the contractility of the ventricle. This suggests that the improvement in the tissue mechanics may be a therapeutic target for heart failure patients.

1.7.2 Significance of Altered Ventricular Viscoelasticity in Heart Failure

The viscoelastic properties of the ventricle can impact on the *in vivo* function. To date, the discussion of the relevance of ventricular viscoelasticity is mainly restricted to the diastolic function. Firstly, because the viscoelastic property is strain-rate dependent and because the early and later diastole have different filling rates, the diastolic viscoelasticity of the ventricle is time-dependent [98,99,143,144]. Furthermore, evidence have shown that the viscoelasticity of the ventricle changes from normal to diseased states. Increased viscosity of the LV has been reported in different types of patients (severe aortic regurgitation, congestive cardiomyopathy with preserved and reduced ejection fraction) with the dilated, hypertrophy LVs [98]. Our preliminary data in pressure-overloaded ovine RVs also showed an increased viscosity in both biaxial directions compared to the healthy RVs **(Fig. 1.6)**. While these data indicate a change of tissue viscoelasticity in HF progression, the exact role of the viscous property in the ventricular function is not well understood.

1.8 Knowledge Gaps

Ventricle dysfunction leads to high morbidity and mortality in heart failure patients. It is known that right and left ventricles (RV&LV) are distinct in their embryologic origins, anatomies and functions, as well as the pathophysiology of ventricular failure. However, how exactly the RV is distinct from the LV in

their biomechanical properties remains incompletely understood. It is well accepted that the passive mechanical properties of the ventricle are important for the diastolic function, and thus heart diseases with a change in myocardial mechanical properties are often associated with diastolic dysfunction [145–149]. However, if and how much of the systolic function is affected by the passive mechanical properties remain unclear. Furthermore, the prevalence of RV failure is significantly increased in the later stages of diseases such as pulmonary hypertension (PH) and heart failure with preserved ejection fraction, and the clinical management and treatment of RV failure are persistently challenging. This calls for a further understanding of the mechanisms of RV failure including the biomechanical mechanism. In addition, ventricular tissues are viscoelastic, which means both energy storage (originated from elasticity) and energy loss (originated from viscosity) are present during the deformation. However, the investigation of ventricular tissue viscoelasticity is much less than that of the elasticity, and it is largely unknown how the RV viscoelastic behavior changes during RV failure progression and impacts on the physiological function of the chamber.

1.9 Special Aims

To fill these knowledge gaps, the overall goal of my study was to investigate the unique biomechanical properties of the RV in its physiological and pathological functions using experimental and constitutive modeling approaches. The Specific Aims are: 1) Develop the experimental protocols and characterize ventricular tissue passive static and dynamic mechanical properties in both large and small animals; 2) Adapted and performed constitutive modeling of ventricular tissue static and dynamic mechanical behaviors; 3) Quantify the changes in RV biomechanics during the maladaptive remodeling induced by pulmonary hypertension.

1.10 Significance

At the completion of my study, I established the ex vivo testing protocols and provided fundamental data regarding static and dynamic mechanical differences between the healthy left and right chambers to

delineate the unique biomechanical properties of the RV. I also adapted the constitutive models to capture static and dynamic mechanical behaviors of the RV. Finally, I quantified the biomechanical changes of the RV during the RV failure development and offered new insights in the contributions of the RV tissue biomechanics to the organ function.

The findings were obtained from both large and small animals' species, which are translational to human diseases and a strong addition to the current literature of RV failure. More importantly, the investigation on the viscoelastic (dynamic) mechanical properties of the RV and the changes of viscoelasticity in RV failure progression is highly novel. The constitutive modeling of the RV biaxial viscoelastic behavior is pioneering and unique in the computational study of the RV. In summary, this study will deepen the understanding of the biomechanical mechanisms of RV failure and assist with the development of new computational tools for diagnosis and treatment strategies.

1.11 Outline

Figure 1.8 is the diagram for the overall goal and specific aims.

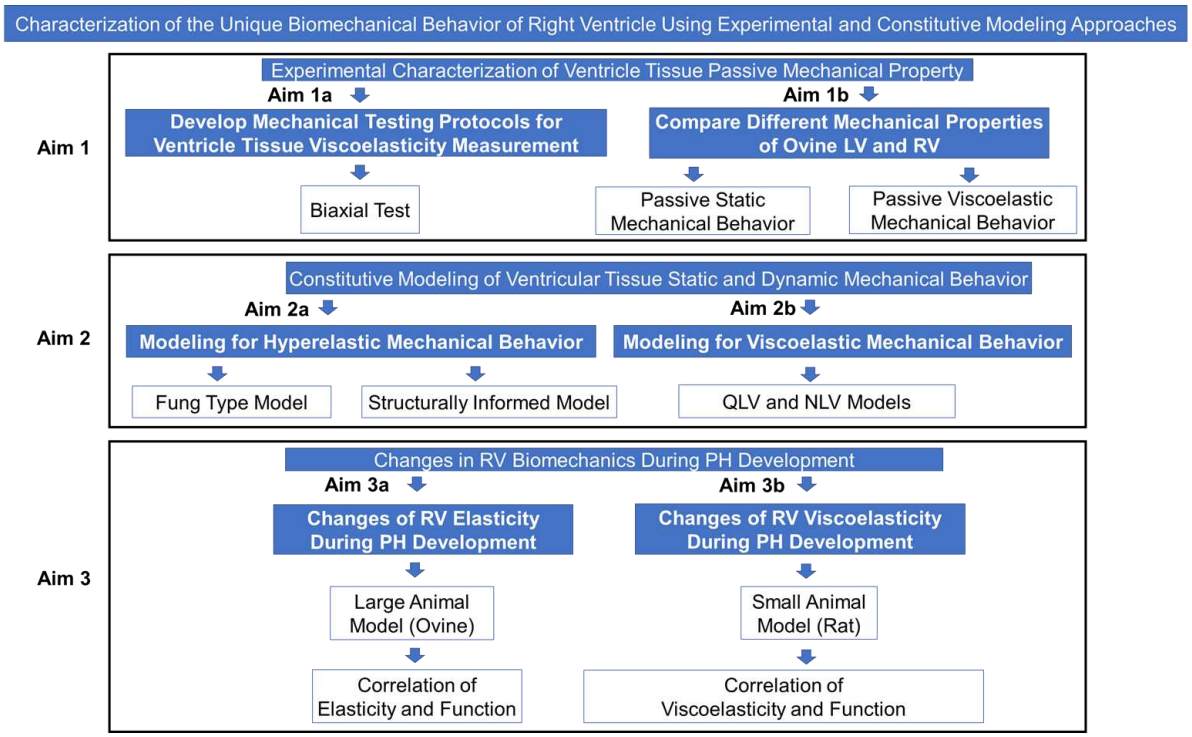

Fig. 1.8. Diagram for the overall goal and specific aims.

AIM 1: EXPERIMENTAL CHARACTERIZATION OF VENTRICLE TISSUE PASSIVE MECHANICAL PROPERTY (CHAPTER 2 TO 4)

For my first **Aim 1**, it includes three chapters (**Chapters 2 to 4**). Within this aim, I developed the mechanical testing protocols and characterized the baseline of the ventricle mechanical property by using the healthy samples experimentally. Briefly, I firstly developed the mechanical testing protocols for both large and small animals' ventricle tissue (**Chapter 2**). These protocols were then applied to measure the left and right ventricles (LV and RV) both passive static and dynamic mechanical properties at both sub-physiological and physiological ranges, respectively (**Chapters 3 and 4**).

In the **Chapters 3 and 4**, I investigated the passive static and dynamic (viscoelastic) mechanical behaviors for LV and RV, respectively. Our results supported that the healthy RV has different static and dynamic (viscoelastic) mechanical properties than the LV. These two chapters were published as peer reviewed research articles, more details can be found in these two chapters. Briefly, the findings within these two chapters lay down fundamental information for RV mechanics and will aid in the understanding of the unique biomechanical mechanisms or RV dysfunction. Furthermore, the findings on the viscoelastic behavior will deepen the understanding of the biomechanical mechanisms of ventricular function.

CHAPTER 2: DEVELOPMENT OF MECHANICAL TESTING PROTOCOLS FOR VENTRICULAR TISSUE MECHANICAL MEASUREMENT FROM LARGE AND SMALL ANIMALS

2.1 Protocols development

We firstly established the *ex vivo* methodology using biaxial mechanical test to quantify ventricle static and dynamic (viscoelasticity) mechanical behaviors in large and small animal subjects under sub-physiological and physiological ranges. **Figure 2.1** shows the previous and current testing systems. The system on the left side of the **Figure 2.1** was the one that been used to test the larger animal ovine RV. Due to the limitation of the testing frequency, we further developed the testing system with the capacity of the testing frequency up to 10Hz (right side of the **Fig. 2.1**) to test the small animal rat RV. After we obtained the data, I also revised and developed the protocols to perform the post analyzing. More details can be found in the appendixes.

Briefly, we isolated the ventricles and performed the biaxial test within 6 hours after we received the hearts for ovine heart and within 3 hours for rat heart. Sample was put in the cardioplegic solution (CPS) combined with the 30 mM of 2,3-butanedione monoxime (BDM) solution before the mechanical test. Outflow track direction was defined as the longitudinal (L) direction and its perpendicular direction was treated as the circumferential (C) direction (**Fig. 2.2**). For larger animal ovine, around 25mm by 25mm by 3mm (length, width and thickness) samples were then cut from different layers of the ventricle such as epicardial layer and myocardium. For small animal rat, the entire RV was used. Sample was then tested either under air with room temperature or immersed in the solution with body temperature. Different stretch ratios (L:C 2:2, 1:2 and 2:1), and different testing frequencies (0.1 to 1Hz (ovine) or 0.1 to 8Hz (rat)) were included. Preload was induced and preconditioning was performed before we obtained the data and resting period was included between each test. After biaxial test, stress relaxation test with five different stretch levels (3, 6, 9, 12 and 15%) was performed and we stretched two directions equally with the ramping speed

same as the speed for the 1Hz biaxial test, and more than 100s for the resting time. For the detailed testing protocol, please refer to **Appendix A**.

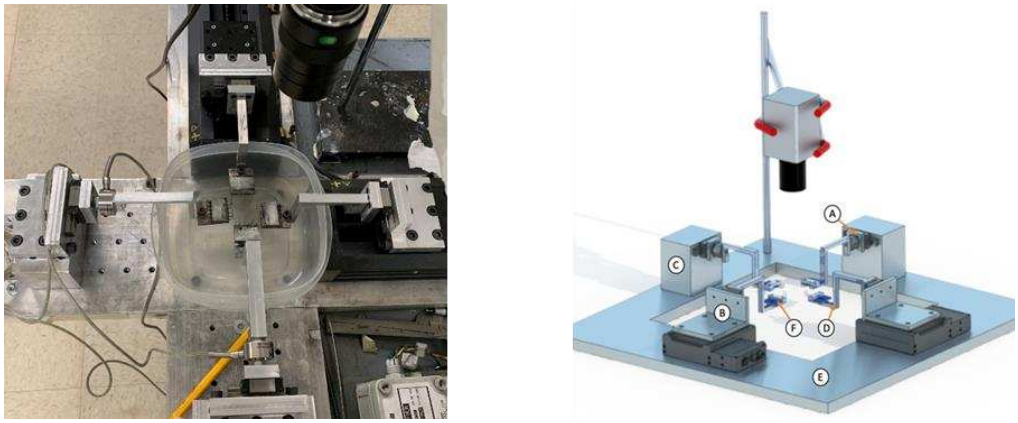

Fig 2.1 Previous (left) and current (Right) ex vivo biaxial testing system.

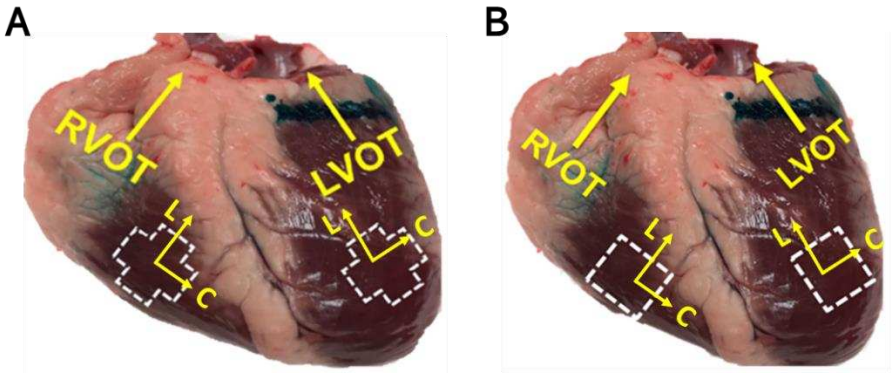

Fig. 2.2 Representative photo of an ovine fresh heart for the direction's definitions. (A) by using a cruciform testing sample. (B) by using a square form testing sample. L: longitudinal direction and C: circumferential direction.

After we obtained the raw data, we performed Digital Image Correlation (DIC) and synchronization analysis to generate the final stress-strain curves for the final tissue mechanical property characterization. For more details about the DIC and synchronization method, please refer to **Appendix B**. For the methodology of the characterization of the tissue mechanical property, please refer to the method sections in each chapter.

2.2 Achievements and key notes

Furthermore, during the development, we tested sample under both room temperature and room air with spray of physiological saline solution (PBS), and under body temperature and immersed in the solution, interestingly, we did not observe significant changes for the loading stress-strain curves between these two testing conditions for the tissue static mechanical property (**Fig. 2.3**). We started testing sample with cruciform (**Fig. 2.2A**), which aimed to reduce the shear deformation. However, we switched to the square form (**Fig. 2.2B**) for the mechanical testing since the cruciform may introduce many artifacts for the ventricle tissue.

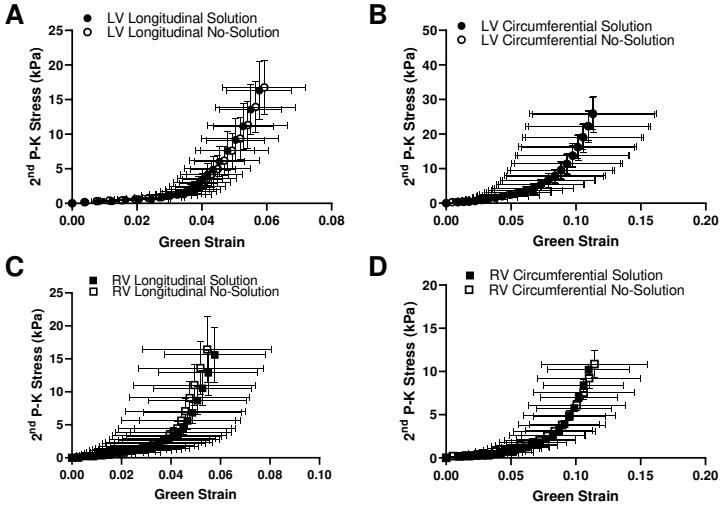

Fig. 2.3 Comparison of the average stress-stain curves obtained from different testing conditions. (A-B) stress-strain curves for the LV at longitudinal and circumferential directions, respectively. (C-D) stress-strain curves for the RV at longitudinal and circumferential directions, respectively.

Lastly, the key points in the protocol for the ventricle static and dynamic (viscoelasticity) investigation are 1) sample should be cut as small and thin as possible for the large animal tissue; 2) immerse in the solution and test under body temperature; 3) enough preconditioning before obtaining the data and enough resting period between each test and 4) test the sample under physiological frequency range.

The established protocols were used to test 30+ ovine and 30+ rat hearts, which led to the published peer reviewed research articles, conference abstracts and the articles under progression. For more details, please refer to the coming chapters.

CHAPTER 3: DIFFERENT STATIC BIAXIAL MECHANICAL PROPERTIES OF THE RIGHT AND LEFT VENTRICLES IN HEALTHY ADULT OVINE [2]

3.1 Introduction

In both the U.S. and worldwide, structural heart diseases (SHDs) are the leading cause of death. The progression of SHDs is associated with unique ventricular biomechanical alterations that affect either single or double sides of the ventricles. Diastolic dysfunction is common in many SHDs and confers poor outcome in both the left and right ventricular diseases including heart failure with preserved ejection fraction and pulmonary hypertension. Despite the development of modern therapies, effective treatments for diastolic dysfunction in heart failure patients remain limited. As diastolic dysfunction is directly influenced by the passive biomechanical behavior of the myocardium, a detailed knowledge of this behavior could facilitate developing new therapeutic targets and personalized treatment approaches for diastolic dysfunction. Although several studies have characterized the passive biomechanics of the myocardium [150], these studies often focus on either the left or right ventricle and the key question of how different the passive behavior of the two ventricles remains unanswered. This question becomes very important as often therapies that work for left ventricle (LV) failure patients (e.g., valsartan and pirfenidone) do not achieve similar effectiveness in the right ventricle (RV) failure patients [151–153], which indicates that different failing

[2] *This chapter is published as a peer reviewed research article in the Frontiers in bioengineering and biotechnology (doi.org/10.3389/fbioe.2022.857638).*

mechanisms, stemming from differences in baseline biomechanical behavior, exist between the ventricles and calls for the development of chamber-specific treatment.

Under physiological conditions, the LV and RV experience dramatically different hemodynamic environments: while the LV experiences a high pressure, high resistance and low compliance circulatory system, the RV experiences a low pressure, low resistance and high compliance circulatory system. The RV has been long considered as a 'compliant' chamber compared to the LV because of its larger chamber compliance, an extrinsic mechanical property calculated by $\Delta V/\Delta P$ over a cardiac cycle (i.e., the ratio of volume change to pressure change from end-diastole to end-systole). However, whether their intrinsic mechanical properties such as elastic modulus differ from each other remains a knowledge gap [154,155]. Moreover, in hypertensive remodeling, the RV can face as high as ~5-fold increase of afterload under pulmonary hypertension, but the LV only faces a ~1.5-fold increase of afterload in systemic hypertension [155–157]. Different baseline mechanics and mechanical afterloads may be responsible for the poor adaptation of the RV to pressure overload compared to the LV [158,159]. The RV also has been shown to have a higher collagen content (key contributor to ventricular biomechanics) than the LV [160], which suggests that the extracellular matrix remodeling may be different for each chamber. Therefore, it is crucial to investigate the baseline biomechanical differences between the ventricles to further delineate the different mechanisms of and subsequent treatment for LV- vs. RV-associated SHDs.

To date, there are only a few studies directly comparing the mechanical properties of the LV and RV. Among earlier studies, Humphrey et al. reported the equibiaxial mechanical behavior of the canine epicardium tissues [55]. The stress-stretch curves were similar between the LV and RV: the tissues were

isotropic at low strains and became stiffer and anisotropic at high strains. But there was no further analysis of the elastic properties. Later, the canine RV biaxial properties were measured and compared with the literature LV data by Sacks et al. [27]. Their data, as well as the human myocardium data from Fatemifar et al. [42], both suggested a stiffer RV compared to the LV in the main fiber direction. Javani et al. [56] and Kakaletsis et al. [161] measured adult ovine hearts by equibiaxial and multi-modal uniaxial tensile/compression and simple shear mechanical tests, respectively. These studies reported a stiffer material property of the LV than the RV in the main fiber direction. This finding is contradictory to the former studies. Recently, human ventricles were examined by Sommer et al. [162] and the results suggested a stiffer RV than LV, although the sample size was small (n=3 for RV). Since both human studies included samples from patients with and without cardiovascular diseases, the baseline information of healthy ventricles still remains unclear. Finally, healthy neonatal porcine hearts were examined by Ahmad et al. [163] and the RV was shown to be stiffer than the LV in the main fiber direction in the developing myocardium. However, the ventricular wall is different in functionality and structure between the neonate and adult [164,165]. Therefore, the mechanical difference between the RV and LV in healthy adults remains inconclusive.

The lack of baseline biomechanics data for LV and RV and particularly in large animal species has limited the expenditure of cardiac research in two main fields. Firstly, ventricular passive biomechanical properties can serve as a benchmark for image-based inverse modeling technologies to non-invasively estimate myocardial properties in the RV and LV [90,93,166,167]. The image-based inverse model technology offers a promising platform to measure tissue-level stiffness and decouple fiber-level contributors to this stiffness. The information derived from this approach can significantly improve the diagnosis and prognosis

that are solely based on global functional metrices (e.g., end-diastolic pressure-volume relation). Second, the design of biomaterials for cardiac tissue engineering and regenerative medicine encompasses a wide range of substrate elasticity from sub- to supra- physiological stiffnesses (20 kPa to 92 MPa), as we recently reviewed [168]. There are two layers of problems here. The biomaterial stiffnesses are oftentimes outside of the physiological range of myocardium stiffness, and most studies used the benchmark of LV stiffness, which leads to the lack of RV-specific therapy development [168] in this rapidly expanding research field.

With the persistent need to establish computational tools for the estimation of large animal (including human) cardiac biomechanics and to guide cellular and tissue bioengineering research, the goal of this study is to compare the biomechanical properties of the LV and RV in healthy adults. We hypothesize that the adult healthy LV and RV have distinct passive anisotropic biomechanical properties. Sheep were chosen for their closer similarities to adult human anatomy, function, and physiology [169] than small animals, and thus the findings are more translatable to human cardiac biomechanics. We measured the passive biaxial properties of ovine LV and RV and quantified collagen distribution in the tissues. Moreover, there is increasing agreement that a constitutive model that incorporates the microstructural information has greater potential to characterize the heterogenous mechanical behavior of myocardium [170,171]. Equibiaxial data were then fitted to a four-parameter Fung type model [56,172] and a structurally informed model [170] with additional measurements from serial histology sections on the myo-/collagen fibers, separately. Our results indicated significant discrepancies between anisotropic behaviors of the LV and RV (relative to OT coordinates) that were concisely described by the anisotropic parameter K derived from the Fung type model. The structurally informed model indicated stiffer collagen fibers in the LV than the RV, which

awaits further investigation. Furthermore, the elasticity at low strains was correlated with type III collagen content in both ventricles. These findings advance the fundamental understanding of the differences between LV and RV biomechanics, which can be used to guide cardiac tissue engineering and regenerative studies with chamber-specific mechanical environments and to develop the image-based inverse modeling technologies to non-invasively estimate myocardial properties in the ventricles.

3.2 Material and methods

3.2.1 Tissue sample preparation

Fresh hearts (n=11) were obtained from 4+ year-old female sheep with no known cardiovascular disease or defects after the animals were euthanized for unrelated studies. Within four hours of sacrifice, the tissues were immersed in physiological saline solution (PBS) at room temperature until mechanical testing [173]. The outflow tract (OT) direction was used as the longitudinal direction as in previous studies [9,174–176] . A cruciform section (total dimensions: 30x30 mm; center square dimensions: 20x20 mm) was cut from each ventricle in a similar anatomic region (anterior free wall, with similar distance to the apex and base) and free of fibrotic deposition (**Fig. 3.1**). For both ventricles, we used the middle layer for mechanical tests after cleaning of the endocardial and epicardial surfaces, including the removal of papillary muscles and trabeculae. The tissue thickness was ~3 to 4 mm in all testing samples to achieve negligible shear deformation requirement for the biaxial test [177].

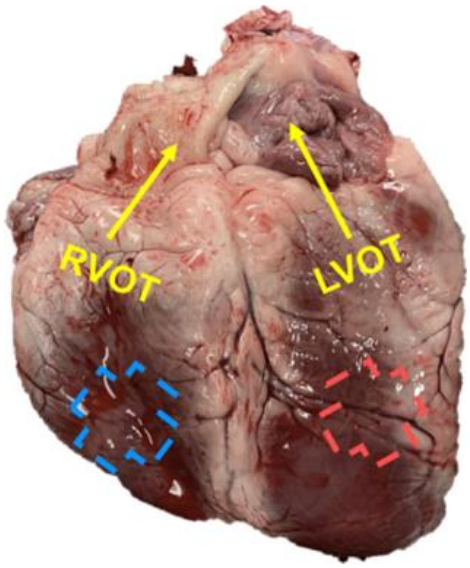

Fig. 3.1. A representative image of the ovine heart with the labeling of the outflow (OT, longitudinal) direction for each ventricle.

3.2.2 Biaxial testing

The sample was then mounted onto an in-house biaxial tester and then *ex vivo* mechanical tests were performed at room temperature, with a regular spray of PBS solution to keep the tissue moist. Prior to testing, graphite powder (AGS, MI) was dusted onto the sample for strain characterization. Before testing, approximately 0.1 N of force was applied to pre-load the tissue in both directions. Next, biaxial testing was performed at two different displacement ratios (longitudinal:circumferential) in random order (2:1 and 1:2) and then at an equibiaxial test (2:2). The first ratio test was completed with 15 cycles including preconditioning cycles. The following ratios' tests were completed with 8 cycles per ratio. Finally, the first ratio test was repeated to confirm that no tissue damage occurred. Data acquisition was performed with an in-house LabVIEW program [177].

Each sample underwent a maximum of 25% strain following the reported physiological strains [178] and the maximum strain rate was 1% s^{-1}. Sample images were taken with a CCD camera (Nikon) at 1 fps

and tissue deformations were obtained by digital image correlation [177]. The digital image correlation was applied to the region of interest (ROI), which was the central, square-shaped region far enough from the boundaries, and we have verified that the deformation in the ROI was nearly homogeneous. The Cauchy ($\boldsymbol{\sigma}$) and the second Piola-Kirchhoff (P-K) (**S**) stresses, and Green strain (**E**) were calculated for each direction ($\sigma = \lambda_i P$, $S = P/\lambda_i$, and $P = F/A_0$, $E = \frac{1}{2}(\lambda_i^2 - 1)$, where F is the measured force, P is the engineering stress, A_0 is the initial cross-section area, and λ_i is the stretch in the $i = \mathrm{L}, \mathrm{C}$ direction with L and C subscripts denoting the longitudinal and circumferential directions, respectively), where the width and thickness were the original dimensions at no load. The elastic moduli (*M*) were derived as the slopes of the stress-strain curves at the low and high strain ranges (i.e., the first and last 20% of the loading stress-strain curve) [9]. Then, the ratio *M*/ε in the low or high strain range was used to assess the modulus (*M*) normalized by the maximal Green strain (ε) in the corresponding strain range and the respective direction [175].

3.2.3 Collagen content measurement

After biaxial testing, the samples were fixed in 10% buffered formalin and embedded in paraffin for collagen content measurement. In some samples (n=3 for LV and n=4 for RV), the tissue blocks were further sectioned into 4-8 serial sections (~125 μm apart) from the epicardial to endocardial side and stained for fiber orientation measurement.

The tissue slices were stained with Picrosirius Red (PSR) and imaged and analyzed via a transmission microscope (Nikon Eclipse E800) and Image Pro Premier software (Media Cybernetics, Rockville, MD) for collagen content quantification. For each sample, three regions were randomly selected

under polarized light microscopy. An image thresholding method in which yellow, green, brown and dark blue colors were chosen to represent type I collagen, type III collagen, ground matrix and muscle, respectively. The amounts of type I and III collagen were quantified as the area percentage to total tissue area, and the amount of collagen content was quantified as the total area percentage of type I and III collagen [129,179].

We further performed immunohistochemistry (IHC) to LV (n=4) and RV (n=4) samples to confirm the area fraction measurement of type III collagen in PSR staining slides. Tissue samples were stained with rabbit polyclonal anti-human collagen III antibody (1:500 dilution, ab7778, Abcam, Cambridge, United Kingdom). Image thresholding via ImageJ (U.S. NIH, Bethesda, Maryland) was used to determine the area fraction of collagen III.

3.2.4 Statistical analysis

Comparisons between directions (longitudinal versus circumferential) were performed with the Wilcoxon signed-rank test for the paired equibiaxial data. For all other statistical comparisons, the Mann-Whitney U test was used for the unpaired data. Pearson correlation analysis was performed to investigate the correlations between the modeling parameters or collagen content and mechanical properties. All analyses were performed in GraphPad Prism (v8.0.2). Data are presented as mean ± SEM and $p<0.05$ was considered statistically significant.

3.3 Results

3.3.1 Differences in elastic behaviors along each direction

The average stress-strain curves from equibiaxial tests are shown in **Fig. 3.2**. The curves for the LV were leftward of the curves for the RV in the longitudinal direction (**Fig. 3.3A**), indicating a stiffer mechanical property of the LV in this direction. The opposite behavior was observed in the circumferential direction (**Fig. 3.3B**), indicating a stiffer mechanical property of the RV in this direction. Similar behavior was observed from the stress-strain data from non-equibiaxial tests.

We further investigated the elastic moduli at low and high strain ranges, which typically represent the mechanical behavior of myofibers and collagen fibers, respectively. At the low strains, the ventricles presented similar properties except that the LV showed a higher circumferential M than the RV for the non-equibiaxial tests (**Fig. 3.3B**, p=0.052). At the high strains, the LV had a higher M or M/ε than the RV in the longitudinal direction, whereas the RV had a higher M or M/ε than the LV in the circumferential direction (**Fig. 3.3**).

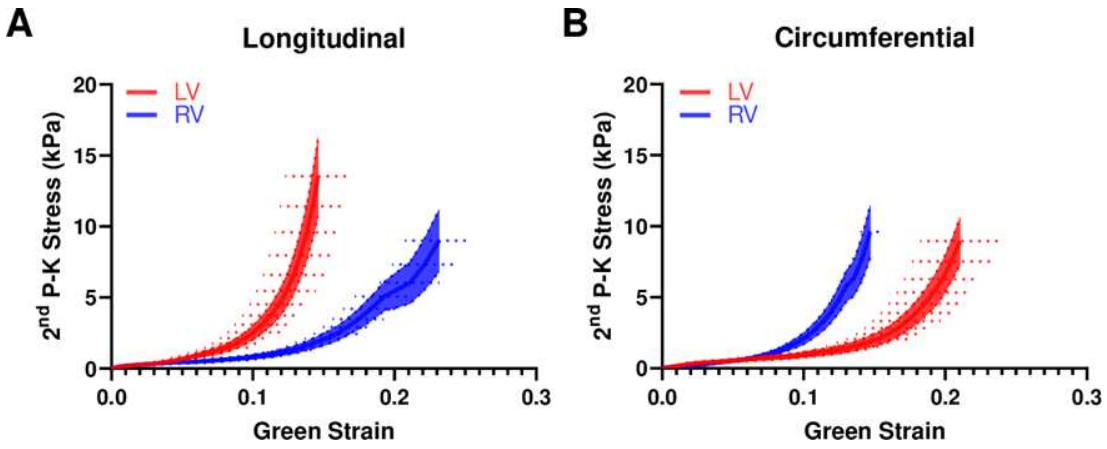

Fig. 3.2. Average equibiaxial stress-strain curves in the longitudinal (A) and circumferential (B) directions in the LV and RV (n=7 per group). The shaded area is the standard error of the stress data, and the dash line is the standard error for the strain data.

3.3.2 Differences in anisotropic behaviors

We compared the M and M/ε between the two axes to examine the anisotropic behavior of the tissue. For the LV, the M and M/ε in the circumferential direction were significantly smaller than those in the longitudinal direction (**Fig. 3.3D**), indicating that the LV was stiffer in the longitudinal direction. In contrast for the RV, the M and M/ε in the circumferential direction were higher compared to the longitudinal direction (**Fig. 3.3D**), suggesting that the RV was stiffer in the circumferential direction. Therefore, the LV and RV had different anisotropic behaviors.

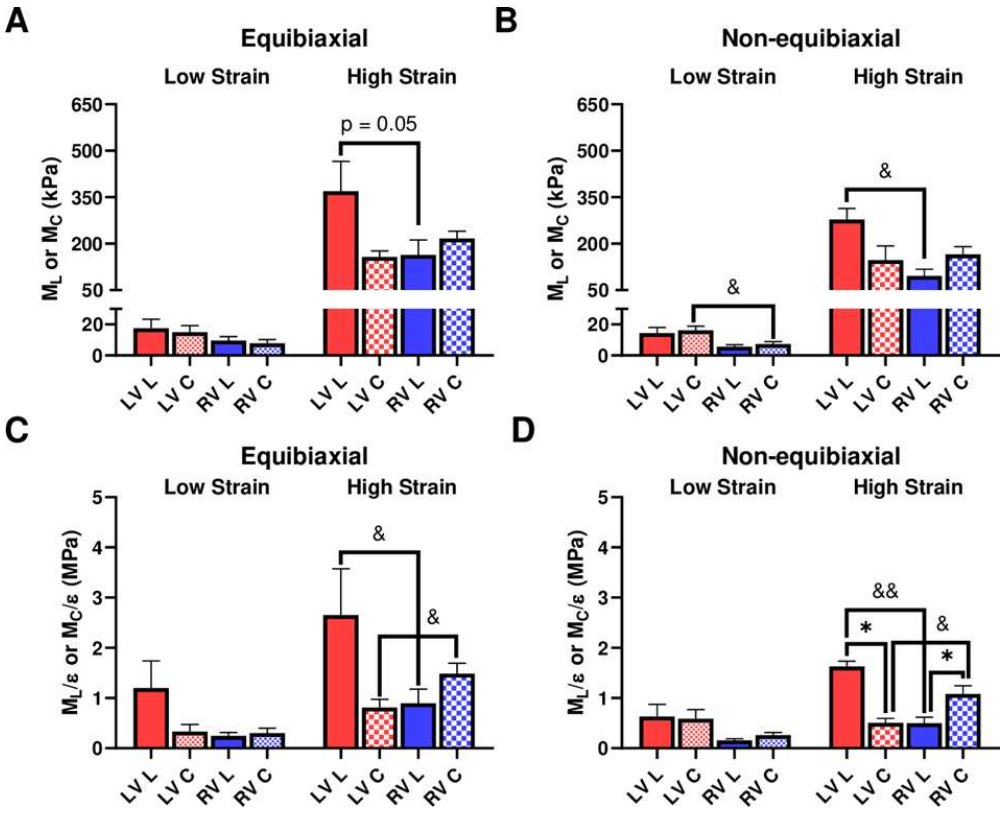

Fig. 3.3. (A-B) Elastic moduli (M) of LVs and RVs from the equibiaxial (A) and non-equibiaxial tests (B). (C-D) Strain-weighted elastic moduli (M/ε) of LVs and RVs from the equibiaxial (C) and non-equibiaxial tests (D). For the equibiaxial tests, n=7 per group; for the non-equibiaxial tests, LV, L: n=4; LV, C: n=5; RV, L: n=7; RV, C: n=6. *: $p < 0.05$ comparison between the directions and &: $p < 0.05$ and &&: $p < 0.01$ for comparison between the ventricles.

3.3.3 Collagen content correlated with low-strain or high-strain elasticity in all ventricles

Next, we examined the difference in collagen content between the LV and RV. There were trends of higher total collagen and type I collagen contents in the RV compared to the LV (**Fig. 3.4A**, $p<0.1$). Our immunohistochemistry measurement of collagen III isoform agreed with the polarized light PSR measurement in collagen III. Furthermore, we observed a significant correlation between type III collagen percentage and the longitudinal M (M_L) at the low-strain range in all samples (**Fig. 3.4B**, **$p<0.05$**). In addition, we observed a significant correlation between the total collagen and circumferential M/ε at the high-strain range (**Fig. 3.4C, $p<0.05$**). The complete results of all correlations between the collagen content and mechanical properties of the LV and RV are summarized in **Table 3.1**.

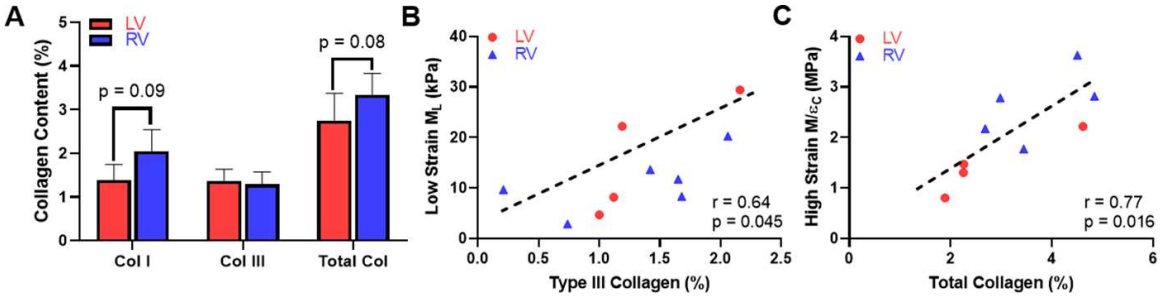

Fig. 3.4. Histological measurement and correlation analysis for the collagen. (A) Variations in the content of collagen isoforms and the total collagen between the LV and RV, (B) Significant correlation between the type III collagen content and longitudinal M (ML) at the low-strain range and (C) Significant correlation between the total collagen content and circumferential M/ε at the high-strain range.

Table 3.1. Summary of all correlation results between the collagen content and the mechanical properties of all LV and RV samples.

	M Low_L	**M/ε** Low_L	**M** High_L	**M/ε** High_L	**M** Low_C	**M/ε** Low_C	**M** High_C	**M/ε** High_C
Col I	NS	NS	NS	NS	NS	NS	NS	p = 0.07
Col III	*	NS	NS	NS	NS	NS	NS	NS
Col T	NS	NS	NS	NS	NS	NS	NS	*

Col I, Col III and Col T are the collagen type I, III and total collagen, respectively. L and C are longitudinal and circumferential directions, respectively. NS: no significance, and *: $p<0.05$.

3.4 Discussion

In this study, we aimed to compare the passive biaxial mechanical properties of the LV and RV in healthy adult ovine. We found that (1) the LV and RV had different anisotropic behaviors, with the LV being stiffer in the longitudinal (OT) than circumferential (cross-OT) direction and the RV showing the opposite result; (2) the RV was more compliant than the LV in the longitudinal direction, and was stiffer than the LV in the circumferential direction; (3) the anisotropic parameter *K* derived from the Fung type model provided consistent finding in the opposite anisotropy of LV and RV as observed experimentally; (4) using the structurally informed model, the LV was predicted to have stiffer collagen fibers than the RV (5) the type III collagen played an important role in the longitudinal elasticity in all ventricles, especially at the low strain range. These findings provide fundamental information on the biomechanics of the LV and RV, which is valuable for the design of tissue and regenerative engineering studies and the development of image-based inverse modeling technologies to non-invasively estimate myocardial properties.

3.4.1 Different anisotropic behaviors between the LV and RV

Both the LV and RV are reported to present anisotropic behaviors in prior studies, but the anisotropic behavior is inconsistent even within the same animal species. For instance, studies have found

the healthy rat RV is stiffer in the longitudinal compared to circumferential direction [174,176]. These findings are supported by longitudinal stress-strain curves being shifted leftward relative to the circumferential stress-strain curves in rodent RV [180]. However, another study reporting the low and high strain *M*'s suggests that the rat RV was stiffer in the circumferential compared to longitudinal direction, and the difference reversed and became larger in pulmonary hypertensive animals [9]. These studies used the same (anatomical) coordinate system as in the present study, yet the anisotropic behavior of the RV still remains inconclusive. Moreover, it is unclear if the small and large animal species share similar anisotropic behaviors in the myocardium, and thus it is imperative to investigate the biaxial properties in large animal species independently.

In this study, we found that the ovine LV and RV had different anisotropic behaviors: the LV had larger *M* in the longitudinal direction compared to the circumferential direction, whereas the RV had the opposite trend of difference between these directions. The anisotropy parameter *K* derived from constitutive modeling was significantly correlated with the experimental data, confirming the different anisotropic behaviors. We speculate that the reason for this difference is the different need to facilitate blood filling and ejection in each ventricle. The LV is more conically shaped and is comprised of helical fibers that allows it to deform more circumferentially during cardiac cycles (majority of LV contractility occurs due to circumferential shortening); in contrast, the RV is crescent shaped and is comprised of wrap-around transverse fibers that deforms more longitudinally (majority of RV contractility occurs due to longitudinal shortening) [181,182]. Thus, our findings show a more compliant passive mechanical property of the wall in the main axis of cyclic deformation for both ventricles, which suggests that passive elasticity is maintained at

a low level to reduce the elastic 'resistance' and facilitate blood filling (as well as 'pumping' potentially). The understanding of the differences in baseline anisotropy between the two ventricles will help to develop chamber-specific therapies aimed at reducing wall stress along the main axis of deformation.

3.4.2 Different elasticity at each axis between the LV and RV

To date, discrepant findings are reported on the comparison of elasticity of the LV and RV. Please note that the intrinsic mechanical property measurements should be distinguished from the general 'consensus' that the RV is a more compliant chamber (an extrinsic mechanical measurement). In human myocardium, the RV tissue tended to achieve higher wall stresses in both biaxial axes compared to the LV tissue, but whether the difference reached statistical significance is unknown [162]. In contrast, various mechanical tests (biaxial test, triaxial shear test, uniaxial tensile/compression tests) on healthy ovine hearts showed that the LV was 'overall' stiffer compared to the RV [56,161]. Another recent study characterized neonatal porcine ventricles and found no difference between LV and RV stress-strain curves nor peak engineering stress [163]. Hence, although all these studies used a different definition of biaxial axes (the main fiber and cross-fiber coordinate system), it remains unclear if the LV and RV have distinct intrinsic elastic property and how different they are.

The present study is the first investigation on the biaxial behavior of the ventricles in large animal species using an anatomical coordinate system (more adopted in the RV research area). Our results showed that the RV was stiffer than the LV in the circumferential direction, and the opposite trend of difference (i.e., LV was stiffer than the RV) was shown in the longitudinal direction (**Figs. 3.2&3.3**). Because of the different trends of comparison at different directions, it *is not appropriate to* simply conclude that the 'LV

is stiffer than the RV' or vice versa at the tissue level. Moreover, the heterogenous organization of myofiber layers and the nonlinear, anisotropic nature determine that one cannot refer to a single value of mechanical parameter (e.g., elastic modulus) to describe the myocardium. Unfortunately, such knowledge has not been well recognized by emerging fields like cell and tissue engineering for cardiac research. There are also mixed citations of 'tensile' and 'compressive' elastic modulus to represent the stiffness of myocardium. As a result, a variety of elastic moduli (from ones of kPa to tens of MPa) has been adopted for the matrix or bioscaffold to simulate ventricles in the tissue engineering or mechanobiology studies [168,183]. Lastly, there is no distinction between the LV and RV tissue mechanics due to the lack of knowledge of baseline contrasts of their biomechanical properties. Our data provides fundamental information on the LV versus RV passive, anisotropic mechanical behaviors. The data collected on large animal species further offers valuable data for translational applications in exploring mechanically regulated disease mechanism and/or regenerative therapy. We highly recommend future studies to incorporate the anisotropic, nonlinear elastic behavior of myocardium into considerations to better mimic *in vivo* conditions.

3.4.3 Correlations between collagen content and ventricle elasticity

In this study, we also found novel correlations between collagen and ventricular biomechanics. Firstly, we observed a trend of higher collagen content including type I collagen in the RV compared to the LV. This is consistent with the prior report of collagen content in human LV and RV determined from hydroxyproline assays [184]. Second, although type I collagen is the most abundant type of collagen in ventricles [185], the type III collagen content was significantly correlated with the M_L in all ventricles and at low strains (**Fig. 3.4B**, **$p<0.05$**). This indicates that the longitudinal elasticity partly stemmed from type III

collagen recruitment. It is known that type III collagen is mesh-like in structure and more compliant than fibrillar type I collagen [186], but how these fibers are recruited during the nonlinear deformation is unclear. Our data suggest that the type III collagen may play an equally important role as myofiber in low-strain tissue mechanics, which is key to ventricular diastolic function [9]. It is also possible that type III collagen is recruited earlier than type I collagen and presents a similar role as elastin in vascular tissues. Lastly, the total collagen content was significantly correlated with the circumferential M/ε in both ventricles and at high strains (**Fig. 3.4C**, **$p<0.05$**). The strong influence of collagen fibers in high-strain elasticity is likely the outcome of more fully recruited collagen at larger deformation.

3.4.4 Limitations

Several limitations were present in the study. Our samples were from female ovine. Sex differences have been found in ventricular function in both physiological and pathological conditions [21], but its effect on the myocardium mechanical property has not been reported. Next, the middle portion of the ventricles were tested to fulfill the plane stress requirement in biaxial test. This was viewed as standard for biaxial tests of myocardium [173]. But it resulted in an incomplete characterization of tissue mechanics and transmural fiber orientation, especially in the LV wall. Such limitation is not rare for *ex vivo* mechanical measurement of myocardium from large animals or human patients due to a large tissue size. Prior studies typically sectioned the LV into two or three layers [42,56,162] or at different anatomical regions [56,163], and then performed the biaxial tests. However, the entire ventricle's mechanical behavior is 'interrupted' by sectioning. Therefore, the full description of mechanical properties of the LV (or hypertrophied RV) would require the development of *in vivo* computational modeling using intact, complete structural information of the patient.

Third, the samples were sectioned in cruciform shape and mounted by clamps in our biaxial tests, similar to a prior rat RV study [173]. We chose this method based on a prior examination of our in-house biaxial system on brain tissues [177]. The impact of sample shape and mounting method on biaxial tests has been explored by Sun et al. [187]. We acknowledge that our methodology is different than other studies with square samples and sutures mounting, but an examination of the strain data indicates relatively homogenous deformation in the center region of the tissue. Thus, we expect that the discrepancy induced by this methodology should be minimal. Furthermore, we tested the samples at room temperature with a regular spray of PBS rather than immerse the tissue in a relaxant solution at body temperature. We investigated the effects of these testing conditions on the passive mechanical properties by using extra ventricles. We compared the stress-strain curves and observed no significant changes of the mechanical behavior between these two conditions.

Lastly, myocardium is a nonlinear, orthotropic, and viscoelastic material. In order to fully characterize the mechanical property, the combination of shear and biaxial tests and the inclusion of viscoelasticity measurement are recommended [162,188]. Nevertheless, the *ex vivo* planar biaxial test is still widely performed in cardiac mechanical testing [189], and it provides an initial examination of passive mechanical properties that are independent of physiological conditions such as *in vivo* pressure and volume, heart rate, sympathetic nervous stimulation, etc. The study of biaxial planar mechanics is critical to understand RV diastolic function as the deformation replicates the physiological motion [23,190,191]. The relatively simple testing protocol minimizes the testing time to ensure tissue viability [171,174]. Therefore, this method remains common to characterize myocardium passive properties [34,42,56,163,176,180,192,193].

3.5 Conclusions

In this study, we examined the biomechanical differences between healthy LVs and RVs in adult ovine. We observed differences in the anisotropic behavior between the LV and RV, with the LV being stiffer in the longitudinal (OT) direction and the RV being stiffer in the circumferential (cross-OT) direction. Interventricular comparison showed that the RV was more compliant than the LV in the longitudinal direction and was stiffer than the LV in the circumferential direction, which suggests different impacts of passive mechanics of these ventricles on the blood filling during diastole. Moreover, type III collagen content was correlated with the low-strain elastic moduli in the longitudinal direction in both ventricles. Our findings provide significant insights for guiding cardiac tissue engineering and regenerative studies and call for the development of RV-specific therapy based on its unique biomechanics. In addition, our results can serve as a benchmark for image-based inverse modeling technologies to non-invasively estimate myocardial properties in various types of heart failure patients.

CHAPTER 4: DIFFERENT DYNAMIC BIAXIAL MECHANICAL PROPERTIES OF THE RIGHT AND LEFT VENTRICLES IN HEALTHY ADULT OVINE [3]

4.1 Introduction

Despite the advances in modern management, heart failure leads to high mortality and morbidity in the U.S. as well as worldwide. More than 5 million Americans have heart failure [11], and ventricular dysfunction, which includes both left and right sides of the heart, is the most common cause of heart failure leading to high mortality and morbidity [12]. The biomechanical properties of the ventricle are considered to have an impact on its organ function, and recently a correlation of right ventricular (RV) elasticity and diastolic function has been reported [9,10].

Biological tissues are known to be viscoelastic [31]. This indicates that the tissue's mechanical behavior is strain and strain-rate dependent, and there is energy loss during the deformation due to the internal friction (viscosity). However, most previous studies on ventricular mechanics have focused on the static mechanical property – elasticity [34,52,54,57,162,174] due to the lack of experimental evidence that passive myocardium is viscoelastic. Recently, a number of studies have reported significant hysteresis responses to shear tests or cyclic biaxial/triaxial tensile tests from passive myocardium in adult pigs (LVs only) [102], adult human (LVs and RVs) [162], and neonatal pigs (LVs and RVs) [163]. But none of these preclinical studies provided a comparison of viscoelastic behavior between LVs and RVs in healthy adults. In the study of

[3] *This chapter is published as a peer reviewed research article in the Journal of biomechanical engineering (doi: 10.1115/1.4052004).*

adult human myocardium [162], the samples were from a variety of patients with and without heart related diseases, and thus the comparison between healthy LVs and RVs was unavailable. Therefore, while it is accepted that the LV and RV are different in its embryologic origin, anatomy and function [194], whether and how they distinguish in the anisotropic and viscoelastic properties remain unclear.

The goal of the study was to investigate and compare the passive viscoelastic behavior of the LVs and RVs in healthy adults. Specifically, we hypothesize that the healthy, adult LV and RV free wall have different viscoelastic behaviors. To test the hypothesis, *ex vivo* mechanical tests including cyclic biaxial tensile mechanical tests and stress relaxation were performed in healthy adult sheep ventricles. We found that the RV had more pronounced frequency-dependent changes in viscoelasticity than the LV. Under the physiological frequency (1Hz), the LV was more anisotropic in its elasticity and stiffer than RV in both directions, whereas the RV was more anisotropic in its viscosity and more viscous than the LV in the longitudinal direction. Furthermore, we found that the LV was quasi-linear viscoelastic in the longitudinal direction only, whereas the RV was non-linear viscoelastic in both directions. To our knowledge, this is the first study to compare the passive, biaxial viscoelasticity of the LVs and RVs in healthy adults. Our findings on the dynamic mechanical behavior will improve the understanding of ventricular biomechanics and function in pulsatile hemodynamic conditions.

4.2 Material and methods

4.2.1 Specimen preparation

Fresh hearts (N=8) were obtained from 36+ months old female sheep with no known cardiovascular diseases from unrelated studies. The hearts were placed in cardioplegic solution (CPS) on ice to maintain tissue viability [173] and mechanically tested within 4-6 hours after tissue harvest. The outflow tract (OT) direction was marked as the longitudinal direction (0°) and its perpendicular direction was denoted as the circumferential direction (90°) (**Fig. 4.1**) [9,55,174,195]. We chose this coordinate system because it provides more consistent and reliable coordinate reference than the fiber/cross-fiber coordinates and it is less dependent on the location of tissue samples harvested from the curved ventricular walls. Prior to the

mechanical tests, square samples (25mm x 25mm) were cut from the same anatomical location (near apex) on the epicardial side of the ventricular free wall (~3mm of thickness) (Fig. 1) , and then placed in CPS combined with 30 mM of 2,3-butanedione monoxime (BDM) [9,174,196] at body temperature (37°C) for at least 30 minutes to ensure muscle relaxation. The tissues were immersed in the same solution at body temperature during the mechanical tests.

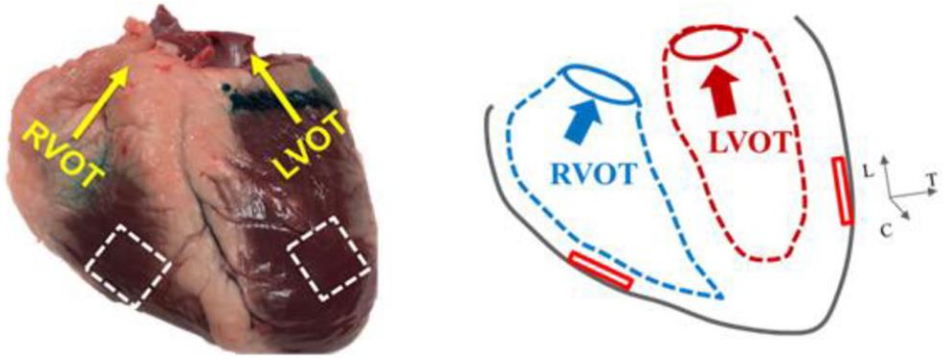

Fig. 4.1. Left: Representative photo of a fresh ovine heart. Testing samples were sectioned from the epicardial side of each ventricle's free wall. The longitudinal direction was determined by the outflow tract (OT) axis of each ventricle. Right: Diagram of the sample extraction in the transmural section. L: longitudinal direction, C: circumferential direction, T: transmural direction. White squares (left) and red rectangles (right) denote the different views of samples used in the mechanical tests.

4.2.2 Cyclic biaxial tensile mechanical test

After mounting, the samples were preloaded by approximately 0.1 N and then underwent 15 cycles of equibiaxial stretch at the speed of 8 mm/s for preconditioning. Next, equibiaxial mechanical tests (with the maximal strain ~20%) at the cycle frequency of 1, 0.1 and 0.01Hz were performed, which included the quasi-static and physiological frequency ranges as a healthy adult sheep's heart rate is about 65 to 80 beats per minute [197]. Between each test, a resting time, which was ten times that of the testing period, was included to ensure that the tissue was fully recovered from the previous test [43,44]. Deformations of the graphite powder speckled samples were tracked with a digital camera (Nikon, Tokyo, Japan), and the strain was derived by digital image correlation using in-house MATLAB codes. Biaxial stretch forces were obtained by 50 lb load cells (Honeywell Sensotec, Columbus, OH) at a sampling frequency of 100 Hz.

The second Piola-Kirchhoff stress ($s = \sigma/\lambda$, and $\sigma = F/A_0$, where F is the force, A_0 is the initial cross-section area, and λ is stretch) and Green's strain ($\varepsilon = \frac{1}{2}(\lambda^2 - 1)$) were calculated from the last cycle

of the stress-strain data, and the hysteresis loops were analyzed to quantify the elastic and viscous mechanical properties. For the elasticity (or stiffness) measurement, the elastic moduli (EM) were derived as the slopes of the stress-strain curves at the low and high strain ranges (i.e., the first and last 20% of the loading stress-strain curve) (**Fig. 4.2A**), and the strain-weighted elastic moduli (EM/ε) were calculated as the EM divided by the maximal strain of the corresponding strain range where EM was derived. The tissue viscosity was measured by the dissipated energy (W_d), the area within the hysteresis loop, and the loop width (a) at the 50% of the maximal stress (σ_{mid}) (Fig. **4.2A**). Furthermore, the stored energy W_s was calculated as the area beneath the unloading curve (**Fig. 4.2A**), and the damping capacity was calculated as $W_d/(W_d+W_s)$ [198].

4.2.3 Stress relaxation

Next, equibiaxial stress relaxation at five different strain levels (3, 6, 9, 12, and 15%) with the ramp rate of 8 mm/s were performed. From the original stress relaxation data, we derived the relaxation modulus as the stress divided by the strain as a function of time, and the normalized stress curves as the ratio of the stress to the maximal stress (σ/σ_{max}) as a function of time. The relaxation modulus and the normalized stress data at 0.01s and 100s of relaxation were used to indicate the tissue viscoelasticity (**Fig. 4.2B**). Furthermore, the logarithmic scale was plotted for the time and stress, and the relaxation rates were calculated as the slopes of the linear fitting to the logarithmic plots using least square analysis. The goodness of the fit was examined by the R^2 value. The calculated relaxation rates were used to determine the type of the tissue viscoelastic behavior, where a non-linear viscoelastic behavior is indicated if the relaxation curves from multiple magnitudes of input strains are not parallel (i.e., to have different slopes) [199–202].

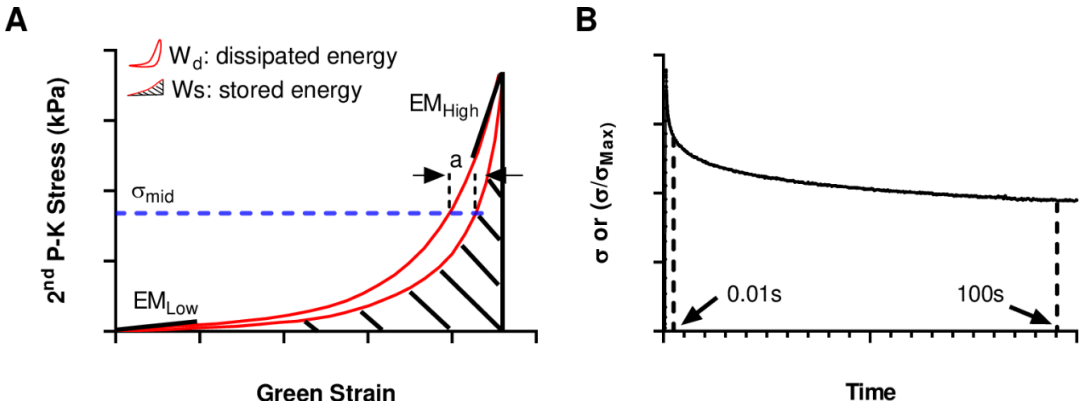

Fig. 4.2. Viscoelastic properties derived from the experimental (A) stress-strain hysteresis loop and (B) original or normalized stress relaxation curve.

4.2.4 Statistical and correlation analyses

For simplicity, we referred to the epicardial side of the LV and RV as the "LV and RV" in our results and discussions below. Data were presented as mean ± SEM. All data were analyzed by the non-parametric paired Wilcoxon test (GraphPad v8.0.2). Pearson correlation analysis was used to investigate the correlations between different viscoelasticity indices derived from the stress relaxation and cyclic biaxial tensile mechanical tests, the relationship between the relaxation modulus and dissipated energy, and the interdependence between the viscoelastic indices derived from the dynamic test (GraphPad v8.0.2). MATLAB (R2019b) was used to perform the fitting in the log scale plots. $P < 0.05$ was considered significant.

4.3 Results

4.3.1 Different frequency-dependent behaviors between the LVs and RVs

Firstly, we compared the average longitudinal or circumferential hysteresis loops at different testing frequencies (**Fig. 4.3**). In the LV, in both directions, all loops were close to each other with a similar non-linear behavior except that as the frequency increased, the loop area increased (**Fig. 4.3A&B**). This indicates a similar elasticity but larger viscosity under a higher frequency. Such frequency-dependent change in viscosity was similarly observed in the RV (**Fig. 4.3C&D**). However, the frequency-dependent change in elasticity was significant in the RV. The loops were shifted rightward from the low frequency

(0.01Hz) to higher frequencies (0.1 and 1Hz). Therefore, this indicates a decreased stiffness and increased viscosity under higher frequencies.

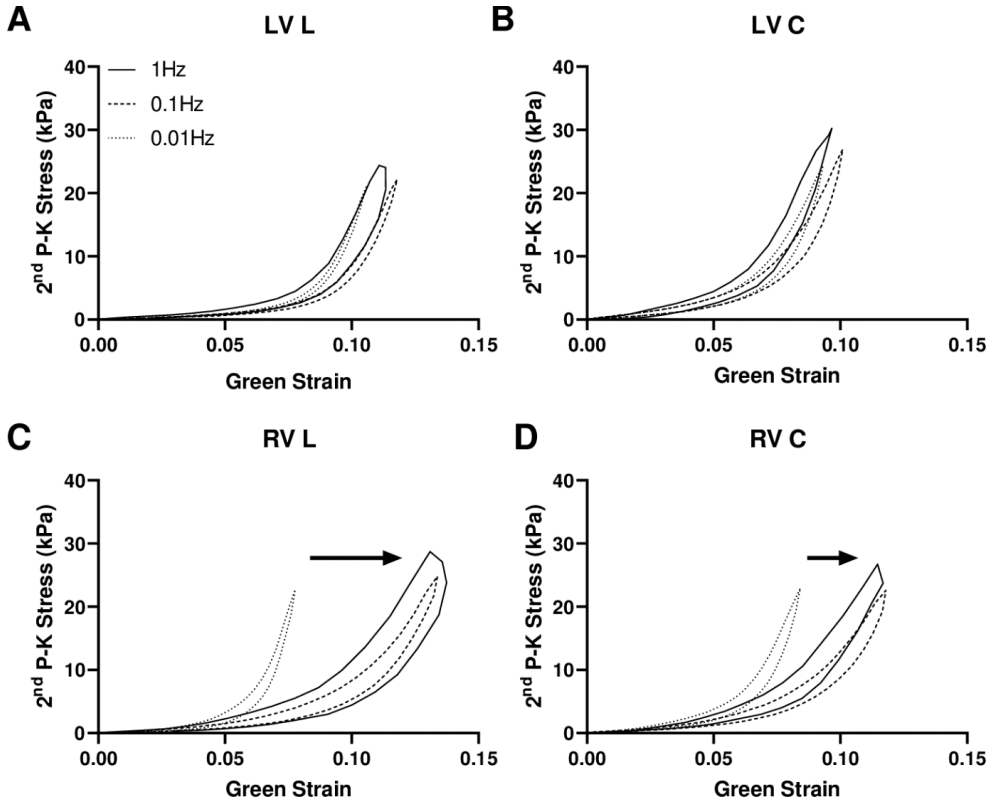

Fig. 4.3. Average hysteresis loops obtained from the ventricles at different frequencies. (A-B) the average loops for the LV in longitudinal (L) and circumferential (C) directions, respectively, and (C-D) the average loops for the RV in longitudinal and circumferential directions, respectively.

4.3.2 Different anisotropic viscoelastic behaviors under physiological frequency

As the viscoelastic property at a stretch rate of heart rate is more physiologically relevant, we then further examined the anisotropic viscoelastic behavior of the ventricles at 1Hz (**Fig. 4.4**). Firstly, the longitudinal and circumferential hysteresis loops were different in both ventricles, indicating that their viscoelastic behaviors are anisotropic. In the LV, the main difference between the loops were in the position and non-linear behavior, not in the loop area (**Fig. 4.4A**). This suggests that the LV's elasticity, rather than its viscosity, is anisotropic. In contrast in the RV, the main difference between the loops lied in the loop area, not in the position or non-linear behavior (**Fig. 4.4B**). This suggests that the RV's viscosity, rather than the elasticity, is anisotropic. Then, we also compared the two ventricles in each direction and found

that the RV had larger viscosity in the longitudinal direction and similar viscosity in the circumferential direction compared to the LV (**Fig. 4.4C&D**).

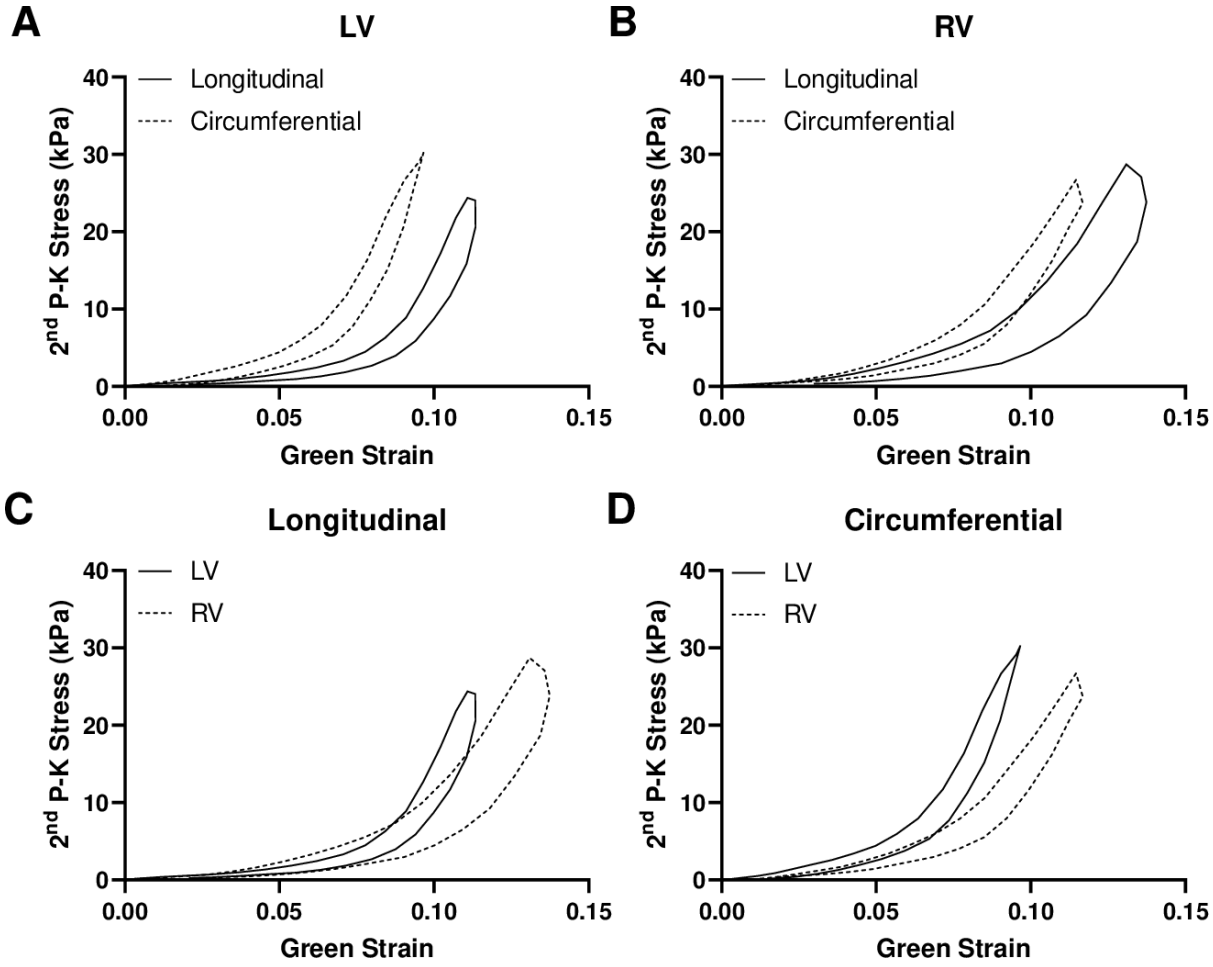

Fig. 4.4. Average hysteresis loops for the ventricles at 1Hz. (A-B) comparison of the average loops from the longitudinal and circumferential directions in the LV and RV, respectively; (C-D) comparison of the average loops from the LV and RV at longitudinal and circumferential directions, respectively.

The differences that we observed from the average hysteresis loops were confirmed by the elasticity and viscosity parameters quantified from these groups (**Fig. 4.5**). From the elasticity measurement, the LV presented stronger anisotropic behavior with a stiffer behavior in the circumferential direction, whereas the RV presented isotropic behavior (**$p<0.05$, Fig. 4.5B**). From the viscosity measurement, the RV was anisotropic with larger viscosity in the longitudinal direction, whereas the LV was isotropic (**$p<0.05$, Fig 4.5D**). Finally, the interventricular comparison showed that the LV was stiffer than the RV in higher strains

in both directions (**p<0.05, Fig. 4.5B**), and the RV was more viscous than the LV in the longitudinal direction (**p<0.05, Fig. 4.5C&D**).

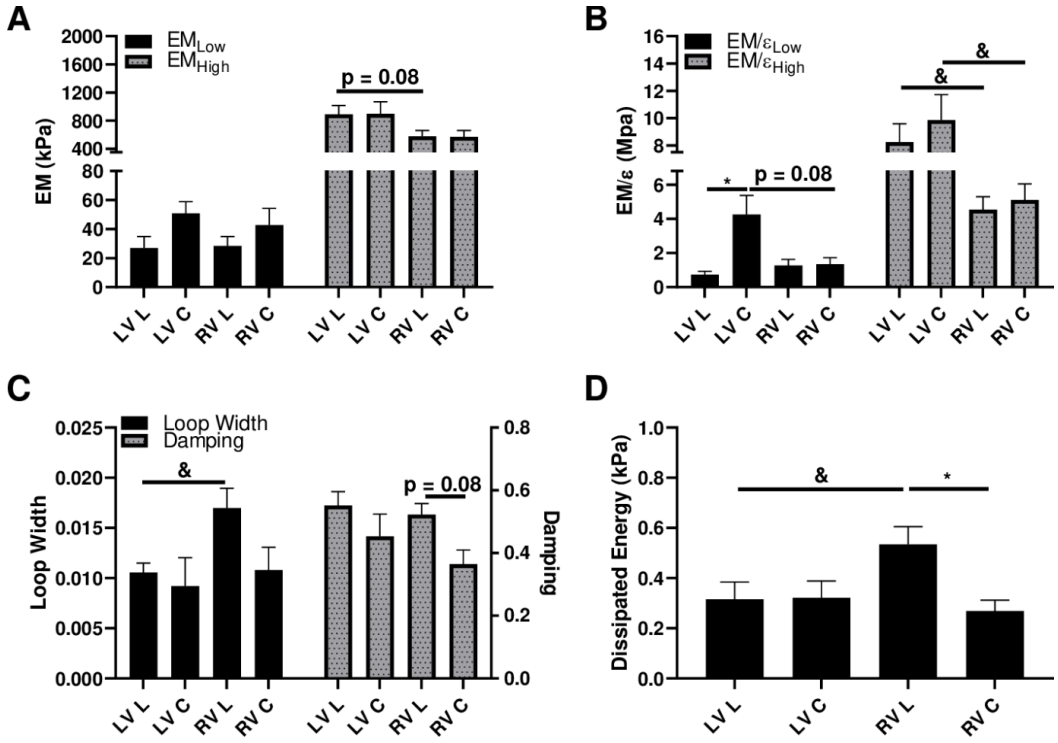

Fig. 4.5. Measurements of ventricular viscoelastic properties in longitudinal and circumferential directions. (A-B) show the comparisons in elasticity measurement and (C-D) show the comparisons in viscosity measurement. *p<0.05 comparison between directions and $^{\&}$p<0.05 comparison between ventricles. Data are presented as mean ± SEM.

4.3.3 Different non-linear viscoelastic behaviors from stress relaxation data

The viscoelastic behaviors of these ventricles were further examined by stress relaxation. We first looked at the log scale of the stress relaxation data at different strain levels (**Fig. 4.6**). To examine if the tissue viscoelasticity is quasi-linear, a fitted line derived from the strain level of 3% was superimposed onto the experimental data by placing the line at the center datapoints at other strain levels, and the 'overlapping' of the data was examined (**Fig. 4.6, Table 4.1**). For the LV, in the longitudinal direction, the experimental data at higher strain levels could be predicted by the 3% strain magnitude fit except for the strain level of 15%; whereas in the circumferential direction, the experimental data at all higher strain levels could not be accurately predicted by the 3% strain magnitude fit. This indicates that the LV is quasi-linear viscoelastic

in the longitudinal direction, but not in the circumferential direction (**Fig. 4.6A&B, Table. 4.1**). For the RV, in both directions, the experimental data at all higher strain levels could not be accurately predicted by the 3% strain magnitude fit. This suggests that the RV is non-linear viscoelastic in the both directions (**Fig. 4.6C&D, Table 4.1**). All fitted lines of the log-scale stress relaxation data had R^2 values > 0.9.

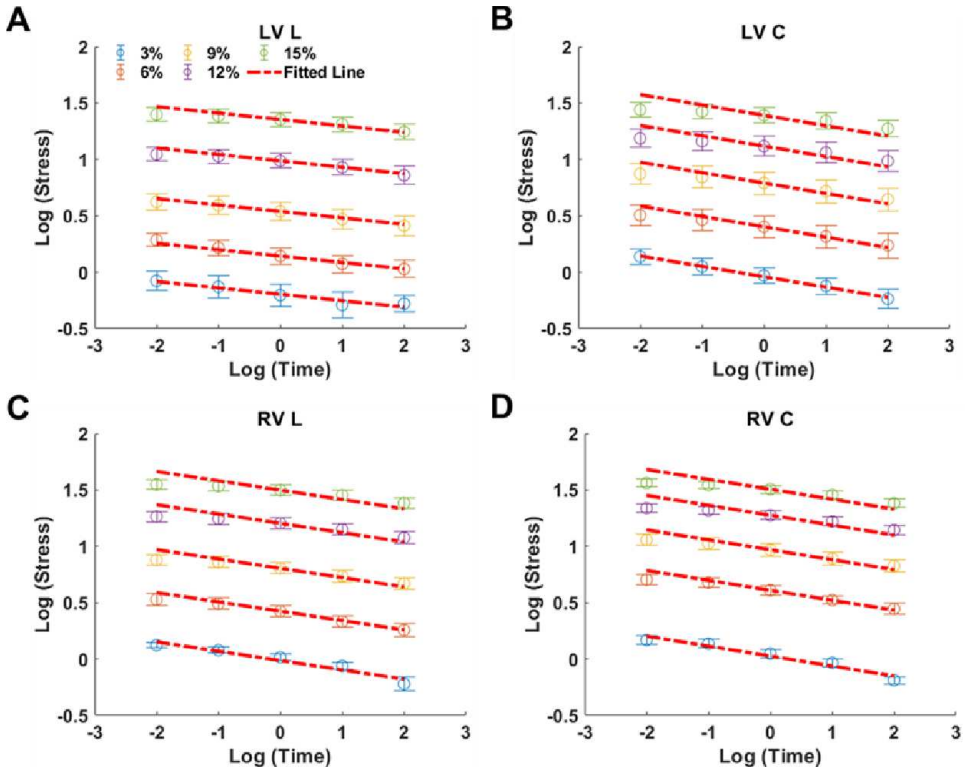

Fig. 4.6. Log scale plots of the stress relaxation data of the ventricles. (A-B) the plots of the LV at input strains of 3% - 15% in the longitudinal (L) and circumferential (C) directions, respectively; (C-D) the plots of the RV at input strains of 3% - 15% in the longitudinal and circumferential directions, respectively. Red dashed line: the fitted line at the strain of 3% superimposed onto the experimental data at all other strain levels. Data are presented as mean ± SEM.

Table. 4.1: The summary of the relaxation rates derived from the log-scale of stress-relaxation curves for both ventricles in both directions. L: longitudinal direction; C: circumferential direction.

	3%	6%	9%	12%	15%
LV L	-0.057 ± 0.005	-0.066 ± 0.008	-0.055 ± 0.006	-0.047 ± 0.005	-0.038 ± 0.004 $
LV C	-0.092 ± 0.007 ^	-0.069 ± 0.006 $	-0.058 ± 0.003 $	-0.050 ± 0.004 $	-0.042 ± 0.002 $
RV L	-0.083 ± 0.010 ^	-0.070 ± 0.006 $	-0.054 ± 0.001 $	-0.047 ± 0.003 $	-0.041 ± 0.003 $
RV C	-0.088 ± 0.005	-0.067 ± 0.005 $	-0.059 ± 0.004 $	-0.048 ± 0.003 $	-0.045 ± 0.002 $

^ : $p < 0.05$ vs LV L 3%, and $: $p < 0.05$ vs 3% fit from the same ventricle in the same direction. Data are presented as mean ± SEM.

Next, we compared the relaxation modulus and the normalized stress (σ/σ_{Max}) at 0.01s and 100s to quantify the tissue viscoelasticity, where larger relaxation modulus and σ/σ_{Max} indicate larger elasticity and viscosity (energy loss) of the material, respectively. **Table 4.2** shows the relaxation modulus obtained at 0.01 and 100s from all five strain levels, and it can be seen that both LVs and RVs had a higher relaxation modulus in the circumferential direction compared to the longitudinal direction ($p<0.05$). This indicates that they are stiffer in circumferential direction, which agreed with the trends shown in the hysteresis loop results (**Fig. 4.4A&B**). However, the RV had or tended to have a larger relaxation modulus than the LV in the longitudinal direction, which suggests that the RV is stiffer than the LV. This finding is opposite to our hysteresis results observed at physiological frequency condition (**Fig. 4.4C**). From the normalized stress, we found that the LV had a larger $\sigma_{100s}/\sigma_{Max}$ at 3% in the longitudinal than circumferential direction (**$p<0.05$, Table. 4.2**). Moreover, the LV had a larger $\sigma_{0.01s}/\sigma_{Max}$ than the RV at 15% in the circumferential direction (**$p<0.05$, Table. 4.2**). Finally, we found a strain-dependent increase in the relaxation modulus at 100s for both ventricles and at both directions (**Fig 4.7**). Similar strain-dependent trends were observed in normalized stress (data not shown). These data suggest that there are increased tissue elasticity and viscosity at higher strains.

Table 4.2. The relaxation modulus (kPa) and normalized stress obtained at initial (0.01s) and later (100s) time points from the stress relaxation data.

		3%	6%	9%	12%	15%
Elastic Index (Relaxation Modulus)						
AT 0.01S	**LV L**	30.0 ± 5.3	34.0 ± 5.0	50.9 ± 8.6	98.0 ± 13.6	178.7 ± 25.4
	LV C	46.8 ± 7.7	61.3 ± 10.5 *	94.4 ± 15.0 *	141.4 ± 19.3 *	197.0 ± 22.8
	RV L	44.7 ± 2.7	58.9 ± 6.8	98.8 ± 13.8 &	159.8 ± 18.1	244.4 ± 24.1 &
	RV C	49.5 ± 3.3	79.1 ± 10.5 *	132.5 ± 14.3 **	185.8 ± 14.7 *	248.0 ± 18.4
AT 100S	**LV L**	17.4 ± 3.3	24.6 ± 6.0	42.1 ± 11.4	78.1 ± 15.5	128.2 ± 19.8
	LV C	19.2 ± 3.7	34.4 ± 6.4	56.7 ± 9.3	91.0 ± 13.7	135.8 ± 17.5
	RV L	21.2 ± 2.8	32.0 ± 4.1	59.7 ± 7.4	104.6 ± 12.0	168.4 ± 17.6
	RV C	19.9 ± 2.4	42.9 ± 7.2 *	78.4 ± 8.8 **	120.3 ± 11.0 *	165.3 ± 14.4
Viscous Index (Normalized Stress)						
AT 0.01S	**LV L**	0.973 ± 0.01	0.995 ± 0.00	0.996 ± 0.00	0.996 ± 0.00	0.998 ± 0.00
	LV C	0.991 ± 0.00	0.992 ± 0.00	0.994 ± 0.00	0.996 ± 0.00	0.998 ± 0.00
	RV L	0.982 ± 0.01	0.994 ± 0.00	0.998 ± 0.00	0.997 ± 0.00	0.997 ± 0.00
	RV C	0.976 ± 0.01	0.991 ± 0.00	0.996 ± 0.00	0.998 ± 0.00	0.997 ± 0.00 &&
AT 100S	**LV L**	0.554 ± 0.05	0.568 ± 0.03	0.614 ± 0.03	0.650 ± 0.03	0.706 ± 0.03
	LV C	0.387 ± 0.05 *	0.541 ± 0.03	0.591 ± 0.02	0.630 ± 0.02	0.680 ± 0.02
	RV L	0.461 ± 0.05	0.539 ± 0.03	0.613 ± 0.01	0.650 ± 0.02	0.683 ± 0.02
	RV C	0.430 ± 0.02	0.504 ± 0.05	0.589 ± 0.02	0.642 ± 0.02	0.661 ± 0.02

*$p<0.05$, **$p<0.01$ vs L from the same ventricle, at the same stretch level, and &$p<0.05$, &&$p<0.01$ vs LV from the same direction, at the same stretch level. Data are presented as mean ± SEM.

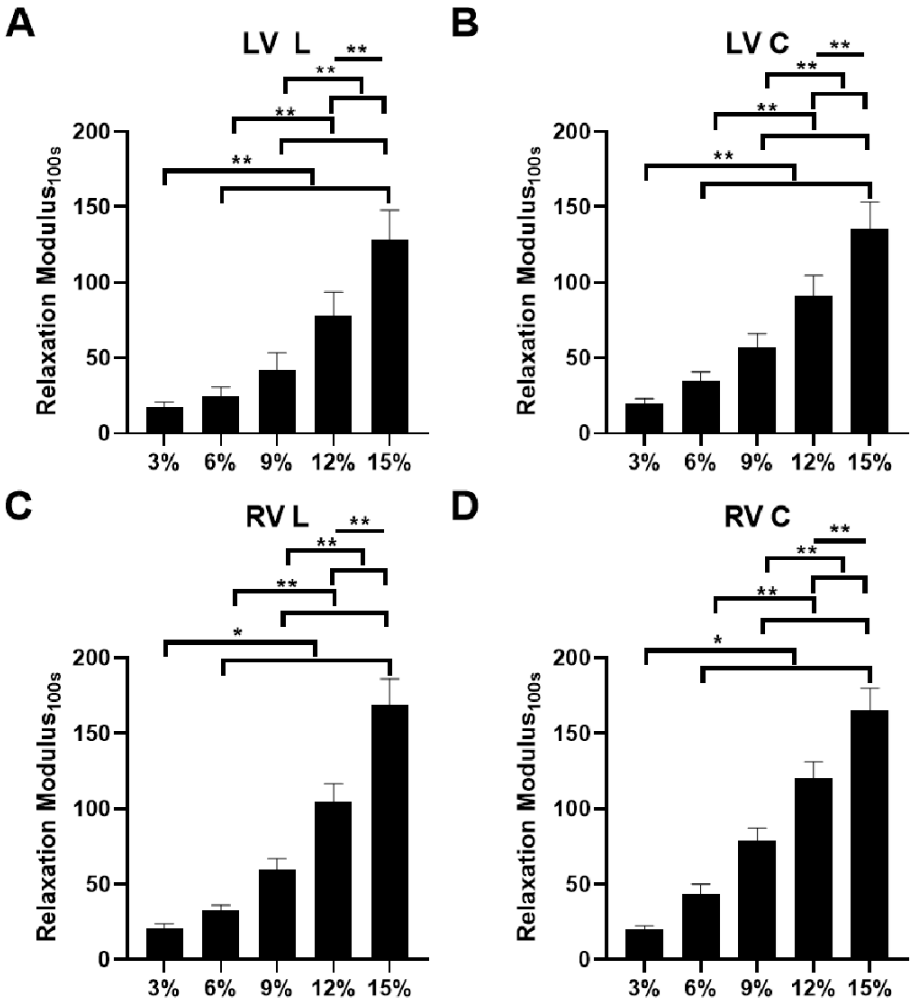

Fig. 4.7. The relaxation modulus at 100s measured at five different strain levels. (A-B) relaxation modulus for the LV in longitudinal and circumferential directions, respectively, and (C-D) relaxation modulus for the RV in longitudinal and circumferential directions, respectively. $^{*}p<0.05$ and $^{**}p<0.01$. Data are presented as mean ± SEM.

4.3.4 Dependence of the viscoelastic indices derived from the cyclic biaxial tests

For the tissue's mechanical properties that present non-linear viscoelastic behavior, we further investigated the interdependence of various elastic and viscous indices derived from the cyclic biaxial test. As shown in the **Figure 4.8**, we found that the EM_{High} was negatively and strongly correlated with the loop width (**Fig. 4.8A**), and the storage energy Ws was also negatively and strongly correlated with the damping (**Fig. 4.8B**). However, the correlation of elastic and viscous indices was absent for the LV mechanical behavior in the longitudinal direction, which was shown to be quasi-linear viscoelastic.

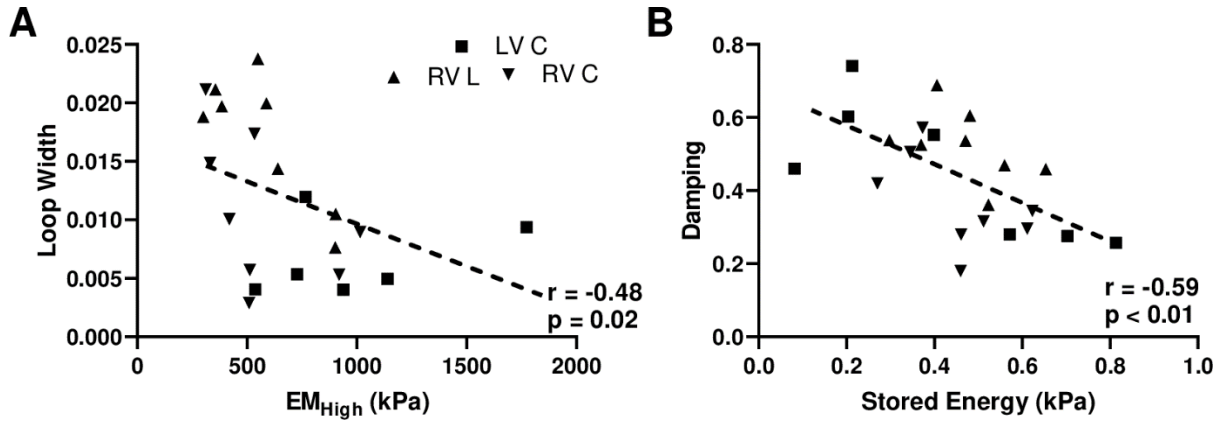

Fig. 4.8. Correlations of elastic and viscous indices measured from cyclic biaxial tests. Only samples that presented non-linear viscoelastic behavior were included– i.e., LVs in the circumferential direction and RVs in both longitudinal and circumferential directions. (A) correlation between high-strain elastic modulus EM_{High} and loop width and (B) correlation between the stored energy (W_s) and damping.

4.3.5 Correlations between the viscoelastic indices derived from the two mechanical tests

Furthermore, since the tissue viscoelasticity was quantified using two different mechanical testing methods (the stress relaxation and cyclic biaxial tests at 1Hz), we investigated the correlations between the viscoelastic indices from these tests to see if we can predict the viscoelastic behavior from one test to the other. Interestingly, we observed a couple of correlations: 1) the relaxation modulus at 3% (0.01s) or 15% (100s) was correlated with the elastic modulus (**Fig. 4.9A&B**); 2) σ/σ_{max} and loop width had positive or negative correlation at 3 or 9% strain (0.01s) (**Fig. 4.9C&D**); and 3) the relaxation modulus at 3 or 15% strain (100s) was correlated with the dissipated energy (W_d) (**Fig. 4.9E&F**). These results suggest that there are some relations between the parameters derived from different types of viscoelasticity tests. Thus, it is possible to use stress relaxation data to predict the behavior obtained from the cyclic biaxial test or vice versa, without using a computational model. However, the correlations need to be confirmed in future studies.

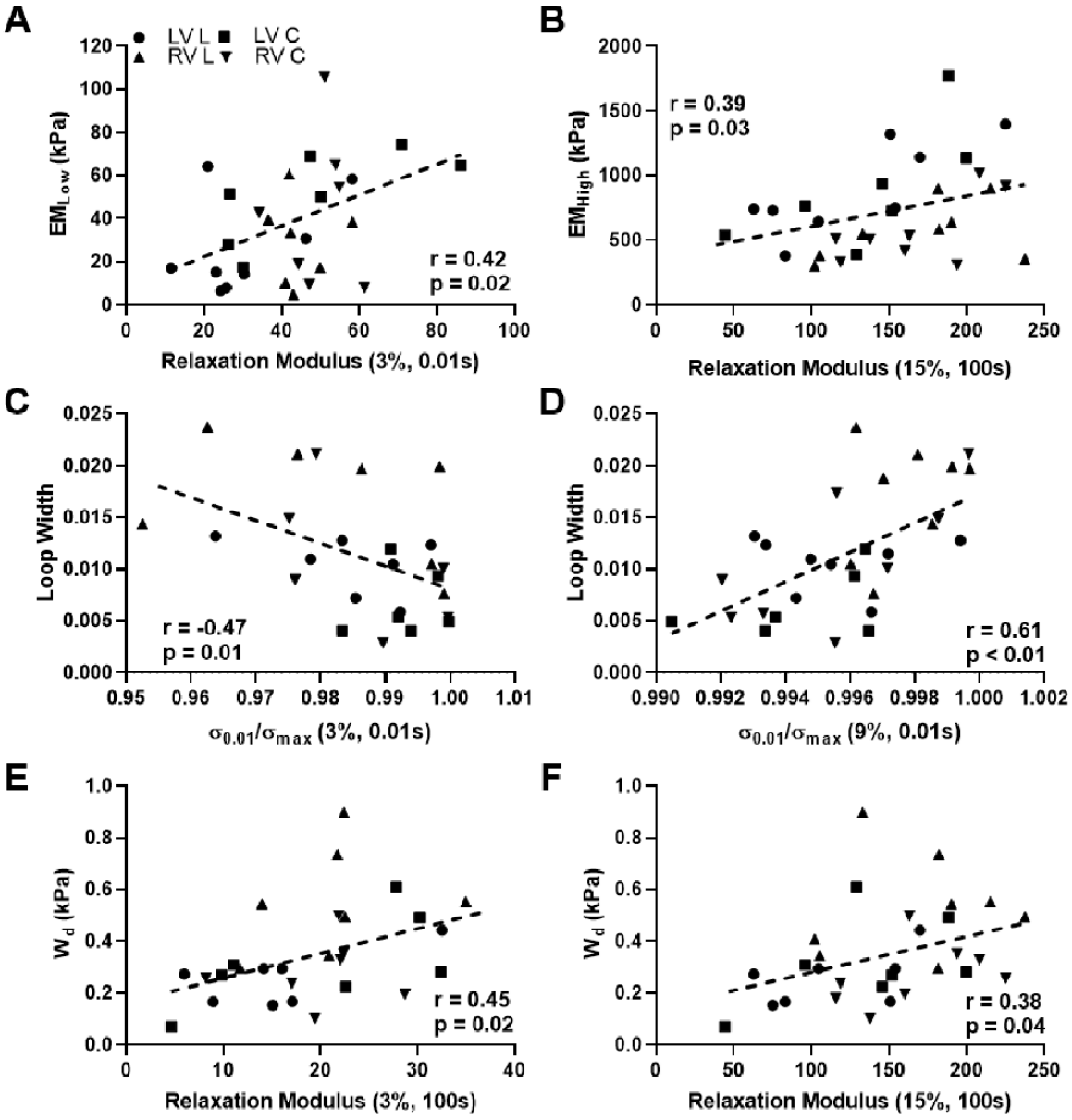

Fig. 4.9. Correlations of viscoelastic indices measured from different mechanical testing methods. (A-B) correlations between the relaxation modulus at 3% (0.01s) and 15% (100s) and low- and high-strain elastic modulus, respectively; (C-D) correlations between the $\sigma_{0.01s}/\sigma_{Max}$ at 3 and 9% strain (0.01s) and loop width , respectively and (E-F) correlations between the relaxation modulus at 3 and 15% strain (100s) and dissipated energy , respectively.

4.4 Discussion

To our knowledge, this study is the first to compare the passive viscoelastic properties of the LV and RV in healthy adult ovine subjects. The main findings include: 1) the RV presented a more significant

frequency-dependent change in viscoelasticity than the LV; 2) under the physiological frequency (1Hz), the LV was more anisotropic in its elasticity whereas the RV was more anisotropic in its viscosity; 3) The LV was stiffer than the RV in both directions; 4) the RV was more viscous than the LV in the longitudinal direction; and 5) the LV was quasi-linearly viscoelastic in the longitudinal direction only, whereas the RV was non-linearly viscoelastic in both directions. Finally, this study used a large animal model (ovine), whose anatomy and physiology are closer to human than those of small animals [169,203,204], and thus the findings are potentially more translatable to human cardiac biomechanics.

4.4.1 Different frequency-dependent behaviors of the LV and RV

The frequency-dependent viscoelastic behavior, also known as strain-rate/stretch-rate dependence, is little investigated from the current literature. Demer et al performed cyclic equibiaxial tests in the canine LVs. From a testing frequency of 0.0005 Hz to 0.05 Hz, they observed minor strain-rate dependence on elasticity and strain-rate independence on loop area [51]. Similarly, we did not observe marked hysteresis area change between 0.01 Hz and 0.1 Hz data (low frequency tests) in all ventricles and in both directions (**Fig. 4.3**).

Our data suggest that the RV had a more significant frequency-dependent change in elastic behavior, but the LV does not (**Fig. 4.3**). Frequency- or rate-dependent increase in elasticity has been reported in other cardiovascular tissues such as healthy blood vessels [4,205–208] and aortic valves [209]. However, frequency-dependent decrease in elasticity was also noted in hypertensive (diseased) pulmonary arteries [4]. We did not know why the LV presented a different behavior than the RV, and further investigation on the molecular mechanism that determines the frequency-dependent changes may explain the difference. Moreover, both ventricles presented increased viscosity as the testing frequency increased, which is consistent with the findings on various types of arteries [4,206] and human ligaments [210]. This suggests that the myocardium may present a 'shear-thickening' behavior, which is opposite to the aortic valves that are 'shear-thinning' [209,211,212]. The extracellular source of myocardial viscosity has been postulated to originate from two aspects – the 'fluidic' components (such as proteoglycans and interstitial fluids) and the sliding between fibers (such as collagen fibers and myofibers) [209]. Intracellularly, the source of myocardial viscosity has been

attributed to titin (a large intracellular matrix protein) [213] and even microtubules recently [214]. How exactly these different extracellular and intracellular components contribute to the tissue level viscous behavior is the next step of research. Nevertheless, these frequency-dependent results emphasize the importance of characterizing cardiovascular tissue viscoelasticity at more physiologically relevant rates, such as our data obtained at 1Hz.

4.4.2 Different anisotropic viscoelastic behaviors of the LV and RV at physiological conditions

Our results showed that the LV and RV had different viscoelastic behaviors when tested at 1Hz (mimicking the resting heart rate) (**Fig. 4.4&4.5**). First, we noticed that the LV and RV presented different anisotropic viscoelastic behaviors. For the elasticity, the LV showed anisotropic elastic behavior (was stiffer in the circumferential direction) whereas the RV showed isotropic elastic behavior (**Fig. 4.5A&B**); but for the viscosity, the LV showed isotropic viscous behavior whereas the RV showed anisotropic viscous behavior (was more viscous in the longitudinal direction) (**Fig 4.5C&D**). These data make us wonder if the viscous and elastic properties of ventricles are coupled or not. For biological materials such as blood vessels, both increased [6,215] and decreased viscosity [4] have been reported in hypertensive arteries (i.e., with stiffened vessel wall). In different types of bones, a positive correlation between elastic modulus and viscosity has been reported [216]. From the non-linear viscoelastic samples, we observed a strong and negative correlation between the elastic and viscous indices (**Fig. 4.8**). We speculate that the positive or negative correlations of material viscosity and elasticity may have to do with the material's internal structures and compositions, which may also be related to the shear-thickening vs. shear-thinning type of behavior. Overall, there is a lack of understanding of the interdependence of tissue's elasticity and viscosity.

4.4.3 Different elastic behaviors of the LV and RV at physiological conditions

Second, the LV was stiffer than the RV in both directions, especially at high strains (**Fig. 4.5B**). This is consistent to the finding of higher strain energy storage in the LV compared to the RV in healthy adult ovine [195]. The investigations on myocardial microfibrils or skinned cardiomyocytes have shown that the sources of myocardial stiffness are mainly from titin and collagen. Particularly, when the deformation

is small (within normal sarcomere length) the passive stiffness is mainly contributed from titin, whereas when the deformation is large (beyond normal sarcomere length) the passive stiffness is mainly contributed from collagen [213]. The more pronounced elastic difference at high strains suggests that collagen fiber arrangement is possibly the primary cause of the chamber's mechanical difference in healthy state. Therefore, factors such as fiber orientation, collagen isoforms or cross-linking should be examined in future investigation to further elaborate the elastic difference.

4.4.4 Different viscous behaviors of the LV and RV at physiological conditions

Third, this study firstly reported different viscous behavior between the two chambers. The RV had larger viscosity than the LV in the longitudinal direction, and this difference was absent in the circumferential direction (**Fig. 4.4&4.5**). We have not observed significant difference in cardiomyocyte size (histology from a separate study, data not shown) between healthy ovine LV and RV. The origin of the viscous difference, to our speculation, may also be attributed to the distribution of collagen fibers that awaits further investigation. The viscous property is considered as a measure of energy dissipation during the dynamic deformation. The different viscous behavior may be related to the different metabolic energy use and the efficiency of cardiac pumping between the ventricles, both of which are currently less understood. At the cellular level, whether the viscosity is needed for normal physiological function of cardiomyocytes (to absorb shock) or impairs the contractile function (due to the resistance to length change) remains unclear [214]. Therefore, it is important to investigate the impact of viscosity on cellular and ventricular (tissue level) function.

4.4.5 Different non-linear viscoelastic behaviors of the LV and RV at physiological conditions

Lastly, our results from the stress relaxation test suggest that the LV was quasi-linear viscoelastic in the longitudinal direction only, whereas the RV was non-linear viscoelastic in both directions (**Fig. 4.6 & Table 4.1**). For a quasi-linear viscoelastic material, the viscoelastic behavior can be separated into elastic and viscous behaviors. However, for a non-linear viscoelastic material, the elastic and viscous behaviors cannot be separated from each other [60,63]. Thus, we investigated the dependence of the elastic and viscous

indices derived from the cyclic biaxial tests. As expected, we found strong and negative correlations between the elastic and viscous indices in the LV in circumferential direction and in the RV in two directions (Fig. 8). However, the correlation was absent for the LV longitudinal direction. Our data suggest that a non-linear viscoelastic model should be considered to investigate the structure-function relations of RV viscoelasticity.

4.4.6 Limitation and future study

First, our samples were from female ovine only due to the limitation in ovine stock. Sex differences have been found in terms of ventricular function in both physiological and pathological conditions [217], but its effect on the mechanical property has not been reported. We thus assumed negligible impact of the sex on the comparison of LV and RV passive viscoelasticity and future study should include male subjects. Second, the stress-strain hysteresis loops obtained from the 1Hz dynamic tests were not as smooth as those from the lower frequency tests. This is because of limited sampling rate of the camera used in the system. However, we were able to capture the main shape of the loop and we think its effect on the calculation of viscoelastic parameters should be minimal. Third, we tested the biaxial viscoelasticity from the epicardial side of the free walls to examine the compartment difference. It has been reported that there is a transmural variation of the myocardial fiber alignment from epicardium to endocardium [54]. Therefore, a better characterization of entire ventricle's viscoelasticity should incorporate other layers of the tissue and shear tests for transmural mechanical behavior. Nevertheless, this study provides an initial examination of the ventricular difference in the epicardial region, which is the main site of occurrence of myocardial infarction (due to coronary artery blockage). The data obtained will provide important baseline viscoelastic mechanics in healthy myocardium for both ventricles that are absent in the current literature. Finally, as the initial study of comparing LV and RV biaxial viscoelasticity, we mainly focused on the mechanical behavior of the tissues and the structural information such as myo-/collagen fiber orientation or individual tissue constituent is not obtained. The future investigation incorporating structural characterization will provide more insights on the structure-function relations of the myocardium anisotropic viscoelasticity.

4.5 Conclusions

In this study, we examined the viscoelastic differences between the LVs and RVs in healthy adult ovine. We found that the RV hysteresis had more significant changes from low to high frequencies than the LV hysteresis. Under the physiological frequency (1Hz), the LV was more anisotropic in its elasticity, whereas the RV was more anisotropic in its viscosity; moreover, the LV was stiffer than the RV in both directions whereas the RV was more viscous than the LV in the longitudinal direction. Lastly, the LV presented quasi-linear viscoelastic behavior in longitudinal direction only, whereas the RV had non-linear viscoelastic behavior in both directions. Our findings provide important baseline information on the passive viscoelasticity of the myocardium and will assist with the understanding of the biomechanical mechanisms of ventricular function.

AIM 2: CONSTITUTIVE MODELING OF PASSIVE BIOMECHANICAL PROPERTIES OF VENTRICLES (CHAPTER 5 TO 6)

For my second **Aim 2**, it includes two chapters (**Chapters 5 to 6**). We moved from experiment method to constitutive method. Within this aim, I revised, adapted and applied the constitutive modeling to our experimental data that described in the previous aim. Briefly, I firstly revised and applied the constitutive model to capture the ventricular tissue static (hyperelastic) mechanical behavior (**Chapter 5**) and then adapted and applied the constitutive model to describe the RV viscoelastic behavior (**Chapter 6**).

In **Chapter 5**, we modeled the ventricle hyperelastic behavior by using the Fung type model and Structurally Informed model. This chapter was published, and our results showed good fitting accuracy and the simulated data agreed with our experimental results, and structurally informed model suggests potentially stiffer collagen fibers in the LV than RV. **Chapter 6** modeled the passive viscoelastic behavior used both quasi-linear and nonlinear approaches. This chapter was just submitted, and our results suggest significant strain-dependent viscoelastic behavior, and the NLV model had a higher capability of predicting the strain-dependent viscoelastic behavior than the QLV model. The work done here will help to develop the RV stimulation study and eventually help the RV diagnostic method and treatment development.

CHAPTER 5: CONSTITUTIVE MODELING OF HYPERELASTIC MECHANICAL BEHAVIOR OF VENTRICLES [4]

5.1 Introduction

Both empirical models and constitutive models have been applied to characterize the nonlinear, biaxial mechanical behavior of ventricles. Because of the nonlinear, 'J'-shaped stress-strain curve, the use of an exponential component is common in empirical models. But these models provide little information on the relations of physical quantities or physiological conditions of the tissue, and thus constitutive models are developed to better describe the myocardium tissue mechanics [54]. With certain assumptions (hyperelasticity, incompressibility, homogeneity, etc.), a strain energy function (W) is defined to relate the mechanical loadings (stress) to the geometry changes (strain). The determination of the strain energy function is the key in constitutive models. Based on the model parameters included in the strain energy function, different material's properties can then be derived. A thorough review of the modeling for tissues biaxial mechanical properties can be found in Ref [53,54].

For the modeling work for the myocardium passive hyperelastic behavior, various constitutive models have been proposed, develop from isotropic to transversally isotropic and eventually orthotropic. A thorough review of the modeling for biomechanical models of myocardium hyperelastic behavior, please refer to Ref [150]. Currently, there are two main types of constitutive models for myocardium mechanics which are phenomenological constitutive model and structurally informed model. It is difficult to precisely infer from these phenomenological constitutive models the micromechanical mechanisms that involve the coupling between myo- and collagen fibers ensembles under physiological or pathological conditions.

[4] *This chapter is published as a peer reviewed research article in the Frontiers in bioengineering and biotechnology (doi.org/10.3389/fbioe.2022.857638).*

Whereas the structurally informed model can, which based on the descriptors that account for compositional and microstructural details.

In this chapter, we include both transversally isotropic constitutive model (Fung type) and orthotropic structurally informed model. We applied these two models to our experimental data from ovine left and right ventricles (LV and RV). We observed good fitting accuracy and the simulated data agreed with our experimental results, and structurally informed model suggests potentially stiffer collagen fibers in the LV than RV. These findings will further assist the development of the computational study for the RV and eventually help the development of the RV diagnostic method and treatment development.

5.2 Constitutive modeling

Next, we fitted our equibiaxial experimental data to a phenomenological constitutive model (Fung type model) and a structurally informed model. We used the phenomenological Fung type model to assess the overall *tissue-level* stiffness and anisotropic behavior in the LV and RV in a comparative manner; and the structurally informed model was used to provide insights into the differences between *fiber-level* mechanical and architectural properties of the LV and RV myocardium. An affine deformation was assumed within the samples under equibiaxial loading as commonly adopted in biaxial soft tissue testing.

5.2.1 Fung type model

We calculated the shear deformations k_{LC} and k_{CL} from our experimental data. (**Table 5.1**). The shear deformation was minimal compared to the in-plane stretches along longitudinal (OT) and circumferential (cross-OT) directions. Accordingly, shear stresses were assumed to be negligible in our modeling work.

Table 5.1. Maximum stretches in the in-plane and shear directions during equibiaxial tests. Data are presented as mean ± SEM.

Ventricle	λ_L	λ_C	k_{LC} (shear)	k_{CL} (shear)
LV (n=7)	1.14±0.02	1.19 ±0.02	1.04 ±0.01 *,†	1.02±0.02 *,†
RV (n=7)	1.20±0.02	1.14±0.01	1.02±0.01 *,†	1.03±0.01 *,†

λ_L: stretch in the longitudinal direction, λ_C: stretch in the circumferential direction, k_{LC} and k_{CL}: stretches in the shear directions. *: p<0.001 vs. λ_L, †: p<0.001 vs. λ_C.

Furthermore, the relevant Green strain tensor (**E**) components were calculated as:

$$E_L = \frac{1}{2}(\lambda_L^2 - 1),\ E_C = \frac{1}{2}(\lambda_C^2 - 1) \tag{5.1}$$

where λ_L and λ_C are the stretch in longitudinal and circumferential directions, respectively.

Next, a four-parameter Fung type constitutive model [56,172] with the following energy function (Ψ) was fit to the biaxial stress-strain data:

$$\Psi = \frac{B}{2}(e^Q - 1),\ Q = b_L {E_L}^2 + 2b_{LC}E_L E_C + b_C {E_C}^2 \tag{5.2}$$

The 2nd P-K and Cauchy stresses for an incompressible tissue were calculated as:

$$\mathbf{S} = 2\,\frac{\partial \Psi}{\partial \mathbf{C}} - p\mathbf{C}^{-1},\ \boldsymbol{\sigma} = \mathbf{FSF}^T \tag{5.3}$$

where **F** is the deformation gradient tensor, **C** is the right Cauchy-Green tensor, p is an unknown hydrostatic pressure to enforce det(**C**) =1, and b_L, b_{LC}, b_C and B are the material constants. The stress-strain relationships in the L and C directions were derived as:

$$\sigma_L = (2E_L + 1)(b_L E_L + b_{LC}E_C)Be^{(b_L {E^2}_L + 2b_{LC}E_L E_C + b_C {E^2}_C)}$$

$$\sigma_C = (2E_C + 1)(b_{LC}E_L + b_C E_C)Be^{(b_L {E^2}_L + 2b_{LC}E_L E_C + b_C {E^2}_C)} \tag{5.4}$$

The Fung strain energy function was fitted to the equibiaxial experimental data for each sample. The fitting was performed in MATLAB. The sensitivity to initial guesses was checked for every fit and a minimal dependency to initial guess was found for all the fits. The root mean square (RMS) was calculated

to assess the fitting results. Finally, the anisotropic parameter *K* and elasticity at zero load in two directions ($M_{0,L}$ and $M_{0,C}$) were calculated as described in previous studies [56,172,218].

5.2.2 Structurally informed model

Next, we used a structurally informed model that incorporates the transmural changes of myo-/collagen fibers to reveal the contributions of each fiber type to the tissue-level myocardial biomechanical behavior [170,219]. Briefly, the total energy function (Ψ) was written as the sum of the mechanical contributions of the ground matrix and myo- and collagen fibers as,

$$\Psi(\mathbf{C}) = \phi^g \Psi^g(\mathbf{C}) + \phi^m \Psi^m(\mathbf{C}) + \phi^c \Psi^c(\mathbf{C}) \tag{5.5}$$

where Φ^g, Φ^m and Φ^c are volume fractions for the ground matrix (including non-structural extracellular matrix proteins, fibroblasts, interstitial fluid, etc.), myo- and collagen fibers, respectively, and Ψ^g, Ψ^m, and Ψ^c are strain energy functions associated with each phase. The volume fraction measurement is described in the next section (see §5.2.3).

At the tissue level, the 2nd P-K stress tensor (**S**) was described in terms of the energy function $\Psi(\mathbf{C})$:

$$\mathbf{S} = 2\frac{\partial \Psi}{\partial \mathbf{C}} - p\mathbf{C}^{-1} = \mathbf{S}^g + \mathbf{S}^m + \mathbf{S}^c \tag{5.6}$$

The stress-strain relationships for ground matrix, myo- and collagen fibers were derived as:

$$\mathbf{S}^g = \phi^g k^g \mathbf{I} - p\mathbf{C}^{-1} \tag{5.7}$$

$$\mathbf{S}^m = \frac{\phi^m k_1^m}{H} \int_0^H \int_{-\pi/2}^{\pi/2} \Gamma^m(\theta^m, z) \frac{(\sqrt{I^m}-1)}{\sqrt{I^m}} \times \exp\left[k_2^m \left(\sqrt{I^m}-1\right)^2\right] (\mathbf{n}^m \otimes \mathbf{n}^m) d\theta^m dz \tag{5.8}$$

$$\mathbf{S}^c = \begin{cases} \frac{\phi^c k_1^c}{H} \int_0^H \int_{-\pi/2}^{\pi/2} \Gamma^c(\theta^c, z) \times (e^{k_2^c E^c} - 1)(\mathbf{n}^c \otimes \mathbf{n}^c) d\theta^m dz, \ for\ E^c \le E_{ub} \\ \frac{\phi^c k^c{}_1}{H} \int_0^H \int_{-\pi/2}^{\pi/2} \Gamma^c(\theta^c, z)\left[\left(e^{k_2^c E^c} - 1\right) + k_2^c\, e^{k_2^c E^c}\, (E^c - E_{ub})\right](\mathbf{n}^c \otimes \mathbf{n}^c) d\theta^m dz, \ for\ E^c > E_{ub} \end{cases} \tag{5.9}$$

where **I** is the identity tensor, $I^m = 2(\mathbf{n}^m \cdot \mathbf{E}\mathbf{n}^m) + 1$, $E^c = \mathbf{n}^c \cdot \mathbf{E}\mathbf{n}^c$ are the pertinent kinematic measures, k's are model parameters, and **n**'s are the defined unit vectors that describe the planar orientations of the myo-and collagen fibers, respectively. We adapted the previous model and derived the fiber orientation parameters $\theta^m \; and \; \theta^c$ (ranged from 0 to $\pi/2$) from serial histology measurements (see §5.2.4). The parameters describing the transmural orientation distribution (Γ) were derived for myo- and collagen fibers using a modified Beta distribution function [170]. In the transmural direction, the normalized tissue thickness was denoted as H and a value of 100 represents the entire tissue thickness. E_{ub} is the upper bound of the transition region derived from the average stress-strain curve calculated from each direction.

The myofiber model parameter k_1^m was estimated from the fit to experimental data in the low strain region as described previously [176], and the parameter for amorphous ground matrix k^g was fixed at a value of 10 kPa due to its much lower contribution to the mechanical behavior of myocardium compared to that of myo-/collagen fibers [95]. The same fitting method was used as described in the above Fung type model section.

5.2.3 Collagen volume friction measurement

The tissue slices were stained with Picrosirius Red (PSR) and imaged and analyzed via a transmission microscope (Nikon Eclipse E800) and Image Pro Premier software (Media Cybernetics, Rockville, MD) for collagen content quantification. For each sample, three regions were randomly selected under polarized light microscopy. An image thresholding method in which yellow, green, brown and dark blue colors were chosen to represent type I collagen, type III collagen, ground matrix and muscle, respectively. The amounts of type I and III collagen were quantified as the area percentage to total tissue

area, and the amount of collagen content was quantified as the total area percentage of type I and III collagen [129,179].

We further performed immunohistochemistry (IHC) to LV (n=4) and RV (n=4) samples to confirm the area fraction measurement of type III collagen in PSR staining slides. Tissue samples were stained with rabbit polyclonal anti-human collagen III antibody (1:500 dilution, ab7778, Abcam, Cambridge, United Kingdom). Image thresholding via ImageJ (U.S. NIH, Bethesda, Maryland) was used to determine the area fraction of collagen III.

5.2.4 Myo- and collagen fibers orientation measurement

From the serial histology sections with PSR staining, the transmural change of fiber orientation was measured using in-house MATLAB codes adapted from a previous study [170]. Briefly, each serial tissue slice was imaged under bright field light microscopy and separated by the color of tissue component using ColorDeconvolution2, a plug-in in ImageJ. Fiber angle was calculated for collagen and myofiber, respectively. The transmural fiber orientation distribution was then represented by a Beta distribution function to fit a surface to the 3D data. The mean transmural fiber orientations for both myo- and collagen fibers were calculated from the Hermitian fit parameters [170]. These data were used to derive the transmural orientation distribution (Γ) for the structurally informed modeling.

5.3 Results

5.3.1 Experimental data fitting with Fung type model

We performed fitting of the equibiaxial stress-strain curves using the four-parameter Fung type model. A good fit to the experimental data was observed for both ventricles and at both directions (low

RMS values), and the fitting results are summarized in **Table. 5.2**. The simulated equibiaxial stress-strain curves using the mean values of the estimated constants showed similar behaviors as our experimental data: the LV and RV had different anisotropic behaviors (**Fig. 5.1**) and the LV was stiffer than the RV in the longitudinal direction (**Fig. 5.1**).

Table 5.2. Fung model fitting results. Average data are presented as mean ± SEM.

Ventricle	b_L	b_C	b_{LC}	B (kPa)	RMS (kPa)
LV #1	145.67	25.16	4.40×10^{-11}	0.15	0.63
LV #2	41.63	17.91	0.01	0.09	0.09
LV #3	103.43	13.94	0.01	0.18	0.58
LV #4	96.74	53.68	0.01	0.17	0.14
LV #5	42.00	83.08	1.33×10^{-10}	0.10	0.28
LV #6	38.36	37.54	0.01	0.03	0.60
LV #7	33.51	27.33	0.01	0.88	0.25
LV (n=7)	71.62±16.52	36.95±9.17	0.007±0.002	0.23±0.11	0.37±0.09
RV #1	17.44	35.07	8.48×10^{-14}	0.23	0.25
RV #2	45.49	20.05	0.01	0.38	0.24
RV #3	20.96	46.14	0.01	0.25	0.22
RV #4	57.19	79.55	1.55×10^{-10}	0.13	0.19
RV #5	51.30	99.99	0.01	0.07	0.42
RV #6	28.42	43.74	8.29×10^{-11}	0.15	0.10
RV #7	20.95	48.57	0.01	0.07	0.17
RV (n=7)	34.54±6.20	53.30±10.32	0.006±0.002	0.18±0.04	0.23±0.04

b_L, b_C, b_{LC} and B are the material constants, and RMS is root mean square.

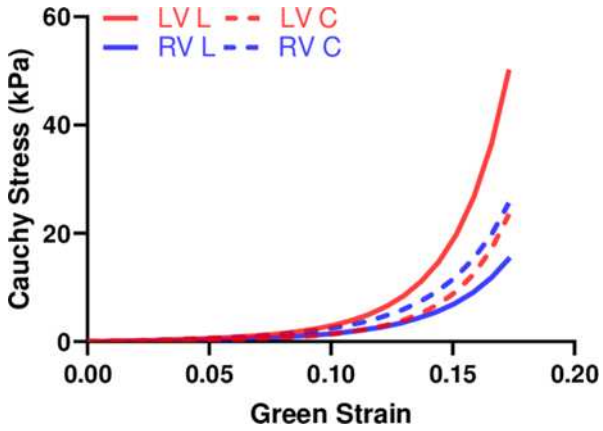

Fig. 5.1. Stimulated equibiaxial stress-strain curves generated by the four-parameter Fung model, using the average values of the fitting parameters for both ventricles in two directions.

We further compared the zero-load modulus M_0 in each ventricle and in each direction, using the model fitting parameters. The $M_{0,C}$ was significantly larger than the $M_{0,L}$ in the RV (**p<0.05**), and there was a strong trend of larger $M_{0,L}$ compared to the $M_{0,C}$ in the LV, indicating different anisotropic behaviors between the ventricles (**Fig. 5.2A**). Expectedly, the anisotropic parameter K was significantly different between the LV and RV (**Fig. 5.2B**, **p<0.01**). Finally, we performed correlation analyses and found that K was significantly correlated with the ratios of longitudinal to circumferential elastic moduli (M and M/ε) in both strain ranges (**p<0.05**, r = 0.75-0.85, data not shown).

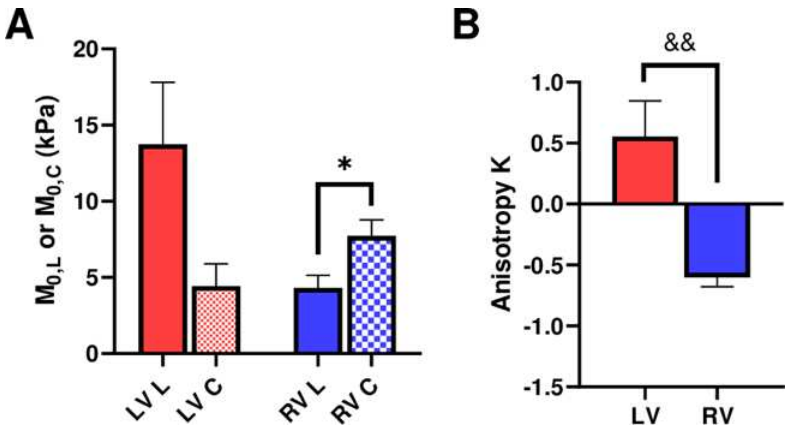

Fig. 5.2. (A) Longitudinal and circumferential zero-load elastic modulus M_0 for each ventricle type, and (B) Anisotropic parameter K for each ventricle type. *: $p < 0.05$ comparison between the directions and &&: $p < 0.01$ comparison between the ventricles, respectively.

5.3.2 Experimental fitting with structurally informed model

We fit the equibiaxial stress-strain curves with the structurally informed model to investigate the different contributions of myocardial components (myo- and collagen fibers) to tissue mechanics in these chambers. The fitting results are summarized in **Table 5.3**, and a representative fitting result is shown in **Fig. 5.3**. The model fit our experimental data well, which is evident by the small values of RMS. Compared to the RV, the LV tended to have larger stiffness for myo- and collagen fibers (see k_1^m and k_1^c). Furthermore, the LV tended to have a larger transition strain (E_{ub}) than that of the RV.

Table 5.3. Structurally informed model fitting results. Average data are presented as mean ± SEM.

	Myofiber		**Collagen**			**RMS**
	k_1^m(kPa)	k_2^m	k_1^c(MPa)	k_2^c	E_{ub}	**(kPa)**
LV #1	5.04	384.38	21.61	56.70	0.14	0.25
LV #2	15.77	301.81	69.41	38.15	0.2	0.65
LV #3	54.65	304.28	12.52	26.35	0.10	0.27
LV (n=3)	25.15±15.07	330.16±27.12	34.51±17.64	40.40±8.83	0.15±0.03	0.39±0.13
RV #1	25.10	10.07	9.73	34.54	0.14	0.87
RV #2	9.87	1.54×10^{-9}	10.08	68.37	0.09	0.37
RV #3	26.55	573.59	12.68	59.94	0.13	1.28
RV #4	18.05	263.93	28.63	25.34	0.14	0.68
RV (n=4)	19.89±3.82	211.89±135.14	15.28±4.50	47.05±10.20	0.12±0.01	0.80±0.19

k's are model parameters, E_{ub} is the upper bond of the transition region.

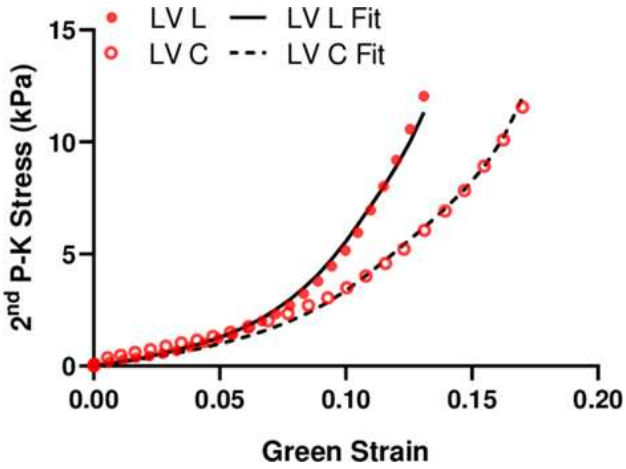

Fig. 5.3. Representative fitting results using the structurally informed model.

5.4 Discussion

5.4.1 Insights from the Fung Type Model

In this study, we found that the ovine LV and RV had different anisotropic behaviors: the LV had larger *M* in the longitudinal direction compared to the circumferential direction, whereas the RV had the opposite trend of difference between these directions. The anisotropy parameter *K* derived from constitutive modeling was significantly correlated with the experimental data, confirming the different anisotropic behaviors. We speculate that the reason for this difference is the different need to facilitate blood filling and ejection in each ventricle. The LV is more conically shaped and is comprised of helical fibers that allows it to deform more circumferentially during cardiac cycles (majority of LV contractility occurs due to circumferential shortening); in contrast, the RV is crescent shaped and is comprised of wrap-around transverse fibers that deforms more longitudinally (majority of RV contractility occurs due to longitudinal shortening) [181,182]. Thus, our findings show a more compliant passive mechanical property of the wall in the main axis of cyclic deformation for both ventricles, which suggests that passive elasticity is maintained at

a low level to reduce the elastic 'resistance' and facilitate blood filling (as well as 'pumping' potentially). The understanding of the differences in baseline anisotropy between the two ventricles will help to develop chamber-specific therapies aimed at reducing wall stress along the main axis of deformation.

5.4.2 Insights from the Structurally Informed Model

The phenomenological computational models typically provide good capture of the macroscopic mechanical behavior; however, they lack detailed information on the structural and material properties of the myocardium constituents [150]. Instead, the structural constitutive model, such as the one used in this study, is formulated to capture the underlying microstructural mechanisms for the macroscopic behavior of the tissue. From our results, the LV tended to have a larger transition strain than the RV, which suggests that the LV recruit collagen later than the RV. Furthermore, the LV tended to have a larger k_1^m value (myofiber stiffness) and a larger k_1^c value (collagen stiffness) than those of the RV, suggesting a stiffer fiber material property. This finding is similar to the recent report of Kakaletsis et. al [161]. The cause for stiffer collagen fibers in the LV than the RV awaits further investigation. The ventricular differences in the diastolic function and the adaptation to mechanical loading conditions depend on microstructural characteristics like myofiber and collagen stiffness. The structurally informed model here can help to highlight the myofiber and collagen contributions to that of organ-level remodeling, which will in turn help to develop targeted therapies that prevent or reverse maladaptive remodeling [166].

5.5 Conclusion

The anisotropic properties obtained from the experimental data were captured by the zero-load elastic moduli as well as the anisotropic parameter *K* derived from the four-parameter Fung type model.

Results from the structurally informed model imply stiffer collagen fibers in the LV than the RV, which awaits further investigation.

CHAPTER 6: CONSTITUTIVE MODELING OF VISCOELASTIC MECHANICAL BEHAVIOR OF RIGHT VENTRICLES [5]

6.1 Introduction

The myocardium is a viscoelastic material presenting elastic and viscous mechanical behaviors. That is, both energy storage (related to tissue elasticity) and energy dissipation (related to tissue viscosity) occur during the tissue deformation [31]. However, compared to the elastic behavior, the viscoelastic behavior of right ventricle (RV) myocardium is less studied. As lately reviewed [31,108,220], the experimental evidence of myocardium passive viscoelasticity was debatable originally, but recent studies demonstrated the presence of significant hysteresis of passive myocardium from animal to human specimens [58,102,221]. This is in contrast to the long known viscoelastic behavior of individual cardiomyocytes or papillary muscles from either side of the heart [51,104,222–226]. As a result, the knowledge about RV myocardium passive viscoelasticity remains a gap in cardiac biomechanics.

Constitutive modeling of myocardial tissues has been receiving growing interests in recent years with evolving experimental findings. Multiscale and multiphysics computational models have been developed to address the complex microstructure of myocardium and its function associated with various physical properties (mechanical behavior, electrical conduction and electromechanical coupling). Detailed reviews of constitutive and computational modeling of the myocardium can be found in [108,150,170,220,227,228]. The most common models to capture the macroscopic viscoelastic behavior of the myocardium are various formats of Maxwell models, composed of springs and dashpots that represent the elastic and viscous behaviors, respectively. A spring connected to two or more Maxwell elements in parallel (a.k.a. generalized Maxwell model) have been used to describe the stress relaxation or cyclic loading mechanical data in papillary muscles [70,229] or the ventricular wall [51,99,103,108,220,227,230]. These models are considered as

[5] *This chapter has been submitted for publication in the Acta biomaterialia. Currently is under revision.*

phenomenological models. Another type of viscoelastic model is the biphasic model which attributes the overall viscoelastic behavior to the fluid and solid components in the tissue [231–233]. In this model, the muscle can be modeled as an incompressible, poroelastic solid saturated by an incompressible, isotropic viscous fluid. The viscoelasticity mainly arises from interstitial fluid flow through pores, and thus viscoelasticity origins from other components (e.g., extracellular matrix proteins) is neglected. Furthermore, Gultekin et al. [108] introduced a new viscoelastic model by decomposing the free energy function into volumetric-isochoric elastic and isochoric-viscoelastic parts (or equilibrium and non-equilibrium parts), assuming incompressible deformation of the myocardium. An important feature of this model is that it combines the mechanical continuum and thermodynamic principles and describes the energy dissipation directly, but more work is needed to further improve the model to reduce the discrepancy between the experimental data and model fits. Finally, the latest viscoelastic model for myocardium was developed by Nordsletten et al. [220]. In this model, a 'fractional viscoelasticity' strategy was adopted to reveal a spectrum of relaxation response of the myocardium presumably caused by different scales of collagen structure (from fibrils to large sheets and bundles). However, this model is unable to capture the nonlinear viscous behavior nor strain-dependent viscoelastic behavior. As a result, the model belongs to the quasi-linear viscoelastic (QLV) model family. To date, Fung's QLV formulation [234] remains a prominent model to describe viscoelasticity in soft tissues and has been used to capture the experimental data of myocardium as the myocardium is neither linear elastic nor linear viscoelastic. The QLV formulation can be found in previous works [68,220,232,233,235,236] covering applications from papillary muscles to ventricle free walls (left ventricle only), including both embryonic and adult heart tissues. This model is popular for other types of soft tissues due to its simplicity with a convenient assumption that the elastic and viscous (time-dependent) mechanical behaviors of the tissue are separable. However, one must note that many biological tissues such as tendon, ligaments and spinal cord exhibit fully nonlinear viscoelastic (NLV) behavior [59,62,105,237].

Our recent empirical study found that the ovine left ventricular (LV) and right ventricular myocardium exhibit different types of viscoelastic behaviors [175]. That is, the RV free wall (RVFW) has

different relaxation rates at different strain levels in both longitudinal (outflow track) and circumferential directions, suggesting a fully NLV behavior of the tissue. In contrast, the LVFW presents a QLV behavior in the longitudinal direction and a NLV behavior in the circumferential direction. This is the first report of distinct viscoelastic properties of LV and RV in healthy adults. Our experimental findings call for a need to characterize the stress relaxation behavior of RVFW by viscoelastic constitutive modeling, which lends into a deeper understanding of the passive elastic and viscous resistances of the tissue during diastole. Such research is clinically relevant due to the increasing awareness of the prevalence of RV failure in the advanced stage of diseases such as pulmonary hypertension, congenital heart diseases, and left heart failure with preserved ejection fraction [21]. The clinical challenge becomes significant as it is evident that the LV and RV are different in their embryologic origin, anatomy and function [238]. Therapies that work for LV failure patients do not achieve similar effectiveness in the RV failure patients [151–153]. To the best of our knowledge, studies on the viscoelastic constitutive modeling of the RVFW remain limited. The only modeling study specific to the RVFW viscoelasticity was reported in rats using indentation tests [239]. However, the focus of that study was on the regenerative therapy for hypertensive hearts failure patients, and only a simple linear viscoelastic model (Maxwell model) was used. As a result, comprehensive viscoelastic constitutive modeling is needed to describe the anisotropic viscoelastic behavior of the RVFW.

Therefore, the goal of this study was to characterize the passive, anisotropic and strain-dependent viscoelastic behavior of healthy RVFW using constitutive modeling. We applied both QLV and NLV theories to the biaxial stress relaxation data obtained from healthy adult ovine RVFW. Our results showed that the RVFW exhibited significantly anisotropic and strain-dependent viscoelastic behavior, and the NLV model had a higher capability of predicting the strain-dependent viscoelastic behavior than the QLV model. From the QLV fitting, the relaxation term associated with the largest time constant played the dominant role in the overall relaxation behavior at most strains from early to late diastole, and the term associated with the smallest time constant was prominent only at small strains in early diastole. Using a power-law fitting, the model parameters (relaxation rate and initial stress) exhibited nonlinear (quadratic polynomial)

relationship with the strain. These findings highlight the importance of characterizing and modeling the anisotropic, nonlinear viscoelastic deformation of the RVFW to fully capture the elastic and viscous resistances and energy expenditure of the tissue during diastole. Such knowledge will deepen the understanding of the mechanical mechanisms of diastolic function of the RVFW and assist with the further development of a fully NLV model for the RVFW.

6.2 Material and method

6.2.1 Specimen and experiments

Details of the experimental work are described in our previous study [175]. Briefly, eight fresh RVFW specimen from adult female ovine with no known cardiac disease were included. The outflow tract direction was marked as the longitudinal (L) direction and its perpendicular direction was the circumferential (C) direction. The tissues were immersed in cardioplegic solution combined with 30 mM of 2,3-butanedione monoxime at body temperature during the *ex vivo* mechanical test. All samples underwent equibiaxial stress relaxation tests at different strain levels (3, 6, 9, 12 and 15%) with the ramp rate of 8mm/s, which is equivalent to the physiological stretch rate (assuming the heart rate of 1Hz).

6.2.2 Microstructural measurements

The tested samples were fixed in 10% buffered formalin and embedded in paraffin. The tissue blocks were further sectioned into 5-8 serial slides for fiber orientation measurement. Briefly, from the serial histology sections, the transmural change of myofiber orientation was measured using in-house MATLAB codes adapted from a previous study [170,240]. Each slide was imaged under bright field light microscopy and the main myofiber direction was derived using an orientation distribution function (ODF). The transmural myofiber orientation distribution was then represented by a Beta distribution function to fit a surface to the 3D data. The mean transmural myofiber orientations was calculated from 1D Hermitian shape function [170,240] and used as the main fiber orientation (θ) in the model fitting.

6.2.3 Model fitting: QLV fitting procedure

First, we used the QLV model to fit the equibiaxial stress relaxation data and evaluated the goodness-of-fit. Assuming incompressibility and negligible shear deformation, the QLV formulation for the 2nd Piola-Kirchhoff (PK) stress tensor (**S**) can be written as [237]:

$$\mathbf{S}(\mathbf{E},t) = \mathbf{S_0} + \int_0^t G(t-\tau)\frac{\partial \mathbf{S^e}}{\partial \mathbf{E}} : \frac{\partial \mathbf{E}(\tau)}{\partial \tau} d\tau \tag{6.1}$$

where t is time, $\mathbf{S_0}$ is the initial tissue pretension in the reference configuration [63], $G(t)$ is the reduced relaxation function tensor, $\mathbf{S^e}$ is the instantaneous elastic stress, τ is a time variable of integration. The instantaneous elastic stress $\mathbf{S^e}$ was derived from an anisotropic Ogden strain energy density function (Ψ) [235,241]:

$$\Psi = \frac{2\mu}{\alpha^2}(\lambda_1^\alpha + \lambda_2^\alpha + \lambda_3^\alpha - 3) + \frac{2k\mu}{\alpha^2}(I_4^{\alpha/2} + 2I_4^{-\alpha/4} - 3) \tag{6.2}$$

using

$$\mathbf{S^e} = 2\frac{\partial \Psi}{\partial \mathbf{C}} - p\mathbf{C}^{-1} \tag{6.3}$$

where the parameters μ, α and k represent the infinitesimal shear modulus, nonlinearity and anisotropy of the tissue, respectively. The principal stretch λ_i are the diagonal elements of the deformation gradient tensor when no shearing is present. Also, **C** is the right Cauchy-Green deformation tensor and **C** = 2**E**+**I**, where **E** is the Green-Lagrange strain tensor. With the longitudinal and circumferential directions aligned to the λ_L and λ_C directions, respectively, the anisotropic invariant I_4 was equal to:

$$I_4 = \mathbf{a_0} \cdot \mathbf{Ca_0} = \lambda_L^2 \cos\theta^2 + \lambda_C^2 \sin\theta^2 \tag{6.4}$$

where $\mathbf{a_0}$ is a vector describing the fiber orientation defined by the θ, and $\theta = 0$ represents the fiber aligned along the longitudinal direction. We assumed the RVFW to be incompressible, and the out-of-plane stretch λ_3 was found:

$$\lambda_3 = \frac{1}{\lambda_L \lambda_C} \tag{6.5}$$

For more information about the equations development, please refer to Appendix D.

In this study, the reduced relaxation function $G(t)$ in each direction was defined by Prony series as:

$$G(t) = G_\infty + \sum_{n=1}^{3} G_n e^{-t/\tau_n} \quad (6.6)$$

such that:

$$G_1 + G_2 + G_3 + G_\infty = 1 \quad (6.7)$$

where G_∞ is the long-term relaxation coefficient, which quantifies the proportion of instantaneous elastic stress $\mathbf{S^e}$ remaining in the RV over a long (infinite) period. G_n are relaxation coefficients corresponding to the time constants: $\tau_1 = 0.3$ s, $\tau_2 = 3$ s, and $\tau_3 = 30$ s, which provided even decadal spacing of the transient behavior in the 100 s relaxation timeframe. Each G_n represents the relaxation strength at the corresponding time constant.

Data from each individual strain of the sample were independently fitted to the QLV model using *fmincon* function in MATLAB to get two sets of coefficients (one for each direction). A two-step fitting strategy was used in which the reduced relaxation function *G*(*t*) was fitted separately from the instantaneous elastic component of the model. That is, we fitted the relaxation phase of the curve first, and then fitted the entire data including the ramping phase. **Eq. 6.6** was fitted directly to the relaxation period, and **Eqs. 6.4&6.5** were fitted to the ramping period [241]. In the first step, due to the disproportionally large number of data points in the relaxation phase, the fitting algorithm minimized a weighted root-mean-squared error (RMSE) with a weighting function:

$$W_{relax}(t_n) = \frac{e^{-t_n/\tau_1} + e^{-t_n/\tau_2} + e^{-t_n/\tau_3}}{3} \quad (6.8)$$

where t_n is the time during the relaxation period such that the peak stress occurs at $t_n = 0$ s. This weighting function was first multiplied by the model error and the RMSE of the weighted error was calculated.

In the second step, the fitting algorithm minimized the weighted error such that the ramping period and the relaxation period were weighted equally. Since the relaxation period had its own weighting function $W_{relax}(t_n)$, the ramping period required a similar function to scale the errors. As a result, the final weighted error function, $RMSE_F$, was minimized as:

$$RMSE_F = 0.5 \times RMS\left[w_{ramp} \cdot (\mathbf{S}_{\text{ramp,m}} - \mathbf{S}_{\text{ramp,e}})\right] + 0.5 \times RMS\left[w_{relax}(t_n) \cdot (\mathbf{S}_{\text{relax,m}} - \mathbf{S}_{\text{relax,e}})\right] \quad (6.9)$$

where $\mathbf{S}_{\mathrm{ramp,m}}$ and $\mathbf{S}_{\mathrm{ramp,e}}$ are the modeling and experimental stresses in the ramping period, respectively, and $\mathbf{S}_{\mathrm{relax,m}}$ and $\mathbf{S}_{\mathrm{relax,e}}$ are the modeling and experimental stresses in the relaxation period, respectively. The goodness of the fitting was determined by the value of the RMSE.

6.2.4 Model fitting: NLV power-law fitting procedure

The QLV theory assumes that the reduced relaxation function $G(t)$ is independent of the input strain level (viscous linearity assumption). For the NLV theory, the relaxation function is dependent on both inputs of the strain and the history (time) of strain. Therefore, the viscoelastic nonlinearities can be captured by [237]:

$$\mathbf{S}(\mathbf{E}(t),t) = \mathbf{S}_0 + \int_0^t \mathbf{M}(\mathbf{E}(\tau), t-\tau) : \frac{\partial \mathbf{E}(\tau)}{\partial \tau} d\tau \tag{6.10}$$

The relaxation modulus **M** is strain-dependent and can be written as:

$$\mathbf{M}(\mathbf{E},t) = \mathbf{A}(\mathbf{E}) t^{m(\mathbf{E})} \tag{6.11}$$

where $\mathbf{A}(\mathbf{E})$ and $m(\mathbf{E})$ are the initial strain-dependent modulus and relaxation rate, respectively. By substituting **Eq. 11** into **Eq. 10**, the stress relaxation becomes:

$$\mathbf{S}(\mathbf{E},t) = \mathbf{S}_{\mathrm{in}}(\mathbf{E})\, t^{m(\mathbf{E})} \tag{6.12}$$

where $\mathbf{S}_{\mathrm{in}}(\mathbf{E})$ is the strain-dependent initial stress. We further transformed Eq. 12 to the logarithmic scale and plotted and performed the linear fitting that includes all five strain levels simultaneously using MATLAB. The log of the initial stress ($\mathbf{S}_{\mathrm{in}}(\mathbf{E})$) and relaxation rate (m) were calculated, which are the ordinate intercept and the slope of the fitted line. Finally, we plotted the initial stress and relaxation rate as a function of strain and fit the data with quadratic polynomial curves. The fitting results were used to reveal the nonlinear relation between the NLV modeling parameters and the strain used in stress relaxation.

6.2.5. Statistical analysis

Comparisons between directions (longitudinal and circumferential), strain levels (3, 6, 9, 12 and 15%) and time constants (τ_1, τ_2 and τ_3) of the relaxation coefficients and the comparisons between the

directions and strain levels of the fitting parameters were performed with the paired Student's t-test. Data are presented as mean ± SEM and $p<0.05$ was considered statistically significant.

6.3 Results

6.3.1. QLV model successfully fitted the data at fixed strain levels

The QLV model offered a good fit to the experimental data for all the fixed-strain tests (i.e., tests at 3, 6, 9, 12, and 15% equibiaxial strain levels). **Figure 6.1** shows the representative fitting results. Although the RMSE values increased with the increase of the strain level (from 0.13 ± 0.02 kPa at 3% strain to 2.56 ± 0.22 kPa at 15%), the RMS values were still relatively small at their corresponding strain level, confirming the goodness-of- fit for the QLV model. Next, we tested the ability of the QLV model, fit to a single strain level, to predict the experimental data at other strain levels. The stress relaxation data from all the strain levels were normalized by their individual maximal stress. The fitting was performed for the 3% strain test and the predictions were compared against experimental data for higher strain levels. We observed that the model fitted to the 3% strain level did not predict the experimental data at higher strains well in either direction (**Fig. 6.2**). We observed similar poor prediction capability for the raw experimental data as seen using the normalized data (**Fig. 6.3**).

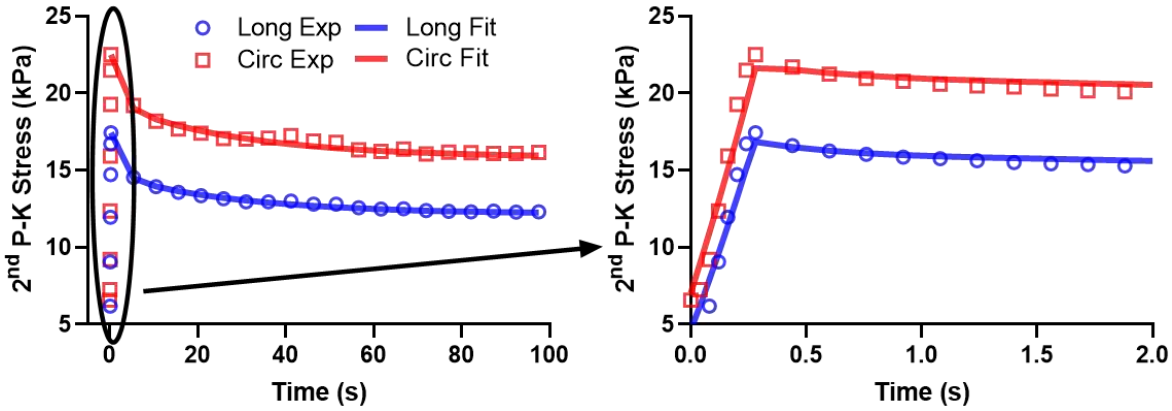

Fig. 6.1. Representative fitting results of the QLV model for a RVFW sample at 12% strain level. Long: longitudinal direction; Circ: circumferential direction; Exp: experimental data; Fit: model fitting data.

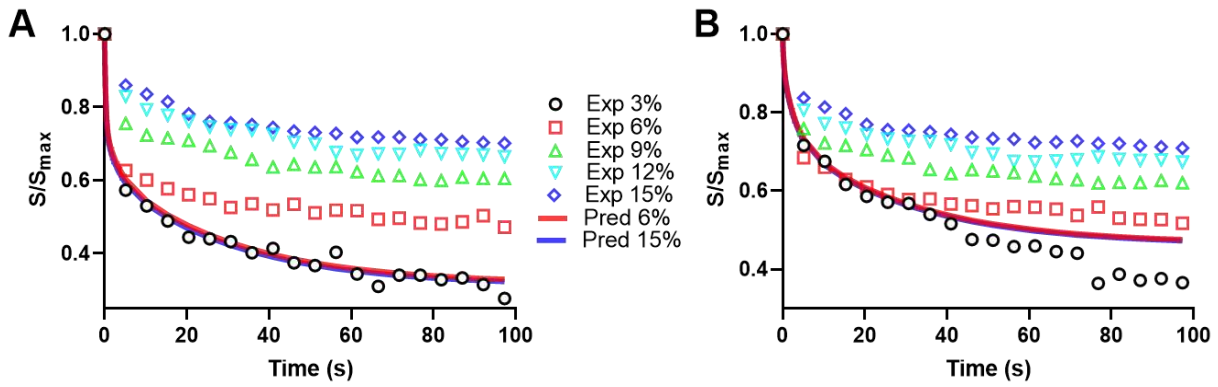

Fig. 6.2. Representative results of the QLV model's capability to predict the normalized relaxation behavior at fixed 6% and 15% strain levels by using the fitting parameters obtained from fits to the 3% strain test in (A) longitudinal direction and (B) circumferential direction. Exp: experimental data, Pred: predication curve.

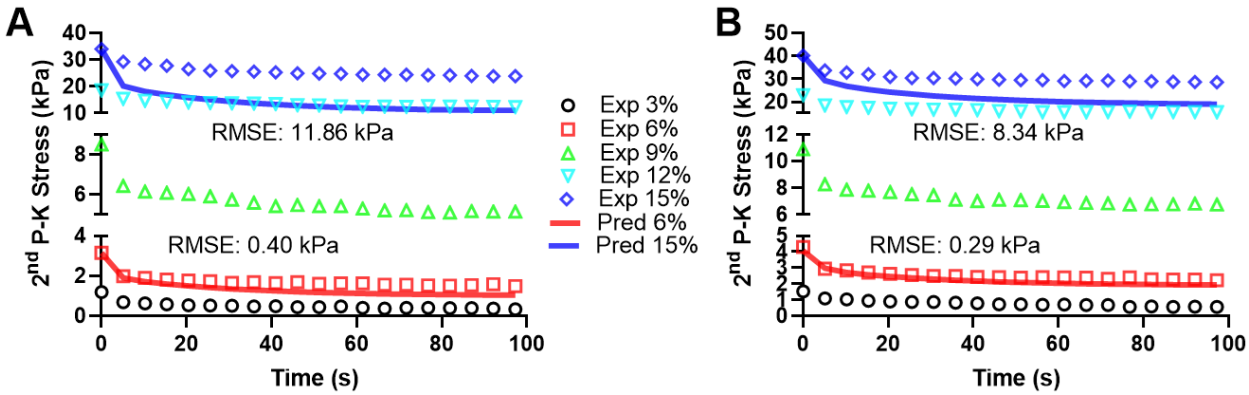

Fig. 6.3. Representative results of the QLV model's capability to predict the relaxation behavior at fixed 6%, and 15% strain levels using the fitting parameters obtained from fits to the 3% strain test in (A) longitudinal direction and (B) circumferential direction. Exp: experimental data, Pred: predication data. RMSE: root mean square error.

6.3.2. Relaxation function, shear modulus, nonlinearity, and anisotropy change with strain

Next, we examined the effect of strain level on the relaxation function $G(t)$. We observed that the relaxation function $G(t)$ was strongly dependent on the strain levels in both directions, and the curve was shifted upward with an increase in strain level (**Fig. 6.4**). Furthermore, we examined the dependence of the shear modulus, nonlinearity and anisotropic on strain levels. We found that the RVFW shear modulus monotonically increased with increasing strains (**Fig. 6.5A**), whereas the RVFW nonlinearity (**Fig. 6.5B**) and anisotropy (**Fig. 6.5C**) exhibited a 'fluctuating' change over strain levels. Lastly, the RVFW anisotropy values were positive (**Fig. 6.5C**), which indicate that the tissue is stiffer along the measured myofiber

orientation. The detailed results of the fiber orientation measurement are presented in **Table 6.1**. The majority of the RVFW samples had myofiber alignment toward the circumferential direction (denoted by 90 degree), and thus the tissue exhibited stiffer behavior in the circumferential direction.

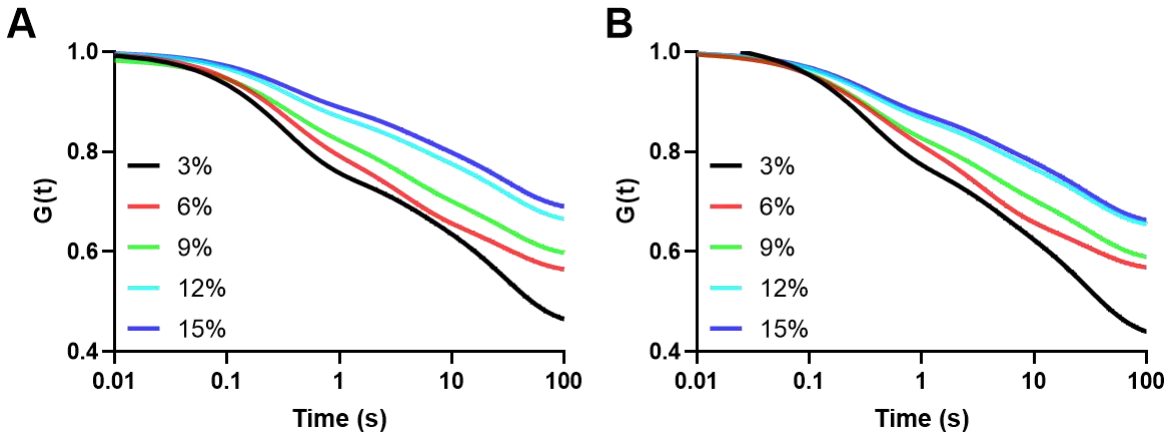

Fig. 6.4. The reduced relaxation function $G(t)$ obtained from the average fitting values of coefficients at each strain level in (A) longitudinal direction and (B) circumferential directions.

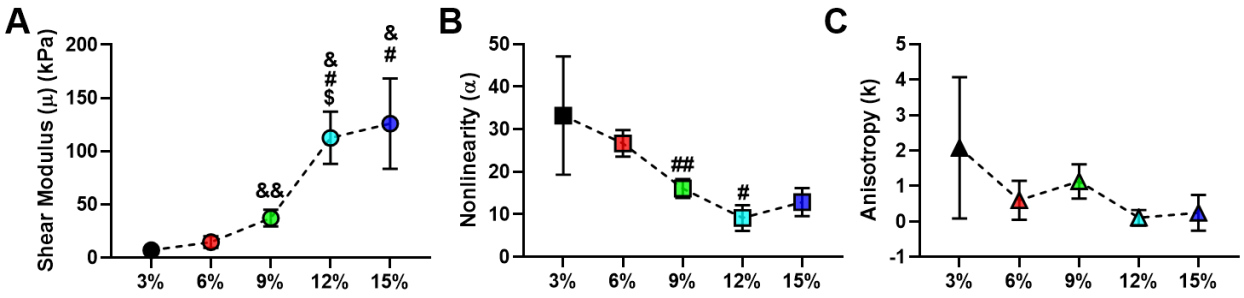

Fig. 6.5. Fitted parameters of the Ogden strain energy density function. (A) Infinitesimal shear modulus (kPa), (B) nonlinearity and (C) anisotropy. &<.05 and &&<.01 vs. 3% strain, #<.05 and ##<.01 vs. 6% strain, and $<.05 and $$<.01 vs. 9% strain.

Table 6.1: Summarized results of the myofiber orientation in all RVFW samples (n=8). Data were presented as mean ± SEM.

Sample #	Orientation (^{0})	Sample #	Orientation (^{0})
1	74.52 ± 0.25	**5**	80.57 ± 2.00
2	51.59 ± 3.56	**6**	65.82 ± 1.74
3	38.15 ± 2.30	**7**	70.19 ± 2.22
4	46.79 ± 0.66	**8**	51.82 ± 1.48

6.3.3. Relaxation coefficients G_n were strain-dependent

Next, we compared the individual relaxation coefficients at different strain levels and in different directions. In both directions, G_∞ and G_n changed significantly with strain levels (**Fig. 6.6**). Interestingly, G_∞ was monotonically increased with increasing strains, whereas the opposite behavior was observed for the G_1 (**Fig. 6.6A&B**). While G_2 increased first and then gradually decreased, the opposite behavior was observed for G_3 (**Fig. 6.6C&D**). Lastly, at most strain levels, the relaxation coefficients did not differ between directions, except that at 15% of strain there was a larger G_∞ in the longitudinal direction compared to that of the circumferential direction (**Fig. 6.6A**). The coefficient G_∞ quantifies the proportion of instantaneous elastic stress S_i^e remaining in the RVFW over a long (infinite) period of time. Lager G_∞ in the longitudinal direction indicates the anisotropic behavior of the RVFW, and RVFW has more remaining elastic stress in the longitudinal direction than the circumferential direction.

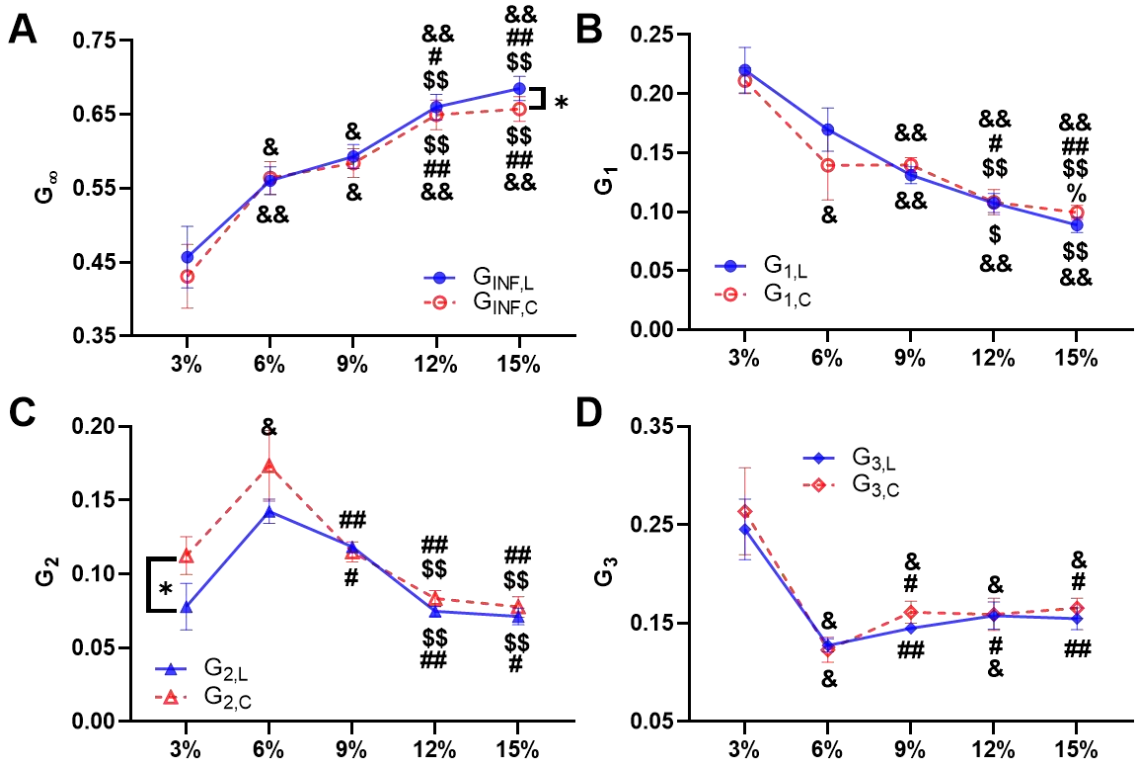

Fig. 6.6. Relaxation coefficients G_n at five different strain levels and in longitudinal (L) and circumferential (C) directions. (A) G_∞, (B) G_1, (C) G_2 and (D) G_3. &<.05, &&<.01, #<.05, ##<.01, $<.05, $$<.01, %<.05 vs 3, 6, 9 and 12%, respectively and *<.05.

6.3.4. Contribution of relaxation coefficients G_n to relaxation response changes with strain

Next, we compared the relaxation coefficients G_n at each individual strain level to reveal the individual coefficient's contribution to the entire relaxation response (**Fig. 6.7**). First, we observed similar values of individual G_n in both directions at all strain levels. This indicates that the relaxation coefficients contribute to the RVFW relaxation behavior equally in each direction. Second, except for the 6% strain, G_1 and G_3 played more significant roles than G_2 for all other strain levels. We also noticed that G_1 and G_3 were both prominent at low strain (3% and 9%) (**Fig. 6.7A&C**), whereas at high strain (12 to 15%) G_3 was more prominent (**Fig. 6.7D&E**). This indicates that the dominant G_n varied at different strain levels.

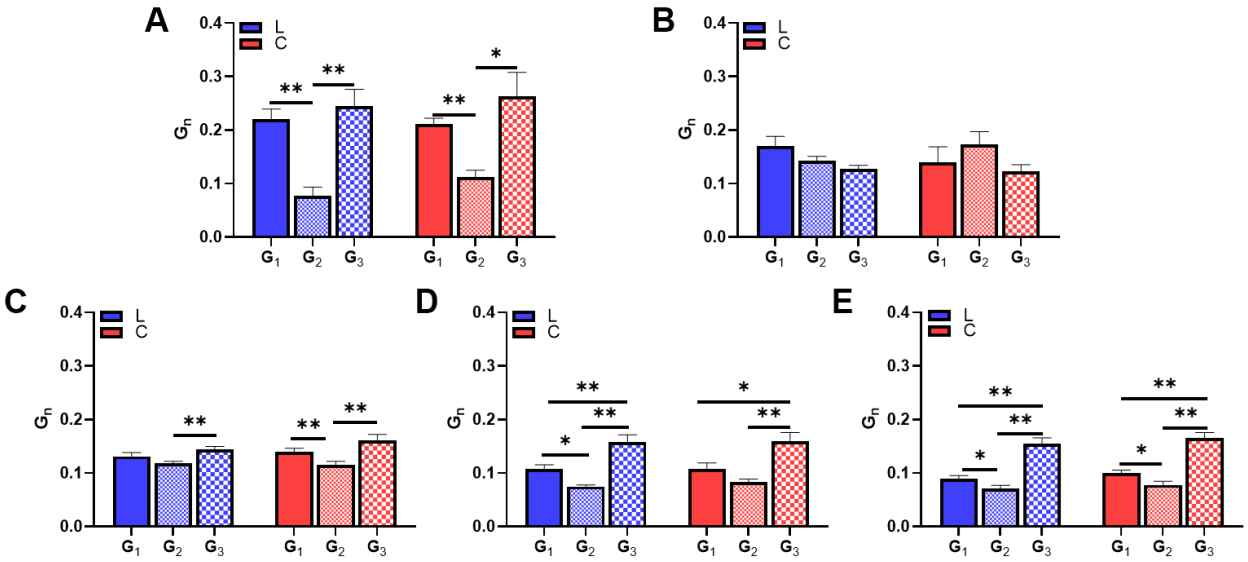

Fig. 6.7. Relaxation coefficients G_n at different strain levels in longitudinal (L) and circumferential (C) directions. (A) 3%, (B) 6%, (C) 9%, (D) 12% and (E) 15%. *<.05 and **<.01.

6.3.5. The relaxation rate and initial stress were anisotropic and nonlinearly correlated with the strain

Lastly, we investigated the effect of strain on the relaxation rate and initial stress using the fitting of the NLV behavior. The RVFW had a slower relaxation rate and larger initial stress with the increasing strain in both directions (**Fig. 6.8**), which is characteristic of fully nonlinear viscoelastic behavior. At some strains, small but significant differences in these parameters were noticed between the longitudinal and

circumferential direction, highlighting the anisotropic relaxation behavior of the RVFW. Further, we found that the relations between these modeling parameters could be fit by quadratic polynomial equations very well (**Table 6.2**, R^2>0.99), indicating a nonlinear dependence of these parameters on the strain.

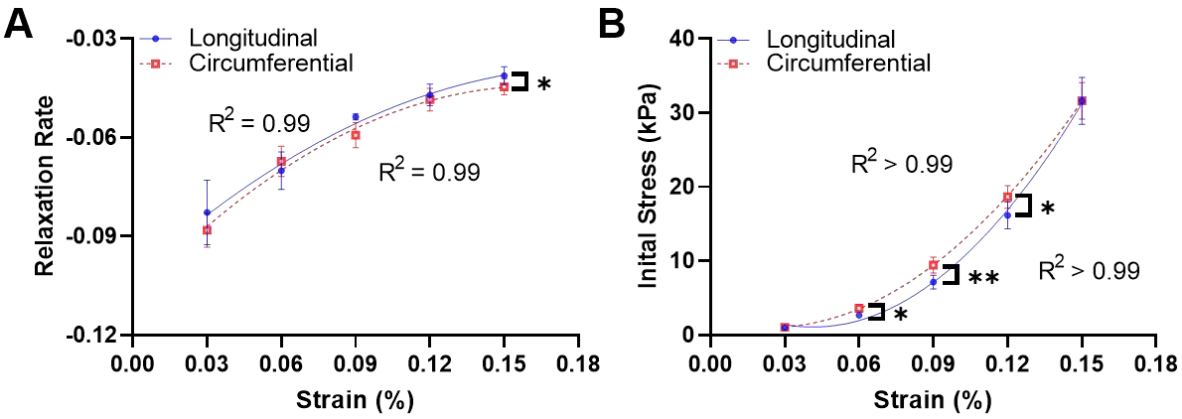

Fig. 6.8. Average (A) relaxation rate and (B) initial stress at five different strain levels in two directions. *<.05, **<.01.

Table 6.2: The fitted relaxation rate and initial stress as a function of strain level where quadratic polynomial equations (R^2 close to 1) represent the strain (ε) dependent behavior of the relaxation rate and initial stress.

		Quadratic fit as a function of strain
Relaxation Rate	Longitudinal	$-1.84\varepsilon^2 + 0.69\varepsilon - 0.10$
	Circumferential	$-2.48\varepsilon^2 + 0.80\varepsilon - 0.11$
Initial Stress (kPa)	Longitudinal	$2547.4\varepsilon^2 - 209.42\varepsilon + 5.34$
	Circumferential	$1911.5\varepsilon^2 - 90.11\varepsilon + 2.07$

Next, we tested the ability of the NLV model to predict the experimental data. The linear fitting was performed for only four strain levels simultaneously (e.g., 3, 6, 9 and 12%) to obtain the relaxation rate and initial stress per sample, and then the average relaxation rate and initial stress were used to determine the quadratic relationships between the relaxation rate/initial stress and the strain. The quadratic relationships were next applied to predict and compare against the average experimental data at the fifth strain level (i.e., 15%). We observed that the NLV model did predict the experimental data well in both directions (**Fig. 6.9**).

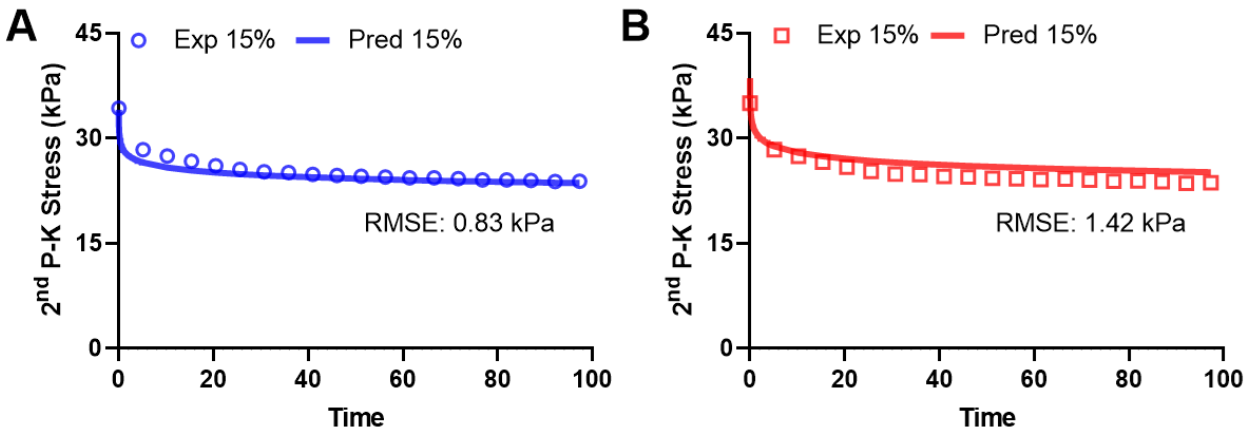

Fig. 6.9. Representative results of the NLV model's capability to predict the average relaxation behavior at 15% strain using the quadratic relationships derived from the fitting to 3 to 12% strain tests. Comparisons of the predicted curve and experimental curve in (A) longitudinal direction and (B) circumferential direction are shown. Exp: experimental data, Pred: predicated data. RMSE: root mean square error.

6.4 Discussion

To the best of our knowledge, this is the first constitutive modeling of the passive, anisotropic viscoelastic behavior of healthy ovine RV. We observed that for RVFW tissues: 1) individual relaxation function coefficients G_n, shear modulus and nonlinearity were all strain-dependent; 2) The relaxation coefficient G_3 was larger than other coefficients at most strains, indicating a dominant role in the overall relaxation behavior from early (low strain) to late (high strain) diastole. In contrast, the relaxation coefficient G_1 was large only at small strain, suggesting a pronounced effect only at early diastole; 3) the NLV fitting parameters (relaxation rate and initial stress) had a quadratic polynomial relation with the strain, indicating the nonlinear dependence of RVFW viscoelastic behavior on the strain; 4) an anisotropic behavior was observed in parameters such as G_n and NLV fitting parameters; 5) the QLV model was able to fit the data at individual strains. However, fitting parameters from one strain level cannot be used to predict other strain levels. In contrast, the NLV model well predicted the strain-dependent viscoelastic behavior. These findings highlight the importance of characterizing and modeling the anisotropic, nonlinear viscoelastic deformation of the RVFW to capture the elastic and viscous resistances and energy expenditure of the tissue during the diastolic filling period. Such knowledge will improve the understanding

of mechanical mechanisms of diastolic function of the RVFW and assist with further development of a fully NLV model for the RVFW.

6.4.1 The relaxation function is strain-dependent

The relaxation function $G(t)$ contains the core characteristics of the time-dependent, relaxation response (i.e., viscosity) of the RVFW. Previous modeling studies for other soft tissues have used different numbers of terms in G_n (from 2 to 4 [233,237,241,242]) and different decadal values of τ_n (0.1, 1, 10…. or 0.3, 3, 30… [237,241,242]). In our data, we explored two to four terms of relaxation function associated with different sets of time constants τ_n, either using assigned decadal values or those determined from the relaxation time distribution spectrum [241]. The fitting results showed that a three-term function associated with decadal values of 0.3, 3 and 30 as the time constants offered best fitting results.

Using a three-term relaxation function and the time constants described above, strain-dependent behavior of the relaxation function $G(t)$ was evident: the relaxation function curve shifted upward in both directions with an increase in strain level (**Fig. 6.4**). The observed up-shift of the curves indicates more viscoelastic behavior of the RV at higher strain levels. This phenomenon may be due to the strain-dependent viscoelasticity of collagen or myofiber (like strain-stiffening typically seen in hydrogels or biological tissues [243]). It can also be a result of the increasing recruitment of collagen fibers as the stretch increases. Moreover, the increasing loading of collagen fibers at higher strain levels will alter the RV viscoelasticity to be dominated by this extracellular matrix protein.

6.4.2 Different roles of G_∞ and G_n in the relaxation response and implications

We also observed strain-dependent behavior for the relaxation coefficients G_n in both directions, which suggests that they have different weights on relaxation response at low and high strain levels. The long-term parameter G_∞ was monotonically increased with increasing strain, suggesting more stress remaining at equilibrium state under larger deformations. In other words, more energy was stored at equilibrium with a larger G_∞. In contrast, the opposite trend was observed for the G_1, G_2 and G_3. As the strain increased, the strength of the relaxation in relatively short terms (e.g., at time constant of 0.3s) became

less pronounced. This suggests that the underlying mechanisms of short-term relaxation response have a strong influence on the overall relaxation behavior at small deformations and a weak influence on the relaxation behavior at large deformations. Furthermore, we observed that at small deformation (3% of strain), G_1 and G_3 had similar strength of the relaxation, whereas at large deformation (15% of strain), G_3 had the most significant strength of the relaxation than other coefficients (**Fig. 6.7**). This implies that different G_{n} dominates the relaxation response at different strain levels. Different trends of increase or decrease in relaxation coefficients $G_{\mathrm{n}}$with the increasing strain have been reported in other soft tissues, and the trends seem to be tissue dependent. For example, the anterior and posterior longitudinal ligament (ALL, PLL) and ligamentum flavum (LF) are collagen rich connective tissues, and they all had decreasing behavior with the increasing strain for the G_∞ [237]. But in terms of G_1, increasing (LF), decreasing (PLL) and no significant changes (ALL) have been observed for these tissues with the increasing strain.

The underlying mechanisms of short- versus long-term relaxation coefficients G_{n} can be related to various relaxation processes, including the atomic and molecular motion processes, coupled effects of multiple fields (electrical, magnetic, thermal or fluidic) and heterogenous relaxation [44]. For composite biological tissues, tissue composition (cellular and extracellular components) and the specific microstructure associated with anatomical location and function may all play a role to determine these relaxation coefficients. Unlike the ligament, the RVFW is mainly composed of cardiac muscle cells (myofibers) that have preferred and transmural changes of orientations from epicardial to endocardial layers. We speculate that as the myofibers are more stretched, less energy will be dissipated due to reduced intermolecular frictions (e.g., less overlapping of actin-myosin), which results in elevated equilibrium stress. But the role of collagen fibers should not be excluded as we recently observed a correlation of type III collagen and low-strain elastic modulus in ovine LV and RV (unpublished data), and a correlation of the type III collagen and RV function [179]. Furthermore, with the increasing strain, the role of collagen will be more significant in determining the entire tissue's mechanical behavior. Therefore, different microstructure components (myofibers, type III collagen, type I collagen, etc.) may be associated with different relaxation

time scales (G_n). Nordsletten et al [220] proposed recently that multiscale mechanisms of molecular friction is likely occurring at different microstructures of collagen, from collagen fibrils to collagen fibers, to bundles and meshes.

6.4.3 Strain-dependent and anisotropic elastic behavior

As the strain increased, the shear modulus increased monotonically. But this trend was absent from the tissue nonlinearity or anisotropy parameter (**Fig. 6.5**). The monotonically increasing behavior of the shear modulus is consistent with the observation that the myocardium elasticity (e.g., measured by tensile modulus) increases nonlinearly with strain. This behavior can be understood by the continuous recruitment of collagen fibers at larger deformations. An increase in collagen fiber recruitment increases its contribution to load bearing and the tissue elasticity becomes more dominated by collagen rather than myofibers.

The nonlinearity parameter α also presented strain-dependent behavior and it may be attributed to different roles of myo- and collagen fibers at different strain levels. It is known that myo- and collagen fibers play key roles in the tissue elasticity at low and high strain levels, respectively [9,170]. We speculate that the reduced nonlinearity of RVFW at high strains is due to the fully recruited and stretched collagen fibers, whereas the nonlinearity at small strains is contributed by the nonlinear muscle fibers. The anisotropic parameter k barely changed with the strain level. As tissue anisotropy has been mostly to the 'fiber' orientation, the results indicate negligible change in the orientation of myo- and collagen fibers within the testing strain range. This is not surprising as we performed equibiaxial stretch and the increase of loading in each direction is identical, therefore the load bearing distribution in different directions does not need to be altered. Furthermore, the anisotropic parameter k has positive values across all strain levels, indicating an anisotropic elastic behavior. Consistently, we also observed the anisotropic RV relaxation response at end-diastole (15% of strain), which is evidenced by a larger G_∞ (**Fig. 6.6A**), a slower relaxation rate (**Fig. 6.8A**), and smaller initial stress (6 to 12%) in the longitudinal direction.

6.4.4 Strong nonlinear correlations between the relaxation rate/initial stress and strain

Lastly, we investigated the parameters derived from the NLV formulation. We observed that in both directions, the relaxation rate or initial stress were nonlinearly negatively or positively correlated with the strain, respectively; and at high strains, the RV has slower relaxation rate associate with larger initial stress (**Fig. 6.8, Table 6.2**). The opposite nonlinear correlative relationship has been observed for other soft tissues such as ligament, in which the relaxation rate became faster with the increasing strain level [237]. These discrepant correlations found in different tissues suggest that the strain-dependent behavior for the relaxation rate is tissue-specific and it is worthy to further investigate if the RV has a unique behavior different than the LV.

Furthermore, the relaxation rate exhibited a "strain-thinning" behavior in both directions; that is, as the strain increases, the relaxation rate become smaller (like the 'shear thinning' behavior for a fluid's viscosity). In contrast, the initial stress has a "strain-thickening" behavior in which the initial stress becomes larger as strain increases (**Fig. 6.8**). A reason behind this difference could be that different tissue constituents such as the myofibers and collagen exhibit strain-thickening and strain-thinning behaviors with the increasing strain, and the relaxation rate and initial stress are contributed by these constituents, respectively.

6.4.5 Contrasts between QLV and fully NLV model to describe RVFW viscoelasticity

There are three main types of viscoelastic behaviors, namely, linear, quasi-linear and fully nonlinear. While all these three behaviors are time-dependent, the linear viscoelastic material exhibits linear elastic and linear viscous behavior, whereas the quasi-linear viscoelastic material exhibits nonlinear elastic and linear viscous behavior. The 'linear viscous behavior' can be revealed by showing the same shape of relaxation or creep curves at different strains. That is, the time-dependent behavior is strain-independent or separable [44,237]. In contrast, both elasticity and viscosity in a fully nonlinear viscoelastic material are strain-dependent. That is, the time-dependent behavior is not separable from the strain. The biological tissues are composite materials that often present nonlinear viscoelastic behaviors, and thus this type of model has

been developed for soft tissues such as cartilage, tendon and spinal cord [59–61,63,237,241,242,244]. However, the modeling of nonlinear viscoelastic behavior is rare in cardiac tissues.

Since the first use of the QLV formulation by Pinto and Fung in rabbit papillary muscles [236], this model has been widely adopted by other researchers to model viscoelastic behavior of myocardium or heart muscles [68,220,232,233,235,236]. This model is relatively simple with low computational cost, and it can produce experimentally-observed stress relaxation, creep, and cyclic hysteresis behaviors. In this study, the QLV model fit the stress relaxation data well at all individual strain levels, and it allowed us to investigate the relaxation behavior contributed by different relaxation coefficients (potentially related to different constituents) at each fixed strain. The insights provided from the modeling outcomes will be valuable to reveal the dynamic structure-function relations of the RV. However, because the RVFW is essentially fully nonlinear viscoelastic [175], the QLV formulation using individual strains prohibits the applicability of the model to the entire physiological strain range (i.e., at all strains).

Our results suggested the NLV power-law model has a superior performance in predicting strain-dependent viscoelastic behavior of the RVFW than that of the QLV model. Using the QLV model, fitting results from one strain level could not predict experimental data obtained at other strain levels (**Fig. 6.2, Fig. 6.3**). In contrast, using the NLV model, the nonlinear (quadratic) relationships derived from four strain levels were able to predict the experimental data at the fifth strain level with high accuracy (**Fig. 6.9**). However, it is important to note that the power-law formulation used in this work was a simplified version of the NLV model which excludes the use of relaxation modulus with Prony series (similar to the reduced relaxation function in the QLV model). Although the simplified version of the NLV model significantly reduced its computational cost, it did not offer the capability of investigating the relaxation behavior at various time constants (stages) similar to the QLV modeling. A further development of a fully NLV constitutive model is expected to combine these advantages.

6.4.6 Limitations

The experimental data we used here were only from the epicardial layer of the RV, and the small variation of transmural fiber angles confirmed a transmurally isotropic mechanical property of the testing samples. But there might be transmural differences in the viscoelastic behavior of the whole RVFW, and a further study that covers the entire thickness of the tissue should be performed. All the data we used here were from female ovine myocardial tissues, and there might be a sex difference in the RV viscoelastic behavior that awaits future research. Prior studies showed that the addition of actual strain/deformation history offered better fitting results than the ideal strain/deformation assumed from the Heaviside step function [63,244]. Since we did not record the images during the testing, the strain/deformation history was not obtained experimentally. Nevertheless, the QLV model still offered good fitting results across all strain levels and the findings here are novel as this is the first constitutive modeling study for the large animal species RV.

6.5 Conclusions

To the best of our knowledge, this is the first constitutive modeling study of the RV free wall passive, anisotropic viscoelastic behavior. Our results from the constitutive modeling showed that the RVFW had anisotropic and strain-dependent viscoelastic behavior, and the NLV model showed a higher predictive capacity in capturing the strain-dependent nature of the stress relaxation behavior than the QLV model. From the QLV fitting, the relaxation coefficient G_3 was larger than other coefficients at most strains, indicating a dominant role in the overall relaxation behavior from early to late diastole. In contrast, the relaxation coefficient G_1 was large only at small strain, suggesting a pronounced effect only at early diastole. From the NLV fitting, the fitting parameters (relaxation rate and initial stress) showed quadratic polynomial relationships with the strain. These findings highlight the importance of characterizing and modeling the anisotropic, nonlinear viscoelastic deformation of the RVFW to fully capture the elastic and viscous resistances and energy expenditure of the tissue during diastole. Such knowledge will deepen the

understanding of the mechanical mechanisms of diastolic function of the RVFW and assist with the further development of a fully nonlinear viscoelastic model for the RVFW.

AIM 3: CHANGES IN RIGHT VENTRICLE BIOMECHANICS DURING PULMONARY HYPERTENSION DEVELOPMENT (CHAPTER 7 to 9)

For my third Aim 3, it includes three chapters (**Chapters 7 to 9**). Within this aim, the pulmonary hypertension (PH) was induced, and then the changes of the RV biomechanical property and the correlations between the RV biomechanical property and function were characterized. Briefly, the diseased model was firstly developed (**Chapter 7**), and then investigated the changes of the static and dynamic RV mechanical behavior, respectively (**Chapters 8 and 9**).

In the **Chapters 8 and 9**, the animal-specific pulmonary artery constriction method that described in **Chapter 7**, and monocrotaline model were used to induce the PH for the ovine and rat, respectively, and then further investigated the changes of the RV static and dynamic mechanical behavior, respectively. **Chapters 7 and 8** were published as peer reviewed research articles, more details can be found in these two chapters. Briefly, the founding within this aim highlighted the importance of the passive mechanical properties of the RV in the progression of RV dysfunction, improved our understanding of RV biomechanics under chronic pressure overload as well as in different physiological conditions. In addition, these findings will assist the development of RV simulation to capture both energy storage and energy dissipation functions and reveal new insights about the role of RV mechanics in RV function.

CHAPTER 7: ESTABLISHMENT OF ADULT RIGHT VENTRICLE FAILURE IN OVINE USING A GRADED, ANIMAL-SPECIFIC PULMONARY ARTERY CONSTRICTION MODEL [6]

7.1 Introduction

Right ventricle failure (RVF) is associated with serious cardiac and pulmonary diseases that contribute significantly to the morbidity and mortality of patients [245]. The prevalence of RVF is significantly increased in the later stages of pulmonary hypertension (PH), congenital heart disease (CHD), and left heart failure with preserved ejection fraction (HFpEF) [21,22,246]. Moreover, the mortality rate of these patients has not improved despite proposed therapeutic interventions [21,247–249]. The lack of effective treatment can be attributed to the incomplete understanding of the mechanisms of RVF and the lack of robust large animal models in adult RVF [250–252].

Preclinical (animal) models are powerful tools to investigate various human diseases including RVF [250]. Compared to small animal models, large animal models better mimic human physiology and pathophysiology [253–256] and thus are advantageous in studying both the pathogenesis and potential therapeutics that are more translatable to human patients [203]. To date, various methods have been used to establish RV pressure overload, the most common etiology of RVF. These methodologies include pulmonary artery (PA) (**Table 7.1**) or pulmonary vein banding [257,258], thromboembolic induction [253,259,260], chronic hypoxia [261], monocrotaline [262,263], and the combination of sugen and chronic hypoxia [73,264,265]. However, some of these models are essentially the models of pulmonary hypertension (PH), which mainly focus on the pulmonary vascular disease and do *not* necessarily involve the establishment of RVF. (Reviews of the PH models are cited here [169,266–268].)

[6] *This chapter is published as a peer reviewed research article in Animal Models and Experimental Medicine (doi: 10.1002/ame2.12124).*

Compared to other RV pressure overload models, the PA banding/constriction (PAB or PAC) model is a model of RV adaptation or dysfunction alone with no pulmonary vascular diseases. While this model has been critiqued less realistic than the other PH models, it is unique and advantageous since the changes in the RV are the sole effect of the hemodynamic insult, i.e., the pressure overload. Such a model provides us an opportunity to investigate the biomechanical mechanism of RV failure without other confounding factors such as altered systemic inflammation from pulmonary vascular diseases [269]. PAB/PAC has been used in different animal species and with a mix of ages (from newborn to young adult) for RV adaptation or RVF studies (**Table 7.1**). To our knowledge, the only large animal study of chronic, adult RVF was performed in canine in the early 1990s, while the clinical standard of RVF was absent at the time [270]. Moreover, both adult and non-adult large animals have been used in the literature, with mixed goals of studying pediatric or adult RV diseases, as well as using PAC as a treatment option or means to induce RV dysfunction. For instance, lambs were commonly used and the response of the RV was associated with congenital heart diseases (CHD) [271–275]. In adult ovine studies, it was the acute changes of the RV that were examined and the chronic remodeling and outcomes were not studied [254,276]. Therefore, despite the 'apparently' widely used PAC model in large animals, to date, no chronic RVF has been established in adult ovine.

The goal of the present study is to adopt an animal-specific, graded pressure overload method to establish the chronic RVF in adult ovine and to investigate the structural and functional changes with RVF development. Ovine were chosen due to the widely reported similarities between human and ovine cardiovascular anatomy, function, and physiology [169,259,277]. Our data suggest that the revised PAC method led to RVF development in sheep and can serve as a large animal model of chronic, adult RVF.

Table 7.1. Review of prior small and large animal models of pulmonary arterial (PA) banding/constriction. All studies adopted the same degree of constriction (i.e., with a fixed diameter, area reduction, or pressure level) except for Leeuwenburgh et al. [271,273,274,278], Ramos et al. [279], Gold et al. [280], Gaynor et al. [281], and Verbelen et al. [276], which used the same criteria as our study to elevate the RV pressure to the individual's systemic pressure.

Study	Animal	Weight/Age	Method	Application	Mortality Rate (%)	Model Duration
Heitmeier et al., 2019 [282]	Mice	20-25 kg/12 weeks (adult)	Titanium clip around PA; reduce cross sectional area to about 66% of original area	Assess ubiquitin proteasome system in right heart hypertrophy; No RVF reported	N/A	3 weeks
Kuroha et al., 1991 [283]	Rat	2-month, 7-month, and 18-month old (non-adult and adult)	Silk thread around PA; increase of RV pressure by 15 mmHg in each animal	Effect of age on RV hypertrophy due to RV pressure overload; No RVF reported	N/A	3 weeks
Schou et al., 2007 [284]	Rat	150-200 g (adult)	Pulmonary trunk clip; compressed to outer diameter of 0.9 mm	Establish rat model of right sided heart failure and characterize systemic and cardiac changes	N/A	17 weeks
Bogaard et al., 2009 [285]	Rat	200 g (adult)	PA silk thread constriction; tightened to outer diameter 18G needle	Investigate if pressure overload alone can explain RVF associated with pulmonary hypertension; No RVF reported with PA constriction	N/A	6 weeks
Hill et al., 2014 [176]	Rat	8 weeks (adult)	PA surgical clip; uniform RV pressure of 45-50 mmHg	Structural and mechanical adaptations of RV free wall; No RVF reported	N/A	3 weeks

Hirata et al., 2015 [286]	Rat	240-260 g (adult)	PA clip or suture ligation; tightened to the outer diameter of an 18G needle	Comparison of methods to constrict PA; signs of RVF indicated by fibrosis and reduced TAPSE but not CO	22	8 weeks
Jang et al., 2017 [9]	Rat	8 weeks (adult)	PA surgical clip; RV maximum systolic pressure > 50 mmHg	RV biomechanical and hemodynamic changes under pressure overload; No RVF reported	N/A	3 weeks
Wang et al., 2017 [287]	Rat	Neonatal	PA constriction with nylon; tightened to outer diameter of 30G needle	Study of pathophysiological remodeling of RV due to congenital heart disease with RV afterload	25	7 days
Chery et al., 2019 [288]	Rat	200-225 g (adult)	PA suture over 18 G tube; PA band peak gradient of 25-60 mmHg	Human neonatal thymus stem cell therapy for RV; No RVF reported	33	100 days
Axelsen et al., 2019 [289]	Rat	112±12 kg (non-adult)	Titanium clip; set to inner diameter of 0.7 mm	Assess treatment of pulmonary hypertension with 6-mercaptopurine	5	7 weeks
McKellar et al., 2015 [290]	Rabbit	2.0-2.5 kg (non-adult)	Weekly PA banding with cuff; RV end systolic pressure > 25 mmHg	To establish chronic, reversible RVF model to study RVF progression and recovery; RVF indicated by RV pressure and morphology, septum position, and histology only	Exact rate unknown; several out of 15 died	43±1.6 days banding or 16.6±3.3 days recovery post RVF

Ramos et al., 2018 [279]	Rabbit	3.00±0.23 kg (non-adult)	Adjustable PA banding with C-shaped ring; weekly inflations to achieve systemic pressures	Early and late cardiac remodeling due to RV pressure loading and therapy with endothelin-1 receptor blockers; No RVF reported	N/A	3-6 weeks
Gold et al., 2019 [280]	Rabbit	3.00±0.23 kg (non-adult)	Adjustable PA banding device (C-shaped ring); weekly PAB inflations to achieve systemic RV pressures by day 21	Relationship between RV wall stress, fibrosis, and function under RV pressure loading; No RVF reported	N/A	3-6 weeks
Hsieh et al., 1992 [270]	Dog	18-23 kg (adult)	PA banding; increase of RVSP to 50 mmHg at the end of first month and then by 20 mmHg monthly increase, if necessary	RVF confirmed by fraction shortening decrease and RV dilation. Study the reversibility of right heart failure	14	3 months PAB and additional 4 months recovery
Gaynor et al., 2005 [291]	Dog	20-25 kg (adult)	PA banding; Weekly 0.3 to 0.5 mL of saline injection (ΔRVP ~10-20 mmHg) to achieve near-systemic pressures	RA and RV hemodynamic adaptations to RV pressure overload; No RVF established	N/A	3 months
Barbera et al., 2000 [292]	Ovine	121±1 day gestation	Inflation of vascular occluder around PA to increase RVSP pressure by ~10-30 mmHg over first 3 days of pressure loading	Assessment of myocyte maturation due to pressure load in fetal ovine	N/A	10 days
Hon et al., 2001 [293]	Ovine	3 months (non-adult)	PA ligation with band; PA systolic pressure > 60 mmHg	Acute effects of overload on RV contractile function; No RVF reported	N/A	30 minutes
Leeuwenburgh et al., 2001 [271]	Lamb	2-3 weeks (non-adult)	PA constriction with an adjustable occluder for up to	Evaluation of biventricular systolic	23	64±8 days

			12-week period; RVSP matched to systolic pressure	function; No RVF reported		
Leeuwenburgh et al., 2002 [274]	Lamb	2-3 weeks (non-adult)	PA constriction with an adjustable occluder for up to 12-week period; RVSP matched to systolic pressure	Evaluation of biventricular diastolic function; No RVF reported	23	64±8 days
Leeuwenburgh et al., 2003 [273]	Lamb	2-3 weeks (non-adult)	PA constriction with an adjustable occluder for up to 12-week period; RVSP elevated to systemic level	Test feasibility of a device for PA constriction as a treatment in children with congenital heart disease; No signs of heart failure	23	64±8 days
Leeuwenburgh et al., 2008 [278]	Lamb	2-3 weeks (non-adult)	PA constriction with an adjustable occluder up to 12-week period; RVSP matched to systolic pressure	Evaluation of cellular and biochemical myocardial response; No RVF reported	23	64±8 days
Yerebakan et al., 2009 [294]	Ovine	4 months (non-adult)	3 mm Dacron band on pulmonary trunk; Elevation of RVSP to 50-60% above baseline	Acute and chronic response of RV to pressure and volume overload; No RVF reported	N/A	Immediately after PAB or 3 months
Verbelen et al., 2015 [276]	Ovine	10.5±0.8 months (adult)	PA constriction as much as was hemodynamically tolerated	Test ventricular assist device for pressure overloaded RV	N/A	10 minutes
Malinowski et al., 2018 [254]	Ovine	50-60 kg (adult)	PA occluder; increase RV peak pressure to >150% of pre-occlusion value	To establish acute RVF model with functional tricuspid regurgitation; No RVF with PA banding alone	N/A	15 minutes

Gufler et al., 2019 [295]	Ovine	25 weeks (adult)	PA banding; target maximal RVSP set to 50-60% above baseline	Adaptive response of RV to chronic pressure overload; No RVF reported	N/A	3 months
Corno et al., 2003 [296]	Porcine (mini-pig)	18.2±0.1 weeks; 8.6± weeks (non-adult)	Adjustable PA band; perimeter range = 23-30 mm	Evaluation of FloWatch (implantable device for PA banding) as a treatment for congenital heart disease; No RVF reported	N/A	24 weeks; 10 weeks

7.2 Material and methods

7.2.1 Animal-specific and graded pulmonary artery constriction (PAC) in ovine

All procedures were approved by Colorado State University Institutional Animal Care and Use Committee. Prior to surgery, 8-month old male sheep (n=3) were placed under general anesthesia with 3.3-5 mg/kg ketamine and 0.1 mg/kg midazolam. During the surgical procedure, animals received 15 mcg/kg/min of ketamine and 35 mcg/kg/min of lidocaine. To induce RV pressure overload, an adjustable hydraulic occluder (AUS-PORT 12x14 mm, Norfolk Vet Products, IL) was placed around the main pulmonary artery and secured with two 2-0 polybutester sutures. Next, under pressure monitoring, saline was injected to the occluder acutely until the RV systolic pressure (RVSP) reached an equivalent number of its left ventricle systolic pressure as described previously [271,273,274,278]. The amount of saline was recorded and the saline was withdrawn from the occluder to allow the animal to recover from surgical procedure for two days. This minimized the 'surgical insult' to the RV and the response was mainly a result of hemodynamic overload induced via saline injections starting two days post-surgery. Besides the baseline measurements in the PAC sheep, age-matched, healthy intact sheep (n=3) were used as additional controls (CTL).

Animal-specific, graded filling of the occluder with saline was induced in awake animals at weeks 0, 1 and 4 post surgery (**Fig. 7.1**). The amount of saline injections was determined by the procedure described above as well as the RV morphology and function from bi-weekly echocardiography. If we observed signs of heart failure (e.g., difficulty in breathing, anorexia, grinding teeth, etc.), continuous RV dilation and RV hypertrophy (e.g., increased RV area or RV wall thickness), or function decline (e.g., decreased pressure gradient and flow velocity across the PA valve and decreased TAPSE), we reduced the injection volume or did not inject any saline further (**Table 7.2**).

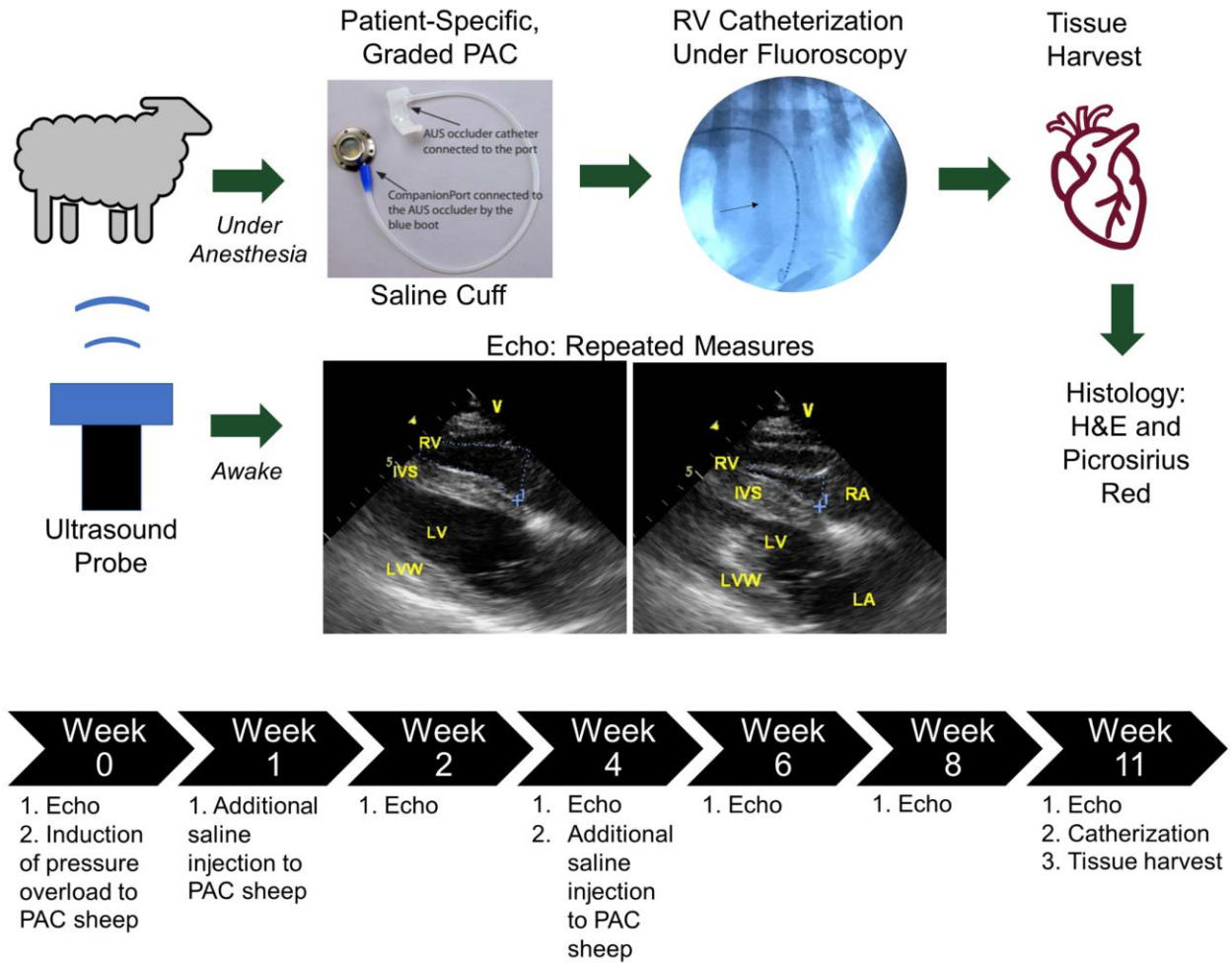

Fig. 7.1. Visualized workflow of PAC sheep model and timeline of study. Saline cuff figure reproduced with permission from Norfolk Vet Prodcuts (https://norfolkvetproducts.com/wp-content/uploads/2019/03/NVP_Catalog_2019-01_email.pdf). Representative 4-chamber view images obtained by echocardiography (echo) are from a PAC sheep at week 2 (left: diastole; right: systole).

Table 7.2. Volumes of saline injections for the PAC animals at three time points over the 11-week study.

	Week 0	**Week 1**	**Week 4**	**Total**
Sheep 1 Injection (mL)	0.4	0.4	0.1	0.9
Sheep 2 Injection (mL)	0.6	0.6	0	1.2
Sheep 3 Injection (mL)	0.2	0.4	0.1	0.7

7.2.2 Echocardiography

Transthoracic two-dimensional echocardiography was performed bi-weekly (week 0, 2, 4, 6, 8, 11) using a 2.5 MHz transducer on a GE Vivid 7 (GE Healthcare, Chicago, IL) ultrasound machine. Briefly, parasternal images were obtained in the awake sheep in lateral recumbency, using American Society of

Echocardiography guidelines with minor imaging plane modifications in the sheep [297]. Ventricular dimensions, tricuspid annular plane systolic excursion (TAPSE) and flow dynamics were measured.

7.2.3 Hemodynamic measurements and terminal procedure

Prior to euthanasia, the CTL and PAC animals were anesthetized and RV catheterization was performed to obtain hemodynamic measurements. A 7 Fr Swan Ganz catheter (Edwards Lifesciences Corporation, Irvine, CA) was floated to the RV through the jugular vein and cranial vena cava under pressure monitoring and fluoroscopic guidance. Cardiac output (CO) and stroke volume (SV) were measured using the thermodilution method [253,258]. Finally, the RV systolic pressure was obtained by a pressure-volume catheter (Millar, Houston, TX). Immediately following the hemodynamic measurements, the animals were euthanized with pentobarbital (IV) at 88 mg/kg and the hearts were harvested. RV tissue hypertrophy was measured by the wet weight, Fulton index (RV/(LV+Septum)), and wall thickness using a digital caliper.

7.2.4 Structural measurements

RV samples from the center of the anterior RV free wall were fixed in 10% formalin. Specimens were then dehydrated, embedded in paraffin, sectioned and stained with H&E for cardiomyocyte morphology and Picro Sirius Red for collagen fibers. Cardiomyocyte morphology was imaged by an inverted microscope (Motic AE31E) and quantified with AmScope software (AmScope, Irvine, CA); collagen content and fiber orientation were imaged under polarized light by a transmission microscope (Nikon Eclipse E800) and quantified with Image Pro Premier software (Media Cybernetics, Rockville, MD). Color thresholding method was used to measure type I collagen, type III collagen and non-collagen areas, respectively [129,261].

7.2.5 Statistical and correlation analysis

One-way ANOVA with repeated measures and Dunnett's post-hoc tests were performed by Prism (GraphPad Software, San Diego, CA) to examine the functional changes of the RV during the PAC. Unpaired Student's t-test was performed between the CTL and PAC groups in Excel (Microsoft). Pearson

correlation analysis was used to investigate the correlations between the structural and functional properties. Data are presented as mean±SD and $p<0.1$ was considered statistically significant [298](we also labeled the results with $p<0.05$ as conventionally used). This level of statistical significance was chosen in accordance with the recent American Physiological Society recommendations [298]. $r>0.8$ was considered as a strong correlation.

7.3 Results

7.3.1 Hemodynamic and functional changes in RV with PAC

Eleven weeks post PAC, there was a significant increase in RVSP compared to the CTL group and a gradual decrease of the ratio of pulmonary artery acceleration time/ejection time (PA AT/ET) over time, with a significant reduction at the endpoint (**Fig. 7.2A-B, $p<0.05$**). These results indicate the successful induction of pressure overload and establishment of RVF in the sheep. Moreover, there was a significant decrease in SV in the PAC group compared to the CTL group at 11 weeks (**Fig. 7.2C, $p<0.05$**). Lastly, we found that TAPSE was significantly decreased at week 11 compared to the baseline (**Fig. 7.2D, $p<0.05$**). These results indicate that pressure elevation was successful, and RVF was evident in these animals.

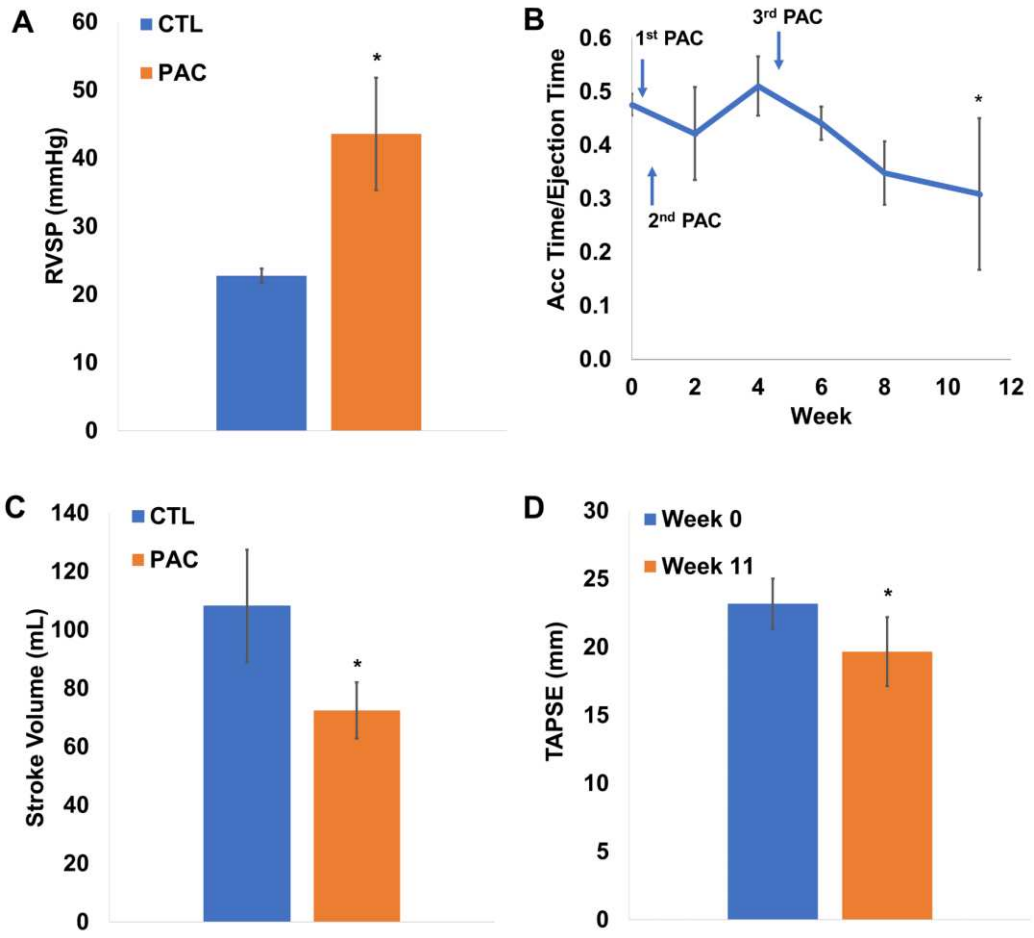

Fig. 7. 2. Decline in RV hemodynamics and function with PAC. A) Increase in RV systolic pressure. B) Decrease in pulmonary artery acceleration time/ejection time. C-D) Decrease in stroke volume and TAPSE in PAC sheep. *p<0.05.

7.3.2 Morphological changes in the RV with PAC

With the chronic pressure overload, there were significant increases in diastolic RV area and inner diameter as measured by echocardiography (**Fig. 7.3**), suggesting a progressive dilatation of the chamber. Some global changes of the hearts were examined after tissue harvest (**Table 7.3**). Both the RV weight/body weight (**p<0.05**) and wall thickness (**p<0.05**) were larger in the PAC group, and the Fulton index as a routine RV hypertrophy index was significantly increased as well (**p<0.05**).

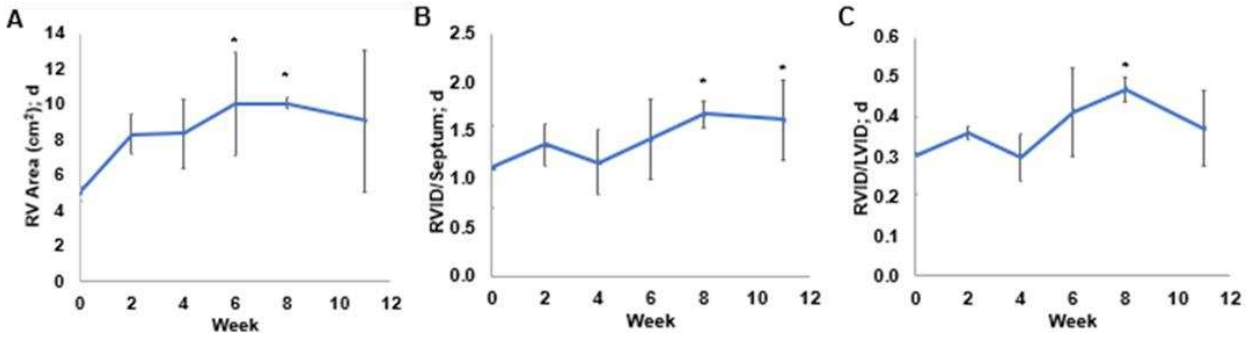

Fig. 7. 3. Temporal changes in diastolic geometry of the RVs over 11 weeks of pressure overload (PAC). PAC led to gradual increases in A) RV diastolic area, B) RV Inner Diameter/Septum diameter at diastole, and C) RV Inner Diameter/LV Inner Diameter at diastole. *p<0.05.

7.3.3 Structural changes in the RV with PAC

From the H&E staining, we quantified RV cardiomyocyte width and found that there was a significant increase in the cell width with PAC (**Table 7.3, p<0.05**). From the Picro Sirius Red staining, we examined RV collagen content and fiber orientation in the CTL and PAC groups using polarized microscope images. PAC led to more collagen accumulation, especially type III collagen accumulation in the RV (**Table 7.3**). There was no difference in collagen fiber orientation between the CTL and PAC groups (**Table 7.3**).

Table 7.3. Overall structural changes in ovine hearts with PAC. Data are presented as mean ± SD.

	CTL	PAC
Body Weight (kg)	81.6±12.2	84.8±4.5
RV Weight (g)	61.7±10.9	84.1±13.1†
RV Weight/Body Weight (g/kg)	0.8±0.0	1.0±0.1*
Fulton Index (%)	28.4±1.3	43.0±3.5*
RV Wall Thickness (mm)	5.9±0.2	7.4±0.6*
Myocyte Width (μm)	13.5±1.2	17.1±0.7*
Collagen Fiber Angle (degrees)	54±8	57±12
Type I Collagen Content (%)	2.9±1.0	4.3±1.3
Type III Collagen Content (%)	0.7±0.1	1.8±0.7ξ
Total Collagen Content (%)	3.6±1.0	6.1±1.4†

*p<0.05; ξp=0.05; †p<0.1.

7.3.4 Correlation analyses of structure and function in the RV

We first examined the relations of RV pressure (RVSP) and the structures. As shown in **Fig. 7.4A&B**, we found a significant correlation between RVSP and the Fulton index (**p<0.05**), which has been used to indicate RV hypertrophy at the tissue level [73]; there was also a trend of correlation between the RVSP and the width of cardiomyocytes. These correlations indicated that the degree of RV pressure overload was associated with RV hypertrophy at both cellular and tissue levels.

As we found that both Fulton index and width of the cardiomyocyte were correlated with the RVSP, we further investigated the relations between these two hypertrophy indices. It was not surprising to see that there was a significant correlation between the myocyte width and Fulton index in the RVs of the experimental groups, suggesting that the enlarged cardiomyocytes would contribute to increased RV mass (**p<0.05, Fig. 7. 4C**). Interestingly, we also found a significant correlation between the type III collagen

and Fulton index (p=0.05, **Fig. 7. 4D**), and this relation was absent between the type I collagen and Fulton index (data not shown). These results indicated that RV fibrosis, especially the accumulation in type III collagen, was correlated with the RV hypertrophy.

Next, we examined the relations between the RV hypertrophy or fibrosis and its function indices. As shown in **Fig. 7.4E&F**, we found a significant correlation between the Fulton index (hypertrophy) and RV ejection time (ET) and a significant correlation between the Fulton index and the stroke volume, respectively (**p<0.05**). Furthermore, we found a significant correlation between type III collagen content and ejection time and a trend of moderate correlation between the type III collagen content and stroke volume (**Fig. 7.4G&H**). However, there were no correlations between the type I collagen content and the RV function (data not shown).

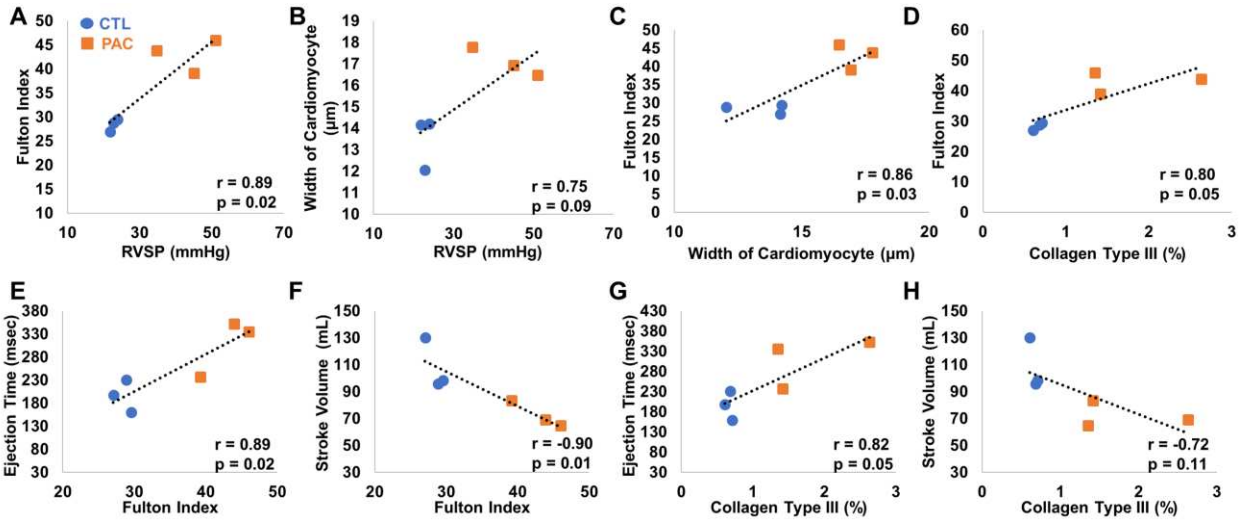

Fig. 7.4. Correlations between the structure and function in the RVs of CTL and PAC groups. A - B) correlations between the RVSP and Fulton index or width of the cardiomyocyte, respectively. C - D) correlations between the width of the cardiomyocyte or the type III collagen content and Fulton index, respectively. E - F) Correlations between the Fulton index and ejection time or stroke volume, respectively. G - H) Correlations between the collagen type III content and ejection time or stroke volume, respectively.

7.4 Discussion

In this study, we described a revised PAC ovine model of adult RVF secondary to pressure overload. This model allowed for a customizable constriction between individual animals and at multiple time points. RV hypertrophy and fibrosis were evident in the pressure overloaded sheep. Surprisingly, the increase in

type III collagen was more pronounced than the increase in type I collagen. Functionally, RV pressure elevation resulted in declines in RV, SV and TAPSE, and progression of chamber dilation and ejection dysfunction, indicating RVF development. The degree of RV hypertrophy and the amount of type III collagen were correlated with the function of the RV.

7.4.1 The revised PAC ovine model of adult RV failure

To date, this study is the first report of an ovine model of adult, chronic RVF. Historically, lambs have been used in the study of RV dysfunction or therapeutics in pediatric patients (**Table 7.1**). Since ovine reach sexual maturity at 6-8 months old [299], we explored the potential of RVF establishment in young adults. From the prior literature, it can be found that not all PAC surgeries induced RVF (**Table 7.1**). If the PAC induction is too mild, RV adaptation rather than RVF will occur; on the other hand, if the PAC induction is too severe, animal deaths often occur prior to data collection [300]. In the present study, we adopted the same criteria as used previously [271,273,274,278] to induce a similar degree of hemodynamic insult in these sheep and then examined the remodeling of the RVs. As a result, different (customized) degrees of PAC were induced (**Table 7.2**) to ensure that the proper degree of pressure overload was achieved for RVF establishment in different individuals. Therefore, even with a small number of animals (n=3 per group), we were able to confirm significant structural changes (i.e., RV hypertrophy and fibrosis) and functional changes (i.e., reduction in systolic function and ejection hemodynamics) in the RVs, from which changes RVF was evident. This pilot study had 0% of mortality in the PAC animals, which was rare in the similarly reported studies since the model is known for its drawbacks in surgical mortality, especially when the goal is to induce RVF [300]. Furthermore, while prior pre-clinical studies examined the development of RVF by either structural or functional changes of the RV, our study examined both aspects comprehensively to fully validate the establishment of RVF in adult sheep.

There are some advantages of the animal-specific, graded PAC methodology. First, this method allows for a PA constriction that results in identical hemodynamic insult between animals. As shown in **Table 7.1**, many preclinical studies used a fixed degree of constriction (i.e., increase to certain pressure value, reduce to certain PA diameter, etc.) to induce pressure overload. However, each animal responds

uniquely to PAC and thus a fixed constriction may lead to varied degrees of RV dysfunction (from adaptation to failure), which may complicate the assessment and diagnoses of RVF among animals. In addition, various degrees of constriction were reported (see **Table 7.1**) and there is a lack of guidance on the induction of PAC. Since RV pressure equivalent to systemic pressure has been reported in clinical and preclinical studies of RVF [301,302], we decided to use this hemodynamic condition as the criterion of PAC in our model. Indeed, from our own data it can be seen that each animal had its own amount of saline injection to elevate the RV pressure to systemic pressure, suggesting that different thresholds are required to induce RVF in individual animals. The animal-specific and graded approach also avoids potential unexpected animal death due to a single, severe constriction as we can progressively increase or halt the insult depending on the animal's individual response.

Second, the use of an adjustable PAC method provides more flexibility in the degree of PA constriction in large animals that is impossible in rodent PAC models. In a rabbit study with a similar PAC method, reversible constriction was induced to investigate the progression and recovery of RVF. This proof of concept study has shown the regression of RV chamber size, hypertrophy and fibrosis by the removal of pressure elevation, which may support the postulate that RVF is reversible [303]. Similarly, the graded or reversible PAC could be induced in large animals such as in this ovine model to further investigate the pathogenesis of RVF, including the development from adaptive to maladaptive RV remodeling. Therefore, the model is very flexible and can be adapted to investigate different questions regarding RVF.

7.4.2 New insights of RV failure from the study

In addition to the clearly adverse functional changes, we have observed morphological and structural changes of the RVs in the PAC group that are characteristic of RVF [253,254,258]. Firstly, RV dilatation and hypertrophy were evident and the RVID/LVID was gradually increased during the progression of RVF (**Fig. 7.3C**). In a recent study, the RVEDV/LVEDV was found to increase with increased RV free wall stiffness in PH patients, and this new index was strongly and inversely correlated with the RV peak contractility [86]. Thus, we speculate that the increased RVID/LVID may indicate a gradual reduction in RV contractility and explain the impaired systolic function (SV) observed in the PAC sheep.

Moreover, RV fibrosis was revealed in the PAC sheep (**Table 7.3**). This is not surprising because collagen deposition is universally reported in clinical and preclinical studies, large and small animals, as well as from early to late stage of RVF [73,258,300,304]. However, it was the collagen type III, not type I, that was more markedly increased in the PAC RVs. This is unexpected because type I collagen is the major isoform of collagen fibers in the RV [29,305], and provides more mechanical strength than type III collagen. We do not know why RVF led to a more significant increase in type III collagen, which will be examined in future investigations. Even in LVs, there is no consensus on whether type I or type III collagen plays a more significant role in its pathogenesis [129,306]. Future studies should also delineate the role of different subtypes of collagen in RVF.

Finally, we found some interesting correlations among the healthy and failing RVs. RV hypertrophy and fibrosis were strongly correlated with RV function (**Fig. 7.4F&H**). This indicated that the severity of RV hypertrophy or fibrosis were linearly linked to the adaptation/of the RV and could be used as diagnostic parameters indicative of RVF. Indeed, both ventricular mass and collagen deposition have been used in preclinical and clinical settings and were found to correlate with the severity of ventricular dysfunction [307,308]. These data also confirm that our ovine model recapitulates the behavior and pathogenesis of human RVF. Furthermore, the amount of type III collagen was strongly correlated to the Fulton index (**Fig. 7.4D**), indicating that certain molecular mechanisms in type III collagen metabolism is linked with the RV hypertrophy. To date, the proof of a mechanistic link between fibrosis and RV dysfunction is insufficient [304,309]. Despite the evidence that increased collagen accumulation is found in severe RVF, the treatment that reversed the collagen deposition in the RV failed to improve the RV function [310,311]. Here, we observed that type III collagen content was strongly correlated with ejection time and stroke volume (**Fig. 7.4G&H**). We suspect that the different roles of type I and type III collagen in RV dysfunction may explain the discrepancy in the literature.

7.4.3 Limitations

There are a few limitations to this study. Firstly, we did not have 3D measurements of the RV volume or strain, which are useful indices of RVF [253,258,312]. Cardiac magnetic resonance imaging or

pressure-volume relations are the gold standard and should be used to investigate adult ovine RVF in the future [302,313]. Secondly, even though we observed significant functional impairment, other clinical signs such as peripheral edema or body weight loss were absent [249,258]. These signs are typically seen in the late stage of RVF and the RVF observed in this study may be in an early rather than a late stage.

7.5 Conclusion

In this study, we reported a revised animal-specific, graded pulmonary artery constriction model in adult ovine. The model led to successful right ventricle failure development with significant structural and functional changes as well as some correlations between right ventricle hypertrophy or fibrosis and functional decline. The model is robust and safe to induce various degrees of pressure overload and at multiple time points, which enables the flexibility to adapt to different protocols to answer various research questions related to the progression or treatment of right ventricle failure.

CHAPTER 8: CORRELATIONS BETWEEN THE RIGHT VENTRICLE PASSIVE ELASTICITY AND ORGAN FUNCTION IN ADULT OVINE [7]

8.1 Introduction

Right ventricle failure (RVF) contributes significantly to the mortality and morbidity in a variety of cardiovascular diseases including pulmonary hypertension (PH), congenital heart disease and left heart failure with preserved ejection fraction [20–24]. The biomechanical properties of the RV free wall are considered to play a role in its organ function [30,31], and a recent rodent study has reported a correlation between the passive elastic modulus and the end-diastolic volume of the RV [9], with the latter often being used as an index of RV function [32]. This is the first study that directly relates the RV tissue mechanics to a clinically relevant hemodynamic index, leading to a new point of view to link the ventricular biomechanics with the organ function to advance the understanding of biomechanical mechanism of RV failure. However, the comprehensive understanding of the roles of RV biomechanical properties in the *in vivo* function remains a key knowledge gap.

This study aimed to explore the correlations between RV tissue mechanical properties and the *in vivo* function in healthy and hypertensive adults. We hypothesized that the RV passive elasticity was correlated with its *in vivo* function. Using a large animal model of RV failure, we observed the correlations between the RV elastic properties and the physiological function, and our findings offer a deepened insight of the biomechanical mechanisms of RVF secondary to chronic pressure overload.

8.2 Materials and Methods

8.2.1 Ovine Model of Pulmonary Hypertension and RV Failure Development

All animal works were approved by the Colorado State University Institutional Animal Care and Use Committee (IACUC#17-7590A). Six PH sheep and three age-matched health sheep were recruited in this

[7] *This chapter is published as a peer reviewed research article in Journal of Integrative Cardiology (doi: 0.15761/JIC.1000294).*

study. Sheep was chosen for this study because its anatomy and physiology are closer to human than those of small animals and thus the findings are more translatable to human physiology and cardiac biomechanics [169]. PH was induced in eight-month old male and female ovine using our recently established animal-specific, pulmonary artery constriction model [179]. Briefly, an adjustable hydraulic occluder (AUS-PORT 12x14 mm, Norfolk Vet Products, IL) was placed around the main pulmonary artery trunk to elevate the pulmonary pressure. The degree of constriction for each animal was determined by the amount of saline injected to elevate the RV systolic pressure comparable to that of the left ventricle (LV) in the same animal. The chronic pressure overload was maintained for 11-20 weeks and thus different phases of RV failure were included in these PH ovine.

8.2.2 In Vivo Functional Measurements

Prior to the euthanasia, RV hemodynamic and function measurements were performed by thoracic echocardiography using a 2.5 MHz transducer on a GE Vivid (GE Healthcare, Chicago, IL) in awake animals, and then by RV catheterization (7 Fr Swan Ganz catheter (Edwards Lifesciences Corporation, Irvine, CA)) in anesthetized animals. RV systolic pressure (RVSP), stroke volume (SV), cardiac output (CO), tricuspid annular plane systolic excursion (TAPSE), fraction shortening (FS), acceleration time (AT), deceleration time (DT) and ejection time (ET) were obtained [179]. RV diameters and areas at end-diastolic and end-systolic phases were measured. After euthanasia, RV hypertrophy was measured by Fulton index, which is the ratio of wet tissue weights calculated as RV/(LV+S), where LV is the left ventricle and S is the septum [74].

8.2.3 Ex Vivo Mechanical Test and Data Analysis

Within four hours of sacrifice, the RVs were dissected and immersed in a physiological saline solution (PBS) on ice. Because the RV free wall is relatively thin, almost the entire wall was used for mechanical tests, after the removal of epicardium layer and the trabeculae from the endocardium. To obtain the biaxial mechanical properties, the outflow tract (OT) direction of the RV was defined as the longitudinal direction in the test axis. A minimal sample aspect ratio of 3:1 (length: thickness) was used to approximate a plane-

stress condition, and a cruciform section was cut to generate more homogenous strain distribution and minimize shear strains in the biaxial tests [173,177]. A ruler and caliper were used to measure the tissue size and thickness, respectively.

The tissues then underwent equibiaxial tensile mechanical tests, either with a regular spray of PBS solution to keep the tissue moist in room air or with the bath of cardioplegic solution (CPS) and 30 mM of 2,3-butanedione monoxime (BDM) at 26 – 37°C. Our supplement experimental data confirmed that there were not significant changes of the stress-strain curves between these testing conditions (**Fig. 8.1**). Graphite powder (AGS, MI) was used for strain characterization via digital image correlation. During the test, images were taken with a digital camera (Nikon) at 1 fps. A MATLAB-based digital imagine correlation program was used to analyze the tissue deformation. Two 250 lb capacity load cells (Honeywell Sensotec, Columbus, OH) were used to obtain the forces. A custom LabVIEW code was used to control the actuators and record the data [177].

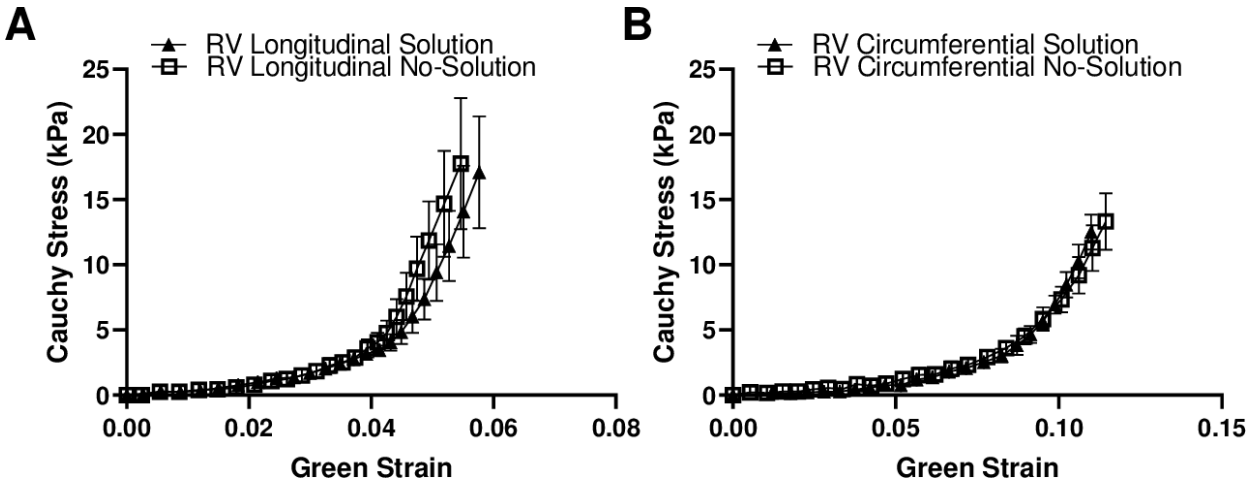

Fig. 8.1 Comparison of the average stress-stain curves obtained from different testing conditions. (A-B) stress-strain curves in the longitudinal and circumferential directions, respectively. N=3.

After mounting, a small preload (~0.1 N) was applied to define the zero-strain configuration, and then the tissue underwent 15 cycles equibiaxial tests including preconditioning cycles (at the stretch rate of 15 mm/min, with ~25% maximal stretch). We further assumed the tissue to be incompressible [56]. Then the last

cycle of the loading curve was used to generate the Cauchy stress – Green strain curve to analyze the RV mechanical properties as previously described [56]. We were unable to obtain complete mechanical data in one control and one PH sheep. From the stress-strain curves, the RV passive stiffness (or elasticity) was quantified by the elastic moduli (EM) at the low and high strain ranges, respectively [9].

8.2.4 Statistical and Correlation Analyses

All data were analyzed by the non-parametric statistical analysis, except for the EM which were confirmed with the normal distribution by the QQ plot (GraphPad (v8.0.2)). Pearson correlation analysis was used to investigate the correlations between the tissue mechanical properties and RV function indices (Microsoft Excel). All the data were presented as mean ± SEM. $P < 0.05$ was considered statistically significant.

8.3 Results

8.3.1 Changes in RV Geometry and Hemodynamic Function with PH Development

The results of the individual RV geometry and hemodynamic function were summarized in **Table. 8.1**. There was a significant increase in RVSP and significant decreases in SV and CO in the PH group compared to the CTL group ($p<0.05$). PH also led to a trend of decrease in the AT ($p = 0.07$) and significant increases in the DT, ET, as well as the AT/ET ratio compared to the CTL group ($p<0.05$). Lastly, the RV became significantly hypertrophic with the PH development ($p<0.05$). These results indicate the successful induction of pressure overload of the RV and the establishment of RV failure in the PH animals.

Table 8.1 Individual hemodynamics, structure and function measurements of the ovine RV.

Sample	RVSP (mmHg)	SV (mL)	CO (mL)	TAPSE (mm)	FS (%)	AT (msec)	ET (msec)	DT (msec)	AT/ET	Fulton Index (%)
CTL1	22.7	96	9.2	19	/	94	231	137	0.41	28.8
CTL2	23.8	99	13.3	21	/	73	160	87	0.46	29.5
CTL3	21.7	130	11.6	28	/	68	198	130	0.34	27.0
Mean ± SEM	*23± 1*	*108 ± 11*	*11 ± 1*	*23 ± 3*	*/*	*78 ± 8*	*196 ± 21*	*118 ± 16*	*0.40 ± 0.03*	*28 ± 1*
PH1	35	69	6.5	17	32.7	/	321	/	/	43.9
PH2	51	65	5.9	20	11.1	69	335	266	0.21	46.0
PH3	45	83	9.4	22	/	59	237	178	0.25	39.2
PH4	42	39	3.8	25	35.9	62	271	209	0.23	58.8
PH5	28	56	5.6	22	11.9	67	360	293	0.19	58.2
PH6	51	47	3.9	20	27.0	44	278	234	0.16	64.1
Mean ± SEM	*42 ± 4**	*60 ± 7**	*6 ± 1**	*21 ± 1*	*24 ± 5*	*60 ± 4*	*300 ± 19**	*236 ± 20**	*0.21 ± 0.02**	*52 ± 4**

CTL: control group, PH: pulmonary hypertension group. RVSP: right ventricle systolic pressure, SV: stroke volume, CO: cardiac output; TAPSE: tricuspid annular plane systolic excursion, FS: fraction shortening, AT: accelerate time and ET: ejection time. /: unable to obtain the data. *: $p < 0.05$ vs CTL group.

8.3.2 Changes in RV Passive Elasticity with PH Development

Figure 8.2 presented the RV passive, biaxial elasticity obtained from the control and PH ovine. Despite a relative small number of the control animals, we observed significant stiffening of the RV in the PH group: compared to the control RVs, the PH RVs had a larger EM at low strain range (EM_{Low}) in the longitudinal direction (**Fig. 8.2A**, $p<0.05$). A similar trend was observed for the EM at high strain range (EM_{High}) in the same direction, but the difference did not reach statistical significance (**Fig. 8.2B**). In contrast, the changes in these EM in the circumferential direction were absent with PH development.

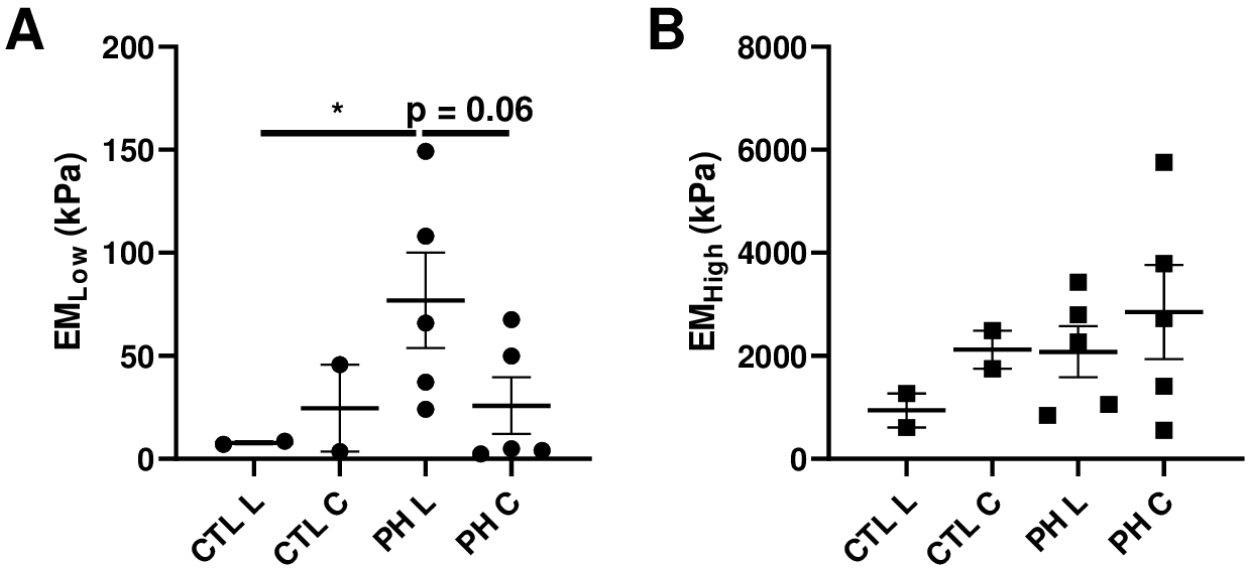

Fig. 8.2 Different RV elasticities derived from the stress-strain curves. (A) the EM at low strain range (EM_{Low}) and (B) the EM at high strain range (EM_{High}) in both longitudinal (L) and circumferential (C) directions. CTL: control group, PH: pulmonary hypertension group. *: $p < 0.05$.

Furthermore, PH led to a strong trend of increased EM_{Low} in the longitudinal direction compared to the circumferential direction (**Fig. 8.2A**, $p=0.06$). However, this was not observed in the control RVs. These results indicate an alteration of the anisotropic behavior at the low strain range with the progression of PH. We did not observe any anisotropic behavior from the high-strain EM in both PH and control groups.

8.3.3 Correlations Between RV Passive Elasticity and Physiological Function Indices

RV elasticity and RV diameter

Among all healthy and diseased RVs, we observed that the longitudinal EM_{Low} was significantly correlated with the long-axis end-diastolic area (**Fig. 8.3A**, $p<0.05$) and it tended to correlate with the end-systolic diameter (**Fig. 8.3B**). Moreover, we also saw a trend that the longitudinal EM_{High} was correlated with the long-axis RV end-systolic diameter (**Fig. 8.3C**). In our study, the definition of longitudinal direction in the biaxial properties was anatomical and aligned with the long-axis of the RV geometry. Thus, these data suggest that the passive elasticity of the RV is strongly related to the ventricular shortening in the same (long-axis) direction.

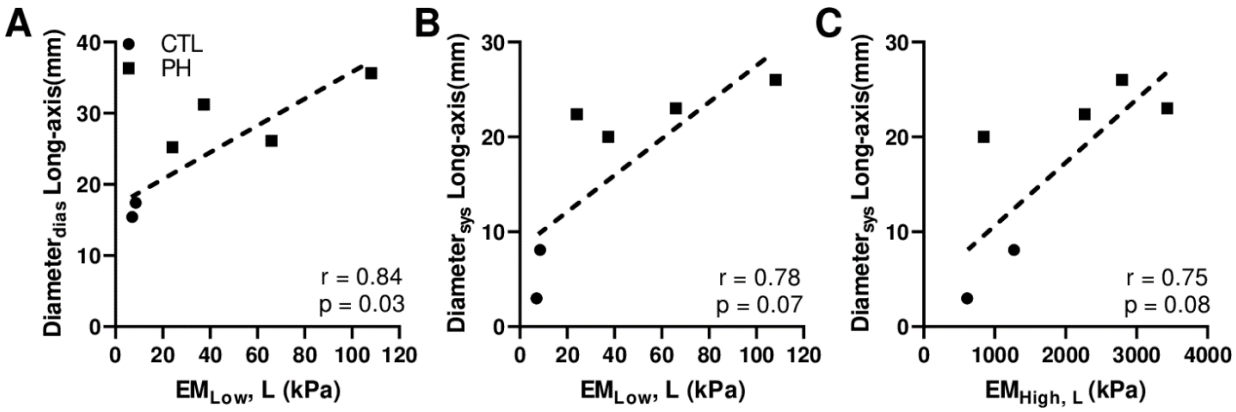

Fig. 8.3 Correlations between the RV passive elasticity and RV diameter at longitudinal direction. (A) correlation between the EM at low strain range and RV end-diastolic diameter, (B-C) correlations between the EM and RV end-systolic diameter at low and high strain ranges, respectively.

RV elasticity and RV area

Similarly, as we observed in the RV diameter, the longitudinal EM_{Low} was significantly correlated with the long-axis RV end-systolic area (**Fig. 8.4B**, $p<0.05$) and it tended to correlate with the RV end-diastolic area (**Fig. 8.4B**). However, the EM_{High} was differently correlated with the RV area than with the RV diameter: instead of the longitudinal EM_{High}, the circumferential EM_{High} showed a trend of correlation with the long-axis RV end-systolic area (**Fig. 8.4C**).

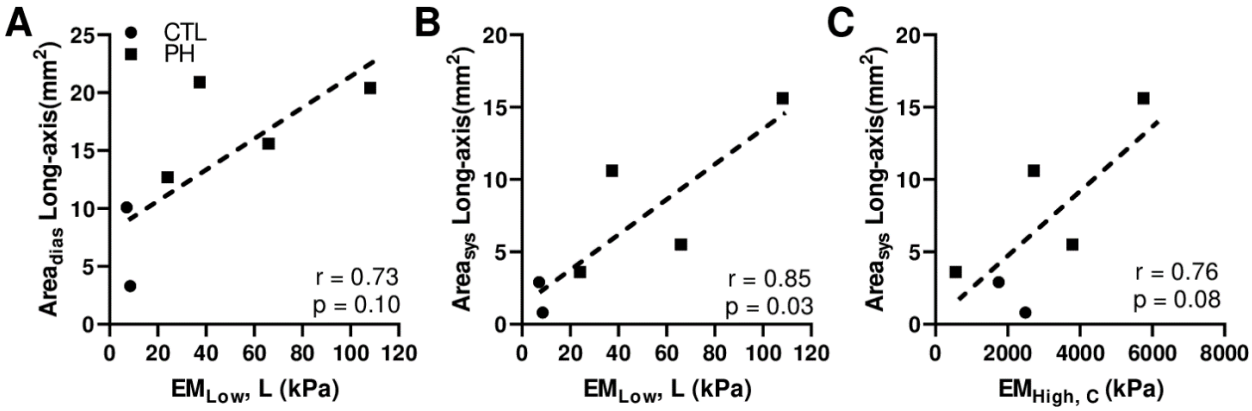

Fig. 8.4 Correlations between the RV passive elasticity and the RV area. (A) correlation between the EM at low strain range and RV end-diastolic area at the longitudinal direction, (B) correlation between the EM and RV end-systolic area at low strain range at the longitudinal direction, and (C) correlation between the circumferential EM at high strain range and RV end-systolic area in the long axis.

RV elasticity and RV hemodynamic profile

Lastly, we found that the RV longitudinal stiffness indices showed strong trends of correlations with the RV hemodynamic profile obtained from the Doppler flow measurements. The longitudinal EM_{Low} tended to be negatively correlated with the AT, and the longitudinal EM_{High} tended to be positively correlated with the ET and DT (**Fig. 8.5**).

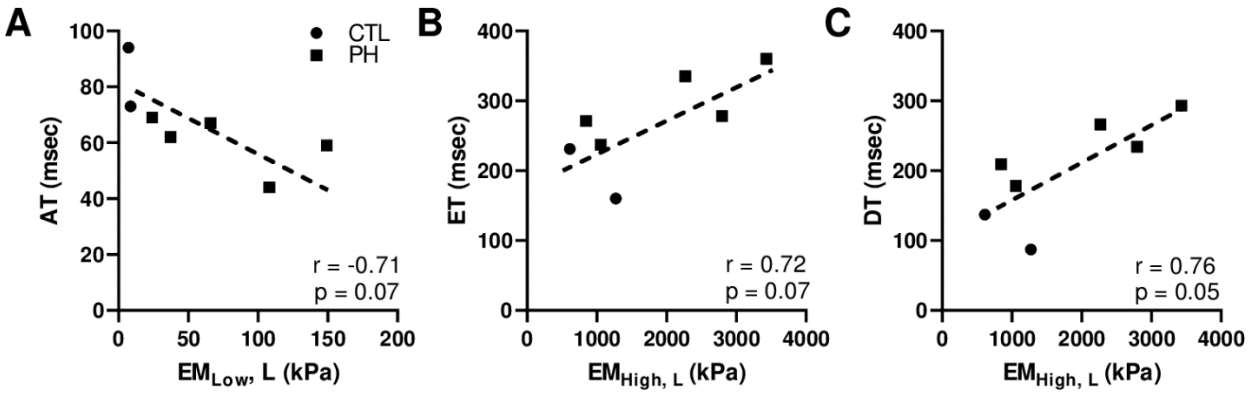

Fig. 8.5 Correlations between the RV passive elasticity and RV hemodynamics. (A) correlation between the low-strain EM and RV acceleratetion time (AT); (B) correlation between the high-strain EM and RV ejection time (ET) and (B) correlation between the high-strain EM and RV deceleration time (DT).

Moreover, we examined the correlations between the RV passive elasticity and other function indices such as the SV and TAPSE. We observed a mild trend of negative correlation between the longitudinal EM_{High} and the SV (r=-0.48, p=0.28), but there were no correlations between the passive elasticity indices and TAPSE (data not shown).

8.4 Discussion

In this study, we originally investigated the relationship between RV passive mechacnial property and its physiological function in healthy and pulmonary hypertensive adults using a sheep model of RV failure. To our knowledge, there is only one rodent study showing a correlation between the RV passive elasticity and its end-diastolic volume [9]. The prior study was the first effort to link the RV biomechanics to the organ function, but the relationships examined were limited. The present study investigated the relations of the RV tissue mechanics and a variety of organ function indices measured in large animal (ovine) species. The anatomy and physiology of sheep are closer to human patients compared with the small animals, and thus the findings here are more translatable to human physiology and cardiac biomechanics [169,204,277].

8.4.1 Correlations Between RV Mechanics and Its Hemodynamic Function

We observed several interesting correlations that support the hypothesis that there is linkage between the RV mechanics and hemodynamic function. First, our results showed that the RV elasticity was correlated with the RV chamber geometry, which is an alternative index of RV function and a useful prognostic parameter for RV failure patients [32,314–316]. Our data showed that the longitudinal EM_{Low} was correlated with the RV end-diastolic diameter and area in the same direction (long axis) (**Fig 8.3&8.4**). The finding is consistent with the report in a pulmonary arterial banding rat study, which showed that the longitudinal EM_{Low} was correlated with the RV end-diastolic volume [9]. It is unclear whether the same degree of RV failure was achieved in the present ovine study as in the previous rodent study. Moreover, we have various durations of PAC in the PH sheep, which may include different stages of RV failure in the animals. Nevertheless, both our study and the previous study identified a correlation between the low-

strain EM (EM_{low}) and RV diastolic geometry (**Fig. 8.3A&8.4A**). These findings confirm a critical role of RV passive mechanical property in the diastolic function.

8.4.2 Alteration of the RV Anisotropic Behavior During PH

Furthermore, we observed a change in the anisotropic behavior of the RV during PH development (**Fig. 8.2**). The stiffening of the RV in the longitudinal direction and the absence of stiffening in the circumferential direction led to a more anisotropic behavior of the RV with the progression of PH. We speculate that the biaxial mechanical changes may partially explain the development of RV failure. Under persistent pressure overload, the RV typically remodels into a spherical shape and requires a higher wall strength in the circumferential direction to maintain the blood flow in the pulmonary circulation. Alternatively, a failure to enhance the circumferential wall strength will impair the ventricular function and result in RV failure. Therefore, a lack of stiffening ('elastic recoil strength') of the wall in the circumferential direction, as we observed in the study, may contribute to the decline of the *in vivo* function (e.g., decreased SV).

8.4.3 Correlations Between the RV Passive Elasticity and Its Systolic Geometry

Next, we also observed new correlations between the RV passive elasticity and its systolic geometry (**Fig. 8.3B-C, 8.4B-C**). This drove us to think how RV passive elasticity may interfere with the overall function including the systolic function. It is known that the myocardial stiffness plays a role in the progression of heart failure [317]. For the RV particularly, the diastolic stiffness derived from the diastolic pressure-volume relation is a better parameter than the systolic parameter such as the load-independent contractility to distinguish different clinical outcomes (survival) of PH patients [318]. This evidence underscores the importance of RV passive stiffness in the overall health of the RV. Our data here add additional support that the role of the passive elasticity may go beyond the diastolic function, and one possible explanation is that the matrix 'stiffness' may be linked with the 'health' state of the cardiomyocytes [319,320], and thus affect the contractile function of the RV. The understanding of the roles of active (systolic) and passive (diastolic) mechanical property in myocardial function has been an ongoing research area,

especially with the development of non-invasive cardiac imaging and computational modeling techniques [321–323]. Therefore, future study should elucidate the linkage between the active and passive stiffness of the RV and their impacts on the RV function.

8.4.4 Correlations Between the Longitudinal Stiffness Indices and Its Hemodynamic Function

Finally, we observed for the first time that the longitudinal stiffness indices (EM_{Low} and EM_{High}) tended to be correlated with the AT ($p=0.07$) and DT ($p=0.05$) (**Fig. 8.5**), both of which are hemodynamic indices associated with the ventricular afterload [324,325]. Unlike the AT, the DT is not a commonly reported hemodynamic parameter. A study in the LV showed that the increased DT was correlated with increased central blood pressure as well as with the increased pulse wave velocity (indicator of arterial stiffness) at rest and during exercise [325]. Therefore, the DT is suggested as a surrogate marker for central hemodynamics, mainly representing LV afterload (both steady and pulsatile). Such measurement in the RV has not been noted to our knowledge, but another group has measured the mid-systolic DT (the deceleration time from the peak to 'notch' in the flow profile) in pulmonary arterial hypertension patients. They found that the mid-systolic DT was associated with the pulmonary vascular resistance and pulmonary pressure, which are measures of the steady RV afterload [326]. Therefore, our observed trends of correlations indicate that the RV longitudinal stiffening is an adaptation to the increased afterload, and the hemodynamic indices (AT and DT) may not only be used to estimate the RV afterload, but also to predict the ventricular wall stiffening.

In addition, the EM_{Low} is a measurement in the diastolic stress range and thus it has been adopted as the diastolic stiffness of the RV [9,42]. It is speculated that the EM_{Low} is mainly contributed by the myofiber stiffness, which is different than the EM_{High} that is measured in the high-strain range and contributed mostly by the collagen fiber stiffness [9,170,189]. We do not know why EM_{Low} and EM_{High} showed different degrees of correlations with the AT and DT, and future study should investigate if RV stiffening in different strain ranges may distinguish adaptive and maladaptive remodeling or is a response to different types of RV afterload (steady or pulsatile). Overall, the suggested relations between the pulmonary hemodynamics and

RV passive elasticity may imply new diagnostic markers for the assessment of RV function and should be further investigated in future preclinical and clinical studies.

8.5 Conclusions

In this study, we performed the *in vivo* RV function assessment and *ex vivo* RV mechanical measurements in healthy and PH ovine, and then investigated the relationship between the passive elasticity and RV function. We observed that the RV longitudinal elasticity was significantly correlated with the RV end-diastolic and end-systolic diameter/area, indicating a contribution of RV passive stiffness in the diastolic function. More importantly, the elastic modulus at the low strain range was correlated with the acceleration time, whereas the elastic modulus at the high strain range was correlated with the deceleration time. This suggests that the RV hemodynamic profile may be an alternative estimation of RV passive elasticity and can be explored as a useful marker for RV failure assessment. Overall, this study highlights the importance of the passive elastic properties of the RV in the progression of RV dysfunction.

CHAPTER 9: ALTERATIONS OF BIAXIAL VISCOELASTIC PROPERTIES OF THE RIGHT VENTRICLE AT REST AND EXERCISE CONDITIONS IN MONOCROTALINE RATS [8]

9.1 Introduction

Right ventricle (RV) failure is a fatal disease and contributes significantly to the mortality and morbidity in a variety of cardiovascular disease including pulmonary hypertension (PH), congenital heart disease and left heart failure with preserved ejection fraction [20–24]. However, there has been lack of effective treatment for these patients and it is due to an inadequate understanding of the structure-function relationship of the right ventricle (RV) in physiological and pathological conditions [20,21].

The biomechanical properties of the RV free wall are considered to have an impact on its organ function [30], and a recent rodent study has reported a correlation between the passive elastic modulus of the RV and the end-diastolic volume [9], which is often used as an index of RV function [32,315,316]. Furthermore, our own previous ovine study showed that RV elasticity is correlated with RV area and hemodynamic property [10]. These studies that directly relate the RV tissue biomechanics to clinically relevant hemodynamics, leading to a new point of view to link the tissue biomechanics with organ function to advance the understanding of biomechanical mechanism of RV failure.

It is well known that the ventricle is an anisotropic and viscoelastic material [28,29,58,102,175]. Such behavior indicates the tissue mechanical behavior is strain/stress dependent, and there are energies stored and dissipated during the deformation due to the tissue elasticity and viscosity, respectively. These energy expenditure events closely impact the use of flow energy (during filling) or metabolic energy from cardiomyocytes (during ejection) in ventricle dilation and contraction in physiological conditions (at rest or exercise). However, most previous studies on RV biomechanics have focused on the passive elasticity

[8] *This chapter will be submitted for publication. Currently is under preparation.*

[27,34,35,52,54,55,57,174]. A few studies that reported the viscoelastic behavior of the RV are either using an indentation test of the RV [239], or the tensile mechanical tests of neonatal RV [58] free walls or the papillary muscles [104,327]. Thus, the biaxial (2D) viscoelastic behavior the RV free wall in adults remains little investigated. Our group recently examined the passive RV biaxial viscoelasticity in adult sheep [175]. But only healthy samples were investigated; as a result, the changes in the viscoelastic behavior in failing RVs are not well understood.

It is found that the exercise capacity and tolerance are reduced in patients with RV failure. The healthy myocardium adapts to the increased loading on the heart during exercise by increasing stroke volume and heart rate, thus increasing the cardiac output (CO). However, in patients with heart failure with preserved ejection fraction (HFpEF), this adaptation (increase in the CO) was not seen [328]. And the HFpEF patients displayed an impaired enhancement of RV systolic and diastolic function, as well as a lower increased in stroke volume, heart rate, and cardiac output compared to healthy controls [328]. Furthermore, Tricuspid annular plane systolic excursion (TAPSE) is another metric for determining RV systolic function, and it is often used to measure the contractile reserve of RV in exercise [328]. A clinical study found that the HFpEF patients without RV dysfunction had a TAPSE of 16mm or higher and exhibited preserved or improved contractile reserve during exercise. However, severe HFpEF patients with RV dysfunction had a TAPSE less than 15.5mm and exhibited reduced contractile reserve during exercise [329]. These results suggest that RV dysfunction is associated with an impaired cardiac reserve in response to exercise and the patients with RV failure may not be able to adapt to the increased myocardial demand at exercise. However, whether the impaired exercise capacity of the RV is associated with any impairment in the RV mechanical properties (viscoelasticity) has not been explored.

The goal of this study was to investigate the alterations of RV biaxial viscoelastic behavior with PH development at both rest and exercise conditions. We hypothesize that the remodeling in pulmonary hypertensive RVs leads to changes in anisotropic and viscoelastic properties of the RV free wall, and the diseased RV has distinct viscoelastic changes in response to exercise condition than the healthy RV. This

is the first study to investigate the changes of the anisotropic and viscoelastic mechanical properties of the RV free wall in physiological and pathological states. Furthermore, we applied a power-law model to capture the RV viscoelastic behavior in both healthy and disease groups and at rest and exercise conditions. We observed that PH increased RV viscoelasticity in both longitudinal (outflow tract) and circumferential directions. The increase in viscosity was similar between directions, whereas the increase in elasticity was greater in the longitudinal direction, leading to a more anisotropic elastic behavior of the RV. The RV viscoelasticity was also altered from resting to exercised conditions – the damping capacity (ratio of dissipated energy to total energy) was decreased in healthy RVs but not in diseased RVs, indicating an impaired adaption to exercise. Furthermore, various nonlinear viscoelastic behaviors of the RV were observed with PH development and in exercised conditions. Lastly, compared to the RV elasticity and viscosity, damping capacity is a better indicator for RV function than elasticity or viscosity alone. These novel findings will improve our understanding of RV biomechanics in response to RV failure progression or increased heart rates from rest to exercise conditions and offer more insights into the reduced exercise capacity in RV failure patients.

9.2 Material and Methods

9.2.1 Animal model and in vivo measurement

All procedures were approved by Institutional Animal Care and Use Committee (IACUC #1438) at Colorado State University. The monocrotaline (60 mg/kg) was injected subcutaneously into 6-week-old male Sprague Dawley rats for 3 weeks to induce PH (MCT). Similar healthy rats were used as controls (CTL). One or two days before the euthanasia, the RV function was obtained by *in vivo* 2D echocardiography. The *in vivo* echocardiography measurement was performed using Philips Ultrasound (XX; transducer) before the euthanasia for both CTL and MCT groups to assess right ventricular function. Briefly, rats were anesthetized using inhaled isoflurane (0.5-2%) and then subjected to transthoracic echo. Ventricular dimensions and function such as end-diastolic diameter (EDD), end-systolic diameter (ESD), and fractional shortening (FS) were measured in the parasternal short-axis or the apical four-chamber view

in 2D M-mode. The pulmonary blood flow dynamics such as pulmonary arterial (PA) peak velocity ($V_{PA\ peak}$), PA acceleration time (AT), ejection time (ET) and RV filling peak velocity ($V_{RV\ max}$) was recorded using pulse wave Doppler echo. Prior to the mechanical tests, rats were euthanized by an *i.p.* injection of urethane (1.2 kg/mg) or CO_2 inhalation. After tissue harvest, RV hypertrophy was measured by the thickness of RV free wall and the Fulton index, which is the ratio of wet tissue weights calculated as RV/(LV+S), where LV is the left ventricle free wall and S is the septum [73,74].

9.2.2 Specimen preparation

Fresh hearts (N=12 for CTL and N=10 for MCT) were obtained from CTL and MCT male rats. The hearts were placed in cardioplegic solution on ice to maintain tissue viability [173] and mechanically tested within 3h after tissue harvest. The RV was dissected, and the out-flow tract direction was marked as the longitudinal direction and its perpendicular direction was defined as the circumferential direction. The samples were then placed in cardioplegic solution combined with 30mM of 2,3-butanedione monoxime (BDM) at body temperature for at least 30 min to ensure muscle relaxation. The tissues were immersed in the same solution during the mechanical tests.

9.2.3 Ex vivo biaxial stress relaxation mechanical tests

After mounting, the equibiaxial stress relaxation tests were performed after the tissues were preloaded and preconditioning by using a newly established in-house biaxial testing system [330]. Two sets of stress relaxation tests were included in this study: 1) using different ramp speeds mimicking the sub-physiological and physiological heart rates at rest and exercise conditions (0.1, 1, 2, 5 and 8Hz) at the fixed strain level (20%); and 2) using different strain levels (6, 9, 12 and 15%) at the fixed ramp speeds selected to mimic the diastolic strain-rates (5 and 8Hz). Between each test, a resting time, which was ten times that of the previous testing period, was included to ensure that the tissue was fully recovered from the previous test. Biaxial stretch forces were obtained by 5 lb load cells (Honeywell) at a sampling frequency of 200 Hz, and the engineering stress (σ) was calculated as the force divided by the initial cross-section area of the tissue. The relaxation modulus was derived as the stress divided by the strain (a fixed value) as a function

of time, and the normalized stress curve, which is the ratio of the stress to the maximal stress (σ/σ_{max}) as function of time [175], was used to derive the tissue's viscous index. Furthermore, from the raw data, we derived the stored energy (W_s) as the area beneath the stress relaxation curve and dissipated energy (W_d) as the area between the stress relaxation curve and the theoretical curve of a purely elastic material at a fixed time of the relaxation (**Fig. 9.1**). We then further derived the damping capacity as $W_d/(W_d+W_s)$ to evaluate the mechanical energy efficiency during tissue deformation. The stored and dissipated energies, damping, relaxation modulus and the viscous index were measured at five different time points (0.01, 0.1, 1, 10 and 100s) to indicate the tissue viscoelasticity at different time scales.

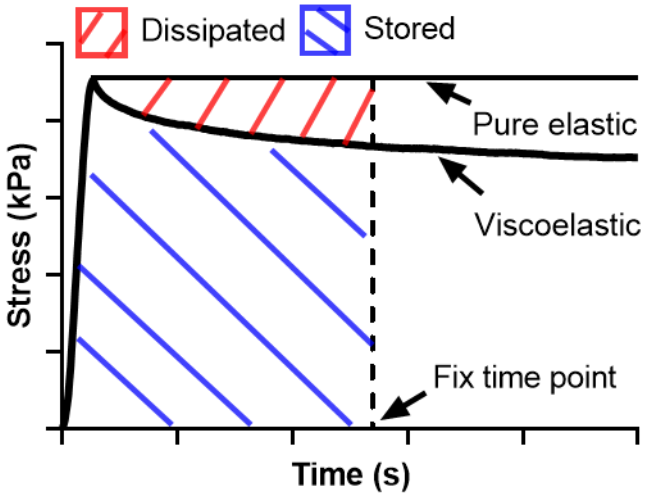

Fig. 9.1. The definitions of stored energy and dissipated energy at any fixed time point from the stress relaxation curve.

9.2.4 Model fitting: power-law fitting procedure

We then applied the power-law viscoelastic model to the experimental data to characterize the strain-dependent relaxation response as described previously [237]. Briefly, **Eq. 9.1** was used to capture the strain- dependent behavior of the relaxation function.

$$\sigma(\mathbf{E}, t) = \sigma_0(\mathbf{E})t^{m(\mathbf{E})} \quad (9.1)$$

where $\sigma_0(\mathbf{E})$ and m are the initial stress and relaxation rate, respectively, and $\mathbf{E}$ is the strain tensor. We further transformed **Eq. 9.1** to a logarithmic scale and plotted and performed the linear fitting that includes all strain levels simultaneously. The log of the initial stress ($\sigma_0(\mathbf{E})$) and relaxation rate (m) were calculated,

which are the ordinate intercept and the slope of the fitted line. Furthermore, we plotted the initial stress and relaxation rate as a function of strain and performed the curve fitting. The fitting results were used to reveal the relation between the modeling parameters, and the strain level used in stress relaxation.

9.2.5 Statistical analysis

Comparisons between groups (CTL and MCT), directions (longitudinal and circumferential), strain levels (3, 6, 9, 12 and 15%), frequencies (0,1, 1, 2, 5 and 8) and time constants (0.01, 0.1, 1, 10 and 100s) were performed with the paired Student's t-test. Pearson correlation analysis was used to investigate the correlations between RV damping capacity and RV function measurement. The analyses were performed by using Microsoft Excel. Data are presented as mean ± SEM and $p<0.05$ was considered statistically significant.

9.3 Results

9.3.1 RV failure establishment and structural changes in MCT rats

From the *in vivo* echocardiography measurement, we observed significant abnormalities with enlarged RV chamber size (EDD and ESD), reduced contractile function (FS), pulmonary artery (PA) outflow characteristics and the filling peak velocity (**Table. 9.1**). These results indicate the establishment of RV failure in the MCT rats. From the tissue measurement, we observed significant increases in the RV free wall thickness and the Fulton index in the MCT group compared to the control group, which indicated RV hypertrophy in the MCT group (**Table. 9.1**).

Table 9.1: Summary of the in vivo functional and ex vivo tissue measurements for both groups. Data were present as mean ± SEM.

Echocardiography	Control (N = 8)	MCT (N = 8)
RV EDD (cm)	0.16 ± 0.01	0.30 ± 0.03 **
RV ESD (cm)	0.09 ± 0.01	0.22 ± 0.02 **
RV Fractional Shortening (%)	41.50 ± 1.66	27.09 ± 3.20 **
Acceleration Time (AT) (s)	0.03 ± 0.002	0.02 ± 0.001 **
Ejection Time (ET) (s)	0.07 ± 0.001	0.07 ± 0.002
AT/ET	0.40 ± 0.02	0.23 ± 0.02 **
Peak Velocity during Filling (cm/s)	70.88 ± 2.79	91.00 ± 2.88 **
Structure Measurement	**Control (N = 12)**	**MCT (N = 10)**
Wall Thickness (mm)	0.81 ± 0.05	1.19 ± 0.09 **
Fulton Index (%)	0.23 ± 0.01	0.56 ± 0.06 **

** : < 0.01 vs CTL.

9.3.2 Stretch-rate dependent viscoelastic behavior altered by PH

We firstly investigated the frequency-dependent viscoelastic behavior quantified by the relaxation modulus and viscous index. Due to the physiological heart rates of rats, we treated the tests obtained from 0.1, 1 and 2 Hz as in the sub-physiological range whereas the tests obtained from 5 and 8 Hz as in the physiological range. Furthermore, we treated the 5Hz as the rest condition and 8Hz as the exercise condition. The data obtained at early time points (e.g., 0.01s after peak force) were considered to represent the short-term viscoelastic behavior of the RV and those obtained at later time points (e.g., 100s after peak force) were considered to represent long-term viscoelastic behavior of the RV.

Figure 9.2 shows significant frequency-dependent changes in the relaxation modulus and viscous index measured at 0.01s after the peak force in both control and MCT groups. Similar frequency-dependent behavior were observed at other time points (0.1, 1, 10 and 100s, data not shown). Firstly, all curves from the MCT group were above those from the control group, indicating increased viscoelasticity in the MCT group. We will further present the detailed changes in the next section (§9.3). In the control group, the relaxation modulus and viscous index in the longitudinal direction presented a biphasic change as frequency increased; but this behavior was absent in the MCT group in the same direction (**Fig. 9.2A&C**). Both groups presented monotonically decreased relaxation modulus and viscous index with the increasing testing in the

circumferential direction (**Fig. 9.2B&D**). Therefore, PH altered the frequency-dependent viscoelastic behavior of the RV only in the longitudinal direction.

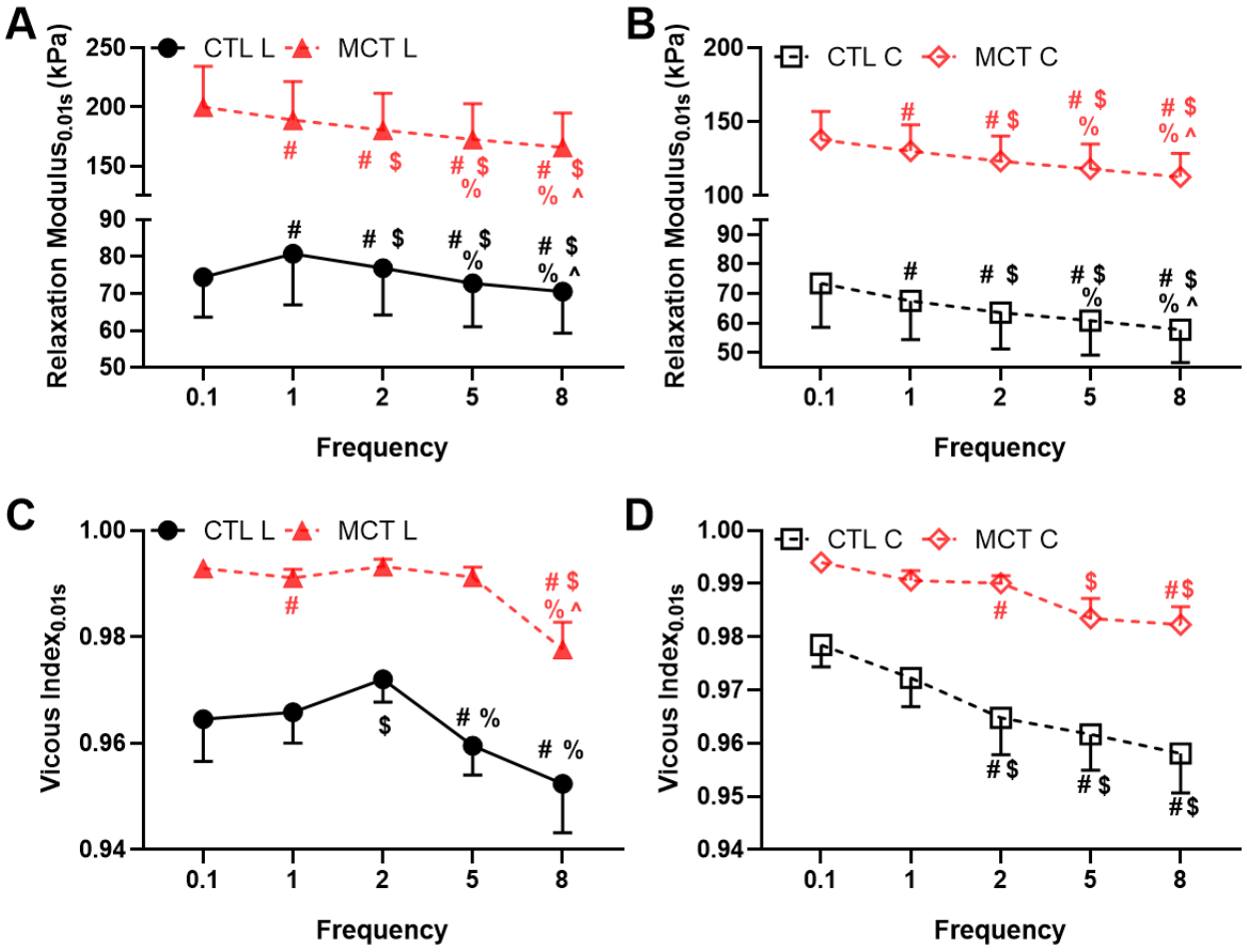

Fig. 9.2. Frequency-dependent changes in the relaxation modulus and viscous index at 0.01s after peak force. (A&B): relaxation modulus in longitudinal and circumferential directions for both groups, respectively; (C&D): viscous index in L and C directions for both groups, respectively. $^{\#}$ < .05 vs 0.1Hz, respectively, $^{\$}$ < .05 vs 1Hz, respectively, $^{\%}$ < .05 vs 2Hz, respectively, $^{\wedge}$ < .05 vs 5Hz, respectively.

9.3.3 PH increased RV biaxial viscoelasticity and enhanced the elastic anisotropy

Next, we focus on the RV biaxial viscoelasticity obtained from 5 and 8Hz since these data are more physiologically relevant. We presented the data at 0.01s after the peak force as similar trends were observed at other time points. As shown in **Figure 9.3A**, we observed that the MCT RV had increased relaxation modulus (an indicator of elasticity) than the control RV in both directions, and the MCT RV became anisotropic in elasticity with PH development. These differences were found in both rest and exercise

conditions. Similarly, we observed that MCT RV had increased viscous index (an indicator of viscosity) than the control RV in both directions, but there was no differences in viscosity between directions for both groups. These changes were observed in both rest and exercise conditions (**Fig. 9.3B**). These results indicate that PH increases RV tissue elasticity and viscosity in both directions and only enhances the RV elastic anisotropy.

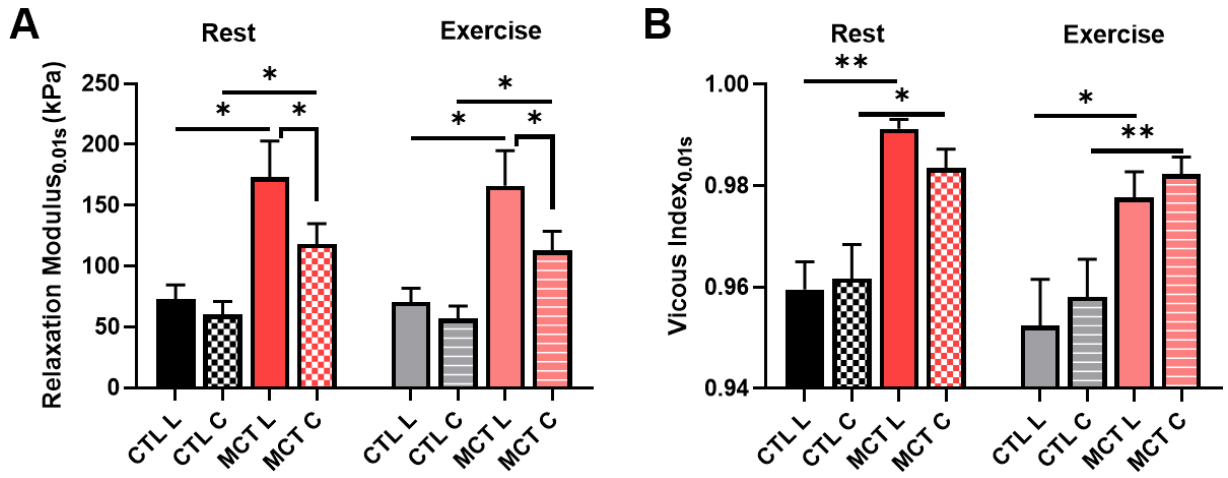

Fig. 9.3 Changes of RV viscoelasticity during PH. (A): increased RV elasticity during PH; (B): increased RV viscosity during PH. * < .05, ** < .01, respectively.

9.3.4 PH decreased RV damping capacity in both directions

We have shown previously that both elasticity and viscosity of the RV were increased with PH development, it is unclear if these increases were equivalent or not. To evaluate the relevant changes between viscosity and elasticity, we examined the damping capacity changes during PH. This parameter also quantifies the mechanical efficiency of the tissue as it is derived as the percentage of dissipated (wasted) energy to the total energy applied to the tissue during the deformation. We observed that the MCT RV had decreased damping capacity (obtained at 0.01 after peak force) than the control RV in both directions, and the same changes were found in both rest and exercise condition (**Fig. 9.4A**). Similar trends of changes were observed at other time points (**Fig. 9.4B** and data not shown). Therefore, this is the first report that the PH-induced remodeling of the RV led to reduced damping capacity of the tissue. Lastly, we found that in the late stage of the relaxation (at 100s after peak stress), the RV damping capacity exhibited an anisotropic

behavior in both rest and exercise conditions (**Fig. 9.4B**). Such anisotropy was absent in earlier stage of the relaxation.

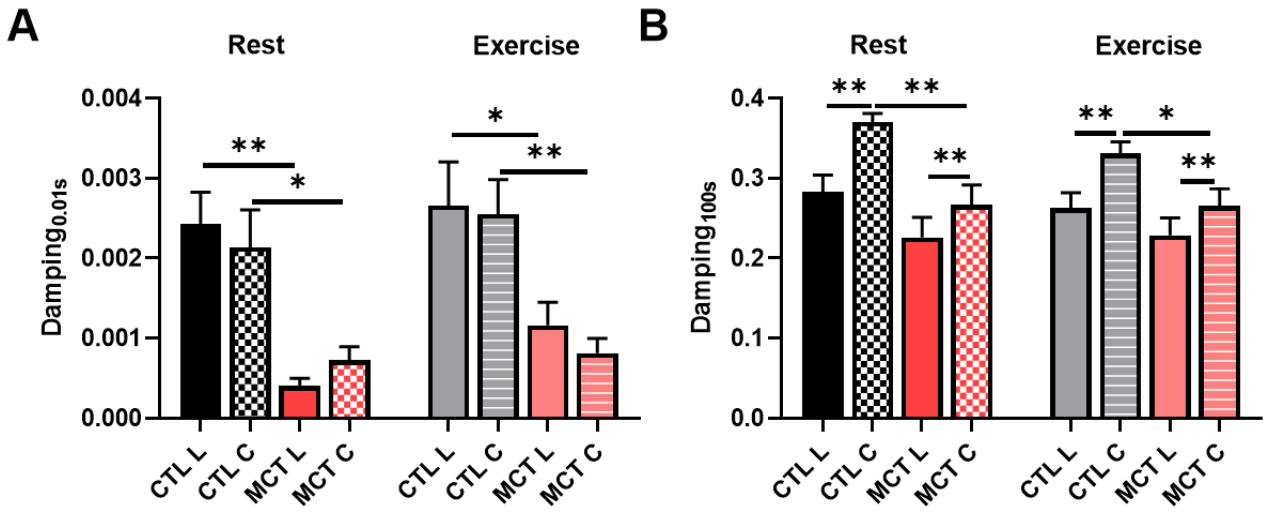

Fig. 9.4 Changes in damping capacity of the RV after PH development quantified at 0.01s and 100s after peak force. Decreased RV damping for both resting and exercise conditions for (A) at 0.01s and (B) at 100s. * < .05, ** < .01, respectively.

9.3.5 Exercise reduced the damping capacity of healthy but not MCT RVs

We further investigated the changes in the damping capacity with exercise for both CTL and MCT groups. We observed that except for the 0.01s after peak force, exercise induced decreased damping capacity in one or both directions in the CTL group at all later stages of the relaxation (**Fig. 9.5**). But in the MCT group, the decrease in damping capacity with exercise was absent in most stages of the relaxation except at 10s after peak force. There was even an increase of the damping capacity by exercise at 0.01s after peak force (**Fig. 9.5A**). These results suggest that the PH induced different responses in energy expenditure in the RV under the exercise condition.

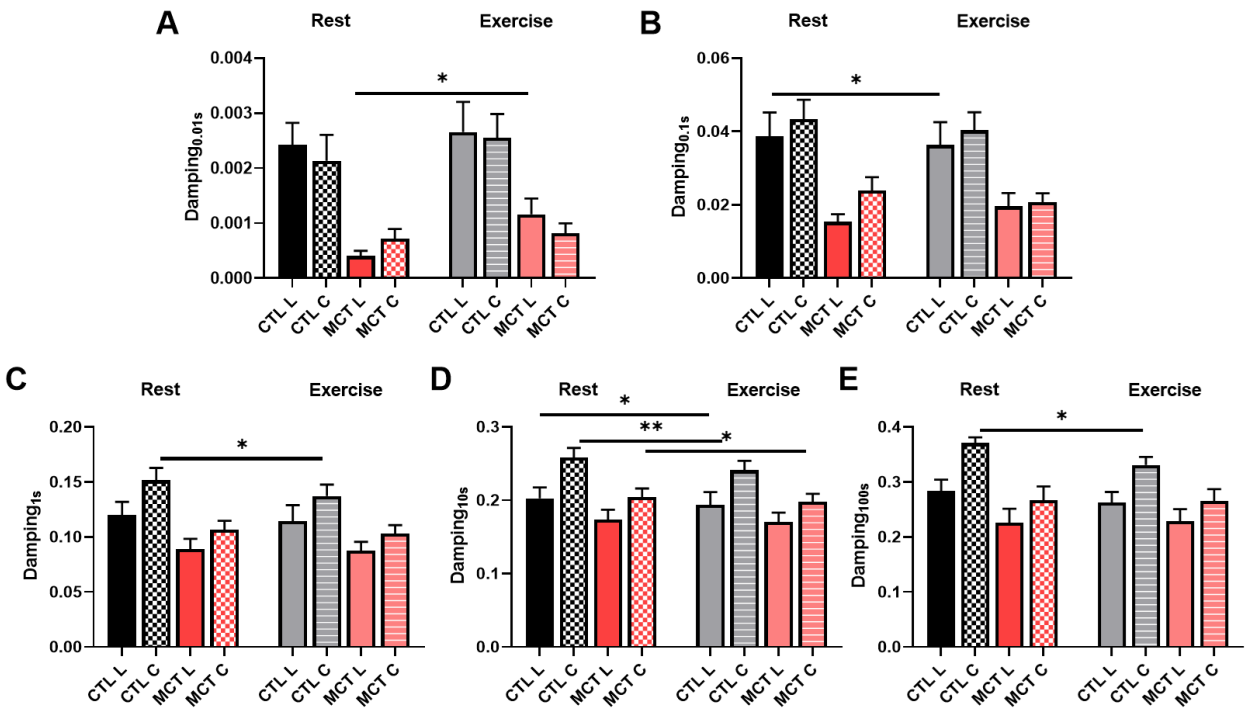

Fig. 9.5 Changes in RV damping capacity during exercise at different stages (time points) of the relaxation. * < .05, ** < .01, respectively.

9.3.6 Correlation between the RV viscoelastic properties and in vivo measurements

We further performed the Pearson correlation analysis to investigate the relationships between the viscoelastic parameter and the echocardiography measurements to explore potential implications of RV viscoelasticity. In both directions, we observed that the RV damping capacity was significantly correlated with the RV EDD, PA AT and AT/ET (**Fig. 9.6**) at almost all stages of relaxation (except for a later time points in the circumferential or longitudinal direction). More details of the correlations between the RV damping capacity and the *in vivo* measurements at various time points are shown in **Table 9.2**. It is worthy of note that neither the elasticity nor viscosity of the RV derived from the stress relaxation was correlated with any of these *in vivo* measurement parameters. These findings suggest that the damping capacity is a better indicator for RV function than the RV elasticity or viscosity alone.

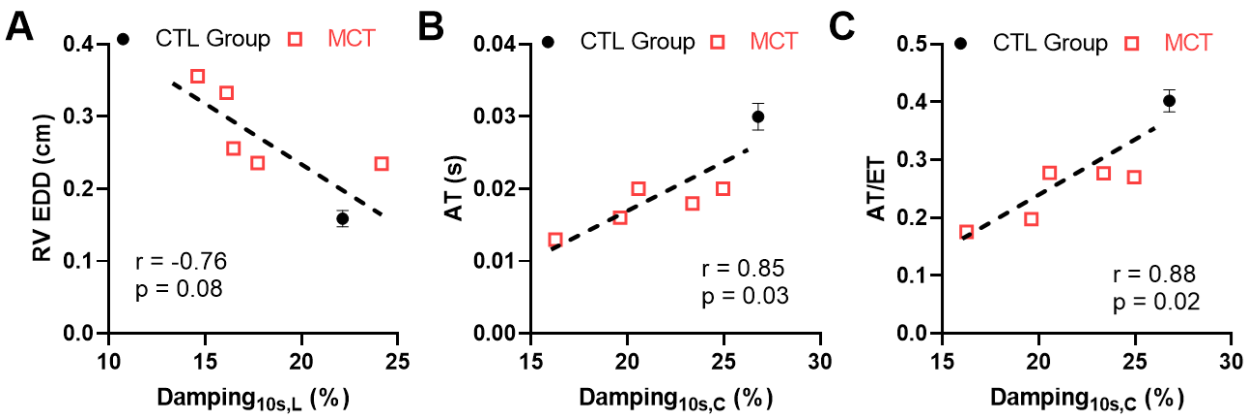

Fig. 6 Significant correlations between the RV damping capacity at 10s after peak force and (A) RV end diastolic diameter in the longitudinal direction, or (B) acceleration time in the circumferential direction, or (C) ratio of acceleration time and ejection time in the circumferential direction. The CTL group data were included as the average measurement (n=8) and the error bar shows the standard error. The MCT group data were included as individual data points (n=5).

Table 9.2: Correlations between the damping capacity and the echocardiography measurements obtained from control and MCT groups. The viscoelastic parameter (damping) was obtained at various time points of the relaxation and in longitudinal (L) and circumferential (C) directions.

Damping Capacity		RV EDD	RV ESD	RV FS	PA Vmax	AT	ET	AT/ET	Filling Time	Filling Vmax
At 0.01s	L	NS	NS	NS	NS	*	NS	*	NS	*
	C	NS	NS	NS	NS	**	NS	*	NS	p = 0.06
At 0.1s	L	*	NS	NS	NS	**	NS	*	NS	NS
	C	p = 0.09	NS	NS	NS	*	NS	*	NS	p = 0.05
At 1s	L	*	NS	NS	NS	p = 0.06	NS	NS	NS	NS
	C	p = 0.09	NS	NS	NS	*	NS	*	NS	p = 0.07
At 10s	L	p = 0.07	NS	NS	NS	NS	NS	NS	NS	NS
	C	NS	NS	NS	NS	*	NS	*	NS	NS
At 100s	L	p = 0.08	NS	NS	NS	NS	NS	NS	NS	NS
	C	NS	NS	NS	NS	*	NS	*	NS	p = 0.1

* < .05, ** < .01, respectively.

9.3.7 Altered nonlinear viscoelastic behavior of the RV by PH or exercise condition

From the second set of mechanical tests (at various strains), we investigated the type of RV viscoelastic behavior for both groups. We observed significant strain-dependent behavior of the relaxation rate in both groups, and in both rest and exercised conditions (**Fig. 9.7**), which indicates that all types of RVs exhibit a fully NLV behavior. Moreover, the shape of the strain-dependent curve was different between healthy and diseased groups, between rest and exercised conditions, as well as between directions at certain strain levels. This indicates that the RV tissue has varied biaxial NLV behaviors in different states (healthy vs. diseased, rest vs. exercise). Therefore, it is necessary to measure the corresponding tissue mechanical behavior in the specific physiological condition.

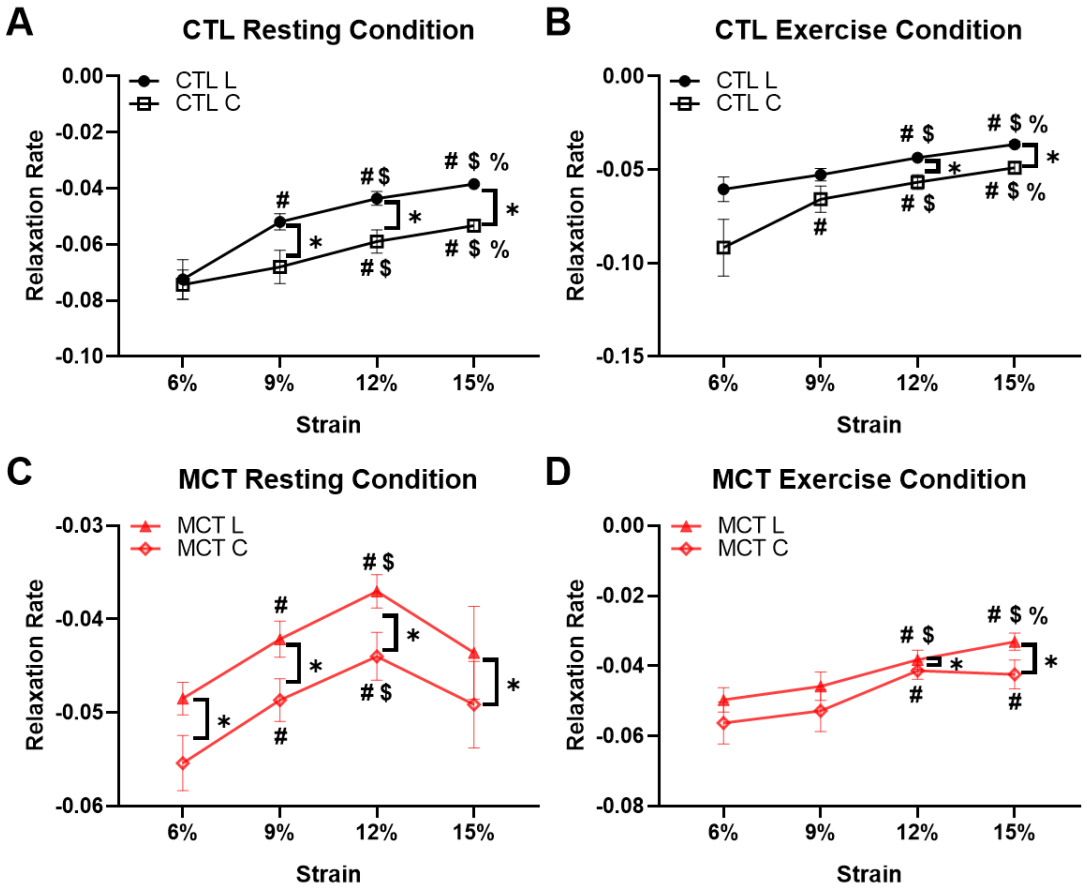

Fig. 9.7. Different strain-dependent and anisotropic behaviors measured by the relaxation rate between the healthy and MCT groups in rest and exercise conditions. (A&B): Strain-dependent relaxation rate of the CTL group at rest and exercise conditions, respectively; (C&D): Strain-dependent relaxation rate of the MCT group at rest and exercise conditions, respectively. $^{\#}$ < .05 vs 6%, respectively, $^{\$}$ < .05 vs 9%, respectively, $^{\%}$ < .05 vs 12%, respectively, * < .05, respectively.

9.3.8 Power-law modeling shows different types of strain dependence in PH or exercise conditions

Using the fitting parameters from the power-law model, we investigated the dependence of these parameters on the induced strain level using either linear or quadratic relations. From the relations with a good fitting (R^2>0.8), we found that the CTL group and MCT group had different fitting equations, which indicate different strain-dependent viscoelastic behavior. Similarly, the fitting equations were different from rest to exercise conditions, indicating that exercise induced altered strain-dependent viscoelastic behavior of the RV. Finally, different fitting equations were observed between the two directions in certain groups (e.g., the initial stress-strain relations in the MCT group at rest condition), which indicates anisotropic viscoelastic behavior of the RV in this group. Therefore, these data showed that the RV viscoelasticity exhibited different types of strain dependence in PH or exercise conditions.

Moreover, we found that at rest, the linear relation provided sufficient fitting to capture the strain-dependent behavior for the CTL group but led to a poor fitting for the MCT group. Thus, a quadratic fitting was needed to describe the relationship between the relaxation rate and strain for the MCT group (**Table 9.3**). These data suggest that at rest, the healthy RV viscoelasticity has a linear dependence on the strain, whereas the diseased RV viscoelasticity has a nonlinear (quadratic) dependence on strain. In exercise condition, either linear relation or nonlinear relation provided sufficient fitting to capture the relationship between the relaxation rate and strain for both CTL and MCT groups (**Table 9.3**).

Table 9.3: The fitted parameters (relaxation rate and initial stress) as a function of strain level (ε) derived from the power-law model. Different linear and quadratic fit equations are shown, which represent different strain-dependent viscoelastic behaviors of the RV in different conditions (healthy vs. diseased, rest vs. exercise).

			Linear fit	**R^2**	**Quadratic fit**	**R^2**
Resting Condition						
CTL	Relaxation Rate	Longitudinal	$0.0037\varepsilon - 0.09$	0.91	$-0.0004\varepsilon^2 + 0.013\varepsilon - 0.13$	0.99
		Circumferential	$0.0024\varepsilon - 0.09$	0.99	$-0.00002\varepsilon^2 + 0.003\varepsilon - 0.09$	0.99
	Initial Stress (kPa)	Longitudinal	$0.54\varepsilon - 2.64$	0.93	$0.056\varepsilon^2 - 0.64\varepsilon + 2.9$	>0.99
		Circumferential	$0.50\varepsilon - 2.56$	0.94	$0.048\varepsilon^2 - 0.51\varepsilon + 2.20$	>0.99
MCT	Relaxation Rate	Longitudinal	$0.0007\varepsilon - 0.05$	0.29	$-0.0004\varepsilon^2 + 0.0082\varepsilon - 0.085$	0.92
		Circumferential	$0.0008\varepsilon - 0.06$	0.42	$-0.0003\varepsilon^2 + 0.0077\varepsilon - 0.09$	0.95
	Initial Stress (kPa)	Longitudinal	$1.03\varepsilon - 3.6$	0.99	$-0.0065\varepsilon^2 + 1.16\varepsilon - 4.25$	0.99
		Circumferential	$0.56\varepsilon - 1.67$	0.95	$-0.0261\varepsilon^2 + 1.11\varepsilon - 4.26$	0.97
Exercise Condition						
CTL	Relaxation Rate	Longitudinal	$0.0027\varepsilon - 0.08$	>0.99	$-0.00002 + 0.0031\varepsilon - 0.08$	>0.99
		Circumferential	$0.0046\varepsilon - 0.11$	0.91	$-0.0005 + 0.015\varepsilon - 0.16$	0.99
	Initial Stress (kPa)	Longitudinal	$0.50\varepsilon - 2.14$	0.93	$0.052\varepsilon^2 - 0.59\varepsilon + 3.0$	>0.99
		Circumferential	$0.49 - 2.42$	0.93	$0.05\varepsilon^2 - 0.57\varepsilon + 2.58$	>0.99
MCT	Relaxation Rate	Longitudinal	$0.0019\varepsilon - 0.062$	0.98	$-0.0004\varepsilon^2 + 0.0011\varepsilon - 0.06$	0.99
		Circumferential	$0.0018\varepsilon - 0.067$	0.84	$-0.0001\varepsilon^2 + 0.004\varepsilon - 0.08$	0.87
	Initial Stress (kPa)	Longitudinal	$1.45\varepsilon - 7.26$	0.95	$0.125\varepsilon^2 - 1.17\varepsilon + 5.11$	>0.99
		Circumferential	$0.92\varepsilon - 4.60$	0.94	$0.08\varepsilon^2 - 0.9\varepsilon + 3.9$	>0.99

9.4 Discussion

To best of our knowledge, this is the first study that investigated the changes of RV viscoelasticity during RV failure progression. We observed that 1) PH increased RV viscoelasticity in both directions. The increase in viscosity was similar between directions, whereas the increase in elasticity was greater in the longitudinal direction, leading to a more anisotropic elastic behavior of the RV. 2) The RV viscoelasticity was altered from resting to exercised conditions – the damping capacity (ratio of dissipated energy to total energy) was decreased in healthy RVs but not in PH RVs, indicating impaired adaption to exercise. 3) Various nonlinear viscoelastic behaviors of the RV were observed with PH development or exercise condition. Lastly, 4) compared to the RV elasticity and viscosity, damping capacity is a better indicator for RV function than elasticity or viscosity alone. These findings will improve the understanding of RV biomechanics in response to pulsatile mechanical loadings at rest and exercise conditions and shed lights on the biomechanical mechanism of RV failure and the reduced exercise capacity.

9.4.1 PH altered the RV anisotropy

The hemodynamic measurement clearly demonstrated that RVF was established in the MCT rats (**Table 1**). Signs of RV failure was further evidenced by the dilation and hypertrophy in the RVs of the MCT group (**Table 9.1**). With the development of RVF, we found significant changes in the biaxial viscoelasticity of the tissue. In terms of the elasticity, we observed more increase in the longitudinal than circumferential direction (**Fig. 9.3A**). Thus, it led to an enhancement in the anisotropic, elastic behavior of the RV tissue. Interestingly, the RV viscosity increased similarly in both directions during PH development, and the viscous anisotropy was absent in the tissue before or after PH development.

Different changes in the RV elastic and viscous anisotropy may be contributed by different microstructural changes during PH. Prior studies have shown the re-orientation of the myofibers toward the long axis during PH progression, and the fiber re-orientation contributes to the changes in both RV diastolic and contractile function significantly [93,170,176,192]. The RV biaxial viscoelasticity is closely related to the amount and orientation of myo- and collagen fibers. It is well known that the tissue is the stiffest in the

main fiber direction, but the degree of tissue viscosity depends on the sources of frictional forces occurred during the expansion. When the fibers get re-aligned and closer to the longitudinal (outflow tract) direction during RV failure progression, the RV became more anisotropic and stiffer in this direction as well. In contrast, the sources of intra-molecular and inter-molecular frictions are diverse – from cytoskeletons (e.g. microtubules) in the cardiomyocytes to extracellular matrix proteins (e.g., collagen, proteoglycans) and even interstitial fluids, and there is no known preferred 'direction' of frictional sliding within the tissue. RV hypotrophy [179,282,283] and collagen accumulation are significant during PH development [179,309,310], and the remodeling process may enhance the frictional sources more uniformly in all directions of the tissue. Therefore, we observed enhanced viscosity (due to a larger frictional force) and this friction was direction independent; as a result, the RV had more viscosity without the alteration of the viscous anisotropy.

9.4.2 RVF impaired the adaption of the RV damping capacity to exercise

It seems there is a clearer role of damping capacity in the RV exercise capacity. In the present study, we exposed the RV tissue to exercise condition by increasing the stretch speed and examined the viscoelastic response of the tissue. Our results showed that when changed from the resting to exercise loadings, the healthy RV had decreased damping capacity whereas the MCT RV had no change or even increased damping capacity at early stage of relaxation (**Fig. 9.5**). It has been noted recently that the heart failure patients, including the RV failure patients, have reduced exercise tolerance [328]. That is, the exercise challenge imposes a negative impact on the RV function and the dysfunctional RV has poor cardiac reserve for exercise [328]. In response to the acute stress such as exercise, the ventricle typically contracts faster and stronger, thus leading to higher heart rate and stroke volume to increase the blood supply and meet the elevated metabolic demand. However, a clinical study showed that in the RV dysfunction patients with reduced exercise capacity, despite an increased heart rate, the increase in cardiac output was limited due to a weaker contractility [329]. Therefore, assuming the RV failure is associated with reduced exercise tolerance, we treat the reduction in damping capacity in healthy RVs as an adaptive response to exercise (to increase the mechanical energy efficiency temporarily), and the absence of change in damping capacity in the failing

RVs is considered as a loss of the capability to adapt to exercise, with more mechanical energy consumed by viscous dissipation and impaired energy efficiency under the acute stress.

Furthermore, a larger value indicates more energy waste or a relatively lower efficiency in mechanical energy use during the tissue deformation. Whether the reduced damping capacity is beneficial for cardiac cells or not is unclear. On one hand, the viscosity may provide a 'cushion' protection to the cardiomyocytes and other cells and this may be more important when the tissue undergoes higher mechanical loads such as in the MCT group. On the other hand, the viscosity indicates some inefficiency of mechanical energy use, and it demands part of the filling or contractile force to be 'wasted/dissipated'. The physiological implications of the tissue viscoelasticity awaits further investigation.

9.4.3 PH altered the type of the RV viscoelastic behavior

Linear, quasi-linear and fully nonlinear are the three main type of viscoelastic behaviors. While all these three behaviors are time-dependent, the linear viscoelastic material exhibits linear elastic and linear viscous behavior, whereas the quasi-linear viscoelastic material exhibits nonlinear elastic and linear viscous behavior. The 'linear viscous behavior' can be revealed by showing the same shape of relaxation or creep curves at different strains. That is, the time-dependent behavior is strain-independent or separable between viscosity and elasticity [44,237]. In contrast, both elasticity and viscosity in a fully nonlinear viscoelastic material are strain-dependent, and the time-dependent behavior is not separable between viscosity and elasticity.

Our results here showed that the RV viscoelastic behavior remained nonlinear viscoelastic in different states (physiological or pathological) and in different heart rates (at rest and exercise). This means that for both healthy and diseased RVs, the tissue elasticity and viscosity are not separable and the RV exhibits fully NLV behavior. Moreover, we observed different shapes of the strain-dependent relaxation rate curves between healthy and diseased groups, between the two axes and between resting and exercise conditions (**Fig. 9.7**). These differences indicate that PH or exercise (increased heart rate) altered the RV

anisotropic strain-dependent NLV behavior, and it is important to obtain the tissue's dynamic mechanical behavior in the corresponding physiological condition.

9.4.4 Implications of RV viscoelasticity in RV function

In the present work, we performed some preliminary work to unravel the implications of the RV viscoelasticity in its physiological performance. The correlation between the passive elastic modulus of the RV in the longitudinal direction and the end-diastolic volume has been reported by a rodent study [9]. Similarly, correlations between the RV longitudinal elasticity and RV end-diastolic diameter and area were found by our group in a recent large animal study [10]. Compared to the RV elasticity, the RV viscoelasticity is much less studied and there is no study that investigated the changes of the RV viscoelasticity during PH. As a result, whether and how the RV viscoelasticity is associated with the RV function is still unknown. Our results showed some significant correlations between the RV damping capacity in the longitudinal direction and the in vivo parameters obtained from echocardiography; however, these correlations were absent for the RV elasticity indices (relaxation modulus and stored energy) and nearly absent for the RV viscosity indices (viscous index and dissipated energy). The discrepant results may be because of the different types of mechanical tests and/or testing conditions. The previous studies derived the tissue elasticity from the loading curve of cyclic tensile mechanical tests and using a sub-physiological stretch rate (quasi-static), whereas the RV elasticity within this study was derived from the stress relaxation with a ramp speed similar to the diastolic stretch rate in rat hearts. Our data highlight the necessity to obtain the mechanical behavior under physiological conditions and bring both tissue elasticity and viscosity in the same picture when assessing RV performance.

Furthermore, we firstly observed a correlation between RV damping capacity and RV EDD. The RV EDD has been used to indicate the severity and mortality of the RV failure patients. Thus, our result indicates that the RV damping capacity may potentially be used to indicate the severity of the RV failure. Our results also showed that the damping capacity was strongly correlated with the PA AT. Preclinical studies of PH subjects has reported a correlation between the ratio of systolic pulmonary artery pressure

(sPAP) to AT and pulmonary vascular resistance (afterload) [331]. The studies used AT and AT/ET to non-invasively estimate RV systolic pressure to indicate the severity of RV dysfunction. The correlations between AT or AT/ET and damping capacity found in this study again suggest that the RV damping capacity may be a potential indicator of the severity of RV dysfunction.

9.4.5 Limitation

All the data we used here were from male rat RV, and there might be a sex difference in the RV viscoelastic behavior that awaits future research. In this study, we mainly used increased heart rate (thus higher stretch speed at diastole) to mimic the blood filling in the exercise condition and characterize the passive mechanical properties. But it's possible that the maximal strain is also increased during exercise as a result of larger venous blood return. We expect the neglect of the maximal strain range change at exercise does not significantly affect our main findings as prior studies showed an increase of heart rate from resting to exercise conditions but the same stroke volume in pulmonary arterial hypertension patients [332]. The power-law model is only a simple model for soft tissue NLV behavior characterization and it prevents us to investigate the RV viscoelastic behavior at different stages of relaxation. Thus, a more comprehensive NLV constitutive model is needed. Furthermore, the sample size for our correlation analysis is small and we used the average value rather than the individual value for the CTL group, more samples and the correlation analysis use individual values are needed to strengthen our correlation findings.

9.5 Conclusion

To the best of our knowledge, this is the first study of the changes of the RV passive viscoelastic behavior during PH development. Our results from the *ex vivo* stress relaxation tests showed that PH increased RV viscoelasticity in both directions. The increase in viscosity was similar between directions, whereas the increase in elasticity was greater in the longitudinal direction, leading to a more anisotropic elastic behavior of the RV. The RV viscoelasticity was altered from resting to exercised conditions – the damping capacity (ratio of dissipated energy to total energy) was decreased in healthy RVs but not in PH RVs, indicating impaired adaption to exercise. RV has various nonlinear viscoelastic behaviors with PH

development or exercise condition. Lastly, compared to the RV elasticity and viscosity, damping capacity is a better indicator for RV function than elasticity or viscosity alone. These novel findings improve our understanding of RV biomechanics in response to pulsatile mechanical loadings under chronic pressure overload as well as in different physiological conditions. In addition, these findings will assist the development of RV simulation to capture both energy storage and energy dissipation functions and reveal new insights about the role of RV mechanics in RV function.

OVERALL CONCLUSIONS

The *ex vivo* mechanical testing protocols were established successfully and have been applied to multiple projects and led to multiple conferences' abstracts and talks, and publications (**Chapter 2**). By using the protocols, we firstly investigated the different static biaxial mechanical properties of the right and left ventricles in healthy adult ovine (**Chapter 3**). We found the unique static biomechanical behavior for the RV. We observed differences in the anisotropic behavior between the LV and RV, with the LV being stiffer in the longitudinal (OT) direction and the RV being stiffer in the circumferential (cross-OT) direction. Interventricular comparison showed that the RV was more compliant than the LV in the longitudinal direction and was stiffer than the LV in the circumferential direction, which suggests different impacts of passive mechanics of these ventricles on the blood filling during diastole. Moreover, type III collagen content was correlated with the low-strain elastic moduli in the longitudinal direction in both ventricles.

We then moved from static property to the dynamic property and investigated the different dynamic biaxial mechanical properties of the RV and LV in healthy adult ovine (**Chapter 4**). We found the unique dynamic mechanical behavior for RV. We found that the RV hysteresis had more significant changes from low to high frequencies than the LV hysteresis. Under the physiological frequency (1Hz), the LV was more anisotropic in its elasticity, whereas the RV was more anisotropic in its viscosity; moreover, the LV was stiffer than the RV in both directions whereas the RV was more viscous than the LV in the longitudinal direction. Lastly, the LV presented quasi-linear viscoelastic behavior in longitudinal direction only, whereas the RV had non-linear viscoelastic behavior in both directions.

After we collected the experimental data for both static and dynamic mechanical properties, we than developed and applied the constitutive studies for both static and dynamic mechanical properties and applied to the data we obtained in previous chapters. We firstly adapted and applied the constitutive modeling of hyperelastic mechanical behavior of both ventricles (**Chapter 5**). We included both Fung type model and structurally informed model. And we found the anisotropic properties obtained from the

experimental data were captured by the zero-load elastic moduli as well as the anisotropic parameter *K* derived from the four-parameter Fung type model. Furthermore, the results from the structurally informed model imply stiffer collagen fibers in the LV than the RV, which awaits further investigation.

We then adapted and applied the constitutive modeling of dynamic mechanical behavior of RV specifically (**Chapter 6**). We applied both quasi-linear viscoelastic (QLV) and fully nonlinear viscoelastic (NLV) approaches to our experimental data and the fitting results showed that the RV free wall had anisotropic and strain-dependent viscoelastic behavior, and the NLV model showed a higher predictive capacity in capturing the strain-dependent nature of the stress relaxation behavior than the QLV model. From the QLV fitting, the relaxation coefficient with largest time constant was larger than other coefficients at most strains, indicating a dominant role in the overall relaxation behavior from early to late diastole. In contrast, the relaxation coefficient with smallest time constant was large only at small strain, suggesting a pronounced effect only at early diastole. From the NLV fitting, the fitting parameters (relaxation rate and initial stress) showed quadratic polynomial relationships with the strain.

Lastly, we moved from healthy stage to disease stage and investigated the changes in RV biomechanics during pulmonary hypertension (PH) development. We firstly successfully established the animal-specific pulmonary artery constriction model to induce the PH for the ovine (**Chapter 7**). We than applied this model to induce the ovine PH and changes of RV elasticity during PH and the correlations between the RV passive elasticity and organ function (**Chapter 8**). We observed that the RV longitudinal elasticity was significantly correlated with the RV end-diastolic and end-systolic diameter/area, indicating a contribution of RV passive stiffness in the diastolic function. More importantly, the elastic modulus at the low strain range was correlated with the acceleration time, whereas the elastic modulus at the high strain range was correlated with the deceleration time.

We then moved from static property to dynamic property for the diseased object and investigated the alterations of the biaxial viscoelastic property of the RV at rest and exercise conditions in PH rats (**Chapter 9**). We found that PH altered the frequency-dependent viscoelastic behavior of the RV only in

the longitudinal direction. PH increased RV viscoelasticity in both directions; however, the increase in viscosity was similar between directions, whereas the increase in elasticity was greater in the longitudinal direction, which leading to more anisotropic elastic behavior of the RV. PH also decreased the damping capacity (ratio of dissipated energy to total energy) of RV in both directions. Furthermore, the RV viscoelasticity was also altered from resting to exercised conditions. The damping capacity was decreased in healthy RVs but not in PH RVs, indicating impaired adaption to exercise. The RV changed from nonlinear viscoelastic to quasi-linear viscoelastic behavior with PH development, and exhibited nonlinear viscoelastic behavior when exposed to exercised conditions. Lastly, our correlation results suggest that compared to the RV elasticity and viscosity, damping is a better indicator for the RV function.

The findings were obtained from both large and small animals' species, which are translational to human diseases and a strong addition to the current literature of RV failure. More importantly, the investigation on the viscoelastic (dynamic) mechanical properties of the RV and the changes of viscoelasticity in RV failure progression is highly novel. The constitutive modeling of the RV biaxial viscoelastic behavior is pioneering and unique in the computational study of the RV. In summary, this study will deepen the understanding of the biomechanical mechanisms of RV failure and assist with the development of new computational tools for diagnosis and treatment strategies.

FUTURE WORKS

The results and conclusions in this study are all based on *ex vivo* biaxial mechanical test, from one gender samples. Future study will perform the 3D measurement and include both male and female samples to have a more comprehensive understanding of the RV static and dynamic mechanical property. Furthermore, for the large animal studies, only different layers of the RV were tested, a study that cover the entire RV thickness is needed to investigate the potential transmural differences.

The modeling work done in this study were all for healthy experimental data. Future study will apply or revise the model to capture the diseased RV both static and dynamic mechanical behavior. Furthermore, the viscoelastic modeling work done in this study was focusing on quasi-linear approach with a simple version of the nonlinear approach. The future study will include a more comprehensive model that includes different time constants and more structural information such as the myo- and collagen fiber content to have a deeper understanding of the RV viscoelastic behavior at multiscale levels.

The discussion related with the implication of the RV mechanical property to its function were based on a relatively small sample size with the 2D in vivo function measurement. Future study will include more samples and more comprehensive in vivo measurements such as 3D echo and PV loop measurements.

Lastly, this study was mainly focusing on the fiber to tissue to organ levels, future study will include more investigation at cellular level to have a more complete view of the how RV mechanical behavior affects its function.

REFERENCES

1. Rapsomaniki, E. *et al. Blood pressure and incidence of twelve cardiovascular diseases: lifetime risks, healthy life-years lost, and age-specifi c associations in 1·25 million people. www.thelancet.com* vol. 383 http://www. (2014).
2. Nguyen-Truong, M., Wang, Z., Nguyen-Truong, M. & Wang, Z. Biomechanical Properties and Mechanobiology of Cardiac ECM. (2018) doi:10.1007/978-3-319-97421-7_1.
3. Kurashima, A. Amaging pathophysiology of tuberculosis. *Japanese J. Chest Dis.* **75**, 458–471 (2016).
4. Wang, Z., Lakes, R. S., Golob, M., Eickhoff, J. C. & Chesler, N. C. Changes in Large Pulmonary Arterial Viscoelasticity in Chronic Pulmonary Hypertension. *PLoS One* **8**, 78569 (2013).
5. M., L. B. & G., T. M. Alterations with Age in the Viscoelastic Properties of Human Arterial Walls. *Circ. Res.* **18**, 278–292 (1966).
6. Ricardo, A. *et al.* Effects of Hypertension on Viscoelasticity of Carotid and Femoral Arteries in Humans. *Hypertension* **26**, 48–54 (1995).
7. Labropoulos, N. *et al.* Viscoelastic properties of normal and atherosclerotic carotid arteries. *Eur. J. Vasc. Endovasc. Surg. Off. J. Eur. Soc. Vasc. Surg.* **19**, 221–225 (2000).
8. Tanaka, H. *et al.* Estimation of Arterial Viscosity Based on an Oscillometric Method and Its Application in Evaluating the Vascular Endothelial Function. *Sci. Rep.* **9**, 1–11 (2019).
9. Jang, S. *et al.* Biomechanical and Hemodynamic Measures of Right Ventricular Diastolic Function: Translating Tissue Biomechanics to Clinical Relevance. *J. Am. Hear. Assoc. Cardiovasc. Cerebrovasc. Dis.* **6**, e006084 (2017).
10. Liu, W. *et al.* Correlations between the right ventricular passive elasticity and organ function in adult ovine. *J. Integr. Cardiol.* **6**, 1–6 (2020).
11. null, null *et al.* Heart Disease and Stroke Statistics—2008 Update. *Circulation* **117**, e25–e146

(2008).

12. D., S. D. *et al.* Prevention of Heart Failure. *Circulation* **117**, 2544–2565 (2008).

13. M., L.-J. D. *et al.* Lifetime Risk for Developing Congestive Heart Failure. *Circulation* **106**, 3068–3072 (2002).

14. Ho, K. K. L., Pinsky, J. L., Kannel, W. B. & Levy, D. The epidemiology of heart failure: The Framingham Study. *J. Am. Coll. Cardiol.* **22**, A6–A13 (1993).

15. Schocken, D. D., Arrieta, M. I., Leaverton, P. E. & Ross, E. A. Prevalence and mortality rate of congestive heart failure in the United States. *J. Am. Coll. Cardiol.* **20**, 301–306 (1992).

16. Levy, D. *et al.* Long-Term Trends in the Incidence of and Survival with Heart Failure. *N. Engl. J. Med.* **347**, 1397–1402 (2002).

17. W., Y. C. *et al.* 2013 ACCF/AHA Guideline for the Management of Heart Failure. *Circulation* **128**, e240–e327 (2013).

18. Dhingra, A. *et al.* Epidemiology of Heart Failure with Preserved Ejection Fraction. *Curr. Heart Fail. Rep.* **11**, 354–365 (2014).

19. Owan, T. E. *et al.* Trends in Prevalence and Outcome of Heart Failure with Preserved Ejection Fraction. *N. Engl. J. Med.* **355**, 251–259 (2006).

20. Konstam, M. A. *et al.* On behalf of the American Heart Association Coun-cil on Clinical Cardiology; Council on Cardiovas-cular Disease in the Young; and Council on Cardiovascular Surgery and Anesthesia. *Circulation* **137**, 578–622 (2018).

21. Lahm, T. *et al.* Assessment of right ventricular function in the research setting: Knowledge gaps and pathways forward an official American thoracic society research statement. *Am. J. Respir. Crit. Care Med.* **198**, e15–e43 (2018).

22. Köhler, D., Arnold, R., Loukanov, T. & Gorenflo, M. Right Ventricular Failure and Pathobiology in Patients with Congenital Heart Disease – Implications for Long-Term Follow-Up. *Front. Pediatr.* **1**, (2013).

23. Haddad, F., Hunt, S. A., Rosenthal, D. N. & Murphy, D. J. Right ventricular function in

cardiovascular disease, part I: Anatomy, physiology, aging, and functional assessment of the right ventricle. *Circulation* **117**, 1436–1448 (2008).

24. Voelkel, N. F. *et al.* Right Ventricular Function and Failure Report of a National Heart, Lung, and Blood Institute Working Group on Cellular and Molecular Mechanisms of Right Heart Failure The Normal Right Ventricle The Right Ventricle in Pulmonary Hypertension Special Report. *Circulation* **114**, 1883–1891 (2006).

25. Golob, M., Moss, R. L. & Chesler, N. C. Cardiac tissue structure, properties, and performance: a materials science perspective. *Ann. Biomed. Eng.* **42**, 2003–2013 (2014).

26. Bellofiore, A. & Chesler, N. C. Methods for measuring right ventricular function and hemodynamic coupling with the pulmonary vasculature. *Ann. Biomed. Eng.* **41**, 1384–1398 (2013).

27. Sacks, M. S. & Chuong, C. J. Biaxial Mechanical Properties of Passive Right Ventricular Free Wall Myocardium. *J. Biomech. Eng.* **115**, 202–205 (1993).

28. Wang, Z., Golob, M. J. & Chesler, N. C. Viscoelas1. Wang Z, Golob MJ, Chesler NC. Viscoelastic Properties of Cardiovascular Tissues. In: Golob MJ, editor. Viscoelastic and Viscoplastic Materials [Internet]. Rijeka: IntechOpen; 2016. p. Ch. 7. Available from: http://www.intechopen.com/books/visc. in *Viscoelastic and Viscoplastic Materials* (ed. Golob, M. J.) Ch. 7 (IntechOpen, 2016). doi:10.5772/64169.

29. Nguyen-Truong, M. & Wang, Z. Biomechanical properties and mechanobiology of cardiac ECM. in *Advances in Experimental Medicine and Biology* vol. 1098 1–19 (2018).

30. Cansız, F. B. C., Dal, H. & Kaliske, M. An orthotropic viscoelastic material model for passive myocardium: theory and algorithmic treatment. *Comput. Methods Biomech. Biomed. Engin.* **18**, 1160–1172 (2015).

31. Liu, W. & Wang, Z. Current Understanding of the Biomechanics of Ventricular Tissues in Heart Failure. *Bioengineering* vol. 7 (2019).

32. Cheatham, M. L., Nelson, L. D., Chang, M. C. & Safcsak, K. Right ventricular end-diastolic volume index as a predictor of preload status in patients on positive end-expiratory pressure. *Crit. Care Med.*

26, (1998).

33. Fung, Y. C., Fronek, K. & Patitucci, P. Pseudoelasticity of arteries and the choice of its mathematical expression. *Am. J. Physiol. Circ. Physiol.* **237**, H620–H631 (1979).

34. Ghaemi, H., Behdinan, K. & Spence, A. D. In vitro technique in estimation of passive mechanical properties of bovine heart: Part I. Experimental techniques and data. *Med. Eng. Phys.* **31**, 76–82 (2009).

35. Sommer, G. *et al.* Biomechanical properties and microstructure of human ventricular myocardium. *Acta Biomater.* **24**, 172–192 (2015).

36. Yin, F. C. P., Strumpf, R. K., Chew, P. H. & Zeger, S. L. Quantification of the mechanical properties of noncontracting canine myocardium under simultaneous biaxial loading. *J. Biomech.* **20**, 577–589 (1987).

37. Humphrey, J. D., Strumpf, R. K. & Yin, F. C. P. Determination of a Constitutive Relation for Passive Myocardium: I. A New Functional Form. *J. Biomech. Eng.* **112**, 333–339 (1990).

38. Novak, V. P., Yin, F. C. P. & Humphrey, J. D. Regional mechanical properties of passive myocardium. *J. Biomech.* **27**, 403–412 (1994).

39. Lin, D. H. S. & Yin, F. C. P. A Multiaxial Constitutive Law for Mammalian Left Ventricular Myocardium in Steady-State Barium Contracture or Tetanus. *J. Biomech. Eng.* **120**, 504–517 (1998).

40. Gupta, K. B., Ratcliffe, M. B., Fallert, M. A., Edmunds, L. H. & Bogen, D. K. Changes in passive mechanical stiffness of myocardial tissue with aneurysm formation. *Circulation* **89**, 2315–2326 (1994).

41. Valdez-Jasso, D., Simon, M. A., Champion, H. C. & Sacks, M. S. A murine experimental model for the mechanical behaviour of viable right-ventricular myocardium. *J. Physiol.* **590**, 4571–4584 (2012).

42. Fatemifar, F., Feldman, M. D., Oglesby, M. & Han, H.-C. Comparison of Biomechanical Properties and Microstructure of Trabeculae Carneae, Papillary Muscles, and Myocardium in the Human Heart. *J. Biomech. Eng.* **141**, 021007 (2018).

43. Ooi, C. Y., Wang, Z., Tabima, D. M., Eickhoff, J. C. & Chesler, N. C. The role of collagen in extralobar pulmonary artery stiffening in response to hypoxia-induced pulmonary hypertension. *Am. J. Physiol. Circ. Physiol.* **299**, H1823–H1831 (2010).

44. Lakes, R. S. *Viscoelastic solids*. *Viscoelastic Solids* (CRC Press, 1998). doi:10.1201/9781315121369.

45. Fung, Y. C. What are the residual stresses doing in our blood vessels? *Ann. Biomed. Eng.* **19**, 237–249 (1991).

46. Xiaodan, S. *et al.* Epicardial prestrained confinement and residual stresses: a newly observed heart ventricle confinement interface. *J. R. Soc. Interface* **16**, 20190028 (2019).

47. Omens, J. H. & Fung, Y. C. Residual strain in rat left ventricle. *Circ. Res.* **66**, 37–45 (1990).

48. Genet, M. *et al.* Heterogeneous growth-induced prestrain in the heart. *J. Biomech.* **48**, 2080–2089 (2015).

49. Jöbsis, P. D. *et al.* The visceral pericardium: macromolecular structure and contribution to passive mechanical properties of the left ventricle. *Am. J. Physiol. Heart Circ. Physiol.* **293**, H3379–H3387 (2007).

50. Hoskins, P. R., Lawford, P. V. & Doyle, B. J. Cardiovascular Biomechanics. *Cardiovasc. Biomech.* 1–462 (2017) doi:10.1007/978-3-319-46407-7.

51. Demer, L. L. & Yin, F. C. Passive biaxial mechanical properties of isolated canine myocardium. *J. Physiol.* **339**, 615–630 (1983).

52. Hill, M. R. *et al.* Structural and Mechanical Adaptations of Right Ventricular Free Wall Myocardium to Pulmonary-Hypertension Induced Pressure Overload. *Ann. Biomed. Eng.* **42**, 2451–2465 (2014).

53. Sacks, M. *Biaxial Mechanical Evaluation of Planar Biological Materials*. vol. 61 (2000).

54. Holzapfel, G. A. & Ogden, R. W. Constitutive modelling of passive myocardium: A structurally based framework for material characterization. *Philos. Trans. R. Soc. A Math. Phys. Eng. Sci.* **367**, 3445–3475 (2009).

55. Humphrey, J. D., Strumpf, R. K. & Yin, F. C. Biaxial mechanical behavior of excised ventricular

epicardium. *Am. J. Physiol. Circ. Physiol.* **259**, H101–H108 (1990).

56. Javani, S., Gordon, M. & Azadani, A. N. Biomechanical Properties and Microstructure of Heart Chambers: A Paired Comparison Study in an Ovine Model. *Ann. Biomed. Eng.* **44**, 3266–3283 (2016).

57. Sirry, M. S. *et al.* Characterisation of the mechanical properties of infarcted myocardium in the rat under biaxial tension and uniaxial compression. *J. Mech. Behav. Biomed. Mater.* **63**, 252–264 (2016).

58. Ahmad, F. *et al.* Biomechanical properties and microstructure of neonatal porcine ventricles. *J. Mech. Behav. Biomed. Mater.* **88**, 18–28 (2018).

59. Ramo, N. L., Troyer, K. L. & Puttlitz, C. M. Viscoelasticity of spinal cord and meningeal tissues. *Acta Biomater.* **75**, 253–262 (2018).

60. Ramo, N. L., Puttlitz, C. M. & Troyer, K. L. The development and validation of a numerical integration method for non-linear viscoelastic modeling. *PLoS One* **13**, (2018).

61. Ramo, N. L. *et al.* Comparison of in vivo and ex vivo viscoelastic behavior of the spinal cord. *Acta Biomater.* **68**, 78–89 (2017).

62. Troyer, K. L. & Puttlitz, C. M. Nonlinear viscoelasticty plays an essential role in the functional behavior of spinal ligaments. *J. Biomech.* **45**, 684–691 (2012).

63. Troyer, K. L., Estep, D. J. & Puttlitz, C. M. Viscoelastic effects during loading play an integral role in soft tissue mechanics. *Acta Biomater.* **8**, 234–243 (2012).

64. Stella, J. A., Liao, J. & Sacks, M. S. Time-dependent biaxial mechanical behavior of the aortic heart valve leaflet. *J. Biomech.* **40**, 3169–3177 (2007).

65. Liao, J., Yang, L., Grashow, J. & Sacks, M. S. The Relation Between Collagen Fibril Kinematics and Mechanical Properties in the Mitral Valve Anterior Leaflet. *J. Biomech. Eng.* **129**, 78–87 (2006).

66. Little, R. & Wead, W. Diastolic viscoelastic properties of active and quiescent cardiac muscle. *Am. J. Physiol. Content* **221**, 1120–1125 (1971).

67. Tsaturyan, A. K., Izacov, V. J., Zhelamsky, S. V. & Bykov, B. L. Extracellular fluid filtration as the reason for the viscoelastic behaviour of the passive myocardium. *J. Biomech.* **17**, 749–755 (1984).

68. Miller, C. E., Vanni, M. A. & Keller, B. B. Characterization of passive embryonic myocardium by quasi-linear viscoelasticity theory. *J. Biomech.* **30**, 985–988 (1997).

69. Miller, C. E. & Wong, C. L. Trabeculated embryonic myocardium shows rapid stress relaxation and non-quasi-linear viscoelastic behavior. *J. Biomech.* **33**, 615–622 (2000).

70. Loeffler, L. & Sagawa, K. *A one dimensional viscoelastic model of cat heart muscle studied by small length perturbations during isometric contraction*. *Circulation Research* vol. 36 http://ahajournals.org (1975).

71. Faconti, L., Bruno, R. M., Ghiadoni, L. & Virdis, S. T. and A. Ventricular and Vascular Stiffening in Aging and Hypertension. *Current Hypertension Reviews* vol. 11 100–109 (2015).

72. Borlaug, B. A. *et al.* Longitudinal changes in left ventricular stiffness: a community-based study. *Circ. Heart Fail.* **6**, 944–952 (2013).

73. Wang, Z., Schreier, D. A., Hacker, T. A. & Chesler, N. C. Progressive right ventricular functional and structural changes in a mouse model of pulmonary arterial hypertension. *Physiol. Rep.* **1**, e00184 (2013).

74. Wang, Z. & Chesler, N. C. Pulmonary vascular mechanics: Important contributors to the increased right ventricular afterload of pulmonary hypertension. *Exp. Physiol.* **98**, 1267–1273 (2013).

75. Wang, Z. & Chesler, N. C. Pulmonary Vascular Wall Stiffness: An Important Contributor to the Increased Right Ventricular Afterload with Pulmonary Hypertension. *Pulm. Circ.* (2011) doi:10.4103/2045-8932.83453.

76. Tabima, D. M., Philip, J. L. & Chesler, N. C. Right ventricular-pulmonary vascular interactions. *Physiology* **32**, 346–356 (2017).

77. Ibrahim, E.-S. H. Myocardial tagging by Cardiovascular Magnetic Resonance: evolution of techniques–pulse sequences, analysis algorithms, and applications. *J. Cardiovasc. Magn. Reson.* **13**, 36 (2011).

78. Seo, Y., Ishizu, T. & Aonuma, K. Current status of 3-dimensional speckle tracking echocardiography: a review from our experiences. *J. Cardiovasc. Ultrasound* **22**, 49–57 (2014).

79. Voigt, J.-U. *et al.* Definitions for a common standard for 2D speckle tracking echocardiography: consensus document of the EACVI/ASE/Industry Task Force to standardize deformation imaging. *Eur. Hear. J. - Cardiovasc. Imaging* **16**, 1–11 (2014).

80. Bossone, E. *et al.* Echocardiography in Pulmonary Arterial Hypertension: from Diagnosis to Prognosis. *J. Am. Soc. Echocardiogr.* **26**, 1–14 (2013).

81. Leng, S. *et al.* Three-Dimensional Tricuspid Annular Motion Analysis from Cardiac Magnetic Resonance Feature-Tracking. *Ann. Biomed. Eng.* **44**, 3522–3538 (2016).

82. Zou, H. *et al.* Quantification of Biventricular Strains in Heart Failure With Preserved Ejection Fraction Patient Using Hyperelastic Warping Method. *Front. Physiol.* **9**, 1295 (2018).

83. Genet, M. *et al. Finite Element Digital Image Correlation for Cardiac Strain Analysis from 3D Whole-Heart Tagging*. https://hal.archives-ouvertes.fr/hal-01571506 (2016).

84. Genet, M., Stoeck, C. T., von Deuster, C., Lee, L. C. & Kozerke, S. Equilibrated warping: Finite element image registration with finite strain equilibrium gap regularization. *Med. Image Anal.* **50**, 1–22 (2018).

85. Phatak, N. S. *et al.* Strain measurement in the left ventricle during systole with deformable image registration. *Med. Image Anal.* **13**, 354–361 (2009).

86. H.N.T., F. *et al.* Computational quantification of patient specific changes in ventricular dynamics associated with pulmonary hypertension. *Am. J. Physiol. Heart Circ. Physiol.* (2019) doi:http://dx.doi.org/10.1152/ajpheart.00094.2019.

87. Khan, S., Fakhouri, F., Majeed, W. & Kolipaka, A. Cardiovascular magnetic resonance elastography: A review. *NMR Biomed.* **31**, e3853–e3853 (2018).

88. Arani, A. *et al.* Cardiac MR elastography for quantitative assessment of elevated myocardial stiffness in cardiac amyloidosis. *J. Magn. Reson. Imaging* **46**, 1361–1367 (2017).

89. Fan, L., Yao, J., Yang, C., Tang, D. & Xu, D. Infarcted Left Ventricles Have Stiffer Material Properties and Lower Stiffness Variation: Three-Dimensional Echo-Based Modeling to Quantify In Vivo Ventricle Material Properties. *J. Biomech. Eng.* **137**, 81005 (2015).

90. Mojsejenko, D. *et al.* Estimating passive mechanical properties in a myocardial infarction using MRI and finite element simulations. *Biomech. Model. Mechanobiol.* **14**, 633–647 (2015).

91. Tang, D., Yang, C., Geva, T. & Del Nido, P. J. Patient-specific MRI-based 3D FSI RV/LV/patch models for pulmonary valve replacement surgery and patch optimization. *J. Biomech. Eng.* **130**, 41010 (2008).

92. Acosta, S. *et al.* Cardiovascular mechanics in the early stages of pulmonary hypertension: a computational study. *Biomech. Model. Mechanobiol.* **16**, 2093–2112 (2017).

93. Avazmohammadi, R. *et al.* A Computational Cardiac Model for the Adaptation to Pulmonary Arterial Hypertension in the Rat. *Ann. Biomed. Eng.* **47**, 138–153 (2019).

94. Xi, C. *et al.* Patient-Specific Computational Analysis of Ventricular Mechanics in Pulmonary Arterial Hypertension. *J. Biomech. Eng.* **138**, (2016).

95. Humphrey, J. D. (Jay D. *Cardiovascular solid mechanics : cells, tissues, and organs* . (Springer, 2002).

96. Fan, R., Tang, D., Yao, J., Yang, C. & Xu, D. 3D Echo-Based Patient-Specific Computational Left Ventricle Models to Quantify Material Properties and Stress/Strain Differences between Ventricles with and without Infarct. *Comput. Model. Eng. Sci.* **99**, 491–508 (2014).

97. Hassaballah, A. I., Hassan, M. A., Mardi, A. N. & Hamdi, M. An inverse finite element method for determining the tissue compressibility of human left ventricular wall during the cardiac cycle. *PLoS One* **8**, e82703–e82703 (2013).

98. Hess, O. M., Grimm, J. & Krayenbuehl, H. P. *Diastolic simple elastic and viscoelastic properties of the left ventricle in man*. *Circulation* vol. 59 http://ahajournals.org (1979).

99. Hess, O. M. *et al. Diastolic function and myocardial structure in patients with myocardial hypertrophy. Special reference to normalized viscoelastic data*. *Circulation* vol. 63 http://ahajournals.org (1981).

100. POULEUR, H., KARLINER, J. S., LEWINTER, M. M. & COVELL, J. W. Diastolic viscous properties of the intact canine left ventricle. *Circ. Res.* **67**, 352–359 (1979).

101. Ahmad, F. *et al.* Region-Specific Microstructure in the Neonatal Ventricles of a Porcine Model. *Ann. Biomed. Eng.* **46**, (2018).

102. Dokos, S., Smaill, B. H., Young, A. A., Legrice, I. J. & Legrice, I. J. Shear properties of passive ventricular myocardium. *Am J Physiol Hear. Circ Physiol* **283**, 2650–2659 (2002).

103. RANKIN, J. S., ARENTZEN, C. E., MCHALE, P. A., LING, D. & ANDERSON, R. W. Diastolic anisotropic properties of the left ventricle in the conscious dog. *Circ. Res.* **69**, 765–778 (1977).

104. STROUD, J. D., BAICU, C. F., BARNES, M. A., SPINALE, F. G. & ZILE1, M. R. Viscoelastic properties of pressure overload hypertrophied myocardium: effect of serine protease treatment. *Am J Physiol Hear. Circ Physiol* **315**, 1691–1702 (2002).

105. Shetye, S. S. *et al.* Nonlinear viscoelastic characterization of the porcine spinal cord. *Acta Biomater.* **10**, 792–797 (2014).

106. Troyer, K. L., Shetye, S. S. & Puttlitz, C. M. Experimental Characterization and Finite Element Implementation of Soft Tissue Nonlinear Viscoelasticity. *J. Biomech. Eng.* **134**, (2012).

107. Wheatley, B. B., Morrow, D. A., Odegard, G. M., Kaufman, K. R. & Haut Donahue, T. L. Skeletal muscle tensile strain dependence: Hyperviscoelastic nonlinearity. *J. Mech. Behav. Biomed. Mater.* **53**, 445–454 (2016).

108. Gültekin, O., Sommer, G. & Holzapfel, G. A. An orthotropic viscoelastic model for the passive myocardium: continuum basis and numerical treatment. *Comput. Methods Biomech. Biomed. Engin.* **19**, 1647–1664 (2016).

109. Huyghe, J. M., van Campen, D. H., Arts, T. & Heethaar, R. M. The constitutive behaviour of passive heart muscle tissue: A quasi-linear viscoelastic formulation. *J. Biomech.* **24**, 841–849 (1991).

110. Rosano, G. M. & Vitale, C. Metabolic Modulation of Cardiac Metabolism in Heart Failure. *Card. Fail. Rev.* **4**, 99–103 (2018).

111. Leonard, B. L., Smaill, B. H. & LeGrice, I. J. Structural Remodeling and Mechanical Function in Heart Failure. *Microsc. Microanal.* **18**, 50–67 (2012).

112. Gupte, R. S. *et al.* Upregulation of Glucose-6-Phosphate Dehydrogenase and NAD(P)H Oxidase

Activity Increases Oxidative Stress in Failing Human Heart. *J. Card. Fail.* **13**, 497–506 (2007).

113. Bijun, C. & G., F. N. Macrophages in the Remodeling Failing Heart. *Circ. Res.* **119**, 776–778 (2016).

114. Helmes, M. *et al. Mechanically driven contour-length adjustment in rat cardiac titin's unique N2B sequence. Titin is an adjustable spring*. *Circulation Research* vol. 84 http://www.circresaha.org (1999).

115. Francisco J. Villarreal. *Interstitial Fibrosis in Heart Failure*. *Interstitial Fibrosis in Heart Failure* http://www.ebooks.kluweronline.com (2005) doi:10.1007/b99419.

116. Bishop, J. E. & Laurent, G. J. Collagen turnover and its regulation in the normal and hypertrophying heart. *Eur. Heart J.* **16**, 38–44 (1995).

117. Brower, G. L. *et al.* The relationship between myocardial extracellular matrix remodeling and ventricular function☆. *Eur. J. Cardio-Thoracic Surg.* **30**, 604–610 (2006).

118. Golob, M. J., Wang, Z., Prostrollo, A. J., Hacker, T. A. & Chesler, N. C. Limiting collagen turnover via collagenase-resistance attenuates right ventricular dysfunction and fibrosis in pulmonary arterial hypertension. *Physiol. Rep.* **4**, e12815 (2016).

119. Plaksej, R. *et al.* Relation of circulating markers of fibrosis and progression of left and right ventricular dysfunction in hypertensive patients with heart failure. *J. Hypertens.* **27**, (2009).

120. Segura, A. M., Frazier, O. H. & Buja, L. M. Fibrosis and heart failure. *Heart Fail. Rev.* **19**, 173–185 (2014).

121. Yu, L. *et al.* Genetic and pharmacological inhibition of galectin-3 prevents cardiac remodeling by interfering with myocardial fibrogenesis. *Circ. Hear. Fail.* **6**, 107–117 (2013).

122. Begoña, L. *et al.* Impact of Treatment on Myocardial Lysyl Oxidase Expression and Collagen Cross-Linking in Patients With Heart Failure. *Hypertension* **53**, 236–242 (2009).

123. López, B., González, A., Querejeta, R., Larman, M. & Díez, J. Alterations in the Pattern of Collagen Deposition May Contribute to the Deterioration of Systolic Function in Hypertensive Patients With Heart Failure. *J. Am. Coll. Cardiol.* **48**, 89–96 (2006).

124. Berk, B. C., Fujiwara, K. & Lehoux, S. ECM remodeling in hypertensive heart disease. *J. Clin. Invest.* **117**, 568–575 (2007).

125. Rossi, M. A. Pathologic fibrosis and connective tissue matrix in left ventricular hypertrophy due to chronic arterial hypertension in humans. *J. Hypertens.* **16**, (1998).

126. Brower, G. L. & Janicki, J. S. Contribution of ventricular remodeling to pathogenesis of heart failure in rats. *Am. J. Physiol. Circ. Physiol.* **280**, H674–H683 (2001).

127. Ryan, T. D. *et al.* Left Ventricular Eccentric Remodeling and Matrix Loss Are Mediated by Bradykinin and Precede Cardiomyocyte Elongation in Rats With Volume Overload. *J. Am. Coll. Cardiol.* **49**, 811–821 (2007).

128. Zheng, J. *et al.* Microarray identifies extensive downregulation of noncollagen extracellular matrix and profibrotic growth factor genes in chronic isolated mitral regurgitation in the dog. *Circulation* **119**, 2086–2095 (2009).

129. Takashi, N. *et al.* Regulation of Fibrillar Collagen Gene Expression and Protein Accumulation in Volume-Overloaded Cardiac Hypertrophy. *Circulation* **95**, 2448–2454 (1997).

130. LeWinter, M. M. & Meyer, M. Mechanisms of diastolic dysfunction in heart failure with a preserved ejection fraction: If it's not one thing it's another. *Circ. Heart Fail.* **6**, 1112–1115 (2013).

131. Fernández-Golfín, C. *et al.* Left ventricular trabeculae: quantification in different cardiac diseases and impact on left ventricular morphological and functional parameters assessed with cardiac magnetic resonance. *J. Cardiovasc. Med.* **10**, (2009).

132. van de Veerdonk, M. C. *et al.* The importance of trabecular hypertrophy in right ventricular adaptation to chronic pressure overload. *Int. J. Cardiovasc. Imaging* **30**, 357–365 (2014).

133. Zile, M. R., Baicu, C. F. & Gaasch, W. H. Diastolic Heart Failure — Abnormalities in Active Relaxation and Passive Stiffness of the Left Ventricle. *N. Engl. J. Med.* **350**, 1953–1959 (2004).

134. Prasad, A. *et al.* Characterization of static and dynamic left ventricular diastolic function in patients with heart failure with a preserved ejection fraction. *Circ. Heart Fail.* **3**, 617–626 (2010).

135. Røe, Å. T. *et al.* Increased passive stiffness promotes diastolic dysfunction despite improved Ca2+

handling during left ventricular concentric hypertrophy. *Cardiovasc. Res.* **113**, 1161–1172 (2017).

136. Sakata, Y., Ohtani, T., Takeda, Y., Yamamoto, K. & Mano, T. Left Ventricular Stiffening as Therapeutic Target for Heart Failure With Preserved Ejection Fraction. *Circ. J.* **77**, 886–892 (2013).

137. Kraigher-Krainer, E. *et al.* Impaired Systolic Function by Strain Imaging in Heart Failure With Preserved Ejection Fraction. *J. Am. Coll. Cardiol.* **63**, 447–456 (2014).

138. Opitz, C. F. *et al.* Pre-Capillary, Combined, and Post-Capillary Pulmonary Hypertension: A Pathophysiological Continuum. *J. Am. Coll. Cardiol.* **68**, 368–378 (2016).

139. Puwanant, S. *et al.* Ventricular geometry, strain, and rotational mechanics in pulmonary hypertension. *Circulation* **121**, 259–266 (2010).

140. Sachdev, A. *et al.* Right Ventricular Strain for Prediction of Survival in Patients With Pulmonary Arterial Hypertension. *Chest* **139**, 1299–1309 (2011).

141. L.A., H. M. *et al.* Prognostic Value of Right Ventricular Longitudinal Peak Systolic Strain in Patients With Pulmonary Hypertension. *Circ. Cardiovasc. Imaging* **5**, 628–636 (2012).

142. Finsberg, H. *et al.* Efficient estimation of personalized biventricular mechanical function employing gradient-based optimization. *Int J Numer Meth Biomed Engng* **34**, (2018).

143. Kennish, A., Yellin, E., Frater, R. W. & Frater, W. *Dynamic stiffness profiles in the left ventricle*. *JOURNALOF APPLIED PHYSIOLOGY* vol. 39 http://citeseerx.ist.psu.edu/viewdoc/download?doi=10.1.1.911.4812&rep=rep1&type=pdf (1975).

144. LeWinter, M. M., Engler, R. & Pavelec, R. S. Time-dependent shifts of the left ventricular diastolic filling relationship in conscious dogs. *Circ. Res.* **45**, 641–653 (1979).

145. Gaasch, W. H. & Zile, M. R. Left Ventricular Diastolic Dysfunction and Diastolic Heart Failure. *Annu. Rev. Med.* **55**, 373–394 (2004).

146. Burlew, B. S. & Weber, K. T. Cardiac Fibrosis as a Cause of Diastolic Dysfunction. *Herz* **27**, 92–98 (2002).

147. Weber, K. T. & Brilla, C. G. Pathological hypertrophy and cardiac interstitium. Fibrosis and renin-angiotensin-aldosterone system. *Circulation* **83**, 1849–1865 (1991).

148. Maron, B. J., Bonow, R. O., Cannon, R. O., Leon, M. B. & Epstein, S. E. Hypertrophic Cardiomyopathy. *N. Engl. J. Med.* **316**, 844–852 (1987).

149. Attila, B. *et al.* Cardiomyocyte Stiffness in Diastolic Heart Failure. *Circulation* **111**, 774–781 (2005).

150. Avazmohammadi, R. *et al.* A Contemporary Look at Biomechanical Models of Myocardium. *Annu. Rev. Biomed. Eng.* **21**, 417–442 (2019).

151. Sharifi Kia, D. *et al.* Angiotensin Receptor-Neprilysin Inhibition Attenuates Right Ventricular Remodeling in Pulmonary Hypertension. *J. Am. Heart Assoc.* **9**, e015708 (2020).

152. Andersen, S. *et al.* Pressure overload induced right ventricular remodeling is not attenuated by the anti-fibrotic agent pirfenidone. *Pulm. Circ.* **9**, (2019).

153. Pfau, D. *et al.* Angiotensin Receptor Neprilysin Inhibitor Attenuates Myocardial Remodeling and Improves Infarct Perfusion in Experimental Heart Failure. *Sci. Rep.* **9**, 5791 (2019).

154. Vonk Noordegraaf, A., Westerhof, B. E. & Westerhof, N. The Relationship Between the Right Ventricle and its Load in Pulmonary Hypertension. *J. Am. Coll. Cardiol.* **69**, 236–243 (2017).

155. Andersen, S., Nielsen-Kudsk, J. E., Vonk Noordegraaf, A. & De Man, F. S. Right Ventricular Fibrosis: A Pathophysiological Factor in Pulmonary Hypertension? *Circulation* **139**, 269–285 (2019).

156. Abel, F. L. Effects of Alterations in Peripheral Resistance on Left Ventricular Function. *Proc. Soc. Exp. Biol. Med.* **120**, 52–56 (1965).

157. Pahuja, M. & Burkhoff, D. Right Ventricular Afterload Sensitivity Has Been on My Mind. *Circ. Hear. Fail.* **12**, e006345 (2019).

158. GUYTON, A. C., LINDSEY, A. W. & GILLULY, J. J. The limits of right ventricular compensation following acute increase in pulmonary circulatory resistance. *Circ. Res.* **2**, 326–332 (1954).

159. LAVER, M. B., STRAUSS, H. W. & POHOST, G. M. Herbert Shubin Memorial Lecture: Right and left ventricular geometry: adjustments during acute respiratory failure. *Crit. Care Med.* **7**, (1979).

160. E., O. D. & J., B. R. Quantitation of Collagen in Human Myocardium. *Circ. Res.* **5**, 357–361 (1957).

161. Kakaletsis, S. *et al.* Right ventricular myocardial mechanics: Multi-modal deformation,

microstructure, modeling, and comparison to the left ventricle. *Acta Biomater.* **123**, 154–166 (2021).

162. Sommer, G. *et al.* Biomechanical properties and microstructure of human ventricular myocardium. *Acta Biomater.* **24**, 172–192 (2015).

163. Ahmad, F. *et al.* Biomechanical properties and microstructure of neonatal porcine ventricles. (2018) doi:10.1016/j.jmbbm.2018.07.038.

164. Wang, B. *et al.* Myocardial scaffold-based cardiac tissue engineering: application of coordinated mechanical and electrical stimulations. *Langmuir* **29**, 11109–11117 (2013).

165. Lindsey, M. L. *et al.* Age-dependent changes in myocardial matrix metalloproteinase/tissue inhibitor of metalloproteinase profiles and fibroblast function. *Cardiovasc. Res.* **66**, 410–419 (2005).

166. Avazmohammadi, R. *et al.* Interactions Between Structural Remodeling and Hypertrophy in the Right Ventricle in Response to Pulmonary Arterial Hypertension. *J. Biomech. Eng.* **141**, 1–13 (2019).

167. Yap, C. H., Park, D. W., Dutta, D., Simon, M. & Kim, K. Methods for using 3-D ultrasound speckle tracking in biaxial mechanical testing of biological tissue samples. *Ultrasound Med. Biol.* **41**, 1029–1042 (2015).

168. Nguyen-Truong, M., Li, Y. V. & Wang, Z. Mechanical Considerations of Electrospun Scaffolds for Myocardial Tissue and Regenerative Engineering. *Bioeng. (Basel, Switzerland)* **7**, (2020).

169. Camacho, P., Fan, H., Liu, Z. & He, J.-Q. Large Mammalian Animal Models of Heart Disease. *J. Cardiovasc. Dev. Dis.* **3**, 30 (2016).

170. Avazmohammadi, R., Hill, M. R., Simon, M. A., Zhang, · Will & Sacks, M. S. A novel constitutive model for passive right ventricular myocardium: evidence for myofiber-collagen fiber mechanical coupling. *Biomech. Model. Mechanobiol.* **16**, 561–581 (2017).

171. Avazmohammadi, R. *et al.* An integrated inverse model-experimental approach to determine soft tissue three-dimensional constitutive parameters: application to post-infarcted myocardium. *Biomech. Model. Mechanobiol.* **17**, 31–53 (2018).

172. Matsumoto, T. *et al.* Biaxial tensile properties of thoracic aortic aneurysm tissues. *J. Biomech. Sci. Eng.* **4**, 518–529 (2009).

173. Witzenburg, C., Raghupathy, R., Kren, S. M., Taylor, D. A. & Barocas, V. H. Mechanical changes in the rat right ventricle with decellularization. *J. Biomech.* **45**, 842–849 (2012).

174. Valdez-Jasso, D., Simon, M. A., Champion, H. C. & Sacks, M. S. A murine experimental model for the mechanical behaviour of viable right-ventricular myocardium. *J. Physiol.* **590**, 4571–4584 (2012).

175. Liu, W. *et al.* Different Passive Viscoelastic Properties Between the Left and Right Ventricles in Healthy Adult Ovine. *J. Biomech. Eng.* **143**, 1–9 (2021).

176. Hill, M. R. *et al.* Structural and mechanical adaptations of right ventricle free wall myocardium to pressure overload. *Ann. Biomed. Eng.* **42**, 2451–2465 (2014).

177. Labus, K. M. & Puttlitz, C. M. An anisotropic hyperelastic constitutive model of brain white matter in biaxial tension and structural–mechanical relationships. *J. Mech. Behav. Biomed. Mater.* **62**, 195–208 (2016).

178. Rappaport, D., Adam, D., Lysyansky, P. & Riesner, S. Assessment of myocardial regional strain and strain rate by tissue tracking in B-mode echocardiograms. *Ultrasound Med. Biol.* **32**, 1181–1192 (2006).

179. Nguyen-Truong, M. *et al.* Establishment of adult right ventricle failure in ovine using a graded, animal-specific pulmonary artery constriction model. *Anim. Model. Exp. Med.* 1–11 (2020) doi:10.1002/ame2.12124.

180. Park, D. W., Sebastiani, A., Yap, C. H., Simon, M. A. & Kim, K. Quantification of Coupled Stiffness and Fiber Orientation Remodeling in Hypertensive Rat Right-Ventricular Myocardium Using 3D Ultrasound Speckle Tracking with Biaxial Testing. *PLoS One* **11**, e0165320 (2016).

181. Friedberg, M. K. & Redington, A. N. Right Versus Left Ventricular Failure. *Differ. Similarities, Interact.* **129**, 1033–1044 (2014).

182. Prisco, S. Z., Thenappan, T. & Prins, K. W. Treatment Targets for Right Ventricular Dysfunction in Pulmonary Arterial Hypertension. *JACC. Basic to Transl. Sci.* **5**, 1244–1260 (2020).

183. Reis, L. A., Chiu, L. L. Y., Feric, N., Fu, L. & Radisic, M. Biomaterials in myocardial tissue

engineering. *J. Tissue Eng. Regen. Med.* **10**, 11–28 (2016).

184. Miles, C. *et al.* Morphometric characterization of collagen and fat in normal ventricular myocardium. *Cardiovasc. Pathol.* **48**, 107224 (2020).

185. LeBar, K. Extracellular Matrix in Cardiac Tissue Mechanics and Physiology: Role of Collagen Accumulation. in (ed. Loewy, Z. W. E.-R. S. M. E.-J. O. P. R. O. E.-Z.) Ch. 2 (IntechOpen, 2021). doi:10.5772/intechopen.96585.

186. Silver, F. H., Horvath, I. & Foran, D. J. Mechanical Implications of the Domain Structure of Fiber-Forming Collagens: Comparison of the Molecular and Fibrillar Flexibilities of the a1-Chains Found in Types I-III Collagen. *J. theor. Biol* **216**, 243–254 (2002).

187. Sun, W., Sacks, M. S. & Scott, M. J. Effects of boundary conditions on the estimation of the planar biaxial mechanical properties of soft tissues. *J. Biomech. Eng.* **127**, 709–715 (2005).

188. Holzapfel, G. A. & Ogden, R. W. Constitutive modelling of passive myocardium: a structurally based framework for material characterization. *Trans. R. Soc. A* **367**, 3445–3475 (2009).

189. Voorhees, A. P. & Han, H.-C. Biomechanics of Cardiac Function. *Compr. Physiol.* **5**, 1623–1644 (2015).

190. Taverne, Y. J. H. J., Sadeghi, A., Bartelds, B., Bogers, A. J. J. C. & Merkus, D. Right ventricular phenotype, function, and failure: a journey from evolution to clinics. *Heart Fail. Rev.* (2020) doi:10.1007/s10741-020-09982-4.

191. Pettersen, E. *et al.* Contraction pattern of the systemic right ventricle shift from longitudinal to circumferential shortening and absent global ventricular torsion. *J. Am. Coll. Cardiol.* **49**, 2450–2456 (2007).

192. Avazmohammadi, R., Hill, M., Simon, M. & Sacks, M. Transmural remodeling of right ventricular myocardium in response to pulmonary arterial hypertension. *APL Bioeng.* **1**, 16105 (2017).

193. Velez-Rendon, D., Pursell, E., Shieh, J. & Valdez-Jasso, D. Contribution of Matrix Remodeling to Biaxial Mechanics of Right-Ventricular Myocardium in Pulmonary Arterial Hypertension. *J. Biomech. Eng.* (2019) doi:10.1115/1.4044225.

194. Reddy, S. & Bernstein, D. Molecular mechanisms of right ventricular failure. *Circulation* **132**, 1734–1742 (2015).

195. Javani, S., Gordon, M. & Azadani, A. N. Biomechanical Properties and Microstructure of Heart Chambers: A Paired Comparison Study in an Ovine Model. *Ann. Biomed. Eng.* **44**, 3266–3283 (2016).

196. Kirton, R. S., Taberner, A. J., Nielsen, P. M. F., Young, A. A. & Loiselle, D. S. Effects of BDM, [Ca2+]o, and temperature on the dynamic stiffness of quiescent cardiac trabeculae from rat. *Am. J. Physiol. - Hear. Circ. Physiol.* **288**, 1662–1667 (2005).

197. Konold, T. & Bone, G. E. Heart rate variability analysis in sheep affected by transmissible spongiform encephalopathies. *BMC Res. Notes* **4**, 539 (2011).

198. Wang, Z. & Chesler, N. C. Role of collagen content and cross-linking in large pulmonary arterial stiffening after chronic hypoxia. *Biomech. Model. Mechanobiol.* **11**, 279–289 (2012).

199. Ambrosetti-Giudici, S., Gédet, P., Ferguson, S. J., Chegini, S. & Burger, J. Viscoelastic properties of the ovine posterior spinal ligaments are strain dependent. *Clin. Biomech.* **25**, 97–102 (2010).

200. Provenzano, P., Lakes, R., Keenan, T. & vanderby, R. Nonlinear Ligament Viscoelasticity. *Ann. Biomed. Eng.* **29**, 908–914 (2001).

201. Hingorani, R. V, Provenzano, P. P., Lakes, R. S., Escarcega, A. & Vanderby, R. Nonlinear Viscoelasticity in Rabbit Medial Collateral Ligament. *Ann. Biomed. Eng.* **32**, 306–312 (2004).

202. Duenwald, S. E., Vanderby, R. J. & Lakes, R. S. Viscoelastic relaxation and recovery of tendon. *Ann. Biomed. Eng.* **37**, 1131–1140 (2009).

203. Dixon, J. A. & Spinale, F. G. Large Animal Models of Heart Failure. *Circ. Hear. Fail.* **2**, 262–271 (2009).

204. Pham, T. & Sun, W. Comparison of biaxial mechanical properties of coronary sinus tissues from porcine, ovine and aged human species. *J. Mech. Behav. Biomed. Mater.* **6**, 21–29 (2012).

205. Bergel, D. H. The dynamic elastic properties of the arterial wall. *J. Physiol.* **156**, 458–469 (1961).

206. Cox, R. H. Viscoelastic properties of canine pulmonary arteries. *Am. J. Physiol.* **246**, H90-6 (1984).

207. Mangoni, A. A., Mircoli, L., Giannattasio, C., Ferrari, A. U. & Mancia, G. Heart rate-dependence of arterial distensibility in vivo. *J. Hypertens.* **14**, 897–901 (1996).

208. Gamero, L. G., Armentano, R. L., Barra, J. G., Simon, A. & Levenson, J. Identification of Arterial Wall Dynamics in Conscious Dogs. *Exp. Physiol.* **86**, 519–528 (2001).

209. Anssari-Benam, A., Bucchi, A., Screen, H. R. C. & Evans, S. L. A transverse isotropic viscoelastic constitutive model for aortic valve tissue. *R. Soc. Open Sci.* **4**, (2017).

210. Lujan, T. J., Underwood, C. J., Jacobs, N. T. & Weiss, J. A. Contribution of glycosaminoglycans to viscoelastic tensile behavior of human ligament. *J. Appl. Physiol.* **106**, 423–431 (2009).

211. Anssari-Benam, A., Barber, A. H. & Bucchi, A. Evaluation of bioprosthetic heart valve failure using a matrix-fibril shear stress transfer approach. *J. Mater. Sci. Mater. Med.* **27**, 42 (2016).

212. Anssari-Benam, A., Bader, D. L. & Screen, H. R. C. A combined experimental and modelling approach to aortic valve viscoelasticity in tensile deformation. *J. Mater. Sci. Mater. Med.* **22**, 253–262 (2011).

213. Linke, W. A. & Fernandez, J. M. Cardiac titin: Molecular basis of elasticity and cellular contribution to elastic and viscous stiffness components in myocardium. *J. Muscle Res. Cell Motil.* **23**, 483–497 (2002).

214. Caporizzo, M. A., Chen, C. Y., Salomon, A. K., Margulies, K. B. & Prosser, B. L. Microtubules Provide a Viscoelastic Resistance to Myocyte Motion. *Biophys. J.* **115**, 1796–1807 (2018).

215. Armentano, R. L. *et al. Carotid Wall Viscosity Increase Is Related to Intima-Media Thickening in Hypertensive Patients*. *Hypertension* vol. 31 http://ahajournals.org (1998).

216. Oyen, M. L. & Ko, C. C. Examination of local variations in viscous, elastic, and plastic indentation responses in healing bone. *J. Mater. Sci. Mater. Med.* **18**, 623–628 (2007).

217. Eisenberg, E., Di Palo, K. E. & Piña, I. L. Sex differences in heart failure. *Clin. Cardiol.* **41**, 211–216 (2018).

218. Nguyen-truong, M. *et al.* The Interventricular Septum Is Biomechanically Distinct from the Ventricular Free Walls. 1–13 (2021).

219. Fan, R. & Sacks, M. S. Simulation of planar soft tissues using a structural constitutive model: Finite element implementation and validation. *J. Biomech.* **47**, 2043–2054 (2014).

220. Nordsletten, D. *et al.* A viscoelastic model for human myocardium. *Acta Biomater.* **135**, 441–457 (2021).

221. Sommer, G. *et al.* Biomechanical properties and microstructure of human ventricular myocardium. *Acta Biomater.* **24**, 172–192 (2015).

222. Caporizzo, M. A., Chen, C. Y., Bedi, K., Margulies, K. B. & Prosser, B. L. Microtubules increase diastolic stiffness in failing human cardiomyocytes and myocardium. *Circulation* 902–915 (2020) doi:10.1161/CIRCULATIONAHA.119.043930.

223. Caporizzo, M. A. & Prosser, B. L. Need for Speed: The Importance of Physiological Strain Rates in Determining Myocardial Stiffness. *Front. Physiol.* **12**, 1–8 (2021).

224. Chung, C. S. *et al.* Titin based viscosity in ventricular physiology: an integrative investigation of PEVK-actin interactions. *J. Mol. Cell. Cardiol.* **51**, 428–434 (2011).

225. Cooper IV, G. Proliferating cardiac microtubules. *Am. J. Physiol. - Hear. Circ. Physiol.* **297**, 510–511 (2009).

226. Harris, T. S. *et al.* Constitutive properties of hypertrophied myocardium: Cellular contribution to changes in myocardial stiffness. *Am. J. Physiol. - Hear. Circ. Physiol.* **282**, 2173–2182 (2002).

227. Propp, A., Gizzi, A., Levrero-Florencio, F. & Ruiz-Baier, R. An orthotropic electro-viscoelastic model for the heart with stress-assisted diffusion. *Biomech. Model. Mechanobiol.* **19**, 633–659 (2020).

228. Sharifi Kia, D., Kim, K. & Simon, M. A. Current Understanding of the Right Ventricle Structure and Function in Pulmonary Arterial Hypertension. *Front. Physiol.* **12**, 1–16 (2021).

229. Stroud, J. D., Baicu, C. F., Barnes, M. A., Spinale, F. G. & Zile, M. R. Viscoelastic properties of pressure overload hypertrophied myocardium: Effect of serine protease treatment. *Am. J. Physiol. - Hear. Circ. Physiol.* **282**, 2324–2335 (2002).

230. Pouleur, H., Karliner, J. S., Lewinter, M. M. & Covell, J. W. *Diastolic Viscous Properties of the*

Intact Canine Left Ventricle. *Ore Res* vol. 45 http://ahajournals.org (1979).

231. Yang, M. & Taber, L. A. The possible role of poroelasticity in the apparent viscoelastic behavior of passive cardiac muscle. *J. Biomech.* **24**, 587–597 (1991).

232. Huyghe, J. M., van Campen, D. H., Arts, T. & Heethaar, R. M. A two-phase finite element model of the diastolic left ventricle. *J. Biomech.* **24**, 527–538 (1991).

233. Huyghe, J. M., van Campen, D. H., Arts, T. & Heethaar, R. M. The constitutive behaviour of passive heart muscle tissue: A quasi-linear viscoelastic formulation. *J. Biomech.* **24**, 841–849 (1991).

234. Fung, Y. *Biomechanics: mechanical properties of living tissues. 1993*. *Springer-Verlag, New York* (2008).

235. Yao, J. *et al.* Viscoelastic material properties of the myocardium and cardiac jelly in the looping chick heart. *J. Biomech. Eng.* **134**, 1–7 (2012).

236. Pinto, J. G. & Fung, Y. C. Mechanical properties of the heart muscle in the passive state. *J. Biomech.* **6**, 597–616 (1973).

237. Troyer, K. L. & Puttlitz, C. M. Human cervical spine ligaments exhibit fully nonlinear viscoelastic behavior. *Acta Biomater.* **7**, 700–709 (2011).

238. Reddy, S. & Bernstein, D. Molecular Mechanisms of Right Ventricular Failure. *Circulation* **132**, 1734–1742 (2015).

239. Rubiano, A. *et al.* Stem cell therapy restores viscoelastic properties of myocardium in rat model of hypertension. *J. Mech. Behav. Biomed. Mater.* **59**, 71–77 (2016).

240. Liu, W., Nguyen-truong, M., Lebar, K. & Labus, K. M. Multiscale Contrasts Between the Right and Left Ventricle Biomechanics in Healthy Adult Sheep and Translational Implications. **10**, 1–13 (2022).

241. Labus, K. M. & Puttlitz, C. M. Viscoelasticity of brain corpus callosum in biaxial tension. *J. Mech. Phys. Solids* **96**, 591–604 (2016).

242. Labus, K. M., Kuiper, J. P., Rawlinson, J. & Puttlitz, C. M. Mechanical characterization and viscoelastic model of the ovine temporomandibular joint Disc in indentation, uniaxial tension, and

biaxial tension. *J. Mech. Behav. Biomed. Mater.* **116**, 104300 (2021).

243. Bertula, K. *et al.* Strain-Stiffening of Agarose Gels. *ACS Macro Lett.* **8**, 670–675 (2019).

244. Shetye, S. S. *et al.* Nonlinear viscoelastic characterization of the porcine spinal cord. *Acta Biomater.* **10**, 792–797 (2014).

245. Haddad, F., Hunt, S. A., Rosenthal, D. N. & Murphy, D. J. Right ventricular function in cardiovascular disease, part I: Anatomy, physiology, aging, and functional assessment of the right ventricle. *Circulation* **117**, 1436–1448 (2008).

246. Konstam, M. A. *et al.* Evaluation and Management of Right-Sided Heart Failure: A Scientific Statement From the American Heart Association. *Circulation* **137**, e578–e622 (2018).

247. Gorter, T. M. *et al.* Right heart dysfunction and failure in heart failure with preserved ejection fraction: mechanisms and management. Position statement on behalf of the Heart Failure Association of the European Society of Cardiology. *Eur. J. Heart Fail.* **20**, 16–37 (2018).

248. Raina, A. & Meeran, T. Right Ventricular Dysfunction and Its Contribution to Morbidity and Mortality in Left Ventricular Heart Failure. *Curr. Heart Fail. Rep.* **15**, 94–105 (2018).

249. Konstam, M. A. *et al.* Evaluation and Management of Right-Sided Heart Failure: A Scientific Statement From the American Heart Association. *Circulation* **137**, e578–e622 (2018).

250. Borgdorff, M. A. J., Dickinson, M. G., Berger, R. M. F. & Bartelds, B. Right ventricular failure due to chronic pressure load: What have we learned in animal models since the NIH working group statement? *Heart Fail. Rev.* **20**, 475–491 (2015).

251. Voelkel, N. F., Bogaard, H. J. & Gomez-Arroyo, J. The need to recognize the pulmonary circulation and the right ventricle as an integrated functional unit: facts and hypotheses (2013 Grover Conference series). *Pulm. Circ.* **5**, 81–89 (2015).

252. Vonk Noordegraaf, A. & Galiè, N. The role of the right ventricle in pulmonary arterial hypertension. *Eur. Respir. Rev.* **20**, 243 LP – 253 (2011).

253. Mulchrone, A. *et al.* A Large Animal Model of Right Ventricular Failure due to Chronic Thromboembolic Pulmonary Hypertension: A Focus on Function. *Front. Cardiovasc. Med.* **5**, 189

(2018).

254. Malinowski, M. *et al.* Large animal model of acute right ventricular failure with functional tricuspid regurgitation. *Int. J. Cardiol.* **264**, 124–129 (2018).

255. Knai, K. & Skjaervold, N. K. A pig model of acute right ventricular afterload increase by hypoxic pulmonary vasoconstriction. *BMC Res. Notes* **10**, 2 (2017).

256. Aguero, J. *et al.* Characterization of right ventricular remodeling and failure in a chronic pulmonary hypertension model. *Am. J. Physiol. Heart Circ. Physiol.* **307**, H1204–H1215 (2014).

257. Aguero, J. *et al.* Intratracheal Gene Delivery of SERCA2a Ameliorates Chronic Post-Capillary Pulmonary Hypertension: A Large Animal Model. *J. Am. Coll. Cardiol.* **67**, 2032–2046 (2016).

258. Aguero, J. *et al.* Characterization of right ventricular remodeling and failure in a chronic pulmonary hypertension model. *Am. J. Physiol. Heart Circ. Physiol.* **307**, H1204–H1215 (2014).

259. Sato, H. *et al.* Large animal model of chronic pulmonary hypertension. *ASAIO J.* **54**, 396–400 (2008).

260. Boulate, D. *et al.* Early Development of Right Ventricular Ischemic Lesions in a Novel Large Animal Model of Acute Right Heart Failure in Chronic Thromboembolic Pulmonary Hypertension. *J. Card. Fail.* **23**, 876–886 (2017).

261. Wang, Z., Schreier, D. A., Abid, H., Hacker, T. A. & Chesler, N. C. Pulmonary vascular collagen content, not cross-linking, contributes to right ventricular pulsatile afterload and overload in early pulmonary hypertension. *J. Appl. Physiol.* **122**, 253–263 (2017).

262. Gomez-Arroyo, J. G. *et al.* The monocrotaline model of pulmonary hypertension in perspective. *Am. J. Physiol. Lung Cell. Mol. Physiol.* **302**, L363-9 (2012).

263. Zeng, G. *et al.* Single Intraperitoneal Injection of Monocrotaline as a Novel Large Animal Model of Chronic Pulmonary Hypertension in Tibet Minipigs. *PLoS One* **8**, e78965 (2013).

264. Wang, Z., Lakes, R. S., Golob, M., Eickhoff, J. C. & Chesler, N. C. Changes in large pulmonary arterial viscoelasticity in chronic pulmonary hypertension. *PLoS One* **8**, e78569 (2013).

265. Wang, Z. *et al.* Organ-level right ventricular dysfunction with preserved Frank-Starling mechanism in a mouse model of pulmonary arterial hypertension. *J. Appl. Physiol.* **124**, 1244–1253 (2018).

266. Colvin, K. L. & Yeager, M. E. Animal Models of Pulmonary Hypertension: Matching Disease Mechanisms to Etiology of the Human Disease. *J. Pulm. Respir. Med.* **4**, (2014).

267. Stenmark, K. R., Meyrick, B., Galie, N., Mooi, W. J. & McMurtry, I. F. Animal models of pulmonary arterial hypertension: the hope for etiological discovery and pharmacological cure. *Am. J. Physiol. Lung Cell. Mol. Physiol.* **297**, L1013-32 (2009).

268. Maarman, G., Lecour, S., Butrous, G., Thienemann, F. & Sliwa, K. A comprehensive review: the evolution of animal models in pulmonary hypertension research; are we there yet? *Pulm. Circ.* **3**, 739–756 (2013).

269. Rabinovitch, M., Guignabert, C., Humbert, M. & Nicolls, M. R. Inflammation and immunity in the pathogenesis of pulmonary arterial hypertension. *Circ. Res.* **115**, 165–175 (2014).

270. Hsieh, C. M. *et al.* Production and reversibility of right ventricular hypertrophy and right heart failure in dogs. *Ann. Thorac. Surg.* **54**, 104–110 (1992).

271. Leeuwenburgh, B. P., Helbing, W. A., Steendijk, P., Schoof, P. H. & Baan, J. Biventricular systolic function in young lambs subject to chronic systemic right ventricular pressure overload. *Am. J. Physiol. Heart Circ. Physiol.* **281**, H2697-704 (2001).

272. Leeuwenburgh, B. P. J. *et al.* Chronic right ventricular pressure overload results in a hyperplastic rather than a hypertrophic myocardial response. *J. Anat.* **212**, 286–294 (2008).

273. Leeuwenburgh, B. P. J. *et al.* Chronic and adjustable pulmonary artery banding. *J. Thorac. Cardiovasc. Surg.* **125**, 231–237 (2003).

274. Leeuwenburgh, B. P. J., Steendijk, P., Helbing, W. A. & Baan, J. Indexes of diastolic RV function: load dependence and changes after chronic RV pressure overload in lambs. *Am. J. Physiol. Heart Circ. Physiol.* **282**, H1350-8 (2002).

275. Barbera, A. *et al.* Right ventricular systolic pressure load alters myocyte maturation in fetal sheep. *Am. J. Physiol. Integr. Comp. Physiol.* **279**, R1157–R1164 (2000).

276. Verbelen, T. *et al.* Mechanical support of the pressure overloaded right ventricle: an acute feasibility study comparing low and high flow support. *Am. J. Physiol. Heart Circ. Physiol.* **309**, H615-24

(2015).

277. Dixon, J. A. & Spinale, F. G. Large animal models of heart failure; A critical link in the translation of basic science to clinical practice. *Circulation: Heart Failure* vol. 2 262–271 (2009).

278. Leeuwenburgh, B. P. J. *et al.* Chronic right ventricular pressure overload results in a hyperplastic rather than a hypertrophic myocardial response. *J. Anat.* **212**, 286–294 (2008).

279. Ramos, S. R. *et al.* Early versus late cardiac remodeling during right ventricular pressure load and impact of preventive versus rescue therapy with endothelin-1 receptor blockers. *J. Appl. Physiol.* **124**, 1349–1362 (2018).

280. Gold, J., Akazawa, Y., Sun, M., Hunter, K. S. & Friedberg, M. K. Relation between right ventricular wall stress, fibrosis, and function in right ventricular pressure loading. *Am. J. Physiol. Heart Circ. Physiol.* **318**, H366–H377 (2020).

281. Gaynor, S. L., Maniar, H. S., Bloch, J. B., Steendijk, P. & Moon, M. R. Right Atrial and Ventricular Adaptation to Chronic Right Ventricular Pressure Overload. *Circulation* **112**, I-212-I–218 (2005).

282. Heitmeier, T. *et al.* Altered proteasome function in right ventricular hypertrophy. *Cardiovasc. Res.* **116**, 406–415 (2020).

283. Kuroha, M., Isoyama, S., Ito, N. & Takishima, T. Effects of age on right ventricular hypertrophic response to pressure-overload in rats. *J. Mol. Cell. Cardiol.* **23**, 1177–1190 (1991).

284. Schou, U. K., Peters, C. D., Wan Kim, S., Frøkiær, J. & Nielsen, S. Characterization of a rat model of right-sided heart failure induced by pulmonary trunk banding. *J. Exp. Anim. Sci.* **43**, 237–254 (2007).

285. Bogaard, H. J. *et al.* Chronic pulmonary artery pressure elevation is insufficient to explain right heart failure. *Circulation* **120**, 1951–1960 (2009).

286. Hirata, M. *et al.* Novel Model of Pulmonary Artery Banding Leading to Right Heart Failure in Rats. *Biomed Res. Int.* **2015**, 753210 (2015).

287. Wang, S. *et al.* A neonatal rat model of increased right ventricular afterload by pulmonary artery banding. *J. Thorac. Cardiovasc. Surg.* **154**, 1734–1739 (2017).

288. Chery, J. *et al.* Human Neonatal Thymus Mesenchymal Stem/Stromal Cells and Chronic Right Ventricle Pressure Overload. *Bioeng. (Basel, Switzerland)* **6**, (2019).

289. Axelsen, J. B. *et al.* Effects of 6-mercaptopurine in pressure overload induced right heart failure. *PLoS One* **14**, e0225122 (2019).

290. McKellar, S. H. *et al.* Animal model of reversible, right ventricular failure. *J. Surg. Res.* **194**, 327–333 (2015).

291. Gaynor, S. L., Maniar, H. S., Bloch, J. B., Steendijk, P. & Moon, M. R. Right Atrial and Ventricular Adaptation to Chronic Right Ventricular Pressure Overload. *Circulation* **112**, I-212-I–218 (2005).

292. Barbera, A. *et al.* Right ventricular systolic pressure load alters myocyte maturation in fetal sheep. *Am. J. Physiol. Integr. Comp. Physiol.* **279**, R1157–R1164 (2000).

293. Hon, J. K., Steendijk, P., Khan, H., Wong, K. & Yacoub, M. Acute effects of pulmonary artery banding in sheep on right ventricle pressure-volume relations: relevance to the arterial switch operation. *Acta Physiol. Scand.* **172**, 97–106 (2001).

294. Yerebakan, C. *et al.* Acute and chronic response of the right ventricle to surgically induced pressure and volume overload--an analysis of pressure-volume relations. *Interact. Cardiovasc. Thorac. Surg.* **10**, 519–525 (2010).

295. Gufler, H. *et al.* Right Ventricular Function After Pulmonary Artery Banding: Adaptive Processes Assessed by CMR and Conductance Catheter Measurements in Sheep. *J. Cardiovasc. Transl. Res.* **12**, 459–466 (2019).

296. Corno, A. F. *et al.* Pulmonary artery banding: long-term telemetric adjustment. *Eur. J. Cardio-Thoracic Surg.* **23**, 317–322 (2003).

297. Mitchell, C. *et al.* Guidelines for Performing a Comprehensive Transthoracic Echocardiographic Examination in Adults: Recommendations from the American Society of Echocardiography. *J. Am. Soc. Echocardiogr. Off. Publ. Am. Soc. Echocardiogr.* **32**, 1–64 (2019).

298. Curran-Everett, D. & Benos, D. J. Guidelines for reporting statistics in journals published by the American Physiological Society. *Am. J. Physiol. Metab.* **287**, E189–E191 (2004).

299. Price, E. O., Dally, M. R. & Borgwardt, R. Early sexual experience improves ram breeding. *Calif. Agric.* **50**, 37–40 (1996).

300. Hirata, M. *et al.* Novel Model of Pulmonary Artery Banding Leading to Right Heart Failure in Rats. *Biomed Res. Int.* **2015**, 753210 (2015).

301. Chua, J. *et al.* Acute right ventricular pressure overload compromises left ventricular function by altering septal strain and rotation. *J. Appl. Physiol.* **115**, 186–193 (2013).

302. Naeije, R. & Manes, A. The right ventricle in pulmonary arterial hypertension. *Eur. Respir. Rev. an Off. J. Eur. Respir. Soc.* **23**, 476–487 (2014).

303. Voelkel, N. F., Gomez-Arroyo, J., Abbate, A. & Bogaard, H. J. Mechanisms of right heart failure-A work in progress and a plea for failure prevention. **3**,.

304. Liu, W. Current Understanding of the Biomechanics of Ventricular Tissues in Heart Failure. *Bioengineering* (2020).

305. Pauschinger, M. *et al.* Differential myocardial abundance of collagen type I and type III mRNA in dilated cardiomyopathy: effects of myocardial inflammation. *Cardiovasc. Res.* **37**, 123–129 (1998).

306. Ishizu, T. *et al.* Left Ventricular Strain and Transmural Distribution of Structural Remodeling in Hypertensive Heart Disease. *Hypertension* **63**, 500–506 (2014).

307. Tandri, H. *et al.* Noninvasive detection of myocardial fibrosis in arrhythmogenic right ventricular cardiomyopathy using delayed-enhancement magnetic resonance imaging. *J. Am. Coll. Cardiol.* **45**, 98–103 (2005).

308. Moreo, A. *et al.* Influence of Myocardial Fibrosis on Left Ventricular Diastolic Function Noninvasive Assessment by Cardiac Magnetic Resonance and Echo. (2009) doi:10.1161/CIRCIMAGING.108.838367.

309. Bogaard, H. J. & Voelkel, N. F. Is Myocardial Fibrosis Impairing Right Heart Function? *Am. J. Respir. Crit. Care Med.* **199**, 1458–1459 (2019).

310. Poble, P.-B. *et al.* Therapeutic effect of pirfenidone in the sugen/hypoxia rat model of severe pulmonary hypertension. *FASEB J. Off. Publ. Fed. Am. Soc. Exp. Biol.* **33**, 3670–3679 (2019).

311. Bogaard, H. J. & Voelkel, N. F. Is Myocardial Fibrosis Impairing Right Heart Function? *Am. J. Respir. Crit. Care Med.* **199**, 1458–1459 (2019).

312. Visser, L. C., Scansen, B. A., Schober, K. E. & Bonagura, J. D. Echocardiographic assessment of right ventricular systolic function in conscious healthy dogs: repeatability and reference intervals. *J. Vet. Cardiol. Off. J. Eur. Soc. Vet. Cardiol.* **17**, 83–96 (2015).

313. Vonk-Noordegraaf, A. & Souza, R. Cardiac magnetic resonance imaging: what can it add to our knowledge of the right ventricle in pulmonary arterial hypertension? *Am. J. Cardiol.* **110**, 25S-31S (2012).

314. Cioffi, G., de Simone, G., Mureddu, G., Tarantini, L. & Stefenelli, C. Right atrial size and function in patients with pulmonary hypertension associated with disorders of respiratory system or hypoxemia. *Eur. J. Echocardiogr. J. Work. Gr. Echocardiogr. Eur. Soc. Cardiol.* **8**, 322–331 (2007).

315. Diebel, L. N., Wilson, R. F., Tagett, M. G. & Kline, R. A. End-Diastolic Volume: A Better Indicator of Preload in the Critically Ill. *JAMA Surg.* **127**, 817–822 (1992).

316. Durham, R., Neunaber, K., Vogler, G., Shapiro, M. & Mazuski, J. Right Ventricular End-Diastolic Volume as a Measure of Preload. *J. Trauma Acute Care Surg.* **39**, (1995).

317. Zile, M. R. *et al.* Myocardial stiffness in patients with heart failure and a preserved ejection fraction: contributions of collagen and titin. *Circulation* **131**, 1247–1259 (2015).

318. Trip, P. *et al.* Clinical relevance of right ventricular diastolic stiffness in pulmonary hypertension. *Eur. Respir. J.* **45**, 1603–1612 (2015).

319. Forte, G. *et al.* Substrate stiffness modulates gene expression and phenotype in neonatal cardiomyocytes in vitro. *Tissue Eng. Part A* **18**, 1837–1848 (2012).

320. Efraim, Y. *et al.* 3D Structure and Processing Methods Direct the Biological Attributes of ECM-Based Cardiac Scaffolds. *Sci. Rep.* **9**, 5578 (2019).

321. Krishnamurthy, A., Villongco, C., Beck, A., Omens, J. & McCulloch, A. Left Ventricular Diastolic and Systolic Material Property Estimation from Image Data: LV Mechanics Challenge. *Stat. atlases*

Comput. Model. Hear. STACOM **8896**, 63–73 (2015).

322. Wang, Z. J. *et al.* Left Ventricular Diastolic Myocardial Stiffness and End-Diastolic Myofibre Stress in Human Heart Failure Using Personalised Biomechanical Analysis. *J. Cardiovasc. Transl. Res.* **11**, 346–356 (2018).

323. Bermejo, J. *et al.* Diastolic chamber properties of the left ventricle assessed by global fitting of pressure-volume data: improving the gold standard of diastolic function. *J. Appl. Physiol.* **115**, 556–568 (2013).

324. Patel, M. D. *et al.* Echocardiographic Assessment of Right Ventricular Afterload in Preterm Infants: Maturational Patterns of Pulmonary Artery Acceleration Time Over the First Year of Age and Implications for Pulmonary Hypertension. *J. Am. Soc. Echocardiogr. Off. Publ. Am. Soc. Echocardiogr.* **32**, 884-894.e4 (2019).

325. Cho, I.-J. *et al.* Deceleration time of left ventricular outflow tract flow as a simple surrogate marker for central haemodynamics at rest and as well as during exercise. *Eur. Heart J. Cardiovasc. Imaging* **18**, 568–575 (2017).

326. Takahama, H., McCully, R. B., Frantz, R. P. & Kane, G. C. Unraveling the RV Ejection Doppler Envelope: Insight Into Pulmonary Artery Hemodynamics and Disease Severity. *JACC. Cardiovasc. Imaging* **10**, 1268–1277 (2017).

327. Yamamoto, S. *et al.* Role of Microtubules in the Viscoelastic Properties of Isolated Cardiac Muscle. *J. Mol. Cell. Cardiol.* **30**, 1841–1853 (1998).

328. Borlaug, B. A., Kane, G. C., Melenovsky, V. & Olson, T. P. Abnormal right ventricular-pulmonary artery coupling with exercise in heart failure with preserved ejection fraction. *Eur. Heart J.* **37**, 3294–3302 (2016).

329. Guazzi, M. *et al.* Right Ventricular Contractile Reserve and Pulmonary Circulation Uncoupling During Exercise Challenge in Heart Failure: Pathophysiology and Clinical Phenotypes. *JACC Hear. Fail.* **4**, 625–635 (2016).

330. Roth, K., Liu, W., LeBar, K., Ahern, M. & Wang, Z. A New High-Speed Biaxial Testing System

for Rodent Myocardium Viscoelastic Measurement under Dynamic Loadings. *FASEB J.* **36**, (2022).

331. Thibault, H. B. *et al.* Noninvasive assessment of murine pulmonary arterial pressure: validation and application to models of pulmonary hypertension. *Circ. Cardiovasc. Imaging* **3**, 157–163 (2010).

332. Groepenhoff, H. *et al.* Exercise stroke volume and heart rate response differ in right and left heart failure. *Eur. J. Heart Fail.* **12**, 716–720 (2010).

APPENDIX A: EX VIVO BIAXIAL TESTING PROTOCOL

DATE: _____ Experimentalist (initials): _____

Species: □ Rat □ Sheep Group/Treatment: _____

Sex: _____ Age: _____ Body weight: _____

TISSUE HARVEST: (rinse with saline and harvest the LV, RV, septum; slice the tissue(s) needed for mechanical tests and put the rest part of fresh tissue in -80C; then quickly transfer testing tissue to CPS or 1x PBS on ice, and then placed in BDM+CPS at 37C in tissue bath to get prepared for mechanical tests)

Tissue preparation: □ fresh tissue (___ hours post harvest) □ frozen tissue

Longitudinal (outflow tract) direction marked □ Yes □ No

LV weight (g): _____ RV weight (g): _____ Septum weight: _____

Original/Testing tissue thickness:

RV: ____, ____, ____, ____, ____ mm

LV: ____, ____, ____, ____, ____ mm

Size _____mm (Length), _____mm (Width)

Layers of myocardium for mechanical tests: □ epicardial □ middle □ endocardial

TISSUE MOUNTING:

□ Load cell force magnitudes are set to zero before mounting

□ Actuators are set home using "Set Home" function in LabVIEW before mounting

□ All the arms are parallel to the sample surface;

□ Each sample's four corners are at right angle (approximate)

□ Each sample is under the stretch stage and flat (approximate)

□ **Bath Check** pH: ____ Temperature: ____ □ **Marker**

PARAMETERS SETTING: (use Master file to calculate the speed)

Strain range (max): _____ % (20% suggested for ventricles)

Strain rate at 0.1Hz: _____ mm/s; Strain rate at 1Hz: _____ mm/s

Strain rate at 2Hz: _____ mm/s; Strain rate at 5Hz: _____ mm/s

Strain rate at 8Hz: _____ mm/s

$Strain\ rate = \frac{displacement\ (mm)}{one\ cycle/2\ (s)}$, $displacement\ (mm) = Preload\ Length \times Strain\ Range$

Type of the cyclic load: ~~□ triangle~~ □ sinusoidal

Type of the test: □ Biaxial □ Constrained Biaxial □ Uniaxial □ Constrained Uniaxial

1. MECHANICAL TEST:

1. Equilibrium (30 min; in tissue bath with CPS + BDM; at 25-37^{o}C)

2. Preconditioning at ___Hz (for 15 cycles),(same as the testing strain range)

3. Equibiaxial test **at each frequency**

1) Cyclic tensile tests (see the Table). (Force data: 2000Hz);

2) Stress relaxation (100 s. at each strain ratio; Ramp speed: the same as the corresponding cyclic test speed and detailed calculation see above "Strain rate") (force data: 100Hz; image data: 50Hz only for 2 seconds)

□ 3% □6% □9% □ 12% □ 15%

3) Repeat for all frequencies and log the Table below:

Frequency (Hz)	FPS	Max Force (N)	Force vs Time Plot	Testing Cycle #	Rest Period (s)	Ramp speed SR (mm/s)
0.1 (10s)	5			5	500	
1 (1s)	50			15	150	
2 (0.5s)	100			15	75	
5 (0.2s)	200			15	37.5	
8 (0.125s)	200			15	25.5	

4. Repeat the 1Hz test to ensure no plastic deformation (damage) in the tissue

5. Colchicine treatment (30 min; in tissue bath with 0.3 mM Col; at 25-37^{o}C)

6. Stress relaxation testing:

a. 15% strain at 1Hz speed: Compare the results to the pre-colchicine treatment; If no change is seen, wait another 15 minutes before running further tests.

b. 15% strain at 5Hz speed (at physiological frequency)

c. 15% strain at 8Hz speed (at exercise)

7. Cyclic equibiaxial testing:

a. 1Hz for 15 cycles

b. 5hz for 15 cycles

c. 8hz for 15 cycles

DIC Settings:

Ratio: _____, Area: _____, Threshold: _____

Tissue storage:

□ Unused sample: store fresh tissue in centrifuge tube in **-80C (FIRSTLY before test)**

□ Tested sample: in 10% formalin (no longer than ~1-2 weeks)

Clean up: *ensure that all equipment and tissue bath container are "sterilized" following usage; wipe the mounting system with alcohol to remove blood stains and tissue residue.

Notes:

APPENDIX B: POST DATA ANALYZING PROTOCOL

PROCEDURES:

Calculate Stretch

1. Go to Matlab_based_DIC_code___Version_1___130814_EJ→Matlab DIC files
2. Open image_setup_GUI and choose open .tif, and leave image skip = 1.
3. Next, run correlate_images_GUI. Choose to run parallel first, if correlation is poor, choose to run in serial with the reference as the 1st image. Correlation can be verified using step 4. You will be prompted with "How would you like to make this grid?". Click "Pick Center and grid size". Click on the center point for the grid on the image. Enter dimensions of 300x300 pixels. Enter step size of 30 pixels. Choose "Keep this grid" if the grid is centered and is acceptable.
4. Run visualize_data_GUI. Run at the default settings and click through the contour plot of the images to ensure the images are well correlated. Redo correlation if there are many white boxes that appear.
5. After we have well correlated reduced data, we can run the correlation with the full data. Perform steps 3-4 again but with the full data.
6. Run compute_data_GUI. Select the F_all to calculate the deformation tensor. The tensor contains the stretches in all directions. Save as gradient(LV/RV/test) file.
7. Go into the raw data folder, open "Image_Timestamps" and copy-paste the time data of the last cycle into column A of a new Excel sheet named Stretch.xlsx.
8. Open the gradient Excel file and copy F11 (column A) and F22 (column D) into column B and C of Stretch.xlsx, respectively.
9. For the data that used marker rather than powder, directly run Marker_tracker, adjust the ratio, area and threshold lines as needed to make sure the four markers were accurately captured. Please refer to the Appendix C for the Marker_tracker code.

Calculate Force (A or B)

Option A: Manual

10. In the raw force file, there are 4 columns. 1: global time, 2: longitudinal force, 3: circumferential force, and 4: local time. The local time is used to find when the camera started taking pictures of the tissue. Scroll through the local time and find the last 0. The last 0 is used to determine the 0 timepoint for our global time. In the 5^{th} column, take the difference of the global and local time for about 0.2 seconds (global time) to find the offset. Using that offset, find where the difference between the offset and global time is equal to 0. Enter a formula (=A1-offset) and copy the formula down the entire column. Match offset time to time scale of Stretch file.
11. Find min (B:B) and min(C:C). Copy Column B and C (from appropriate time scale) into a new excel file. Use the min B and min C to adjust the force data by adding the minimum (if it is offset in the negative direction) and subtracting (if it is offset in the positive direction) to the force data in column B and C respectively.
12. In a new excel sheet, place new time data in column A and new force data in Column B and C, respectively. Name this file Force.xlsx

Option B: Mat lab

13. To use Find_Force.m, first save the raw force data (labeled 0-1, 1-0, 1-1, 1-2, or 2-1) as an excel file names Force_1.xlsx in the mat lab DIC folder. Run Find_Force.m code and it will produce a Force.xlsx file in the DIC folder. This is your force file.

Sync Stress and Strain

14. Place both Force.xlsx and Stretch.xlsx into the same directory as Biaxial_Sync.m.
15. Run Biaxial_sync. Enter in the thickness and width of the tissue slice.
16. This will produce an EngStress_resampled.xlsx file with stress resampled to the strains. This is because the camera snaps an image of the tissue every 1 s, whereas the load cell measures force every 0.1 s. Engineering stress is calculated by taking the force/(thickness*width). After the raw force has been converted into engineering stress, the MATLAB code uses a cubic smoothing spline function to fit the engineering stress with stretch.

Determine Stress vs Strain

17. Next, run the StressvsStrain.m file. This code will calculate **Green strain** from stretch and calculate **2nd PK stress** from engineering stress. The output file will be a Stress_Strain.xlsx with all the stress vs strain data in both longitudinal and circumferential directions.
18. The Stress_Strain.xlsx should then be renamed to Stress_Strain_LV or Stress_Strain_RV and placed into the appropriate folder containing the date and heart number.

APPENDIX C: MATLAB CODE FOR THE DEFORMATION ANALYSIS USED MARKERS

```
clc
clear all
imageData = imfinfo('image000.tif');%input('Enter name of movie file (with extension): ', 's');
imagePre = 'image';
excelFile = 'data';%input('Enter the name you want for output Excel file: ', 's');
%BiaxVid = VideoReader(movieFile);
%nFrames = BiaxVid.NumberOfFrames;
vidHeight = imageData.Height;
vidWidth = imageData.Width;
%fprintf('The total frames in this movie are: %d\n', nFrames);
startFrame = str2num(input('Enter starting frame number (Enter 1): ', 's'));
%startFrame = startFrame + rem(startFrame,3) + 1;
endFrame = str2num(input('Enter ending frame number (Enter Total Number of Frames): ', 's'));
ratioConstant = 100; % shape contant (circularity vs oval)                % NOTE This value can be altered
to better run code
isoperimetricRatio = ratioConstant;
areaConstant = 100; %Threshold for marker size                             % NOTE This value can be altered to
better run code
areaThreshold = areaConstant;
numBlobs = 4; % Number of markers to track                                 % EDITED TO NUMBER OF
BLOBS NEEDED
nthFrame = 1; % Analyze every nth frame of the video
centArray = zeros(numBlobs,2,endFrame/nthFrame);
```

```
frames = zeros(vidHeight, vidWidth, 3, endFrame/nthFrame);
isgrey = imread('image000.tif');
matrix = size(isgrey);
matrix_length = length(matrix);
if matrix_length ~= 3
    for r=startFrame:nthFrame:endFrame
        p = r-1;
        file = sprintf('image%03d.tif',p);
        photo = imread(file);
        rgbImage = cat(3, photo, photo, photo);
        imwrite(rgbImage,file);  % may need to add "append"
    end
end
% EDITED: Lines 55-69 were added to be able to crop the images to the desired ROI
% when the ROI selection comes up on the first image starting in the top left
% corner click and drag to the bottom right corner to create a box. When the
% desired box is created for the select ROI right clip and select "crop image"
%
% firstimage = imread(cat(2,'image000.tif'));
% [cropped,rec] = imcrop(firstimage);
% xmin = floor(rec(1));
% ymin = floor(rec(2));
% wide = ceil(rec(3));
% high = ceil(rec(4));
% newrec = [xmin ymin wide high];
% imwrite(cropped, 'image000.tif');
```

```
% imdata2 = imfinfo('image000.tif');
% height = imdata2.Height;
% width = imdata2.Width;
% frames = zeros(height,width,3, endFrame/nthFrame);
%
% for k=startFrame:nthFrame:endFrame
%     if k < 10
%         imcrop = imread(cat(2,imagePre,'00',num2str(k),'.tif'));
%         file = sprintf('image%03d.tif',k);
%         newimage = imread(file);
%         cropped = imcrop(newimage,newrec);
%         imwrite(cropped,file);
%     elseif k < 100
%          imcrop = imread(cat(2,imagePre,'0',num2str(k),'.tif'));
%          file = sprintf('image%03d.tif',k);
%          newimage = imread(file);
%          cropped = imcrop(newimage,newrec);
%          imwrite(cropped,file);
%     end
% end
for i=startFrame:nthFrame:endFrame                    % EDITED to be startFrame rather than
nth frame
   j = i-1;                                           % EDITED (was i+11)
   if j < 10
      im1 = imread(cat(2,imagePre,'00',num2str(j),'.tif'));
   elseif j < 100
```

```
        im1 = imread(cat(2,imagePre,'0',num2str(j),'.tif'));
%     elseif j < 1000                                   %EDITED: Likely never using over 1000 images
so this part commented out
%         im1 = imread(cat(2,imagePre,'0',num2str(j),'.tif'));
    else
        im1 = imread(cat(2,imagePre,num2str(j),'.tif'));
    end
    frames(:,:,:,i/nthFrame) = im1;
    gray1 = rgb2gray(im1);
    gray2 = imcomplement(gray1);
    background = imopen(gray2, strel('disk', 40));
    gray3 = gray2 - background;
    threshold = 0.35;%graythresh(gray3); % Threshold for segmenting markers from background
    BW = im2bw(gray3, threshold);
    BW4 = bwareaopen(BW,areaThreshold);
    BW4 = imfill(BW4,'holes');
    cc1 = bwconncomp(BW4, 8);
%     while cc1.NumObjects < numBlobs %optional - adjust marker size threshold
%         areaThreshold = areaThreshold - 10;
%         BW4 = bwareaopen(BW4,areaThreshold);
%         cc1 = bwconncomp(BW4, 8);
%     end
    areaThreshold = areaConstant; % keep original size threshold
    blobdata1 = regionprops(cc1, 'Area', 'Centroid', 'Perimeter');
    c = zeros(cc1.NumObjects,1);
    for j=1:cc1.NumObjects
```

```
    Area = blobdata1(j).Area;
    Perimeter = blobdata1(j).Perimeter;
    c(j) = 4*3.141592*Area/Perimeter^2;
end
idx = find(c > isoperimetricRatio); %Count only markers over shape threshold
while length(idx) ~= numBlobs % optional - adjust shape threshold
    if (length(idx) < numBlobs)
        isoperimetricRatio = isoperimetricRatio - 0.005;
    end
        if (length(idx) > numBlobs)
        isoperimetricRatio = isoperimetricRatio + 0.005;
    end
    idx = find(c > isoperimetricRatio );
 end
temp=isoperimetricRatio;
isoperimetricRatio = ratioConstant; % keep original shape threshold
c=0;
BW3 = ismember(labelmatrix(cc1), idx);
cc2 = bwconncomp(BW3, 8);
labeled = labelmatrix(cc2);
blobdata2 = regionprops(cc2, 'Area', 'Centroid', 'Perimeter');
RGB_label = label2rgb(labeled, @spring, 'c', 'shuffle');
imshow(RGB_label);
%hold on;
fprintf('Frame Number: %d\n',i);
centroids = cat(1, blobdata2.Centroid);
```

```
    centArray(:,:,i/nthFrame) = centroids;
    for k = 1:numBlobs
        text(centroids(k,1),centroids(k,2), num2str(k));
        text(vidHeight/10, vidWidth/10, num2str(i));                %EDITED (made i from i-startframe)
    end
    currFrame = getframe;

    %writeVideo(vidObj, currFrame);
    end
%Get marker locations
temp1 = 10000;
arrayFinal = zeros(numBlobs,2,length(centArray));
arrayFinal(:,:,1) = centArray(:,:,1);
%arrayFinal = centArray;
for g = 2:length(centArray)
    for h = 1:numBlobs
        for j = 1:numBlobs
            distance = sqrt((centArray(h,1,g) - arrayFinal(j,1,g-1))^2 + (centArray(h,2,g) - arrayFinal(j,2,g-
1))^2);
            if distance < temp1
                temp1 = distance;
                index = j;
%             else index = j;     %ADDED
            end
        end
        arrayFinal(index,:,g) = centArray(h,:,g);
```

```
        temp1 = 1000;
        index = 0;
    end
end
% Create video
vidObj = VideoWriter(cat(2,excelFile,'_Video'));
open(vidObj);
for i = nthFrame:nthFrame:endFrame
    imshow(cast(frames(:,:,:,i/nthFrame),'uint8'));
    hold on;
    for k = 1:numBlobs
        text(arrayFinal(k,1,i/nthFrame),arrayFinal(k,2,i/nthFrame), num2str(k));
        text(vidHeight/10, vidWidth/10, num2str(i));                    %EDITED (made i from i-startframe)
    end
    c = getframe;
    writeVideo(vidObj, c);
end
close(vidObj);
% % This was specific to a particular marker orientation - adjust strain
% % calculation to meet your configuration.
% clc
% matrix = input('Enter blob order starting from lower left corner and up: ', 's');
% x = zeros(length(matrix),1);
% for f=1:length(matrix)
%     x(f) = str2num(matrix(f));
% end
```

```
hold off;
%xlswrite(cat(2,excelFile,'_Longitudinal.xlsx'), [strain1',strain2',strain3']);
%% Finite Strain Calculation
% MATT EDITED WHOLE SECTION - Commented out old parts
% Points = [1,3,4];
% Gradients = zeros(length(arrayFinal),9,size(Points,1));
% Strains = zeros(length(arrayFinal),3,size(Points,1));
% Gradients = zeros(length(arrayFinal),9,size(Points,1));
% Strains = zeros(length(arrayFinal),3,size(Points,1));
Identity = [1,0;0,1];
% Undeformed coordinates
x01 = arrayFinal(1,1,1);
x02 = arrayFinal(2,1,1);
x03 = arrayFinal(3,1,1);
x04 = arrayFinal(4,1,1);
x0 = [x01,x02,x03,x04];
x0average = mean(x0);
y01 = arrayFinal(1,2,1);
y02 = arrayFinal(2,2,1);
y03 = arrayFinal(3,2,1);
y04 = arrayFinal(4,2,1);
y0 = [y01,y02,y03,y04];
y0average = mean(y0);
% dXA1 = arrayFinal(pA,1,1) - arrayFinal(po,1,1);
% dXA2 = arrayFinal(po,2,1) - arrayFinal(pA,2,1);
% dXB1 = arrayFinal(pB,1,1) - arrayFinal(po,1,1);
```

```
% dXB2 = arrayFinal(po,2,1) - arrayFinal(pB,2,1);
% XMatrix = [dXA1,dXB1;dXA2,dXB2];
% Deformed Coordinates
x = zeros(numBlobs,1);
y = zeros(numBlobs,1);
xs = zeros(2,1);
ys = zeros(2,1);
Xdisplacements = zeros(1,numBlobs,length(arrayFinal));      % displacements in x-direction for each dot
per image
Ydisplacements = zeros(1,numBlobs,length(arrayFinal));      % displacements in y-direction for each dot
per image
Xaverages = zeros(1,1,length(arrayFinal));                  % Average of x-displacements for all dots per
image
Yaverages = zeros(1,1,length(arrayFinal));                  % Average of y-displacements for all dots per
image
Xshear = zeros(1,2,length(arrayFinal));                     % Shear distances in x-direction
Yshear = zeros(1,2,length(arrayFinal));                     % Shear distances in y-direction
XshearAvg = zeros(1,1,length(arrayFinal));                  % Average of shear distances in x-direction
YshearAvg = zeros(1,1,length(arrayFinal));                  % Average of shear distances in y-direction
for j=2:length(arrayFinal)
   for k = 1:numBlobs
        x(k,1) = arrayFinal(k,1,j)-arrayFinal(k,1,j-1); % x displacement from previous to current image
        y(k,1) = arrayFinal(k,2,j)-arrayFinal(k,2,j-1); % y displacement from previous to current image
        x_avg = mean(x);                        % Average of the four x-displacements
        y_avg = mean(y);                        % Average of the four y-displacements
        xs = ((x(1,1)-x(2,1))+(x(3,1)-x(4,1)))/2;       %shear calculation in x direction (averaged)
```

```
        ys = ((y(1,1)-y(3,1))+(y(2,1)-y(4,1)))/2;       %shear calculation in y direction
    end
%       xs = x(1,1,j)-x(2,1,j
%       xs(1,1) = (arrayFinal(1,1,j)-arrayFinal(2,1,j));
%       xs(2,1) = (arrayFinal(3,1,j)-arrayFinal(4,1,j));
%       ys(1,1) = (arrayFinal(4,2,j)-arrayFinal(2,2,j));
%       ys(2,1) = (arrayFinal(3,2,j)-arrayFinal(1,2,j));
Xdisplacements(1,:,j) = x;
Ydisplacements(1,:,j) = y;
Xaverages(1,1,j) = x_avg;
Yaverages(1,1,j) = y_avg;
Xshear(1,:,j) = xs;
Yshear(2,:,j) = ys;
for i=1:length(arrayFinal)              %measures the accumulation of x and y normal and shear
displacements
    Y=sum(Yaverages(1,1,1:i))/y0average+1;   %y direction stretch
    X=sum(Xaverages(1,1,1:i))/x0average+1;   %x direction stretch
    Ys=sum(Yshear(2,1,1:i))/y0average+1;       %y direction shear stretch
    Xs=sum(Xshear(1,1,1:i))/x0average+1;       %x direction shear stretch
    F = [X,Y;Xs,Ys];
    Strains(i,1) = 0.5*(F(1,1)*F(1,1)-1); % Principle direction 1
    Strains(i,2) = 0.5*(F(1,2)*F(1,2)-1); % Priciple direction 2
    Strains(i,3) = 0.5*(F(2,1)*F(2,1)-1); % Shear direction 1
    Strains(i,4) = 0.5*(F(2,2)*F(2,2)-1); % Shear direction 2
%     C = transpose(F)*F;
%     E = 0.5*(C-Identity);       % Green Lagrange Strain Tensor
```

```
%     Strains(i,1) = E(1,1); % Principle direction 1
%     Strains(i,2) = E(1,2); % Priciple direction 2
%     Strains(i,3) = E(2,1); % Shear direction 1
%     Strains(i,4) = E(2,2); % Shear direction 2
end
end
plot(Strains(:,:))
xlabel('number of images')
ylabel('Green Strain')
legend('Longitudinal','Circumferential','ShearL','ShearC')
xlswrite(cat(2,excelFile,'_E_L.xlsx'),Strains);
% xlswrite(cat(2,excelFile,'_E_L.xlsx'),Strains);
%     dxA1 = arrayFinal(pA,1,j) - arrayFinal(po,1,j-1);
%     dxA2 = arrayFinal(po,2,j) - arrayFinal(pA,2,j);
%     dxB1 = arrayFinal(pB,1,j) - arrayFinal(po,1,j);
%     dxB2 = arrayFinal(po,2,j) - arrayFinal(pB,2,j);
%     xMatrix = [dxA1,dxB1;dxA2,dxB2];
%     F = xMatrix/XMatrix;
%     Gradients(j,1,i) = F(1,1); % Principle direction 1
%     Gradients(j,2,i) = F(1,2);  % Shear direction 1
%     Gradients(j,4,i) = F(2,1);  % Shear direction 2
%     Gradients(j,5,i) = F(2,2); % Priciple direction 2
%     Gradients(j,9,i) = 1/(F(1,1)*F(2,2)-F(1,2)*F(2,1)); %???
%     C = transpose(F)*F; % Right Cauchy-Green Strain Tensor
%     E = 0.5*(C-Identity);       % Green Lagrange Strain Tensor
%     Strains(j,1,i) = E(1,1);
```

```
%     Strains(j,2,i) = E(2,2);
%     Strains(j,3,i) = E(1,2);
%
% plot(Strains(:,1,i), '-');
%
% % end
%
% %Mean F and E
% Gradient = mean(Gradients,3);
% Strain = mean(Strains,3);
% plot(Strain(:,1),'b');                % EDITED to plot strain in all directions on one graph
% hold on
% plot(Strain(:,2),'r');
% plot(Strain(:,3),'g');
% xlabel('number of images')
% ylabel('Green Strain')
% legend('Longitudinal','Circumferential','Shear')
% hold off
% xlswrite(cat(2,excelFile,'_F_L.xlsx'),Gradient);
% xlswrite(cat(2,excelFile,'_E_L.xlsx'), Strain);
```

APPENDIX D: EQUATIONS DEVELOPMENT FOR THE QLV MODEL

$$\Psi = \frac{2\mu}{\alpha^2}(\lambda_1^\alpha + \lambda_2^\alpha + \lambda_3^\alpha - 3) + \frac{2k\mu}{\alpha^2}(I_4^{\alpha/2} + 2I_4^{-\alpha/4} - 3)$$

$$\mathbf{S}^e = 2\frac{\partial \Psi}{\partial \mathrm{C}} - p\mathbf{C}^{-1}$$

Since we performed the biaxial test and the 2nd term on the right side is relate with the fiber orientation and we only consider two main directions. As a result, when to derive the p, I did not include 2nd term.

Recall:

Original: $I_1 = \lambda_1^2 + \lambda_2^2 + \lambda_3^2$,

For our case, define $I_1 = \lambda_1^\alpha + \lambda_2^\alpha + \lambda_3^\alpha$

Then 1st term

$$\Psi = \frac{2\mu}{\alpha^2}(I_1 - 3)$$

Recall: $\mathbf{S}^e = 2\frac{\partial \Psi}{\partial I_1}\frac{\partial I_1}{\partial C}$

$$\mathbf{S}^e = 2\frac{\partial\left(\frac{2\mu}{\alpha^2}(I_1 - 3)\right)}{\partial I_1}\frac{\partial I_1}{\partial C} - p\mathbf{C}^{-1}$$

$$\frac{\partial\left(\frac{2\mu}{\alpha^2}(I_1 - 3)\right)}{\partial I_1} = \frac{2\mu}{\alpha^2}$$

$$\frac{\partial I_1}{\partial C} = \frac{\partial(\lambda_1^\alpha + \lambda_2^\alpha + \lambda_3^\alpha)}{\partial C} = \begin{bmatrix} \alpha/2((\lambda_1^2)^{\frac{\alpha}{2}-1}) & 0 & 0 \\ 0 & \alpha/2((\lambda_2^2)^{\frac{\alpha}{2}-1}) & 0 \\ 0 & 0 & \alpha/2((\lambda_3^2)^{\frac{\alpha}{2}-1}) \end{bmatrix}$$

$$= \begin{bmatrix} \alpha/2(\lambda_1^{\alpha-2}) & 0 & 0 \\ 0 & \alpha/2(\lambda_2^{\alpha-2}) & 0 \\ 0 & 0 & \alpha/2(\lambda_3^{\alpha-2}) \end{bmatrix} = \alpha/2\begin{bmatrix} (\lambda_1^{\alpha-2}) & 0 & 0 \\ 0 & (\lambda_2^{\alpha-2}) & 0 \\ 0 & 0 & (\lambda_3^{\alpha-2}) \end{bmatrix}$$

So:

$$\mathbf{S}^e = 2 * \frac{2\mu}{\alpha^2} * \alpha/2 \begin{bmatrix} (\lambda_1^{\alpha-2}) & 0 & 0 \\ 0 & (\lambda_2^{\alpha-2}) & 0 \\ 0 & 0 & (\lambda_3^{\alpha-2}) \end{bmatrix} - p\mathbf{C}^{-1}$$

$$\mathbf{S}^e = \frac{2\mu}{\alpha} \begin{bmatrix} (\lambda_1^{\alpha-2}) & 0 & 0 \\ 0 & (\lambda_2^{\alpha-2}) & 0 \\ 0 & 0 & (\lambda_3^{\alpha-2}) \end{bmatrix} - p\mathbf{C}^{-1}$$

$$\mathbf{S}^e = \frac{2\mu}{\alpha} \begin{bmatrix} (\lambda_1^{\alpha-2}) & 0 & 0 \\ 0 & (\lambda_2^{\alpha-2}) & 0 \\ 0 & 0 & (\lambda_1^{2-\alpha}\lambda_2^{2-\alpha}) \end{bmatrix} - p\mathbf{C}^{-1}$$

Recall:

$$\mathbf{C} = \begin{bmatrix} \lambda_1^2 & 0 & 0 \\ 0 & \lambda_2^2 & 0 \\ 0 & 0 & \lambda_3^2 \end{bmatrix}$$

$$\mathbf{C}^{-1} = \mathbf{F}^{-1}\mathbf{F}^{-T}$$

$$\mathbf{C}^{-1} = \begin{bmatrix} \frac{1}{\lambda_1^2} & 0 & 0 \\ 0 & \frac{1}{\lambda_2^2} & 0 \\ 0 & 0 & \frac{1}{\lambda_3^2} \end{bmatrix}$$

$$\mathbf{S}^1 = \frac{2\mu}{\alpha} \begin{bmatrix} (\lambda_1^{\alpha-2}) & 0 & 0 \\ 0 & (\lambda_2^{\alpha-2}) & 0 \\ 0 & 0 & (\lambda_1^{2-\alpha}\lambda_2^{2-\alpha}) \end{bmatrix} - p \begin{bmatrix} \frac{1}{\lambda_1^2} & 0 & 0 \\ 0 & \frac{1}{\lambda_2^2} & 0 \\ 0 & 0 & \lambda_1^2\lambda_2^2 \end{bmatrix}$$

Then

$$S_1^1 = \frac{2\mu}{\alpha}\lambda_1^{\alpha-2} - p\frac{1}{\lambda_1^2}$$

$$S_2^1 = \frac{2\mu}{\alpha}\lambda_2^{\alpha-2} - p\frac{1}{\lambda_2^2}$$

$$S_3^1 = \frac{2\mu}{\alpha}(\lambda_1^{2-\alpha}\lambda_2^{2-\alpha}) - p\lambda_1^2\lambda_2^2$$

Assume $S_3^e = 0$

$$\frac{2\mu}{\alpha}(\lambda_1^{2-\alpha}\lambda_1^{2-\alpha}) = p\lambda_1^2\lambda_2^2$$

$$p = \frac{\frac{2\mu}{\alpha}(\lambda_1^{2-\alpha}\lambda_1^{2-\alpha})}{\lambda_1^2\lambda_2^2}$$

$$I_4 = \lambda_1^2 cos\theta^2 + \lambda_2^2 sin\theta^2$$

Then 2nd term

$$\Psi = \frac{2k\mu}{\alpha^2}(I_4^{\alpha/2} + 2I_4^{-\alpha/4} - 3)$$

Recall: $\mathbf{S}^e = 2\frac{\partial\Psi}{\partial I_1}\frac{\partial I_1}{\partial C}$

$$\mathbf{S}^e = 2\frac{\partial\left(\frac{2k\mu}{\alpha^2}(I_4^{\alpha/2} + 2I_4^{-\alpha/4} - 3)\right)}{\partial I_4}\frac{\partial I_4}{\partial C}$$

$$\mathbf{S}^e = 2\frac{\partial\left(\frac{2k\mu}{\alpha^2}(I_4^{\alpha/2})\right)}{\partial I_4}\frac{\partial I_4}{\partial C} + 2\frac{\partial\left(\frac{2k\mu}{\alpha^2}(2I_4^{-\alpha/4}\right)}{\partial I_4}\frac{\partial I_4}{\partial C}$$

$$\frac{\partial\left(\frac{2k\mu}{\alpha^2}(I_4^{\alpha/2})\right)}{\partial I_4} = \frac{2k\mu}{\alpha^2} * \frac{\alpha}{2} * I_4^{\frac{\alpha}{2}-1} = \frac{k\mu}{\alpha}I_4^{\frac{\alpha}{2}-1}$$

$$\frac{\partial\left(\frac{2k\mu}{\alpha^2}(2I_4^{-\alpha/4}\right)}{\partial I_4} = \frac{2k\mu}{\alpha^2} * 2 * \left(-\frac{\alpha}{4}\right) * I_4^{-\frac{\alpha}{4}-1} = -\frac{k\mu}{\alpha}I_4^{-\frac{\alpha}{4}-1}$$

$$\frac{\partial I_4}{\partial C_{2\ by\ 2}} = \frac{\partial(\lambda_1^2 cos\theta^2 + \lambda_2^2 sin\theta^2)}{\partial C_{2\ by\ 2}} = \begin{bmatrix} cos\theta^2 & 0 \\ 0 & sin\theta^2 \end{bmatrix}$$

So:

$$\mathbf{S}^2 = 2\frac{k\mu}{\alpha}\left(I_4^{\frac{\alpha}{2}-1} - I_4^{-\frac{\alpha}{4}-1}\right)\begin{bmatrix} cos\theta^2 & 0 \\ 0 & sin\theta^2 \end{bmatrix}$$

$$S_1^2 = 2\frac{k\mu}{\alpha}\left(I_4^{\frac{\alpha}{2}-1} - I_4^{-\frac{\alpha}{4}-1}\right) * cos\theta^2$$

$$S_2^2 = 2\frac{k\mu}{\alpha}\left(I_4^{\frac{\alpha}{2}-1} - I_4^{-\frac{\alpha}{4}-1}\right) * sin\theta^2$$

As a result,

$$S_1^T = S_1^1 + S_1^2$$

$$S_1^T = \frac{2\mu}{\alpha}\lambda_1^{\alpha-2} + 2\frac{k\mu}{\alpha}\left(I_4^{\frac{\alpha}{2}-1} - I_4^{-\frac{\alpha}{4}-1}\right) * cos\theta^2 - p\frac{1}{\lambda_1^2}$$

$$S_2^T = \frac{2\mu}{\alpha}\lambda_2^{\alpha-2} + 2\frac{k\mu}{\alpha}\left(I_4^{\frac{\alpha}{2}-1} - I_4^{-\frac{\alpha}{4}-1}\right) * sin\theta^2 - p\frac{1}{\lambda_2^2}$$

And

$$p = \frac{\frac{2\mu}{\alpha}(\lambda_1^{2-\alpha}\lambda_2^{2-\alpha})}{\lambda_1^2\lambda_2^2}$$

$$S_1^T = \frac{2\mu}{\alpha}\lambda_1^{\alpha-2} + 2\frac{k\mu}{\alpha}\left(I_4^{\frac{\alpha}{2}-1} - I_4^{-\frac{\alpha}{4}-1}\right) * cos\theta^2 - \frac{2\mu}{\alpha}(\lambda_1^{-\alpha-2}\lambda_2^{-\alpha})$$

$$S_2^T = \frac{2\mu}{\alpha}\lambda_2^{\alpha-2} + 2\frac{k\mu}{\alpha}\left(I_4^{\frac{\alpha}{2}-1} - I_4^{-\frac{\alpha}{4}-1}\right) * sin\theta^2 - \frac{2\mu}{\alpha}(\lambda_2^{-\alpha-2}\lambda_1^{-\alpha})$$

$$\frac{\partial S_1^T}{\partial \lambda_1} = (\alpha-2)\frac{2\mu}{\alpha}\lambda_1^{\alpha-3} + 2\frac{k\mu}{\alpha}\lambda_1 * cos\theta^4\left((\alpha-2)I_4^{\frac{\alpha}{2}-2} + \left(\frac{\alpha}{2}+2\right)I_4^{-\frac{\alpha}{4}-2}\right) + (\alpha+2)\frac{2\mu}{\alpha}(\lambda_1^{-\alpha-3}\lambda_2^{-\alpha})$$

$$\frac{\partial S_2^T}{\partial \lambda_2} = (\alpha-2)\frac{2\mu}{\alpha}\lambda_2^{\alpha-3} + 2\frac{k\mu}{\alpha}\lambda_2 * sin\theta^4\left((\alpha-2)I_4^{\frac{\alpha}{2}-2} + \left(\frac{\alpha}{2}+2\right)I_4^{-\frac{\alpha}{4}-2}\right) + (\alpha+2)\frac{2\mu}{\alpha}(\lambda_2^{-\alpha-3}\lambda_1^{-\alpha})$$

$$\frac{\partial S_1^T}{\partial \lambda_2} = 2\frac{k\mu}{\alpha}\lambda_2 * sin\theta^2 cos\theta^2\left((\alpha-2)I_4^{\frac{\alpha}{2}-2} + \left(\frac{\alpha}{2}+2\right)I_4^{-\frac{\alpha}{4}-2}\right) + 2\mu(\lambda_1^{-\alpha-2}\lambda_2^{-\alpha-1})$$

$$\frac{\partial S_2^T}{\partial \lambda_1} = 2\frac{k\mu}{\alpha}\lambda_1 * sin\theta^2 cos\theta^2\left((\alpha-2)I_4^{\frac{\alpha}{2}-2} + \left(\frac{\alpha}{2}+2\right)I_4^{-\frac{\alpha}{4}-2}\right) + 2\mu(\lambda_2^{-\alpha-2}\lambda_1^{-\alpha-1})$$

Validation:

Use one direction as an example

The eq I derived for 2nd PK: $S_1^1 = \frac{2\mu}{\alpha}\lambda_1^{\alpha-2} - p\frac{1}{\lambda_1^2}$

Recall: $\sigma = \frac{1}{J} * F * S * F^T$

$$\sigma_1^1 = \lambda_1 * S_1^1 * \lambda_1$$

$$\sigma_1^1 = \lambda_1 * \left(\frac{2\mu}{\alpha}\lambda_1^{\alpha-2} - p\frac{1}{\lambda_1^2}\right) * \lambda_1 = \frac{2\mu}{\alpha}\lambda_1^{\alpha} - p$$

$$\sigma_1^1 = \frac{2\mu}{\alpha}\lambda_1^{\alpha} - p$$

From the website you shared

Using the Ogden material model, the three principal values of the Cauchy stresses can now be computed as

$$\sigma_j = -p + \lambda_j \frac{\partial W}{\partial \lambda_j} = -p + \sum_{p=1}^{N} \mu_p \lambda_j^{\alpha_p}.$$

Which means:

$$\sigma_1^1 = \mu\lambda_1^{\alpha} - p$$

The difference is $\frac{2}{\alpha}$, this is because on the web, the equation is

In the Ogden material model, the strain energy density is expressed in terms of the principal stretches λ_j, $j = 1, 2, 3$ as:

$$W(\lambda_1, \lambda_2, \lambda_3) = \sum_{p=1}^{N} \frac{\mu_p}{\alpha_p}\left(\lambda_1^{\alpha_p} + \lambda_2^{\alpha_p} + \lambda_3^{\alpha_p} - 3\right)$$

But we are:

$$\Psi = \frac{2\mu}{\alpha^2}(\lambda_1^{\alpha} + \lambda_2^{\alpha} + \lambda_3^{\alpha} - 3)$$

The difference for the original eqs is $\frac{2}{\alpha}$.

As a result, I think what I derived for the first term are correct.

Derive for the $\mathbf{I}_4$ term:

$$\mathbf{I}_4 = a_0 \cdot \mathbf{C} \cdot a_0$$

$$a_0 = [cos\theta, sin\theta]$$

$$\mathbf{I}_4 = [cos\theta, sin\theta]\begin{bmatrix}\lambda_1^2 & 0\\ 0 & \lambda_2^2\end{bmatrix}\begin{bmatrix}cos\theta\\ sin\theta\end{bmatrix}$$

$$\mathbf{I}_4 = [cos\theta\lambda_1^2 \quad sin\theta\lambda_2^2]\begin{bmatrix} cos\theta \\ sin\theta \end{bmatrix}$$

$$\mathbf{I}_4 = cos\theta^2\lambda_1^2 + sin\theta^2\lambda_2^2$$

For the code that calculate the time derivative of the moduli, please refer to Appendix E

APPENDIX E: MATLAB CODE FOR TIME DERIVATIVE OF THE MODULI

```
%-------------------------------------------------------------------------
%This function solves for the time derivative of the moduli
%-------------------------------------------------------------------------
function [dAA,dAT,dTA,dTT] = dsde_ogden_QLV(stretchA,stretchT)


global mu alpha k
FA = stretchA;
FT = stretchT;


angle = orientation value.*pi/180;
I4 = (FA.^2.*cos(angle).^2 + FT.^2.*sin(angle).^2);
%-------------------------------------------------------------------------
% sA = 2.*mu./alpha.*(FA.^(alpha) + FA.^(-alpha).*FT.^(-alpha) + ...
%     k.*(FA.^alpha - FA.*(-alpha/2)));
% sT = 2.*mu./alpha.*(FT.^(alpha) + FA.^(-alpha).*FT.^(-alpha));


%d_stressA/d_stretchA
% dAA = 2.*mu.*(FA.^(alpha-1) + FA.^(-alpha-1).*FT.^(-alpha)) + ...
%     4.*cos(angle).^2.*k.*mu./alpha.*FA.* (I4.^(alpha./2-1) - I4.^(-alpha./4-1)...
%     + FA.^2.*cos(angle).^2.*((alpha./2-1).*I4.^(alpha./2-2) + ...
%     (alpha./4+1).*I4.^(-alpha./4-2)));
% 2nd PK
dAA = (alpha-2).*2.*mu./alpha.*FA.^(alpha-
3)+2.*k.*mu./alpha.*FA.*cos(angle).^4.*((alpha-2).*I4.^(alpha./2-
```

```
2)+(alpha./2+2).*I4.^(-alpha./4-2))+(alpha+2).*2.*mu./alpha.*FA.^(-alpha-3).*FT.^(-
alpha);
%-------------------------------------------------------------------------
%d_stressA/d_stretchT
% dAT = 2.*mu.*FA.^(-alpha).*FT.^(-alpha-1) + ...
%     4.*cos(angle).^2.*sin(angle).^2.*k.*mu./alpha.*FA.^2.*FT.* ...
%     ((alpha./2-1).*I4.^(alpha./2-2) + (alpha./4+1).*I4.^(-alpha./4-2));
% 2nd PK
dAT = 2.*k.*mu./alpha.*FT.*sin(angle).^2.*cos(angle).^2.*((alpha-2).*I4.^(alpha./2-
2)+(alpha./2+2).*I4.^(-alpha./4-2))+2.*mu.*FA.^(-alpha-2).*FT.^(-alpha-1);
%-------------------------------------------------------------------------
%d_stressT/d_stretchA
% dTA = 2.*mu.*FT.^(-alpha).*FA.^(-alpha-1) + ...
%     4.*cos(angle).^2.*sin(angle).^2.*k.*mu./alpha.*FT.^2.*FA.* ...
%     ((alpha./2-1).*I4.^(alpha./2-2) + (alpha./4+1).*I4.^(-alpha./4-2));
% 2nd PK
dTA = 2.*k.*mu./alpha.*FA.*sin(angle).^2.*cos(angle).^2.*((alpha-2).*I4.^(alpha./2-
2)+(alpha./2+2).*I4.^(-alpha./4-2))+2.*mu.*FT.^(-alpha-2).*FA.^(-alpha-1);


%-------------------------------------------------------------------------
%d_stressA/d_stretchA
% dTT = 2.*mu.*(FT.^(alpha-1) + FT.^(-alpha-1).*FA.^(-alpha)) + ...
%     4.*sin(angle).^2.*k.*mu./alpha.*FT.* (I4.^(alpha./2-1) - I4.^(-alpha./4-1)...
%     + FT.^2.*sin(angle).^2.*((alpha./2-1).*I4.^(alpha./2-2) + ...
%     (alpha./4+1).*I4.^(-alpha./4-2)));
% 2nd PK
dTT = (alpha-2).*2.*mu./alpha.*FT.^(alpha-
3)+2.*k.*mu./alpha.*FT.*sin(angle).^4.*((alpha-2).*I4.^(alpha./2-
```

```
2)+(alpha./2+2).*I4.^(-alpha./4-2))+(alpha+2).*2.*mu./alpha.*FT.^(-alpha-3).*FA.^(-
alpha);
%-------------------------------------------------------------------------
end
```